Extreme Ultraviolet Lithography

Extreme Ultraviolet Lithography

Harry J. Levinson

SPIE PRESS
Bellingham, Washington USA

Library of Congress Control Number: 2020944342

Published by

SPIE
P.O. Box 10
Bellingham, Washington 98227-0010 USA
Phone: +1 360.676.3290
Fax: +1 360.647.1445
Email: books@spie.org
Web: http://spie.org

Copyright © 2020 Society of Photo-Optical Instrumentation Engineers (SPIE)

All rights reserved. No part of this publication may be reproduced or distributed in any form or by any means without written permission of the publisher.

The content of this book reflects the work and thought of the author. Every effort has been made to publish reliable and accurate information herein, but the publisher is not responsible for the validity of the information or for any outcomes resulting from reliance thereon.

Printed in the United States of America.
First Printing.
For updates to this book, visit http://spie.org and type “PM326” in the search field.
Cover foreground image by MS Mikal, courtesy of Shutterstock.

Table of Contents

Preface *ix*

1 Introduction **1**

1.1 Historical Background 1
1.2 Components of Lithographic Technology 3
1.3 Material Considerations and Multilayer Reflectors 4
1.4 General Issues 12
Problems 13
References 13

2 Sources of EUV Light **17**

2.1 Laser-Produced Plasma Light Sources 17
2.2 Discharge-Produced Plasma Sources 32
2.2.1 Z-pinch light sources 33
2.2.2 Electrode-based DPP sources 34
2.3 Free-Electron Lasers 36
Problems 40
References 41

3 EUV Exposure Systems **45**

3.1 Lithography in Vacuum 45
3.2 Illumination Systems 50
3.3 Projection Optics 54
3.4 Alignment Systems 60
3.5 Stages in EUV Lithography Systems 61
3.6 Focus Systems 61
Problems 63
References 63

4 EUV Masks **71**

4.1 Structure of EUV Masks 71
4.2 Multilayer and Mask Substrate Defects 77
4.3 Mask Flatness and Roughness 83
4.4 EUV Mask Fabrication 86
4.5 EUV Pellicles 87

4.6 Reticle Pods for EUV Masks 97
4.7 Alternative EUV Absorbers and Mask Architectures 98
Problems 102
References 102

5 EUV Resists 111
5.1 Exposure Mechanisms of Chemically Amplified EUV Resists 111
5.2 Stochastic Effects in EUV Lithography 115
5.3 New Concepts for Chemically Amplified Resists 126
5.4 Metal-Oxide EUV Resists 129
5.5 Scissioning Resists 130
5.6 Vacuum-Deposited Resists 130
5.7 Underlayers 131
Problems 134
References 134

6 Computational Lithography for EUV 141
6.1 Conventional OPC Considerations 142
6.2 The 3D Aspects of EUV Masks 147
6.3 Resist Physics 156
6.4 Imaging Optimization for EUV Lithography 159
Problems 162
References 162

7 Process Control for EUV Lithography 169
7.1 Overlay 170
7.2 Critical Dimension Control 176
7.3 Yield 178
Problems 183
References 183

8 Metrology for EUV Lithography 187
8.1 Mask Blank Defect Inspection 188
8.2 EUV Mask Qualification Tools 191
8.3 Tools for Qualifying Fabricated Masks 193
8.4 Tools for Material Testing 196
Problems 198
References 198

9 EUV Lithography Costs 203
9.1 Wafer Costs 203
9.1.1 Capital costs 203
9.1.2 Maintenance costs 208
9.1.3 Operating costs 209
9.1.4 Metrology costs 210

9.1.5 Wafer cost summary 211
9.2 Mask Costs 212
Problems 213
References 213

10 Extending EUV Lithography 215
10.1 How Low k_1 Can Go 215
10.2 Higher NA 217
10.3 Shorter EUV Wavelengths 225
10.4 EUV Multiple Patterning 226
10.5 The Future of EUV Lithography 227
Problems 228
References 228

Index 231

Preface

While writing the chapter on EUV lithography for *Principles of Lithography*, I found myself challenged with covering many key topics while limiting the length of the chapter to something appropriate for a book that surveyed all major aspects of lithography. It seemed that a book fully dedicated to EUV lithography might be useful. Although there are already a number of fine books that survey the various aspects of EUV lithography, these books are generally compilations of chapters written by multiple experts in individual subjects. I thought that it might be useful to have a book where every chapter is written from a single perspective: that of the practicing lithographer in a wafer fab.

To bring EUV lithography to full readiness for high-volume manufacturing, considerable development (and a fair amount of research) was needed in nearly facet of lithographic technology—equipment, resists, masks, metrology, and computational methods. Each of these topics is discussed in this book, with an emphasis on those aspects that are unique to EUV lithography. It is assumed that the reader has familiarity with optical lithography, since many of the concepts relevant to EUV lithography were developed and brought to maturity in the context of lithography at optical wavelengths.

For many years, it has been my privilege and a pleasure to have worked with numerous outstanding and inspiring engineers and scientists on EUV lithography. Many of these people were co-workers at Advanced Micro Devices (AMD), the Advanced Mask Technology Center (AMTC), and GLOBALFOUNDRIES, while I engaged with others through consortia, such as Sematech, the EUV LLC, INVENT, and Imec. I also benefitted from interactions with engineers, managers, and executives from companies who supply equipment or materials for lithography. Much of the material in this book originated with colleagues and co-workers whose names appear in the references. I hope that this book does justice to their work.

Numerous people provided material for this book, many through their publications, while others were kind enough to provide figures specifically for this book. I would like to thank the following people who provided figures and gave permission for their use: Dr. Bruno La Fontaine of ASML (Figs. 1.1 and 1.3); Mr. Kevin Nguyen and Ms. Shannon Austin of SEMI (Fig. 1.7);

Mr. Athanassios Kaliudis and Mr. Florian Heinig of Trumpf GmbH (Fig. 2.4); Dr. Torsten Feigl of optiX fab GmbH (Fig. 2.6); Dr. Hakaru Mizoguchi of Gigaphoton, Inc. (Fig. 2.8); Dr. Igor Fomenkov of ASML (Fig. 2.12); Dr. Anthony Yen of ASML (Figs. 2.13, 4.25, and 4.26); Dr. Patrick Naulleau of Lawrence Berkeley National Laboratory (Figs. 2.14 and 4.18); Mr. Toru Fujinami and Mr. Sam Gunnell of Energetiq (Fig. 2.18); Dr. Erik Hosler (Figs. 2.25 and 2.28); Dr. Winfried Kaiser of Carl Zeiss (Figs. 3.4 and 3.5); Dr. Yulu Chen of Synopsys, Inc. (Fig. 3.7); Dr. Sudhar Raghunathan (Fig. 3.9); Dr. Carlos A. Duran of Corning, Inc. (Figs. 3.11 and 3.12); Dr. David Trumper of MIT and Dr. Won-Jon Kim of Texas A&M University (Fig. 3.17); Dr. Obert Wood (Fig. 4.6); Dr. Uzodinma Okoroanyanwu of Univ. of Massachusetts (Fig. 4.22); Mr. Preston Williamson of Entegris (Fig. 4.31); Prof. Takahiro Kozawa of Osaka University (Fig. 5.1); Prof. Takeo Watanabe of Hyogo University (Fig. 5.11); Dr. Timothy Weidman of Lam Research, Inc. (Fig. 5.23); Dr. Lieve Van Look of Imec (Fig. 6.13); Dr. Peter De Bisschop of Imec (Fig. 6.18); Dr. Jan Van Schoot of ASML (Fig. 7.5); Dr. Yuya Kamei of Tokyo Electron Ltd. (Fig. 7.7); Mr. Masashi Sunako of Lasertec USA, Inc. (Fig. 8.4); Ms. Anna Tchikoulaeva of Lasertec USA, Inc. (Fig. 8.5); Dr. Klaus Zahlten of Carl Zeiss SMT GmbH (Fig. 10.7); and Dr. Vadim Vanine of ASML (Fig. 10.12).

Finally, I would like to thank my wife, Laurie, for her enduring patience.

Harry J. Levinson
August 2020

Chapter 1
Introduction

1.1 Historical Background

For several decades, the resolution capability of optical lithography was extended by a succession of transitions to shorter imaging wavelengths. The first commercially available wafer stepper operated at a visible wavelength (436 nm), while later generations of exposure tools imaged at mid-ultraviolet and deep-ultraviolet wavelengths (Table 1.1). During efforts to continue this process of improving resolution by using a wavelength of 157 nm, with F_2 excimer lasers as the light sources, a number of difficulties were encountered, and optical lithography was eventually extended not by using light with a wavelength of 157 nm but by adapting ArF lithography to an immersion configuration that enabled the numerical aperture (NA) to be increased to 1.35. There were some additional efforts to increase the numerical aperture of ArF immersion lithography further, but development activities were eventually suspended because progress was slow.[1] The shortest wavelength used in optical lithography continues to be 193 nm.

In spite of the lack of success in developing HVM-capable lithographic technologies at 157 nm (or shorter optical wavelengths), lithographers were not ready to discontinue the pursuit of extending lithographic capability. Considerable amounts of money and engineering effort were invested in developing x-ray lithography, with a very short wavelength of ~1 nm.

Table 1.1 The wavelengths used for lithography.

Wavelength	Light source	Year of first use in high-volume manufacturing (HVM)
436 nm	Mercury arc lamp (g-line)	1982
365 nm	Mercury arc lamp (i-line)	1990
248 nm	KrF excimer laser	1994
193 nm	ArF excimer laser	2001
13.5 nm	Laser-produced plasma	2019

Unfortunately, projection optics at this wavelength could not be fabricated, principally because there are no materials that are sufficiently transparent at $\lambda \approx 1$ nm to form refractive optics, or have sufficient reflectivity for near-normal incident light, thus precluding reflective optics. This meant that x-ray lithography involved proximity printing, resulting in two significant problems. First, the patterns on wafers are replicated 1:1 from the mask, so mask quality, in terms of registration, dimensional control and defects, had to be exceedingly good. Second, fundamentally and ultimately more consequential, were the diffraction effects that became insurmountable for printing features with dimensions <100 nm.

These problems with extending optical lithography to wavelengths shorter than 193 nm involved the lack of suitable transmissive or reflective optical materials for lenses, masks, and pellicles for enabling projection lithography with reduction lenses. However, in the 1980s, multilayer films were developed that provided practical reflectivities at wavelengths $4\ \text{nm} < \lambda < 25\ \text{nm}$.[2,3] This development led to proposals for lenses with all-reflecting optics that could be used for projection lithography.[4,5,6] Initially, this was referred to as soft x-ray lithography, but the name "extreme ultraviolet" was later adopted to distinguish this new type of projection lithography from proximity $1\times$ x-ray lithography. A nice review of the early history of EUV lithography was written by two pioneers of this technology, Dr. Obert Wood and Dr. Hiroo Kinoshita.[7] Another set of key early activities involved a consortium, the EUV Limited Liability Corporation (LLC), which produced the first full-field EUV exposure system.[8]

The consortium Sematech played a critical role in the next phase of EUV lithography development. In addition to co-sponsoring annual EUV lithography symposia, Sematech engaged in development activities directly. A small pilot line was established to produce low-defect EUV mask blanks.[9,10,11,12] The associated metrology capabilities were used to support mask blank fabrication at commercial suppliers. Sematech also funded an EUV Micro-Exposure Tool (MET) that was placed at a synchrotron light source at Lawrence Berkeley National Laboratory.[13,14] The EUV MET provided essential capability for improving EUV resists.[15,16]

Another key event in the development of EUV lithography was the decision by ASML to build a pair of full-field exposure tools, the Alpha Demo Tools (ADTs). These were installed at the consortia INVENT in Albany, NY and Imec in Leuven, Belgium, further expanding access to EUV exposure capability. The full-field exposure capability enabled the accomplishment of an important milestone in moving EUV lithography from the laboratory to the factory: the fabrication of functioning SRAMs on a test chip from Advanced Micro Devices with an interconnect layer patterned with EUV lithography.[17]

1.2 Components of Lithographic Technology

As noted, new wavelengths of light have been introduced repeatedly for use in semiconductor lithography. In order to bring the lithographic technologies at each wavelength to readiness for HVM, there were always engineering problems that needed to be solved. For example, in the transition from i-line lithography to deep-ultraviolet lithography, chemically amplified resists were introduced in order to achieve adequate exposure tool throughput, and the mercury arc lamp sources of light were later replaced by KrF excimer lasers. These were significant changes that required substantial development effort, even though many other aspects of lithography were largely unchanged. For example, photomask technology for DUV was nearly identical to that for i-line (except for pellicles, which did require the use of new materials). Few changes were required for computational models to describe the lithographic process, aside from performing calculations with a shorter wavelength of light.

For EUV lithography, every aspect of the technology is changed substantially (see Table 1.2). The optics are fully reflective, a substantial departure from what is found in optical tools. The masks are reflective as well, which is significant for mask blank manufacturing, mask metrology, process control, and computational aspects of EUV lithography. EUV resists have

Table 1.2 The components of lithographic technology in optical and EUV lithography. The aspects of lithographic technology that are new for EUV lithography will be the subjects of subsequent chapters of this book.

Component of lithographic technology	Optical lithography	EUV lithography
Light source	Mercury arc lamps and excimer lasers	Laser-produced plasmas
Illuminator	Highly flexible, large number of pixels, polarization control	Moderate flexibility, fewer pixels, only unpolarized light
Projection optics	All-refractive or catadioptric lenses	All reflective lenses
Resist	Capable of supporting patterning to near the optical diffraction limit	Patterning capability falls far short of diffraction limit
Reticles	Transmission, mature metrology available	Reflection, new metrology needed
Pellicles	Mature technology used routinely	Pellicles undergoing development
Process control	Have been addressing most sources of variation for many years	Multiple new sources of variation
Computational lithography	Models based on well-known physics	New physics required

been undergoing development for over two decades. For the most part, EUV resists have been chemically amplified resists based on KrF or ArF platforms. However, departures from chemically amplified resists are being explored, after a quarter century during which chemically amplified resists have composed the predominant resist platform for leading-edge lithography.

The objective for this book is to address the numerous aspects of lithography that, for EUV lithography, are significantly different from what is found in optical lithography. For example, the optics of EUV exposure tools differ significantly from lenses at optical wavelengths, while other key components, such as interferometers and encoders for stage control, are very similar. It is assumed that the reader is generally familiar with optical lithography, which will be referenced frequently.

1.3 Material Considerations and Multilayer Reflectors

The high absorbance of light by all materials for wavelengths shorter than 40 nm influences all aspects of EUV lithography (see Fig. 1.1). This absorption occurs largely at the atomic level; hence, it is principally determined by the elemental constituents of materials and otherwise only weakly dependent on other aspects of chemical composition. The Center for X-Ray Optics (CXRO) at the Lawrence Berkeley National Laboratory provides a convenient database of optical properties at EUV and x-ray wavelengths (see the X-Ray Database at http://cxro.lbl.gov/).

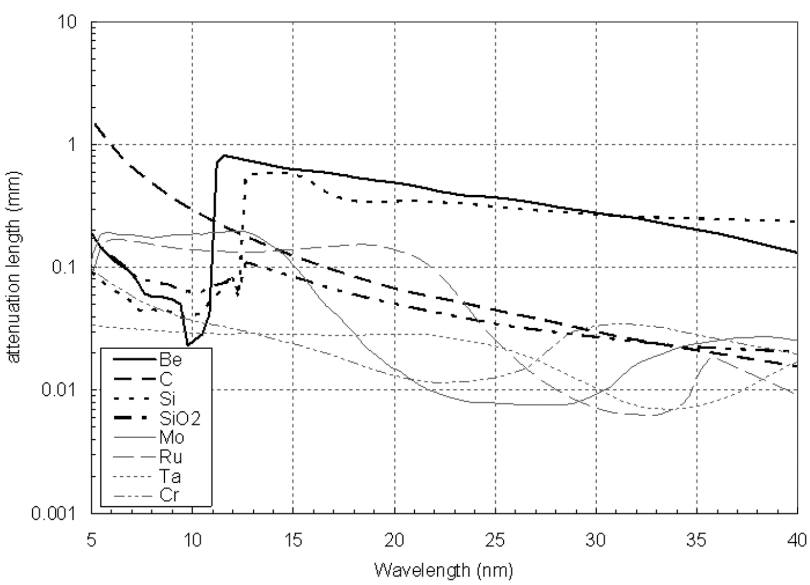

Figure 1.1 Attenuation length for selected materials at short wavelengths.[18] The attenuation length is the distance at which the intensity of light propagating through a material falls to 1/*e* of its initial value.

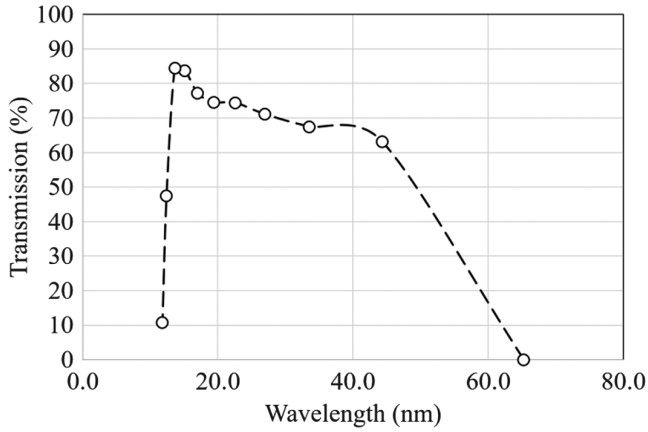

Figure 1.2 Calculated transmission of light through 100-nm-thick membranes of silicon, using the transmission calculator provided by the Center for X-Ray Optics (CXRO) at Lawrence Berkeley National Laboratory.

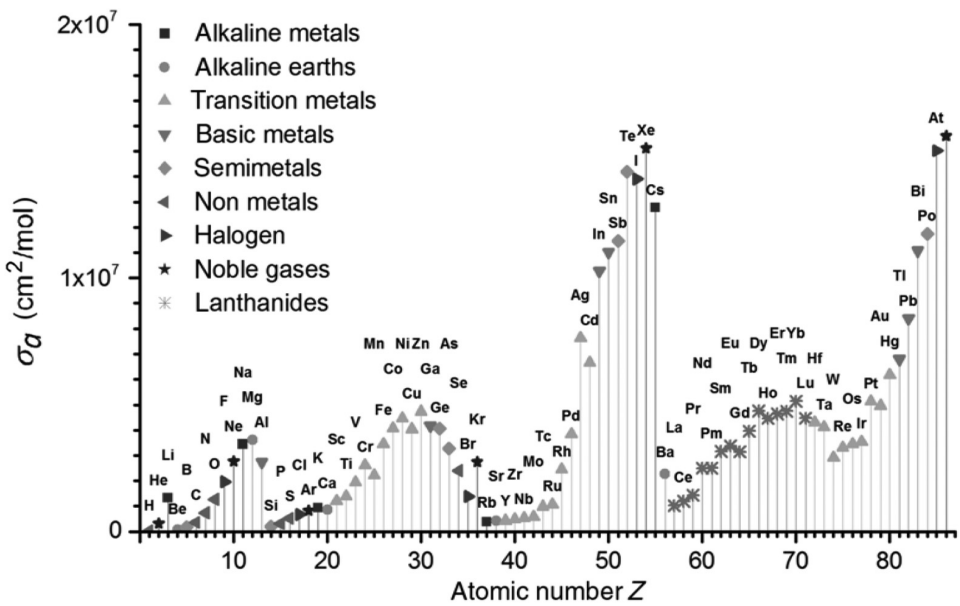

Figure 1.3 Atomic absorption cross-sections σ_a for elements between atomic numbers 1 and 86.[19,20]

The high absorbance of EUV light is illustrated in Fig. 1.2, which shows the transmission of EUV light at λ = 13.5 nm through 100-nm-thick films of silicon. As can be seen, transmission is less than 90% at all wavelengths for which data are plotted, for a thin film of an element that is less absorbent than most at λ = 13.5 nm (Fig. 1.3). Transmission would be effectively zero for

solids at thicknesses that are typical (millimeters) for lens elements in refractive lenses. Not only does this preclude refractive or catadioptric projection optics for EUV lithography exposure tools, but it has significance for many optical elements commonly found in lithography exposure tools—filters, polarizers, and components in illumination systems.

Further complicating the construction of imaging optics, the reflectivities of all homogenous materials become very small at EUV wavelengths, at least at the near-normal angles of incidence relevant to high-resolution imaging optics (see Fig. 1.4). Reflection occurs at interfaces between materials that have different indices of refraction. The larger the difference between the refractive indices of the materials is, the greater the reflectivity. At wavelengths <50 nm, all materials have indices of refraction ≈ 1. Thus, it is difficult to create high reflectance from a single interface, except at grazing angles of incidence.

However, at EUV wavelengths, it has proven possible to make mirrors with moderate reflectivity at near-normal angles of incidence, in the range of 60–70%, by the use of coatings consisting of multiple layers. Multilayer reflectors are made by depositing alternating layers of high-Z (Z is the atomic number) and low-Z materials, giving a small but effective difference between refractive indices at each interface. The net effect of small reflectivity at each interface can lead to moderately high reflectivity overall when the stack has a sufficient number of layers (Fig. 1.5), provided the layer stacking satisfies, at least approximately, the Bragg condition, where all of the reflected light rays

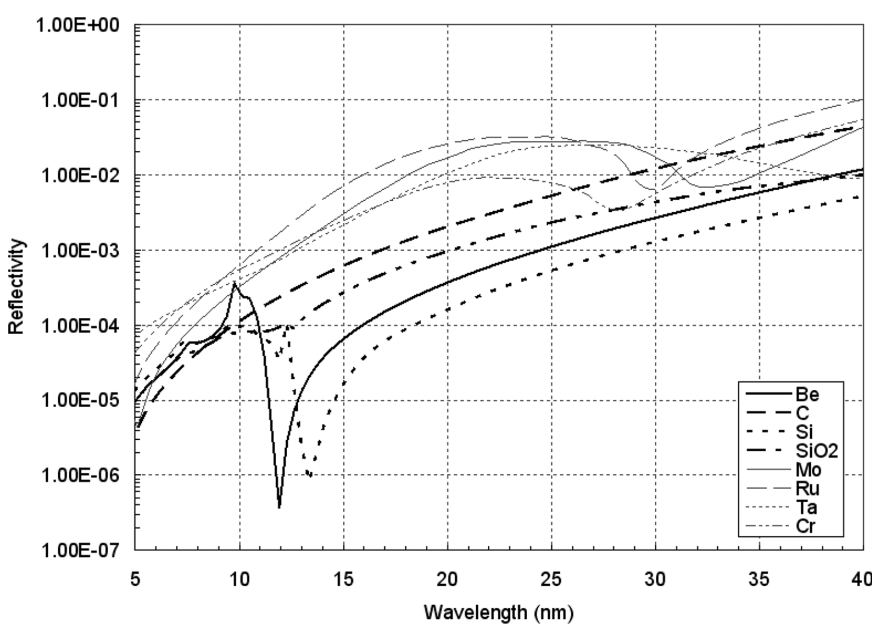

Figure 1.4 Reflectivity of selected materials at short wavelengths for normal incidence.[18]

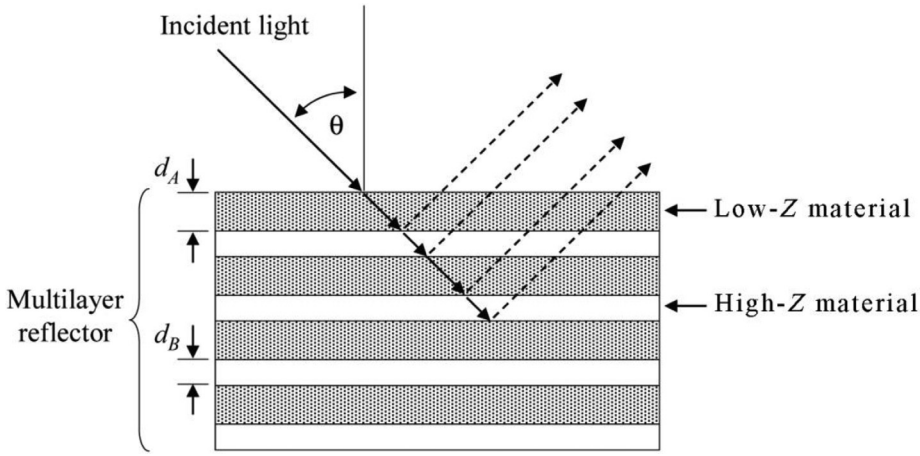

Figure 1.5 Illustration of how high total reflectivity is achieved from reflections from multiple interfaces.

are in-phase:[3]

$$d = \frac{m\lambda}{2\cos\theta\sqrt{1 - \frac{2\bar{\delta} - \bar{\delta}^2}{\cos^2\theta}}}, \quad m = 1,\ 2,\ \ldots, \tag{1.1}$$

where

$$\bar{\delta} = \frac{\delta_A d_A + \delta_B d_B}{d_A + d_B}. \tag{1.2}$$

The index of refraction of each layer is given by $n = 1 - \delta + i\beta$, while d_A, d_B, and θ are defined in Fig. 1.5, and $d = d_A + d_B$.

Although all materials are highly absorbent at EUV wavelengths, some are less absorbing than others. The materials chosen to comprise the multilayer stack must be relatively weak absorbers of EUV light, since the light must be able to penetrate to the lower layers of the film stack to achieve high total reflectivity. Several stacks have been identified as possible reflectors in the EUV, and these are listed in Table 1.3.

In the early days of EUV lithography development, it was not obvious what wavelength should be chosen for use in lithography. A shorter wavelength has theoretical advantages for better resolution, which suggested that EUV lithography should be based on a multilayer film, such as Mo/Be. However, because of beryllium's toxicity, there was a reluctance to adopt that metal for EUV lithography, and nearly all effort in EUV lithography today is focused on Mo/Si reflectors. For Mo/Si multilayers designed for near-normal reflectance, the molybdenum layers are ~3 nm thick, while the silicon layers are ~4 nm thick.[21] Because reflectance is angle dependent [Eq. (1.1)], graded

Table 1.3 EUV multilayer reflectors.[22,23,24,25]

Multilayer film stack	Peak wavelength of near-normal incidence	Reflectance achieved
Mo/Si	13.4	68.2%
$Mo/B_4C/Si$	13.5	70.0%
Mo_2C/Si	13.0	61.8%
Ru/Si	13.5	58.2%
Mo/Be	11.3	70.2%
MoRu/Be	11.3	69.3%

depositions are needed on optics that have light incident at varying angles over the mirror surfaces in order to maintain constant reflectance at the operating wavelength. This dependence on angle affects the imaging of mask patterns, as will be discussed further in subsequent chapters.

Reflectance versus wavelength for a Mo/Si multilayer stack is shown in Fig. 1.6. As can be seen in this figure, reflectance peaks around a given wavelength (in this case, ~13.4 nm). From Eq. (1.1), it is apparent that only a very small change in the thickness of layer films will cause a shift in peak wavelength (see Problem 1.3). Even if every mirror in the EUV system has very high peak reflectance, the overall system transmission can be low if these peak reflectances do not occur at nearly the same wavelength. A similar statement is true regarding the need to match the reflectance properties of the masks to those of the projection-optics mirrors.[26] When specifying the "operating" wavelength, it is important to pay attention to detail. As can be seen in Fig. 1.6, the curve of reflectance versus wavelength is asymmetric. It is standard to specify the operating wavelength as the center of the full-width at half-maximum (FWHM) range (Fig. 1.7).[27] Because of the asymmetry, this median wavelength typically differs from the peak wavelength.

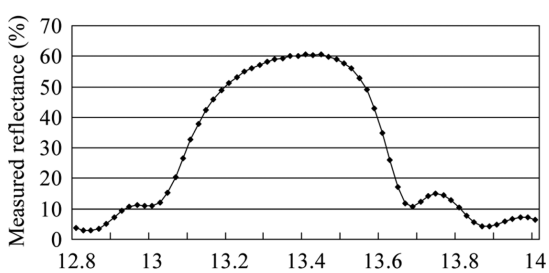

Figure 1.6 Reflectance at near-normal incidence versus wavelength for a multilayer reflector. The measurements were made at the Advanced Light Source (synchrotron) at Lawrence Berkeley National Laboratory on a substrate that was made into an EUV mask at Advanced Micro Devices.

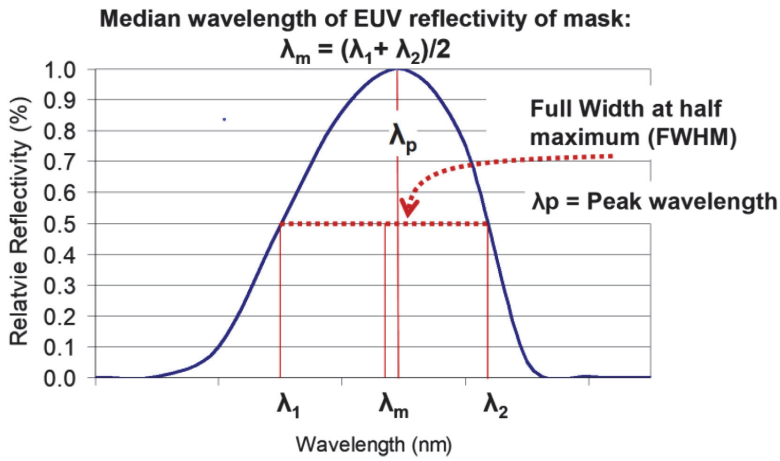

Figure 1.7 Curve showing the definition of median wavelength (λ_m) and how it can differ from the peak wavelength (λ_p).[27]

A consequence of the wavelength dependence of reflectivity, as shown in Fig. 1.6, is a narrowing bandwidth following multiple reflections by multilayer mirrors (see Problem 1.4). Only EUV light that is within the multiple-reflection bandwidth of the entire optical path will reach the wafer plane and expose resist. Each mirror in the illuminator and lens reduces the amount of light that can be used for exposing resist as a consequence of peak reflectances that are less than 100% and by bandwidth narrowing. Because peak reflectances are less than 70% for mirrors with Mo/Si multilayer reflectors, an additional pair of optical elements within the exposure path will reduce reflectance by more than a factor of two. For reasons of productivity, it is important to minimize the number of mirrors in the illuminator and projection optics.

Optical lithography has always been practiced at wavelengths where there are light sources that satisfy certain key requirements, particularly a narrow bandwidth and high intensity. For each optical lithographic technology, the optics and masks have been engineered around a wavelength where such a source exists. For EUV lithography, there are few options for masks and optics. EUV lithography must necessarily be practiced at wavelengths where there are multilayer reflectors with high reflectance. The light source needs to be engineered around the wavelength chosen on the basis of multilayer reflector capability, rather than the other way around. Because EUV lithography is practiced at wavelengths where high-intensity light sources were not established first, productivity due to low light intensity at the wafer has long been a concern with EUV lithographic technology, and considerable attention has been paid to maximizing multilayer reflectance and source-output power. EUV light sources will be discussed in detail in Chapter 2.

For EUV lithography, the semiconductor industry has settled on an operating wavelength of 13.5 nm. This choice was dictated in part by the selection of Mo/Si multilayers, which determined a range for possible operating wavelengths. The operating wavelength was further refined by matching the chosen wavelength to the peak outputs of candidate light sources at the time the wavelength was selected.[28]

The photon energy for light with a 13.5-nm wavelength is 91.8 eV. Such energy is above the ionization potential of all molecules and greater than the work functions of solids. As will be discussed in subsequent chapters, much of the radiation chemistry relevant to EUV lithography is mediated by photoelectrons generated by the absorption of photons rather than through direct photochemistry. The high energy of EUV photons also has an impact on the contamination of EUV optics.

High mirror reflectance is important for EUV exposure-tool productivity. Consider a system with six mirrors in the projection optics, five near-normal reflection mirrors in the illuminator, and a reflection mask. The EUV light reflects twelve times in such a system. A system in which each multilayer has 70% peak reflectance produces over 40% more light at the wafer plane than a system in which each multilayer reflector has 68% reflectance. Thus, even a small difference in reflectance is important for system productivity. Measured reflectances from multilayer stacks have typically been a few percent lower than the theoretical maximum. This is due in large measure to the nonideal density and homogeneity of the individual layers, as well as interface roughness and diffusion between layers.[2] Efforts to improve multilayer reflectance are focused on these factors.

The situation depicted in Fig. 1.5 is an idealization of a multilayer film. Transmission electron micrographs have revealed that the boundaries between molybdenum and silicon layers are not sharp in actual deposited films, and there are additional layers comprising mixtures of the two materials between the layers made purely of molybdenum and silicon (see Figs. 1.8 and 1.9). The degree of intermixing is dependent upon deposition conditions, and it differs between silicon deposited on molybdenum and molybdenum deposited on silicon.

Calculations of reflectance from multilayer stacks provide additional insight into the ramifications of intermixing. Notably, the wavelength at which peak reflectance occurs is shifted, and the height of the peak is reduced as a consequence of the intermixing. Optimized multilayers for maximum reflectance of the mirrors of the projection optics are useful for improving throughput and reducing lens heating (since most of the light that isn't reflected is absorbed). As will be seen in Chapter 6, maximizing reflectances of EUV masks may not provide the most optimized condition overall.

Intermixing can also increase when multilayers are heated. This can be mitigated to some extent by engineering the interfaces. In Mo/Si multilayers, the molybdenum and silicon films begin to intermix at

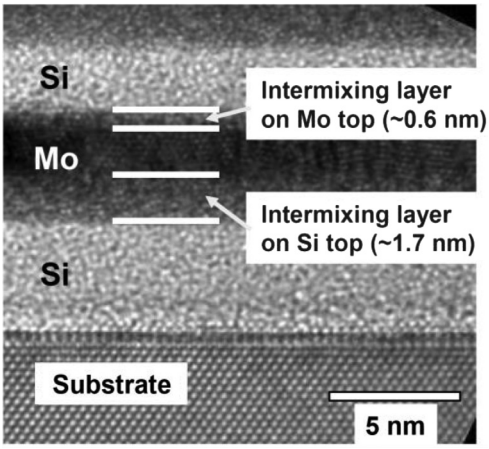

Figure 1.8 A high-resolution transmission electron micrography of a Mo/Si multilayer film deposited on the (001) surface of silicon.[29]

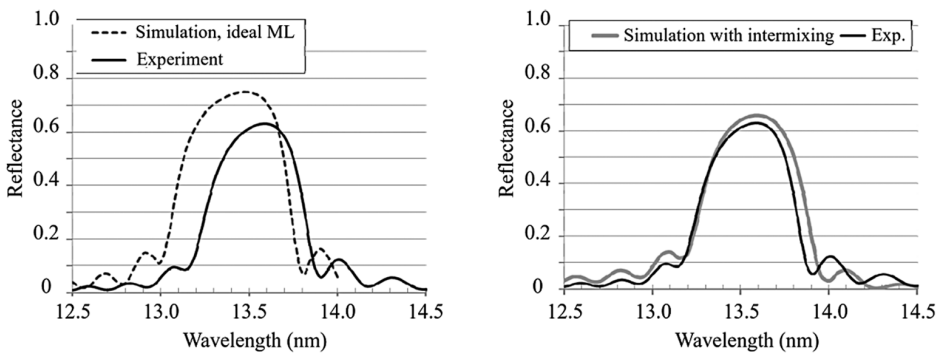

	Thickness (nm)	n	k
Si	4.16	0.99932	0.00183
Mo	2.78	0.92108	0.00644
Periodicity	6.94		

	Thickness (nm)	n	k
Si	2.506	0.99932	0.00183
$MoSi_X$	0.802	0.9693	0.004333
Mo	1.904	0.92108	0.00644
$MoSi_Y$	1.844	0.9693	0.00433
Periodicity	7.056		

Figure 1.9 Comparison of calculated reflection from Mo/Si multilayers with experiment for 6° angles of incidence. The parameters for the calculations are in the tables below the figures to which they apply.[30]

~150°C, while Mo_2C/Si films remain stable at temperatures approaching 600°C, with only a slightly lower peak reflectance (66.8%) than high-quality Mo/Si multilayers (68.6%).[31] With a B_4C layer inserted between the molybdenum and silicon films, a reflectance of 70% was achieved at a wavelength of 13.5 nm.[32,33] Even if the peak reflectance is maintained during heating, there may be a shift of the wavelength at which peak reflectance

occurs, as was observed in Mo/C/Si multilayers.[18,34] Films that are expected to experience high temperatures can be annealed prior to use, thereby shifting the wavelength at which peak reflectance occurs to the desired value. Instability at elevated temperatures limits the processes used to deposit and etch the absorbers on EUV masks. Without interface-engineered multilayers, only low-temperature processes can be used to fabricate EUV masks, including cleaning operations.

1.4 General Issues

When establishing a lithographic technology, it is essential that all relevant factors meet the requirements for high-volume manufacturing, which means that few factors can be considered in isolation. On the other hand, a book such as this one must necessarily have a linear flow for comprehensibility, so topics relevant to one subject may not be covered in the book until a later chapter. In this section, some brief mention will be made of important considerations that will be important for all aspects of EUV lithography but that will not be discussed in detail until later chapters.

One principal concern that affects all aspects of EUV technology is cost. There has been an enormous investment made into EUV lithography, and these investments need to be recovered. Moreover, extremely tight process requirements drive up the costs of equipment. This makes exposure tool productivity, driven by equipment reliability and throughput, very important.

A key issue that makes it challenging to achieve high throughput is light source power. As just discussed, EUV lithography must necessarily be practiced at wavelengths where there are multilayer films with high reflectance, not where there are strong sources of light. This is in stark contrast to optical lithography, which has always been practiced where there are intense sources of narrow-bandwidth light, such as at the spectral lines of mercury or at the emission wavelengths of excimer lasers. With EUV technology, there never seems to be enough photons.

Something else to keep in mind is that EUV lithography was first used in high-volume manufacturing for the 7-nm logic node, with a ~40-nm minimum metal pitch, and future use will be at even smaller dimensions. Device requirements for such small features drive the levels of performance necessary for EUV lithography. Overlay, critical dimension control, and line-edge roughness (LER) must be very tight, and all aspects must meet these demanding requirements. The world of EUV lithography is one in which 0.1 nm—an angstrom—is significant.

EUV lithography is practiced only for very-leading-edge integrated circuit processes. As such, all wafer equipment is designed for 300-mm wafers, and throughout this book it will always be assumed that wafers are 300 mm in diameter.

Problems

1.1 Show that the Rayleigh resolution of an EUV (λ = 13.5 nm) lithography system with NA = 0.25 is 33 nm, and that the Rayleigh depth of focus is 216 nm. Show that the resolution and depth of focus are 20.5 nm and 84 nm, respectively, for an EUV lens with 0.4 NA.

1.2 Show that Eq. (1.1) reduces to the conventional Bragg condition

$$d = \frac{m\lambda}{2\cos\theta},$$

when the indices of refraction of the materials in a multilayer film stack → 1.0.

1.3 Using the above formula for the conventional Bragg condition, show that each pair in a multilayer reflector should be 6.8 nm thick to produce peak reflectivity at a wavelength of 13.5 nm when the incident light is 6° from normal. (Assume that m = 1.) Show that a change in the film-pair thickness of 1 Å changes the peak wavelength by 0.2 nm.

1.4 Suppose the reflected light produced by a single multilayer mirror as a function of wavelength (Fig. 1.7) is approximated by a Gaussian

$$R(\lambda) = R_0 e^{\frac{-(\lambda-\lambda_0)^2}{2\sigma^2}}$$

where $FWHM \approx 2.355\sigma$. Show that the full width at half maximum is $FWHM/\sqrt{N}$ after N reflections.

1.5 The attenuation length of carbon for light with a wavelength of 13.5 nm is 155 nm. Show that the transmission of light through a six-mirror lens, where each mirror is coated with 1 nm of carbon, is 92.6% of an identical lens for which the mirrors have no carbon coating. (Remember that the light will travel twice through the carbon coating on each mirror.)

References

1 Details of the problems that led to the suspensions of F_2 lithography and high NA immersion lithography R&D are discussed in Chapter 10 of *Principles of Lithography*, 4th Edition, SPIE Press, 2019.
2 T.W. Barbee, S. Mrowka, and M.C. Hettrick, "Molybdenum-silicon multilayers for the extreme ultraviolet," *Appl. Optic.* **24**, p. 883 (1985).
3 S. Yulin, "Multilayer interference coatings for EUVL," in *Extreme Ultraviolet Lithography*, B. Wu and A. Kumar, Eds., McGraw Hill, New York (2009).

4 A.M. Hawryluk and L.G. Seppala, "Soft x-ray projection lithography using an x-ray reduction camera," *J. Vac. Sci. Technol. B* **6**, pp. 2161–2166 (1988).
5 H. Kinoshita, T. Kaneko, H. Takei, N. Takeuchi, and S. Ishihara, "Study on x-ray reduction projection lithography," presented at the 47th Autumn Meeting of the Japan Society of Applied Physics, Paper No. 28-ZF-15 (1986).
6 W. T. Silfast and O. R. Wood II, "Tenth micron lithography with a 10 Hz 37.2 nm sodium laser," *Microelectron. Eng.* Vol. **8**, pp 1711–1726 (1988).
7 H. Kinoshita and O. Wood, "EUV lithography: an historical perspective," in *EUV Lithography,* Chapter 1 in *EUV Lithography*, 2nd edition, Ed. V. Bakshi, SPIE Press (2018).
8 S. Wurm, "The EUV LLC: An Historical Perspective," Chapter 2 in *EUV Lithography*, 2nd edition, Ed. V. Bakshi, SPIE Press (2018).
9 A. O. Antohe, D. Balachandran, L. He, P. Kearney, A. Karumuri, F. Goodwin, and K. Cummings. "SEMATECH produces defect-free EUV mask blanks: defect yield and immediate challenges," *Proc. SPIE* Vol. **9422**, p. 94221B, 2015.
10 V. Jindal, P. Kearney, J. Sohn, J. Harris-Jones, A. John, M. Godwin, A. Antohe, et al. "Ion beam deposition system for depositing low defect density extreme ultraviolet mask blanks," *Proc. SPIE* Vol. **8322**, p. 83221W, 2012.
11 F. Goodwin, P. Kearney, A. J. Kadaksham, and S. Wurm. "Recent advances in SEMATECH's mask blank development program, the remaining technical challenges, and future outlook," *SPIE* Vol. **8886**, p. 88860C, 2013.
12 V. Jindal, P. Kearney, A. Antohe, M. Godwin, A. John, R. Teki, J. Harris-Jones, E. Stinzianni, and F. Goodwin, "Challenges in EUV mask blank deposition for high volume manufacturing," *Proc. SPIE* Vol. **8679**, p. 86791D, 2013.
13 P. P. Naulleau, C. N. Anderson, L. Baclea-an, P. Denham, S. George, and K. A. Goldberg M. Goldstein et al. "The SEMATECH Berkeley microfield exposure tool: learning at the 22-nm node and beyond," *SPIE* Vol. **7271**, p. 72710W, 2009.
14 P. P. Naulleau, C. N. Anderson, J. Chiu, K. Dean, P. Denham, S. George, K. A. Goldberg, et al. "Latest results from the SEMATECH Berkeley extreme ultraviolet microfield exposure tool," *Journal of Vacuum Science & Technology B: Microelectronics and Nanometer Structures Processing, Measurement, and Phenomena* **27**, no. 1 (2009): 66–70.
15 P. P. Naulleau, C. N. Anderson, J. Chiu, K. Dean, P. Denham, K. A. Goldberg, B. Hoef, et al., "Advanced extreme ultraviolet resist testing using the SEMATECH Berkeley 0.3-NA microfield exposure tool," *SPIE* Vol. **6921**, p. 69213N, 2008.

16 T. Wallow, C. Higgins, R. Brainard, K. Petrillo, W. Montgomery, C. Koay, G. Denbeaux, O. Wood, and Y. Wei, "Evaluation of EUV resist materials for use at the 32 nm half-pitch node," *SPIE* Vol. **6921**, p. 69211F, 2008.
17 B. La Fontaine, Y. Deng, R. Kim, H. J. Levinson, S. McGowan, U. Okoroanyanwu, R. Seltmann, C. Tabery, A. Tchikoulaeva, T. Wallow, O. Wood, J. Arnold, D. Canaperi, M. Colburn, K. Kimmel, C. Koay, E. McLellan, D. Medeiros, S. P. Rao, K. Petrillo, Y. Yin, H. Mizuno, S. Bouten, M. Crouse, A van Dijk, Y. van Dommelen, J. Galloway, S. Han, B. Kessels, B. Lee, S. Lok, B. Niekrewicz, B. Pierson, R. Routh, E. Schmitt-Weaver, K. Cummings, and J. Word, "The use of EUV lithography to produce demonstration devices," *Proc. SPIE* **6921**, 69210P (2008).
18 B. La Fontaine, "EUV optics," in *Extreme Ultraviolet Lithography*, B. Wu and A. Kumar, Eds., McGraw Hill, New York (2009).
19 R. Fallica, J. Haitjema, L. Wu, S. C. Ortega, A. M. Brouwer, and Y. Ekinci. "Absorption coefficient of metal-containing photoresists in the extreme ultraviolet." *Journal of Micro/Nanolithography, MEMS, and MOEMS* **17**, no. 2 (2018): 023505.
20 This graph was generated using values tabulated in B. L. Henke, E. M. Gullikson, and J. C. Davis. "X-ray interactions: photoabsorption, scattering, transmission, and reflection at E= 50-30, 000 eV, Z= 1-92." *Atomic data and nuclear data tables* **54**, no. 2 (1993): 181–342.
21 E. Spiller, S.L. Baker, P.B. Mirkarimi, V. Sperry, E.M. Gullikson, and D.G. Stearns, "High-performance Mo-Si multilayer coatings for extreme-ultraviolet lithography by ion-beam deposition," *Appl. Opt.* **42**(19), pp. 4049–4058 (2003).
22 A.A. Krasnoperova, R. Rippstein, A. Flamholz, E. Kratchmer, S. Wind, C. Brooks, and M. Lercel, "Imaging capabilities of proximity x-ray lithography at 70 nm ground rules," *Proc. SPIE* **3676**, pp. 24–39 (1999).
23 J.A. Folta, S. Bajt, T.W. Barbee, R.F. Grabner, P.B. Mirkarimi, T. Nguyen, M.A. Schmidt, E. Spiller, C.C. Walton, M. Wedowski, and C. Montcalm, "Advances in multilayer reflective coatings for extreme-ultraviolet lithography," *Proc. SPIE* **3676**, pp. 702–709 (1999).
24 S. Bajt, "Molybdenum-ruthenium/beryllium multilayer coatings," *J. Vac. Sci. Technol. A* **18**(2), pp. 557–559 (2000).
25 O. R. Wood, K. Wong, V. Parks, P. A. Kearney, J. Meyer-Ilse, V. Luong, V. Philipsen, et al. "Improved Ru/Si multilayer reflective coatings for advanced extreme-ultraviolet lithography photomasks." *Proc. SPIE* **9776**, pp. 977619-1–97761-10, (2016).
26 S.D. Hector, E.M. Gullikson, P. Mirkarimi, E. Spiller, P. Kearney, and J. Folta, "Multilayer coating requirements for extreme ultraviolet lithography masks," *Proc. SPIE* **4562**, pp. 863–881 (2001).

27 SEMI Standard P37-0613, "Specification for extreme ultraviolet lithography substrates and blanks," *Semiconductor Equipment and Materials International*, 3081 Zanker Road, San Jose, California (2013). Republished with permission from SEMI © 2020.
28 M. Richardson, "EUV sources," from *Chapter 3 in Extreme Ultraviolet Lithography*, B. Wu and A. Kumar, Eds., McGraw-Hill, New York (2009).
29 H. Seo, J. Park, S. Lee, J. Park, H. Kim, S. Kim, and H. Cho. "Properties of EUVL masks as a function of capping layer and absorber stack structures," *SPIE* Vol. **6517**, p. 65171G, 2007.
30 V. Philipsen, E. Hendrickx, R. Jonckheere, N. Davydova, T. Fliervoet, and J. Timo Neumann, "Actinic characterization and modeling of the EUV mask stack," *Proc. SPIE* Vol. **8886**, p. 88860B, 2013.
31 S. Yulin, T. Kuhlmann, T. Feigl, and N. Kaiser, "Damage-resistant and low-stress EUV multilayer mirrors," *Proc. SPIE* **4343**, pp. 607–614 (2001).
32 S. Bajt, J. Almeda T. Barbee Jr, W.M. Clift, J.A. Folta, B. Kaufmann, and E. Spiller, "Improved reflectance and stability of Mo-Si multilayers," *Opt. Eng.* **41**(8), pp. 1797–1804 (2002).
33 S. Braun, H. Mai, M. Moss, R. Scholz, and A. Leson, "Mo/Si multilayers with different barrier layers for applications and extreme ultraviolet mirrors," *Jpn. J. Appl. Phys.* **41**, pp. 4074–4081 (2002).
34 S. Yulin, N. Benoit, T. Feigl, and N. Kaiser, "Interface-engineered EUV multilayer mirrors," *Microelectron. Eng.* **83**, pp. 692–694 (2006).

Chapter 2
Sources of EUV Light

In Chapter 1, it was explained that the wavelength of light at which EUV lithography is practiced was chosen largely by the availability of multilayers with high reflectance. This can be contrasted with the situation in optical lithography, which has always been operated at wavelengths where there are strong sources of light with narrow bandwidths. The result is that EUV lithography has suffered from light sources that are relatively weak, and a great deal of R&D has therefore gone into the development of EUV light sources in order to improve the situation.

Several methods have been used to generate EUV light. Early researchers used synchrotron light sources, but smaller light sources became needed as a practical matter as EUV lithography moved from research to development. This was true for metrology applications as well as for exposure tools, and stand-alone systems provided greater flexibility for development pilot lines. Moreover, it was eventually determined that synchrotrons of a practical size could not provide sufficient EUV light to be cost-effective, even with the use of undulators or wigglers.[1] The EUV source used currently in manufacturing tools, the laser-produced plasma (LPP) source, is discussed in this chapter, and a source that might be used in the future for wafer exposures, the free-electron laser (FEL), will also be described. Plasma-based sources used in a number of EUV metrology tools will also be described.

2.1 Laser-Produced Plasma Light Sources

The concept behind using plasmas to generate EUV light is that energetic photons can be emitted when electrons combine with highly (positively) ionized atoms. In laser-produced plasma light sources, ions are created by the strong electric fields of intense pulses of coherent laser light. These rapidly oscillating electric fields cause repeated collisions between electrons and ions, creating ions stripped of multiple electrons (see Problem 2.1). Energetic photons are produced when electrons recombine with these highly charged ions. Although atomic emissions typically occur at quantized wavelengths, for

plasma-produced light, the emissions can occur over a range of wavelengths because the kinetic energy of the recombining electrons and ions also contributes to the energy of the emitted photons. The net result is emissions over a broad range of wavelengths. This is fortunate because an exact match between high multilayer reflectivity and a sharp emission line would be difficult. On the other hand, this also means that much of the light produced is not useable for wafer exposures, limiting the efficiency of plasma sources. Moreover, plasmas will produce long-wavelength DUV light that can expose resist if transmitted to the wafer plane.

The target material, often referred to as the fuel, is chosen by considering several factors. Conversion efficiency from laser light to in-band EUV light is one of the most important considerations. Xenon, tin, and lithium plasmas were found to have strong emissions in the EUV portion of the electromagnetic spectrum. A xenon jet was used in the source of the first full-field EUV exposure tool, the Engineering Test Stand (ETS), that was produced by the EUV LLC. Xenon was thought also to have an advantage in terms of optics contamination, because xenon is a noble gas. Protecting optics from chemical contamination is needed because there are no glass windows that can be used to separate the source and optics. In practice, considerable erosion of collector mirrors was observed in light sources with Xe as a fuel, even though a noble gas was used. Experiments revealed that the erosion was caused by sputtering by Xe ions with high kinetic energy.[2]

Because the mirrors needed protection from even chemically inert materials, measures were developed to reduce significantly the amount of material from the plasma (often referred to as "debris") that reaches the condenser mirror. Consequently, non-inert materials could be considered as fuel. This led to increased consideration of tin as a fuel, because it has stronger EUV emissions than xenon, and EUV light is produced by multiple charge states of tin ions, while appreciable emission near $\lambda = 13.5$ nm is produced by only a single Xe ion (see Figs. 2.1 and 2.2). Eventually, tin became the material used in all sources for ASML's 0.33-NA exposure tools, although Xe continues to be used for some EUV light sources, particularly for metrology (see Section 2.2).

The Engineering Test Stand (ETS) that was produced by the EUV LLC featured an LPP light source that used a pulsed Nd:YAG laser (1064-nm wavelength) to generate the plasma. There were significant doubts regarding the possibility of scaling up the power using this type of laser, and the operating and maintenance costs were high. This led to questioning LPP sources in general and resulted in substantial efforts to develop discharge-produced plasma (DPP) EUV light sources. However, these systems were unable to meet light output and reliability targets for exposure systems, so LPP sources were reconsidered. An example of a DPP source will be discussed in the next section.

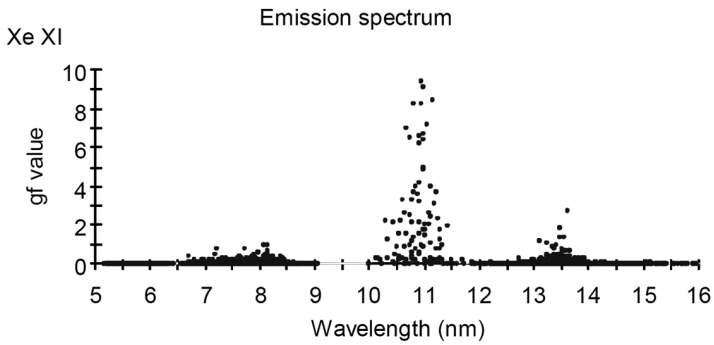

Figure 2.1 Calculated oscillator strength (gf value) vs. wavelength for Xe^{10+} (Xe XI), the only ion for Xe that produces appreciable light near the wavelength of 13.5 nm. Each point is for a single spectral line.[3]

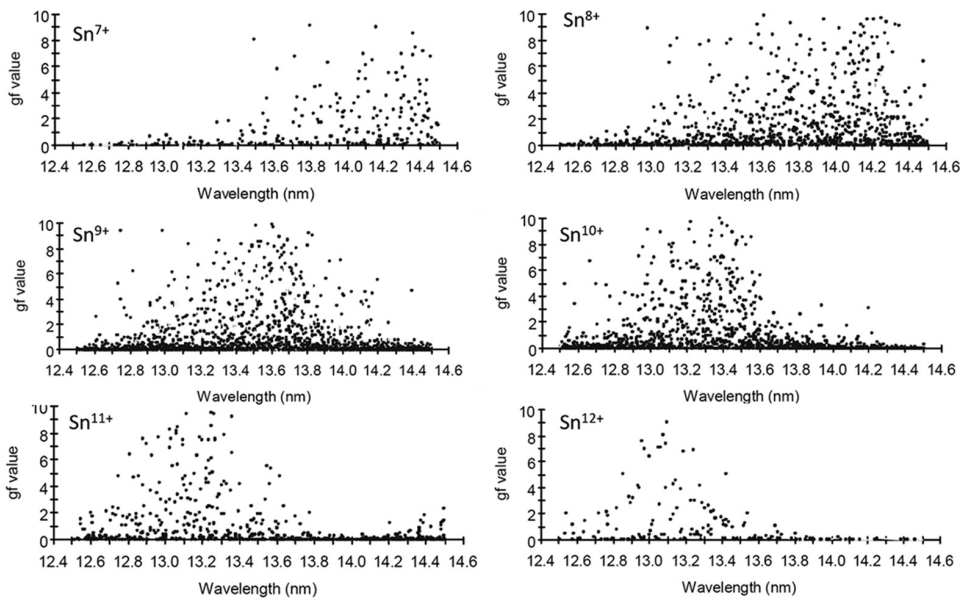

Figure 2.2 Calculated oscillator strength (gf value) vs. wavelength for various ions of tin, from Sn^{7+} (Sn VIII) to Sn^{12+} (Sn XIII). Each point is for a single spectral line. As can be seen, light near λ = 13.5 nm is emitted from several ions.[3]

One of the significant changes made in the renewed efforts to develop LPP sources was the adoption of high-power CO_2 lasers for producing the plasmas, with a wavelength of 10.6 μm, much longer than that of Nd:YAG lasers. CO_2 laser technology had matured significantly and was used extensively for welding and cutting, giving confidence that such lasers would have the reliability and operating costs suitable for high-volume manufacturing. Note that the requirements placed on the CO_2 lasers for LPP source applications are much more stringent than those for cutting and welding. R&D has been

needed to develop the nearly-diffraction-limited beam quality at high output power required for LPP sources.[4] Today, CO_2 lasers, suitable for use in LPP sources, are capable of very high power (>25 kW) and repetition rates (≥50 kHz). "Wall plug efficiency," the ratio of laser output power to electrical consumption and an important consideration when calculating operating costs, is ~2%.[5]

To achieve high laser power, a master-oscillator power-amplifier (MOPA) configuration has been adopted (Fig. 2.3). In this arrangement, a pulse of laser light is generated in the oscillator stage and then passes through a series of power amplifiers that increase the energy of the pulse. The MOPA separates the function of forming a quality seed pulse from the generation of high power. As can be seen in Fig. 2.4, CO_2 lasers for LPP light sources are significantly larger than the excimer lasers used for DUV lithography. Source optimization involves a large number of parameters for the main pulse, such as peak power, which is related to pulse duration (typically 10–20 nsecs).[6] Other aspects of source optimization will be discussed later in this section.

In the current generation of sources for EUV exposure tools, light is generated by creating plasmas from droplets of molten tin (Fig. 2.5). Conveniently, tin is a relatively strong source of EUV light around the 13.5-nm wavelength and has a low melting point of 232°C. Solid targets were used with early LPP sources,[8] which produced EUV light but also resulted in the generation of considerable debris that did not emit short wavelength light but did contaminate the source collector optics. With the use of small droplets, material consumption can be minimized, an important first step to

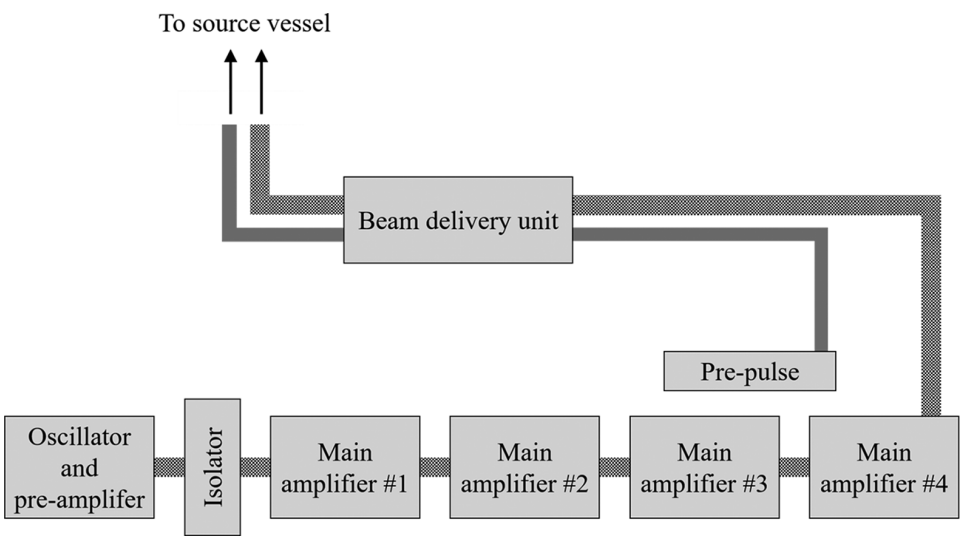

Figure 2.3 Layout of a high-power CO_2 laser used for LPP sources. In some configurations, the pre-pulse can follow the same path in the beam delivery unit as the main pulse.

Figure 2.4 Picture of a Trumpf CO_2 laser used for LPP EUV sources.[7]

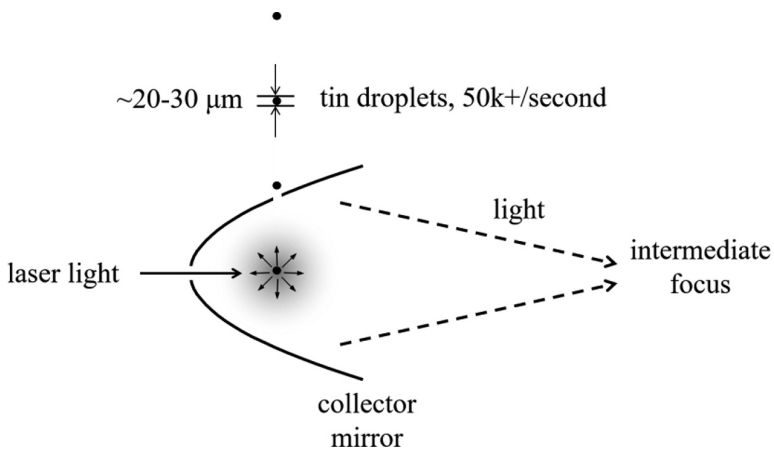

Figure 2.5 Schematic of a laser-produced light source.

keeping collector mirrors clean. The low melting point of tin simplifies the design of sources that utilize droplets of that metal.

In plasma-based EUV sources, EUV light needs to be collected and directed towards the illuminator optics of the exposure tool. By convention, the output power of EUV light sources is the in-band (2% bandwidth) power at the focus of the collector mirror, which is referred to as the intermediate focus[9] (Fig. 2.5). As can be seen in Fig. 2.6, there is an intrinsic inefficiency in the collection of EUV light, in that 100% of the EUV light produced cannot be collected and focused. A collection solid angle of 5 sr has

Figure 2.6 Collector mirror with graded multilayers, 650-mm diameter, 5-sr collection angle, with reflectance ~40%.[11]

been reported.[10] An elliptical shape for the collector mirror is convenient, with the plasma being generated at one focus and the light power delivered to the other focus.

Active measures are needed to prevent accumulation of tin on the collector mirror, which will reduce light reflectance, and flows of hydrogen are used (Fig. 2.7). The hydrogen reduces tin contamination on the mirrors by two processes. One is by the flow itself, with hydrogen molecules colliding with tin atoms or clusters, and redirecting them away from the mirror. Hydrogen radicals can also react chemically with tin, forming stannane (tin hydride), SnH_4, which is volatile at room temperature. Attenuation of EUV light by a background partial pressure of hydrogen is less of a problem than it had been for xenon, because hydrogen has a much smaller absorption cross-section than does xenon at wavelengths around 13.5 nm. For example, light at a wavelength of 13.5 nm will have >98% transmission through a 1-cm path length of (molecular) hydrogen gas at 10 Torr, while the transmission through xenon at the same pressure will be <1%. Although 10 torr is considerably less than atmospheric pressure, gas flows at low pressure can still be useful in EUV sources and exposure tools. (See Table 2.1.)

Mirror degradation is a concern for EUV lithography. Because of the harsh environment in the source module, the Mo/Si multilayers on the collector mirrors have an additional coating as protection, but this reduces reflectance for new mirrors to ~45%.[12] Reflectance typically declines during usage, primarily due to the deposition of tin, although thinning of the

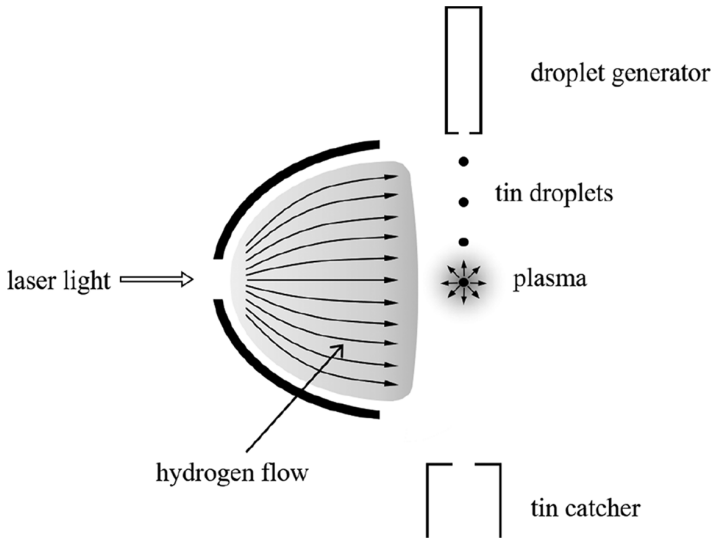

Figure 2.7 The use of hydrogen to reduce contamination of the collector mirror.

Table 2.1 Transmission of light at a wavelength of 13.5 nm through a 1-cm-long path filled with gas at 10 Torr.

Gas	Transmission through 1 cm at 10 Torr
H_2	98%
He	85%
N_2	46%
O_2	26%
CO_2	22%
Ar	64%

protective coating can lead to small increases in reflectance. Reflectance degradation is usually measured in terms of percentage change per billion pulses (%/Gp). A benchmark degradation rate is 0.1%/Gp, which will result in a 10% total mirror reflectance change, relative to the initial reflectance, after 100 Gp. If we assume that EUV light is being produced 25% of the time, then 100 Gp will be used over ~13 weeks. The decision to replace the collector mirror at this point is based partly on operating costs; the cost of replacing the mirror needs to be weighed against the productivity loss due to the collector mirror's lower reflectance. The cost of EUV lithography is discussed in further detail in Chapter 9.

Because the degradation in reflectance is typically non-uniform over the mirror surface, the decision to replace the collector mirror may be based on more than just the overall reduction in the integrated intensity of light at the intermediate focus or even reduced illumination uniformity across the slit. For example, consider quadrupole illumination. If the intensities in the poles are not nearly equal, there can be dimensional changes that vary with pitch, while shifts in the source's center can lead to pattern placement shifts, effects that have been observed in optical lithography.[13] Such effects need to be monitored in order to ensure that the degradation of source collector mirrors has not reached unacceptable levels.

The hydrogen flows shown in Fig. 2.7 protect the collector mirror to a large extent by redirecting the tin away from the mirror. Although the hydrogen pressure must necessarily be low in order to maintain transmission of EUV light (Table 2.1), studies have shown that such flows can redirect atoms, molecules, and small clusters in the path of the flow.[14,15] Much of this redirected tin will ultimately condense on the walls of the source chamber. The other mechanism by which hydrogen protects optics from tin is by the formation of SnH_4 through chemical reaction between hydrogen and tin. While SnH_4 is volatile, it can easily decompose on contact with metal surfaces, further contributing to the condensation of tin on surfaces within the source chamber.[16] In practice, the collector mirror is located towards the bottom of the source chamber (Fig. 2.8), and there is the potential for condensed tin to drip down onto the collector mirror. Preventing this necessitates additional engineering for tin management, since the low-pressure hydrogen flows used to prevent tin accumulation on collector mirrors can handle atoms, ions, and small clusters of tin, but not large drops.

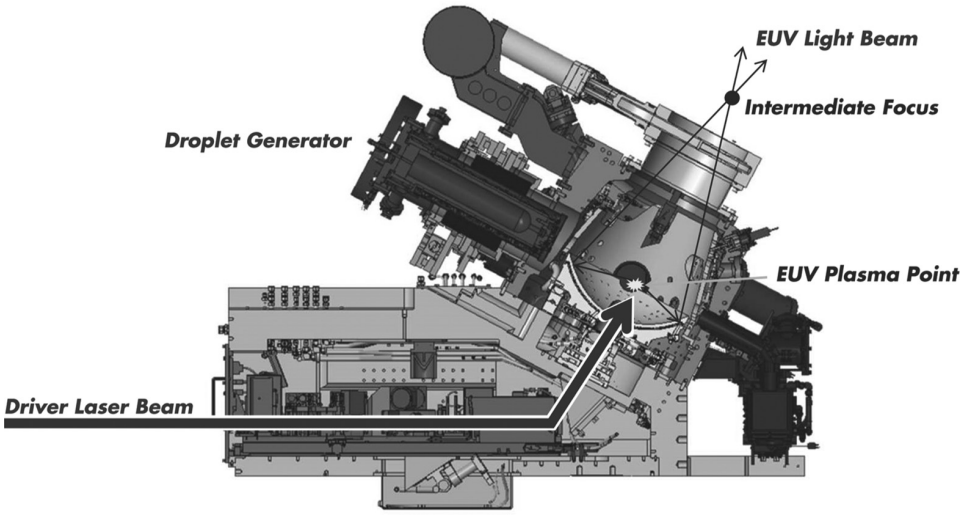

Figure 2.8 Cross-section of a Gigaphoton LPP source.[17]

One of the most important characteristics of an LPP source is the conversion efficiency between infrared light and EUV light. Since operating costs vary little with efficiency, productivity improves substantially with higher conversion efficiency. An important innovation for increasing efficiency was the introduction of the pre-pulse.[18, 19] With this approach, the tin droplet is first hit with a pulse of infrared light that is much lower power than the main pulse that produces the plasma from which EUV light is emitted, but this pre-pulse still has sufficient energy to transform the tin drop to a disk or cloud of partially ionized tin mist.[20] When this disk is subsequently hit with a high-energy pulse from a CO_2 laser, conversion efficiencies approaching 6% have been achieved,[19] a substantial improvement over what had been attained prior to the introduction of the pre-pulse. Note that conversion efficiency is usually defined in terms of the amount of in-band EUV light generated and potentially collected over 2π sr, even though the collection solid angle in actual exposure tools is usually substantially less than 2π.

In addition to being of lower power than the main pulse, the temporal duration of the pre-pulse is also typically much shorter (~10 ps)[21] than that of the main pulse (10–20 ns).[17] It has been found that pre-pulses of short duration produce targets that result in greater conversion efficiency than longer pre-pulses. Such pre-pulses can be achieved using Nd:YAG lasers at a wavelength of 1064 nm. This is also a different wavelength than that of the main pulse from the CO_2 laser.

One issue with a disk-shaped target is the potential for main-pulse infrared light reflecting from the disk and back into the CO_2 laser, which can result in lasing at times other than intended.[22,23] This in turn can lead to sub-optimal performance in terms of output power, and it can also cause damage to optical components. For example, it is important for the pulse power to rise very rapidly in time; otherwise, the target will deform non-optimally.[24] Example CO_2 light pulses are shown in Fig. 2.9, where a premature rise in power,

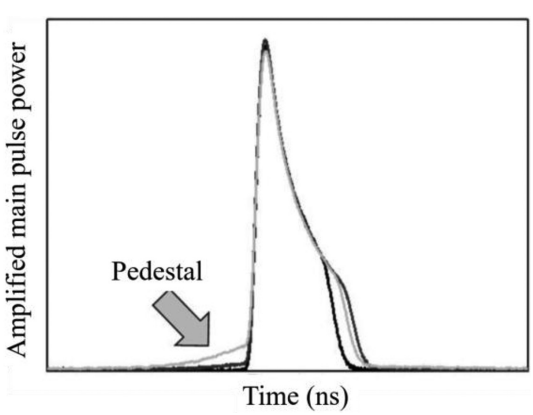

Figure 2.9 Three main pulses with different levels of pedestal.[24]

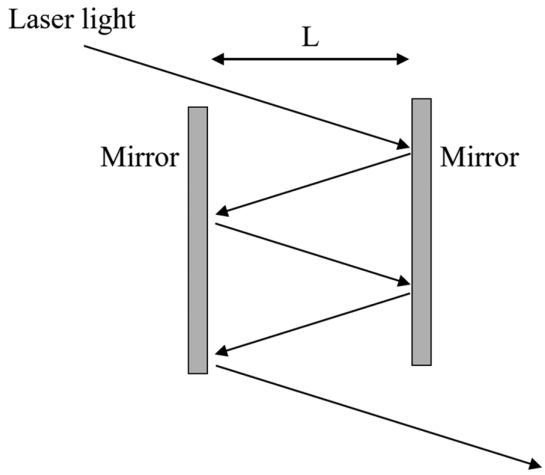

Figure 2.10 Method for lengthening the time for a pulse to travel between the pre-amplifier and main power amplifiers.

Table 2.2 Parameters used to estimate the output power of an LPP EUV source.

Parameter	Value
CO_2 laser power	25 kW
Conversion efficiency	5%
Collection solid angle	5 sr
Collector mirror reflectance	40%

referred to as the "pedestal," can be seen for some of the pulses. To prevent reflected light from changing the laser light pulse, components are added to the beam optics to isolate the oscillator and pre-amplifier module. One way to isolate the pre-amplifier from the main power amplifiers is to insert an optical switch. However, typical switches, such as those based on acousto-optic modulation, have switching times that are several hundreds of nanoseconds long, and the reflected light must be incident on the switch at times greater than this after the forward pulse passes through the switch. A simple means of delaying the return pulse is to increase the distance between the pre-amplifier and the main power amplifiers and rely on the finite speed of light. Such lengthening of the beam path in a compact module is illustrated in Fig. 2.10, where the light is reflected between mirrors multiple times[25] (see Problem 2.3). Isolation methods include the use of polarization of the light and time delay.[26]

Typical values for various source parameters are listed in Table 2.2. Using these parameters, the power at the intermediate focus is ~400 W. Boosting the output power to a higher level necessitates increasing one or more of these

parameters. It requires significant innovation in optical design and fabrication to increase the collection solid angle above 2π, and the theoretical maximum reflectance of a Mo/Si multilayer is ~75%.[27] Increases in CO_2 laser power have long been contemplated.

Even with efforts to protect the collector mirrors, they do degrade over time and need periodic replacement. Although the requirements for such mirrors are not as stringent as for EUV projection optics, in terms of figure and finish, they still require careful polishing and multilayer deposition. Accordingly, collector mirrors are expensive items, and regular replacement is a significant contributor to EUV costs. One way to reduce such replacement costs is to refurbish previously used mirrors. Collector mirrors that are replaced because they have become excessively coated with tin can be cleaned using hydrogen radicals, which are more reactive with tin than molecular hydrogen.[28,29,30] For mirrors which have damaged multilayers or outer protective layers, the damaged films can, in principle, be stripped and redeposited, obviating the grinding and polishing of new mirrors.

The tin droplets are formed by a "droplet generator," shown schematically in Fig. 2.11. Pressurized gas is used to push liquid tin though a filter and out a nozzle, with a modulator causing this to happen at a rate of 50 kHz or higher. Since the orifice of the nozzle must be comparable in size to the droplets (tens of microns), it is important to avoid having small particles in the liquid tin that could plug the nozzle. Plugged nozzles usually require replacement, resulting in downtime. Accordingly, it is important to use extremely pure tin in the source. Because tin can react chemically (particularly with oxygen and water) to form particles, the gas used to push the liquid tin must be inert, and care must be taken to remove oxygen and water from within the droplet generator before melting the tin. Refilling the tin is also a complex process, not only because of the need to avoid contamination and particulate formation but also because of the elevated temperature of the

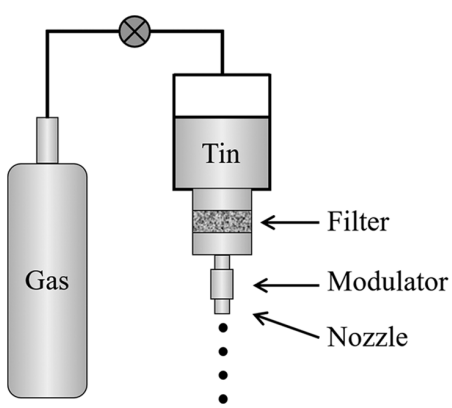

Figure 2.11 Schematic of the tin droplet generator.[31]

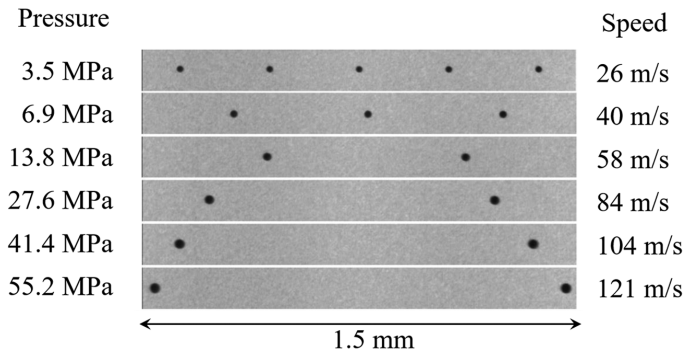

Figure 2.12 Speed of tin droplets vs. gas pressure. Photographs of the resulting tin droplets are shown, illustrating increasing separation with faster speeds. The rate of droplet formation was 80 kHz.[32]

liquid tin. It is important that additional tin can be added to the source without incurring downtime, which further complicates the refill process.

The applied pressure will determine the speed of the droplets, which affects the spacing between the droplets. It is important to have adequate spacing between droplets, so that the plasma from one droplet does not interfere with proper plasma formation from the next droplet. In this regard, higher pressures are advantageous (see Fig. 2.12), but higher speeds increase the difficulty of hitting the droplet with the laser light. Indeed, it is very challenging to hit small droplets (20–25-μm diameter) moving ~100 m/s with a pulsed laser at 50+ kHz. The laser beams, both for the pre-pulse and the main pulse, must be aligned with the path of the droplet stream, and the laser pulses must be synchronized to hit the droplets near a focal point of the elliptical collector mirror. The initial set-up is time consuming, and alignment and synchronization must be maintained during operation. Moreover, this set-up needs to be repeated following any significant maintenance event, such as droplet generator or collector mirror replacements, increasing the mean-time-to-repair.

The droplet size can be optimized. A small droplet has certain advantages. Most of the tin can be ionized and few tin clusters will be formed. Clusters are problematic because they produce little EUV light but will contaminate the collector optics. Overall, there will be less tin that can coat mirrors. On the other hand, droplets that are too small will produce little total EUV light. Today, droplets are 20–25 μm in diameter.

The cross-sectional area from which EUV light is emitted will be larger than the original tin droplet, because the tin droplet expands due to the pre-pulse and then expands further after being hit by the main pulse. The actual emission source cross-sectional area is therefore 90 μm in diameter or larger.[33] This is fine for EUV exposure systems but may be too large for

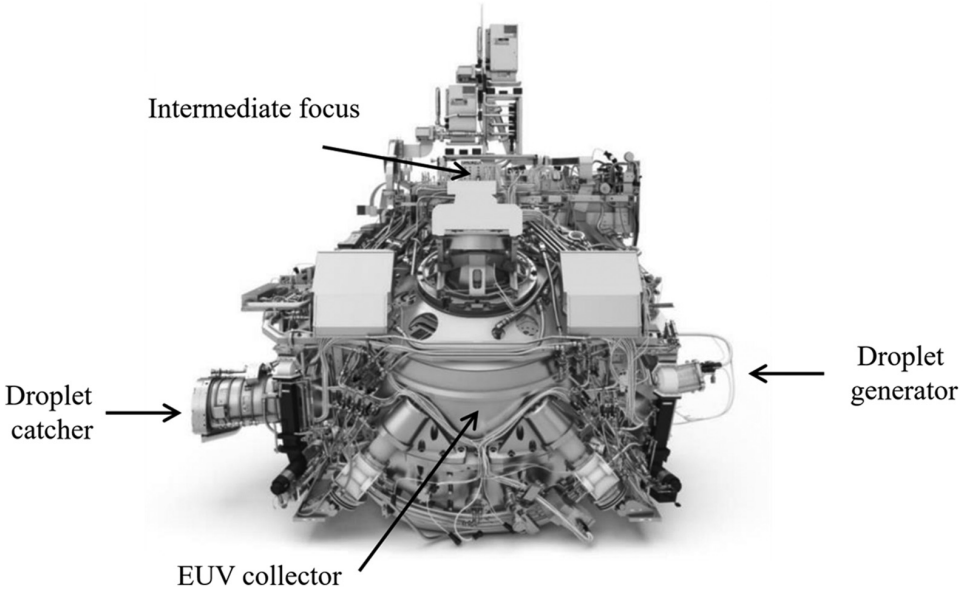

Figure 2.13 Picture of a Cymer LPP source.[35]

metrology applications, which often require very small, but bright, light sources.

The amount of EUV light varies from pulse to pulse. To ensure that each point on the wafer receives the same exposure dose as any other point, less than 100% of pulses can be utilized. Exposure time can be reduced not only by increasing the power at the intermediate focus but by reducing the amount of pulse-to-pulse energy variation. In fact, higher energy per pulse means that fewer pulses are needed to achieve a given exposure doses, thereby reducing the amount of averaging.[34] Increases in source power cannot be fully exploited without commensurate improvement in the pulse-to-pulse energy variation.

A picture of an LPP source is shown in Fig. 2.13.[35] As can be seen, the LPP source is very complex. The need to operate EUV lithography tools at wavelengths where there are multilayer reflectors with high reflectivity, rather than at a wavelength where there are simpler, intense sources of narrow-bandwidth EUV light is a large part of the reason for this complexity. It is a general principle of engineering that complexity increases the difficulty of ensuring reliability, and the reliability of LPP sources has proven to be a challenge.

Because there are no materials that are highly transparent at EUV wavelengths, the source cannot be separated from the exposure tool's illuminator by a window. This means that the source must be under vacuum of a similar quality as the rest of the exposure system, in order to avoid

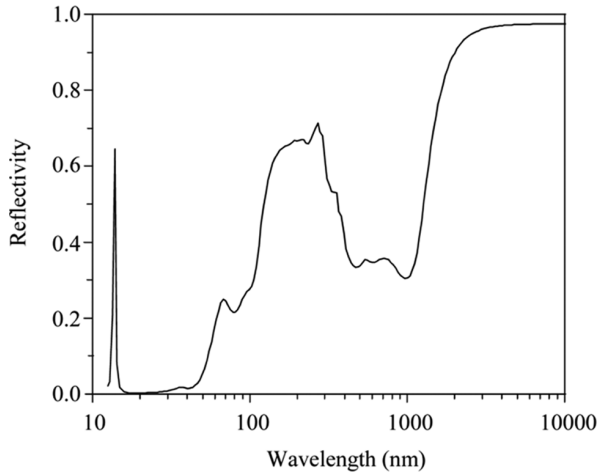

Figure 2.14 Calculated reflectivity of normally incident light from a 40-pair Mo/Si multilayer film.[36]

contamination of the projection optics. (The issue of optics contamination will be discussed in Chapter 3.) For serviceability, it is useful to have a vacuum gate valve between the source and the rest of the exposure tool so that the vacuum on each subsystem can be broken for maintenance while vacuum integrity is maintained in the rest of the exposure system.

As mentioned previously, plasma sources can produce DUV light, as well as light at the desired EUV wavelengths. Shown in Fig. 2.14 is the calculated reflectivity of Mo/Si multilayers. As can be seen, such mirrors have considerable reflectance at DUV wavelengths, so an appreciable amount of DUV light can be transmitted through the optics of EUV lithography tools. Light produced by the plasma source at wavelengths other than ~13.5 nm, referred to as out-of-band light, can be relevant. Many EUV resists can be exposed by DUV light. With a 0.33 NA, the resolution of DUV light will be

$$\text{resolution} > 0.25\frac{\lambda}{\text{NA}} \tag{2.1}$$

$$\approx 0.25\frac{200}{0.33}\,\text{nm} \tag{2.2}$$

$$= 150\,\text{nm}, \tag{2.3}$$

which is an order of magnitude larger than the features to be printed using EUV lithography. Consequently, DUV light will behave like background flare, a topic that is discussed in more detail in Chapter 6.

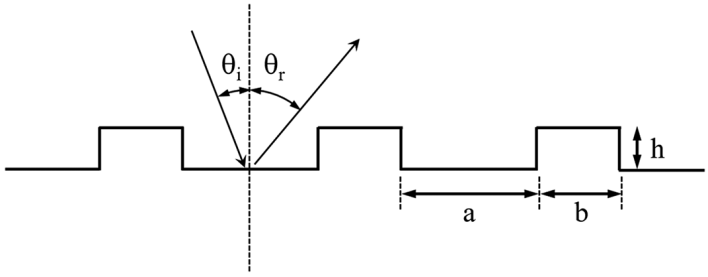

Figure 2.15 Reflection diffraction grating.

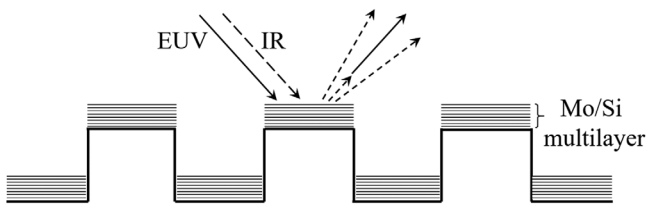

Figure 2.16 Illustration of the suppression of zeroth-order infrared (IR) light.

For laser-produced plasmas, even a small fraction of the light from the CO_2 laser still constitutes a considerable amount of infrared light, which can heat silicon wafers if transmitted through the optics. Wafer heating is problematic, because it affects overlay control. One way to reduce the amount of 10.6-μm-wavelength light reaching the wafer is to form diffraction gratings on the collector mirrors. Consider the situation depicted in Fig. 2.15, with a grating pitch of 100 μm. For EUV light, the lower-order diffracted beams, which will have the greatest intensities, will have angles very close to the specular beam ($m = 0$):

$$\sin\theta_r = \sin\theta_i + \frac{m\lambda}{d}, \text{ where } m = 0, \ \pm 1, \ \pm 2, \ \ldots \tag{2.4}$$

The zeroth-order beam for the infrared light can be suppressed by having $a = b$ and

$$\frac{h}{\cos\theta_r} = \frac{\lambda_I}{4} + m\frac{\lambda_I}{2}, \tag{2.5}$$

where m is an integer, and λ_I is the wavelength of the infrared light. The result is illustrated in Fig. 2.16. In this way, the infrared light is directed out of the optical path, significantly reducing the amount of infrared radiation that reaches the wafers.

Even within the EUV portion of the spectrum, light is emitted from tin plasmas over a range of wavelengths. Measurements of source output power

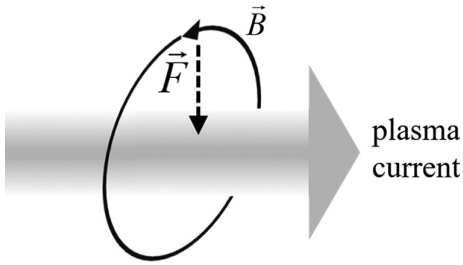

Figure 2.17 Illustration of the forces causing self-compression in a plasma current.

relevant to exposure tool productivity need to be confined to those wavelengths that contribute to exposing resist. The bandwidth of these wavelengths can be estimated by considering the reflectivity of multilayer mirrors (Fig. 1.6). The reflectance from a single multilayer mirror has a bandwidth of ~0.5 nm, which is approximately 3.7%. Current exposure tools have six mirrors in the projection optics and four mirrors in the illuminator. With the addition of the mask, EUV light is reflected 11 times between the intermediate focus and the wafer. This narrows the bandwidth to ~1.8%. By convention, source power is specified over a 2% bandwidth, even though the bandwidth is slightly smaller for current exposure tools.

2.2 Discharge-Produced Plasma Sources

As mentioned at the beginning of this chapter, discharge sources were tried for exposure tools but found wanting, and LPP sources are thus used currently on EUV exposure tools. However, LPP sources have some disadvantages, particularly size and cost. While these are problems regardless of application, they are particularly problematic in the context of metrology, because high light source costs and large sizes for measurement tools will change the balance in budgets and space allocations for process and metrology equipment. Fortunately, the high power requirements for exposure tools are typically not needed for measurement systems. Accordingly, DPP sources are currently used in a number of tools that measure at EUV wavelengths.

One of the problems typical of discharge sources is electrode erosion, which often occurs when the discharge is created by applying a high voltage between an anode and cathode. DPP EUV light sources for metrology applications and for which the erosion problems have been circumvented in novel ways will be discussed in this section.

An important principle common to many discharge sources is the self-compression of plasma currents, which is illustrated in Fig. 2.17. Plasmas, which consist of ions and electrons, will flow when subjected to an electrical field, with the electrons and ions flowing in opposite directions. The resulting current will generate a magnetic field, and charges at the outer edges of the

plasma flow will experience forces directed inward due to this magnetic field. Very large currents will create strong magnetic fields, which will serve to compress the plasma. Compression, in turn, will cause the temperature of the plasma to rise and result in further ionization. As described in the prior section, EUV light will be emitted from highly charged ions of appropriate elements.

2.2.1 Z-pinch light sources

As mentioned at the beginning of this chapter, discharge sources were tried for exposure tools but found wanting, and LPP sources are thus used currently on EUV exposure tools. However, one type of discharge source, the Z-pinch plasma source, has long been used for metrology tools[37] and merits description. Light source requirements are different for exposure tools and metrology tools. Exposure systems need high power, but the source size is not highly constrained. On the other hand, metrology tools often need sources with small spot sizes, but lower power requirements. This makes simple and low-cost Z-pinch plasma sources suitable for use in EUV metrology tools.

To avoid the problem of electrode erosion, induction is used to generate current flow in the Z-pinch source produced by Energetiq (Figs. 2.18 and 2.19). A high-voltage pulse is applied across the upper and lower plates. The potential difference between the plates will cause plasma flow (Fig. 2.18(a)) of xenon gas through the three outer holes in the source. The applied voltage will also cause current to flow across the upper plate, through the core, and across the lower plate. Since this applied voltage is a pulse, electromotive force induces plasma flow through the core via induction.

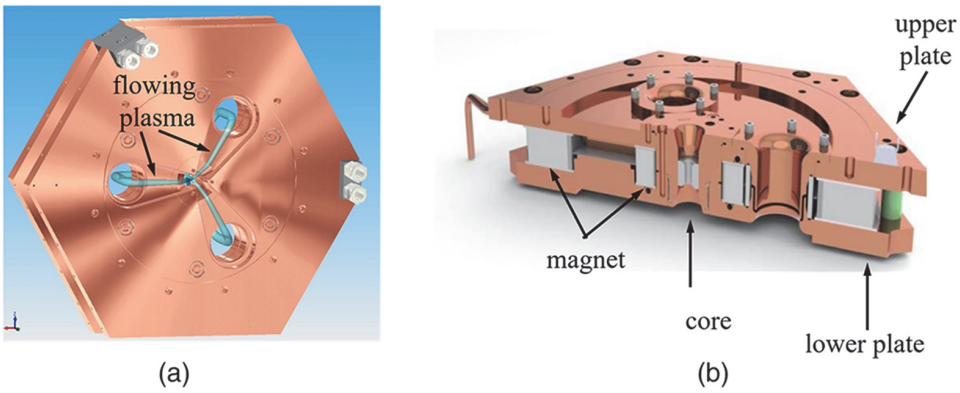

Figure 2.18 Models of the Energetiq Z-pinch light source: (a) Illustration of the flow of the Xe plasma, and (b) cross-section of the source.[38]

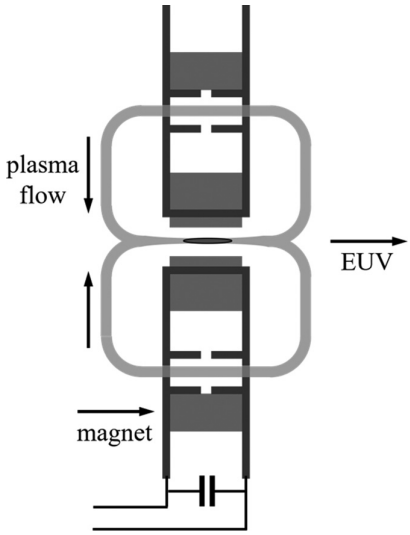

Figure 2.19 Illustration of the Energetiq Z-pinch source.[38]

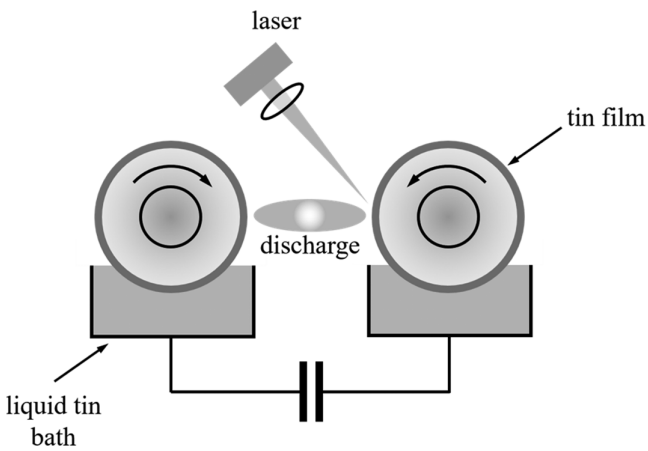

Figure 2.20 Schematic of a laser-assisted DPP source.[40]

2.2.2 Electrode-based DPP sources

DPP sources are intrinsically more compact and less expensive than LPP sources, so they continue to be developed for use in metrology tools. As mentioned at the beginning of this chapter, the erosion of electrodes is a potential problem with discharge sources. To circumvent this issue, a DPP source has been developed in which the electrode surfaces are composed of liquid tin.

In this configuration, discs that form the electrodes are rotated through baths of liquid tin (Fig. 2.20). In this manner, the surfaces of the electrodes are

covered by films of liquid tin that get replenished as the discs rotate. This significantly reduces the problem of electrode erosion. Since the portions of the discs that were in proximity to plasma discharges will be at highly elevated temperatures, above that of molten tin,[39] immersion in the tin bath will actually serve to cool the discs in the regions heated by discharges. Conveniently, tin is an electrical conductor.

In the DPP configuration shown in Fig. 2.20, an infrared laser is used to create the plasma, which is then further heated and ionized by means of electrical discharge. Light source characteristics are dependent on the type of laser and whether the laser is directed at the anode or cathode. The source produced by Ushio utilizes a pulsed laser that is directed at the cathode. The result is an emission region that is approximately 200 μm × 450 μm in size.[41]

As with all EUV sources using tin as a fuel, mitigation schemes are required to prevent the collector optics from becoming quickly coated with tin. One approach that has been adopted is the foil trap, which consists of closely spaced, very thin vanes of metal, with the thin edge of the metal facing the light source region (Fig. 2.21). The set of vanes is then rotated to deflect ions, atoms, and clusters of tin. This can be further facilitated by the addition of a low-pressure buffer gas, which will redirect tin that might be on a trajectory to pass through the foil trap (Fig. 2.22). Again, hydrogen is a convenient gas to use, both for its ability to combine with tin to form stannane and for its relatively low absorbance at EUV wavelengths. Particles must be moving very fast in order to pass through the rotating foil trap. For example, for a foil trap with 150 blades that are 20 mm long and rotate at 100 Hz, particle speeds of 500 m/s or greater are required to pass through the foil trap. EUV radiation, traveling at the speed of light, will mostly pass through to the collection optics.

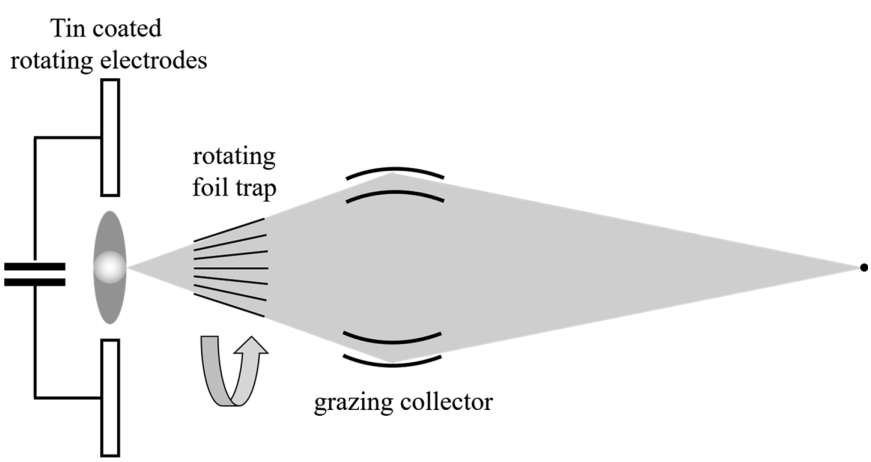

Figure 2.21 Illustration of a DPP source with a foil trap to prevent the collector optics from becoming coated with tin.[42]

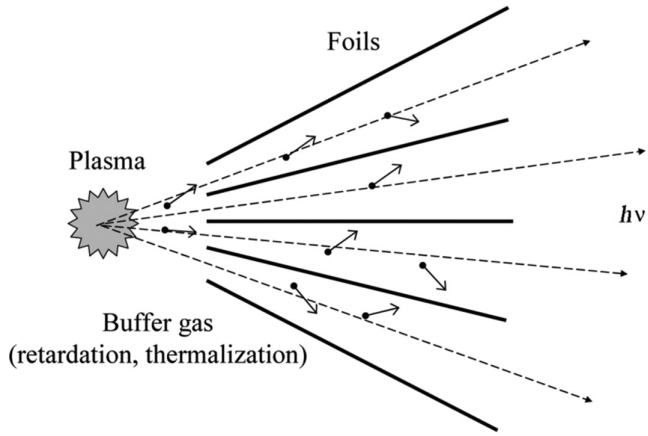

Figure 2.22 Use of a buffer gas to inhibit the flow of tin to the collector optics.[43]

2.3 Free-Electron Lasers

A completely different concept for a high-power EUV light source is the free-electron laser (FEL). Because all matter absorbs light very strongly at EUV and soft x-ray wavelengths, constructing a high-power laser at such wavelengths using a material lasing medium and resonating cavity with semireflecting mirrors has not proven possible. However, short-wavelength lasers have been created using free-electron lasers, which produce coherent light by using an entirely different approach that avoids the problem of light absorption by matter.

In a free-electron laser, short-wavelength light is produced by emission from electrons moving at relativistic speeds.[44] Intense emission at VUV and x-ray wavelengths has long been achieved by undulators, which move the electrons transversely to the general beam direction. This results in light emitted in the direction of travel (Fig. 2.23).

A general configuration for an FEL is shown in Fig. 2.24. For lasing, electrons need to be formed into microbunches, which facilitates the in-phase emission of light. The chicane achieves partial bunching.

The speed v of the electrons as well as the period λ_u of the undulator are selected to produce light at the desired wavelength λ, which is given by the following expression:

$$\lambda = \frac{\lambda_u}{2\gamma^2}\left(1 + \frac{K^2}{2}\right), \tag{2.6}$$

where

$$K = \frac{eB_0\lambda_u}{2\pi mc}, \tag{2.7}$$

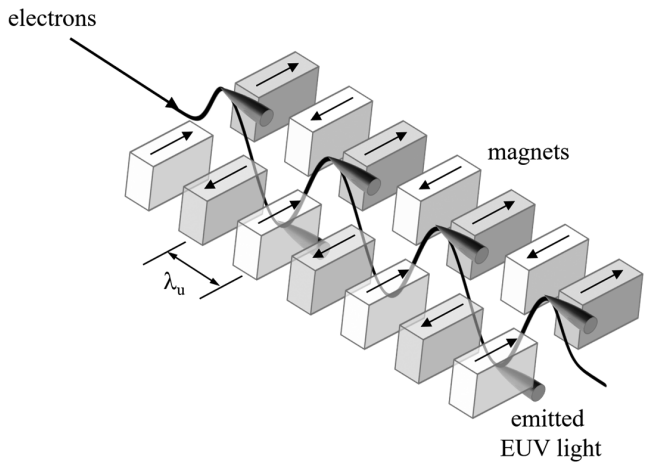

Figure 2.23 Schematic of an undulator, with multiple pairs of magnets that cause the electron beam to oscillate transversely to the primary beam direction, resulting in the emission of synchrotron radiation.

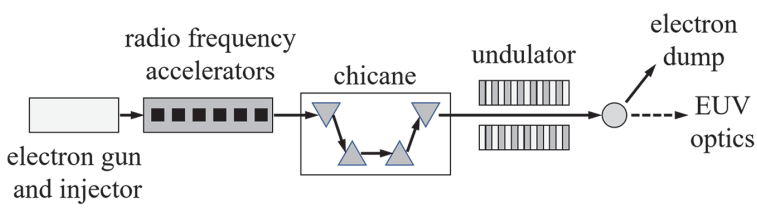

Figure 2.24 General configuration for an EUV free-electron laser.

where B_0 is the peak magnetic field in the undulator, m is the mass of an electron, c is the speed of light, and γ is the relativistic factor:

$$\gamma = \frac{1}{\sqrt{1 - \left(\frac{v}{c}\right)^2}}. \tag{2.8}$$

It may at first seem counter-intuitive that lasing can be achieved at nanometer-scale wavelengths with centimeter-scale undulator periodicities. However, the relativistic speeds of the electrons result in two things. First, light traveling in the direction of the electron beams are Doppler shifted from the wavelength λ_0 in the reference frame of the undulator to a wavelength λ in the reference frame of the electrons, according to

$$\lambda = \lambda_0 \sqrt{\frac{1+\frac{v}{c}}{1-\frac{v}{c}}}, \tag{2.9}$$

where v is the speed of the electrons relative to undulator, and c is the speed of light. Moreover, the period λ_u of the undulator in the reference frame of the electron is contracted:

$$\lambda_u \rightarrow \lambda_u \sqrt{1-\left(\frac{v}{c}\right)^2}. \tag{2.10}$$

The net result is that an undulator with a period of 2 cm, with 800-MeV electrons, can produce 13.5-nm EUV light.[45]

Several FEL configurations have been conceived, and the design most appropriate for lithographic applications has yet to be determined. With the self-amplified spontaneous emission (SASE) configuration, electrons in bunches enter the undulator with random phases and a velocity distribution. The resulting emission near the entrance of the undulator is incoherent. The electric field from this emission drives electrons of similar velocities into microbunches that emit coherently (Fig. 2.25). The result is lasing at the EUV wavelength.

There is the potential for higher gain by injecting EUV light into an undulator. One way to do this is to have an undulator upstream that can produce EUV light to seed the undulator that produces the final output, as illustrated in Fig. 2.26. A monochromator is used to select the desired wavelength, and a

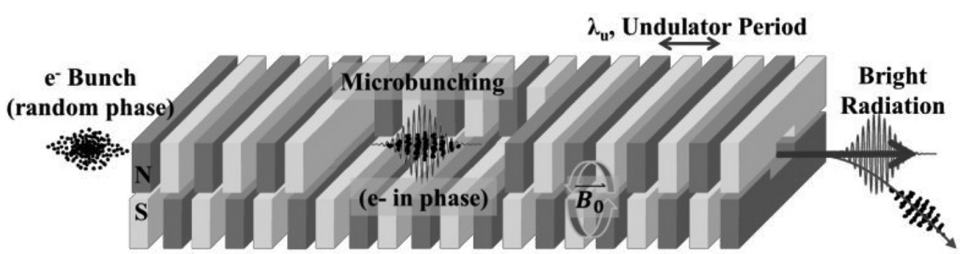

Figure 2.25 Illustration of a generic undulator for the self-amplified spontaneous emission (SASE) configuration.[46]

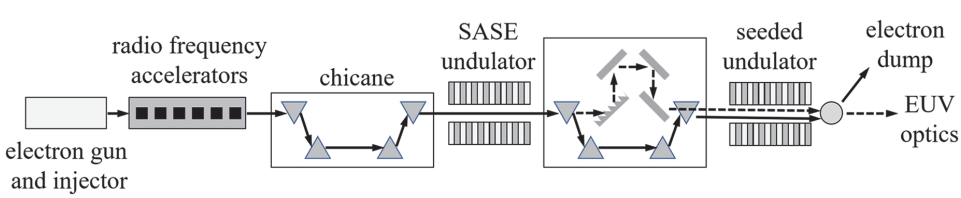

Figure 2.26 Illustration of a seeded EUV free-electron laser.

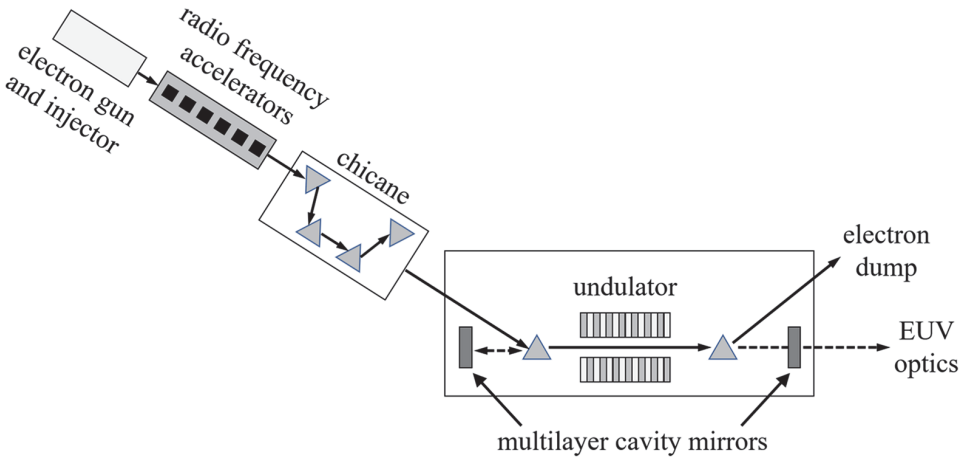

Figure 2.27 Illustration of a regenerative amplifier free-electron laser (RAFEL).

chicane is used between the two undulators to recompress the electron bunches. The potential for higher output comes at the cost of the additional hardware.

An approach that resembles the more conventional laser configuration involving mirrors is the regenerative amplifier free-electron laser (RAFEL), illustrated in Fig. 2.27. This differs from a traditional laser resonant cavity in that most of the light is emitted, while only small part is reflected back through the undulator to achieve microbunching and saturation. RAFEL-type free-electron lasers have not yet been demonstrated at EUV wavelengths.

There are two options for treating the electrons after they pass through the undulator. Either the electrons can be "dumped" and their energy deposited into a solid as heat, or they can be decelerated first and then dumped once the beam energy is below a certain threshold. While dumping the electrons at high energy is in some ways the easiest approach, the deposited energy can generate radioactive tritium, which is generated by the radiation emitted from the beam dump into the surrounding cooling water. This radioactive material needs to be contained well past its half-life of 12.3 years. By recirculating the electron beam into the superconducting accelerator module out of phase with the accelerating beam, the electron bunch can be decelerated and its energy redeposited into the RF cavities to be used to accelerate the next bunch. On the surface, recirculation would then seem to be the more energy-efficient option, but it substantially increases the complexity (both in operation and components) and size of the FEL.

The polarization of light from FELs is a factor that needs to be addressed. For low-NA imaging, unpolarized light has typically been used to illuminate reticles, since polarization provides little improvement in image contrast at low NAs, and there is less susceptibility to imaging artifacts with unpolarized light. There are many options for depolarizing light at DUV wavelengths, but these typically involved transmission optical elements that are not applicable

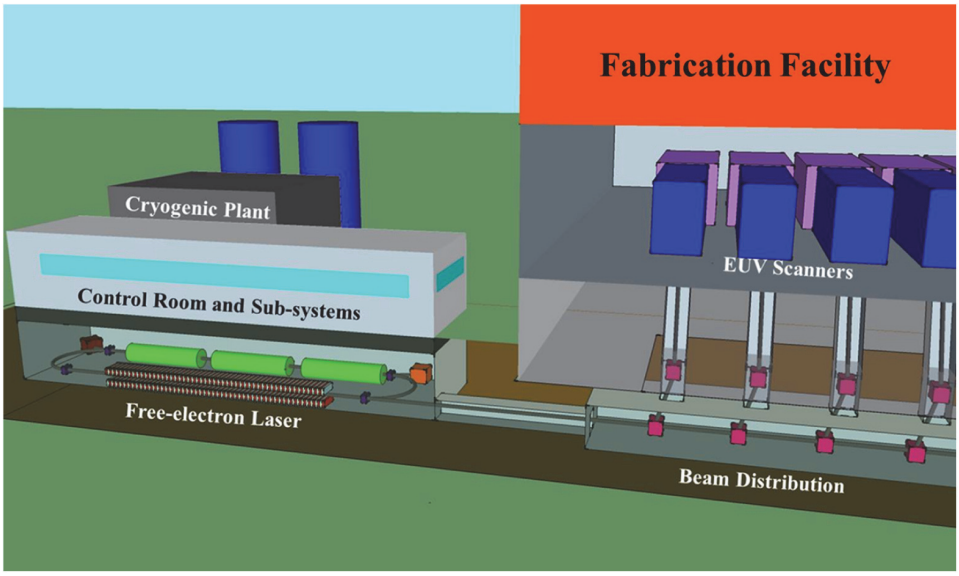

Figure 2.28 Illustration of a high-power FEL used to provide light for multiple EUV exposure tools.[47]

at EUV wavelengths. On the other hand, there will be image contrast lost at high NAs (0.55) with unpolarized light, so the polarization of light produced by free-electron lasers could prove advantageous for later generations of EUV lithographic technology.

Accelerating electrons to relativistic velocities typically requires large accelerators, and FEL's are typically tens to hundreds of meters in length, affecting the practicality of their use. One conceptual implementation involves the creation of a 10–20-kW beam, which is then split to provide light for ten or more exposure tools[47] (Fig. 2.28). Although FEL technology has proven to be very reliable, any failures would have a significant impact on a wafer fab when using a configuration where the output of a single FEL is used to provide light for multiple-exposure tools. Accordingly, redundant FELs have been proposed for this configuration.

Problems

2.1 The duration of a pulse of a CO_2 laser is typically 10–20 ns. Show that the fuel in LPP sources is subjected to ~28,300 cycles of an oscillating electric field during a 10-ns pulse.

2.2 Show that a source with the parameters in Table 2.2 will produce 200 W of light at the intermediate focus.

2.3 Show that 90 reflections are needed in a unit such as that illustrated in Fig. 2.10 with the optical path between the mirrors = 1 m in order to impart a 300-ns delay to the transit time of a laser pulse.

References

1 G. Dattoli, A. Doria, G. P. Gallerano, L. Giannessi, K. Hesch, H. O. Moser, P. L. Ottaviani et al. "Extreme ultraviolet (EUV) sources for lithography based on synchrotron radiation," *Nuclear Instruments and Methods in Physics Research Section A: Accelerators, Spectrometers, Detectors and Associated Equipment* **474**, no. 3 (2001): 259–272.

2 R. J. Anderson, D. A. Buchenauer, K. A. Williams, W. M. Clift, L. E.Klebanoff, N. V. Edwards, O. R. Wood II, S. Wurm. "Investigation of plasma-induced erosion of multilayer condenser optics," *Proc. SPIE* Vol. **5751**, pp. 128–139, 2005.

3 G. D. O'sullivan, A. Cummings, G. Duffy, P. A. Dunne, A. Fitzpatrick, P. Hayden, L. McKinney, et al. "Optimizing an EUV source for 13.5 nm," *Proc. SPIE* Vol. **5196**, pp. 273–281, 2004.

4 B. Schmidt and M. Schaefer. "Advanced industrial laser systems and applications," *Proc. SPIE* Vol. **10525**, p. 1052502, 2018.

5 Dr. Erik Hosler, Private Communication.

6 H. Mizoguchi, H. Nakarai, T. Abe, K. M. Nowak, Y. Kawasuji, H. Tanaka, Y. Watanabe, et al., "Performance of 250W high-power HVM LPP-EUV source," *Proc. SPIE* Vol. **10143**, p. 101431J, 2017.

7 The picture of the Trumpf CO_2 laser was provided by Florian Heinig and Athanassios Kaliudis of Trumpf Lasersystems for Semiconductor Manufacturing GmbH.

8 J. M. Bridges, C. L. Cromer, and T. J. McIlrath. "Investigation of a laser-produced plasma VUV light source." *Applied optics* Vol. **25**, No. 13, pp. 2208–2214 (1986).

9 V. Bakshi, *EUV Sources for Lithography*. Vol. **149**. SPIE press, 2006.

10 I. Fomenkov, "EUVL Exposure Tools for HVM: Status and Outlook," *presented at the EUVL Workshop*, Berkeley, CA, 2016, https://www.euvlitho.com/2016/P2.pdf

11 T. Feigl, M. Perske, H. Pauer, T. Fiedle, C. Laubis, and F. Scholze, "LPP collector mirrors – coating, metrology and refurbishment," presented at *2013 International Workshop on EUV and soft X-Ray Sources*, https://euvlitho.com/2013/S34.pdf

12 T. Feigl, M. Perske, H. Pauer, T. Fiedler, S. Yulin, N. Kaiser, A. Tünnermann, et al. "Lifetime and refurbishment of multilayer LPP collector mirrors," *Proc. SPIE* Vol. **8679**, p. 86790C, 2013.

13 W. Gao and L. De Winter, "Sensitivity of hyper-NA immersion lithography to illuminator imperfections," *Proc. SPIE* Vol. **6520**, p. 652039, 2007.
14 M. P. Kanouff and A. K. Ray-Chaudhuri, "Gas curtain for mitigating hydrocarbon contamination of EUV lithographic optical components," *Proc. SPIE* Vol. **3676**, pp. 735–742, 1999.
15 M. P. Kanouff and A. K. Ray-Chaudhuri, "Wafer chamber having a gas curtain for extreme-UV lithography." U.S. Patent 6, 198, 792, issued March 6, 2001.
16 D. Ugur, A. J. Storm, R. Verberk, J. C. Brouwer, and W. G. Sloof, "Decomposition of SnH_4 molecules on metal and metal–oxide surfaces," *Applied Surface Science* **288** (2014): 673–676.
17 H. Mizoguchi, H. Nakarai, T. Abe, K. M. Nowak, Y. Kawasuji, H. Tanaka, Y. Watanabe, et al. "High Power HVM LPP-EUV Source with Long Collector Mirror Lifetime," EUVL Workshop 2017 https://www.euvlitho.com/2017/P2.pdf
18 H. Mizoguchi, H. Nakarai, T. Abe, T. Ohta, K. M. Nowak, Y. Kawasuji, H. Tanaka, et al., "LPP-EUV light source development for high volume manufacturing lithography," *Proc. SPIE* Vol. **8679**, p. 86790A, 2013.
19 H. Mizoguchi, K. M. Nowak, H. Nakarai, T. Abe, T. Ohta, Y. Kawasuji, H. Tanaka, et al., "Update of EUV Source Development Status for HVM Lithography," *Journal of Laser Micro/Nanoengineering*, Vol. **11**, no. 2 (2016).
20 W. van der Zande, "EUVL exposure tools for HVM: It's under (and about) control." In *Proceedings of the EUV and Soft X-ray Source Workshop*, 2016, https://www.euvlitho.com/2016/S1.pdf
21 J. Fujimoto, T. Hori, T. Yanagida, and H. Mizoguchi, "Development of laser-produced tin plasma-based EUV light source technology for HVM EUV lithography," *Physics Research International, 2012*.
22 I. V. Fomenkov, Cymer Inc, Laser produced plasma EUV light source, *U.S. Patent* **7**, **928**, 416, 2011
23 I. V. Fomenkov and R. J. Rafac. "EUV LPP source with dose control and laser stabilization using variable width laser pulses." U.S. Patent 9, 832, 852, issued November 28, 2017.
24 A. A. Schafgans, D. J. Brown, I. V. Fomenkov, R. Sandstrom, A. Ershov, G. Vaschenko, Rob Rafac, et al. "Performance optimization of MOPA pre-pulse LPP light source," *Proc. SPIE* **9422**, p. 94220B, 2015.
25 K-C. Hou, R. L. Sandstrom, W. N. Partlo, D. J. W. Brown, and I. V. Fomenkov. "Oscillator-amplifier drive laser with seed protection for an EUV light source," U.S. Patent 8, 462, 425, issued June 11, 2013.
26 M. Purvis, I. V. Fomenkov, A. A. Schafgans, M. Vargas, S. Rich, Y. Tao, S. I. Rokitski, et al. "Industrialization of a robust EUV source for

high-volume manufacturing and power scaling beyond 250W," *Proc. SPIE* **10583**, p. 1058327, 2018.

27 S. Yulin, "Multilayer interference coatings for EUVL," *Chapter 5 in Extreme Ultraviolet Lithography*, eds. B. Wu and A. Kumar, McGraw Hill, 2009.

28 D. Ugur, A. J. Storm, R. Verberk, J. C. Brouwer, and W. G. Sloof. "Generation and decomposition of volatile tin hydrides monitored by in situ quartz crystal microbalances," *Chemical Physics Letters* **552** (2012): 122–125.

29 V. M. C. Crijns, "Hydrogen atom based tin cleaning," *Masters Thesis*, Eindhoven University of Technology, 2014.

30 D. T. Elg, G. A. Panici, S. Liu, G. Girolami, S. N. Srivastava, and D. N. Ruzic. "Removal of tin from extreme ultraviolet collector optics by in-situ hydrogen plasma etching," *Plasma Chemistry and Plasma Processing* **38**, no. **1**, pp. 223–245, 2018.

31 A. Pirati, R. Peeters, D. Smith, S. Lok, M. van Noordenburg, R. van Es, E. Verhoeven, et al. "EUV lithography performance for manufacturing: status and outlook," *Proc. SPIE* Vol. **9776**, p. 97760A, 2016.

32 I. Fomenkov, "Status and outlook for LPP light sources HVM EUVL," *presented at the EUVL Workshop*, Berkeley, CA, 2015.

33 D. C. Brandt, I. V. Fomenkov, A. I. Ershov, W. N. Partlo, D. W. Myers, N. R. Bowering, G. O. Vaschenko, O. V. Khodykin, A. N. Bykanov, J. R. Hoffman, C. P. Chrobak, and S. Srivastava, "Laser produced plasma EUV source system development," *Sematech EUV Source Workshop*, 2008.

34 S. Carson, "EUV Lithography: 0.33 NA in HVM and Preparation for Future Nodes," EUVL Workshop, 2020.

35 This picture was provided by Dr. Anthony Yen of ASML, from his presentation, "EUV lithography to enable semiconductor manufacturing at 7 nm and beyond," *Semicon West*, 2019.

36 S.A. George, "Out-of-band exposure characterization with the SEMATECH Berkeley 0.3-NA microfield exposure tool," *Lawrence Berkeley National Laboratory* (2009). http://escholarship.org/uc/item/3g458337

37 S. F. Horne, M. M. Besen, D. K. Smith, P. A. Blackborow, and R. D'Agostino. "Application of a high-brightness electrodeless Z-pinch EUV source for metrology, inspection, and resist development," *Proc. SPIE* Vol. **6151**, p. 61510P, 2006.

38 The pictures of the Z-pinch source were provided by Mr. Sam Gunnell of Energetiq Technology, Inc.

39 H. Verbraak, "EUV light source – the path to HVM," International Workshop on EUV and Soft X-ray Sources, 2011, https://www.euvlitho.com/2011/S45.pdf

40 Y. Teramoto, "High-brightness LDP source for mask inspection," *in EUV Lithography*, ed. Vivek Baski, SPIE Press (2018).

41 Y. Teramoto, B. Santos, G. Mertens, M. Kops, R. Kops, R. Bayemani, and K. Bergmann, "Characterization and performance improvement of laser-assisted and laser driven EUV sources for metrology applications," EUV Source Workshop 2019, https://euvlitho.com/2018/S56.pdf
42 D. Ruzic, R. Bristol, and B. J. Rice. "Plasma-based debris mitigation for extreme ultraviolet (EUV) light source." U.S. Patent 7, 230, 258, issued June 12, 2007.
43 L. A. Shmaenok, C. C. de Bruijn, H. F. Fledderus, R. Stuik, A. A. Schmidt, D. M. Simanovskii, A. A. Sorokin, T. A. Andreeva, and F. Bijkerk, "Demonstration of a foil trap technique to eliminate laser plasma atomic debris and particles," *Proc. SPIE* **3331**, pp. 90–94, 1998.
44 W. A. Barletta, J. Bisognano, J.N. Corlett, P. Emmah, Z. Huang, K.-J. Kim, R. Lindberg, J.B. Murphy, G.R. Neil, D.C. Nguyen, C. Pellegrini, R.A. Rimmer, F. Sannibale, G. Stupakov, R.P. Walker, and A.A. Zholents, "Free electron lasers: Present status and future challenges," *Nuclear Instruments and Methods in Physics Research A 618*, pp. 69–96 (2010).
45 E. Hosler, O. R. Wood II, W. A. Bartletta, P. J. S. Mangat, and M. E Preil, "Considerations for a free-electron laser-based extreme-ultraviolet lithography program," *SPIE* Vol. **9422**, pp. 94220D–1–94220D-15 (2015).
46 This figure was provided by Dr. Erik Hosler.
47 E. Hosler, O. R. Wood II, and M. E Preil, "Extending extreme-UV lithography technology," *SPIE Newsroom*, https://spie.org/news/6323-extending-extreme-uv-lithography-technology?SSO=1

Chapter 3
EUV Exposure Systems

EUV lithography exposure systems are conceptually similar to optical ones, involving light sources (discussed in the previous chapter), illumination and projection optics, alignment and focus systems, wafer stages, and sub-systems to mechanically handle wafers and reticles. Most of these need to be designed to meet the specific requirements for operation at EUV wavelengths, and the focus of this chapter is on those aspects specific to EUV lithography.

Currently, only one exposure tool supplier, ASM Lithography (ASML), is producing EUV exposure systems for use in high-volume manufacturing (HVM), and all of the projection optics are provided by Carl Zeiss. Consequently, many of the details presented in this chapter regarding EUV exposure systems are the result of specific choices made by ASML or Zeiss, while at other times, system characteristics are compelled by the physics of EUV lithography, independent of supplier. Throughout the chapter, it will be noted what is required generally and what is used specifically in the systems built by ASML. For example, the systems currently available from ASML have $NA = 0.33$, while systems with $NA = 0.55$ are under development. For both current and future systems, there was latitude for choosing the NA, but actual exposure tools have specific numerical apertures due to the choices made by the equipment and optics suppliers.

3.1 Lithography in Vacuum

An important and essential characteristic of EUV lithography systems is that exposures take place with wafers, lenses and masks under vacuum. EUV light is strongly absorbed by air, so there must be vacuum, or very low pressures, wherever actinic light is going to transit in EUV exposure tools. (The transmission of 13.5-nm light through 1 mm of air at atmospheric pressure is only ~0.1%.) There are a number of ramifications of vacuum. In optical exposure tools, air and gases perform a number of tasks, including thermal, chemical contamination, and defect control, and different approaches are required for addressing these issues in EUV exposure systems.

Temperature control is essential for stable exposure tool operation. In optical exposure tools, much attention has been paid to lens, wafer, and mask heating, since lens heating can lead to aberration errors, particularly defocus, as well as overlay errors, and the heating of wafers and masks also has an impact on overlay. Air flow is one method by which lens and wafer temperature is controlled in optical exposure tools, but the vacuum requirements in EUV systems limit the applicability of this approach. Temperature control in vacuum is more difficult than in air.

Consider, for example, a flat, solid surface over which air is flowing, with a temperature difference ΔT between the air and the solid. The rate of heat transfer per unit time q is given by[1]

$$q = h_C A \Delta T, \tag{3.1}$$

where h_C is the convective heat coefficient, and A is the area of the surface over which heat is being transferred. A useful approximation for h_C is given by

$$h_C = 10.45 - v + 10\sqrt{v}, \tag{3.2}$$

where v (m/s) is the speed of the air relative to the surface, and h_C is measured in units of W/m^2K. If we assume that there is a temperature difference of $\Delta T = 0.1$ K and $v = 1$ m/s, then the heat transfer per unit area is given by

$$\frac{q}{A} = 1.95 \mathrm{W/m^2}. \tag{3.3}$$

In EUV lithography systems, there cannot be air flows at pressures that are an appreciable fraction of atmospheric pressure. Gas flows at low pressure can be used to achieve levels of heat transfer that are sometimes useful, but the efficacy of such flows is much reduced compared to what occurs at atmospheric pressure. The remaining mechanisms of heat transfer are conduction and radiation. The rate of radiative transfer per unit area between two flat, parallel surfaces is given by[2]

$$\frac{q}{A} = \frac{\sigma\left(T_1^4 - T_2^4\right)}{\frac{1}{\varepsilon_1} + \frac{1}{\varepsilon_2} - 1}, \tag{3.4}$$

where σ is the Stefan–Boltzmann constant, and ε_1 and ε_2 are the emissivities of the two surfaces, which are at temperatures T_1 and T_2. If we assume $\varepsilon_1 = \varepsilon_2 = 1$, and that one surface is at a temperature of 300.0 K while the other has a temperature of 300.1 K, then the rate of heat transfer by radiation is approximately 0.2 W/m^2. Comparing this with Eq. (3.3), one can see that convection is a much more efficient means for controlling temperatures by approximately an order of magnitude.

For EUV lithography, convection can be used to a limited extent for helping to control temperatures, but it must be done using gases that are well below atmospheric pressure,[3,4] thereby reducing its effectiveness, or by using differential pumping so that the spaces at higher gas pressures are separated from EUV light paths.[5] Because of the vacuum, maintaining wafers, masks, and optical elements at near-constant temperature for good control is a very challenging engineering problem for EUV lithography, and extra attention needs to be paid to all parameters that can be affected, such as focus and overlay. Lens and overlay adjustments by active control are needed at shorter time scales and to higher levels of accuracy than are required for optical lithography.

In addition to controlling temperature, air and other gases at or near atmospheric pressure have been used in optical exposure tools for other functions. For example, it has long been common practice to purge the lenses of optical exposure tools with extremely pure gases, in order to avoid contamination of the lens surfaces. In dry exposure tools, airflow is used to prevent contamination of the bottom lens elements from materials outgassed from photoresists, and the flow of water in immersion systems serves a similar function. A problem experienced early during the development of EUV lithography was optics contamination. This was not unexpected, since contamination had been observed on the mirrors and diffraction gratings at synchrotrons used for producing vacuum ultraviolet and soft x-ray light for R&D.[6,7] With short-wavelength light, some of the energetic photons incident on mirrors and gratings are absorbed, producing photoelectrons. These photoelectrons, in turn, can cause organic molecules adsorbed on the surfaces of the optical elements to crack, resulting in a buildup of carbon films.[8] Such contamination had been observed previously to occur in the ultrahigh vacuum of research instruments involving soft x-rays, and such a problem was expected to be worse in manufacturing tools that contain optics, stages, sensors, and motors—all of which provide surfaces on which contaminants can adsorb and later outgas. In production lithographic exposure tools, resist-coated wafers are inserted repeatedly, increasing the potential for contamination by hydrocarbons and other materials that can outgas from the resist. Moreover, exposure systems containing sensitive and complex components cannot be baked to achieve ultrahigh vacuum. An example of carbon contamination on the optics of an early EUV exposure tool is shown in Fig. 3.1.

Similarly, surface oxidation can result from adsorbed water. Concern about oxidation of multilayer reflectors led to the addition of a ruthenium capping layer on top of the Mo/Si multilayer for EUV masks, since ruthenium oxidizes less readily than molybdenum or silicon.[10] Regardless of whether mirror surfaces are being oxidized or coated with carbon, reflectivity will be reduced relative to uncontaminated mirrors, reducing productivity.

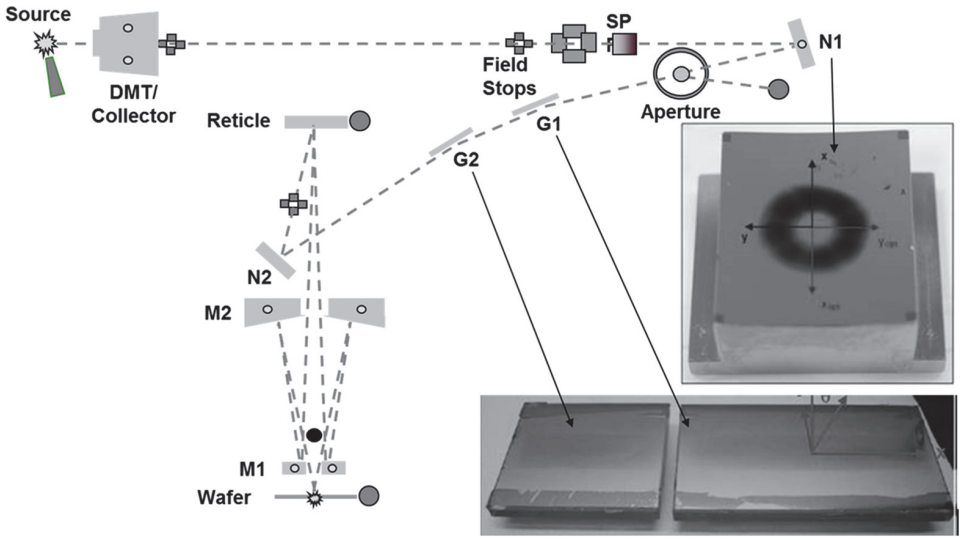

Figure 3.1 Contamination seen on mirrors in an early EUV micro-exposure tool.[9]

Contamination that is non-uniform may result in illumination non-uniformity, apodization, and a general degradation of linewidth control.

Initially, maintaining a low partial pressure of oxygen or oxygen-containing molecules in the exposure tools was considered for suppressing the build-up of carbon films on optical elements.[11,12] Although a background of oxygen did prove effective at suppressing carbon buildup, there was concern over oxidation of mirror surfaces. Consequently, it was ultimately decided to use hydrogen to reduce carbon contamination instead, an approach that has proven to be effective. Moreover, hydrogen can ameliorate oxidation by reducing oxides. Note that the use of hydrogen is not without issues, and care must be taken to avoid the blistering of Mo/Si multilayer films.[13,14,15]

Hydrogen has proven effective at preventing the build-up of carbon and oxides on mirror surfaces, and it was seen in Chapter 2 that it also can help to remove tin. However, resists can also contain elements other than carbon, hydrogen, oxygen, and tin. For example, photoacid generators containing sulfur are common, and metal-oxide resists have been created using hafnium.[16] Thus, additional mechanisms are needed to prevent contamination of the projection optics from material outgassed from resists.

One method for protecting optics from contamination is the so-called "gas curtain," where gas at low pressure is flowed across the wafer surface, which will carry contaminants away from[17,18,19] (Fig. 3.2) or towards the optics.[20] ASML refers to this as the *dynamic gas lock* (DGL). On the other hand, inserting a solid membrane window between the wafer and lens is a highly effective means of safeguarding the optics.[21] ASML refers to this as the *DGL membrane*, because it is located in the vicinity of the dynamic gas lock.

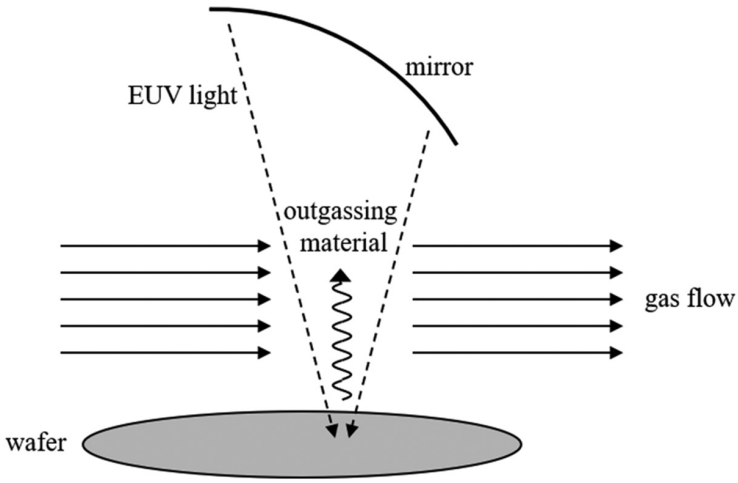

Figure 3.2 Illustration of a gas curtain, also referred to as a dynamic gas lock. Outgassing material is carried along with the gas flow, thereby reducing contamination of the projection optics.

In addition to protecting the optics from materials outgassed from resist, such membranes can also serve as spectral filters, significantly reducing the amount of out-of-band DUV and infrared light that reaches the wafer. The impact of the out-of-band light on process control is discussed further in Chapter 7. Considerable effort has been invested in developing alternatives to such windows, because the solid membranes produced to date have <85% transmission at EUV wavelengths, and their use will reduce scanner throughput and productivity. Nevertheless, given the benefits of protecting the optics from contamination and filtering the out-of-band light, such membranes are used.

In EUV lithography systems, contamination on surfaces will affect more than the optics. Deposition on masks will cause changes in critical dimensions,[22] while contamination buildup on sensors[23] will cause drifts in measurements. Hence, it is necessary to provide some method of controlling contamination on all surfaces that may be illuminated by EUV light. In optical exposure tools, the optics and masks are typically purged with ultrapure gases. Different approaches are used for EUV lithography, such as using low partial pressures of hydrogen.

Today, the prevention of optics and mask contamination is typically a concern primarily of engineers involved in the creation of lithography equipment, but chip makers also need to be conscious that such contamination can occur. After all, such difficulties occurred in optical lithography, in spite of many years of experience without such problems occurring. It is worthwhile for process engineers to be aware of problems that can potentially occur in EUV lithography.

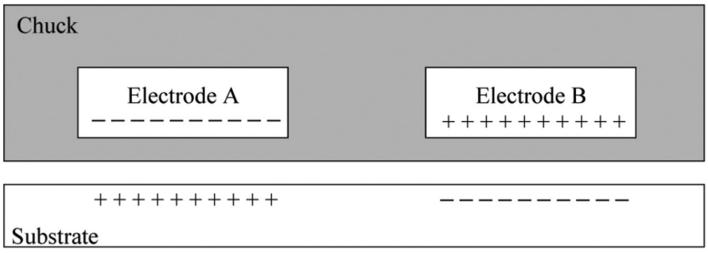

Figure 3.3 Basic configuration of a bipolar Coulomb electrostatic chuck.[25,26]

To avoid breaking vacuum, load locks are used for transferring wafers and masks into and out of the EUV exposure system. Rapid air flows during pump-down or venting can cause particulate contamination, and quick changes in air pressure can also cause temperatures to vary. The subsequent need for slow pump downs and returns to atmospheric pressure can have an impact on system throughput, although such effects will be small during steady-state exposures of a long sequence of wafers, since the transfer of masks and wafers can occur while other wafers are being exposed with other masks.

In optical lithography, wafers and reticles are clamped to their respective chucks by means of vacuum, which relies on air pressure to provide the force for pressing the substrates to chucks. Such an approach cannot be used for EUV lithography, and electrostatic chucks, which are found in many other semiconductor processing tools,[24] are used instead. In a basic bipolar Coulomb electrostatic chuck, electrodes within the chuck are charged. When the backside of a substrate is electrically conducting, charges can move freely and lead to electrostatic attraction between the chuck and the substrate (Fig. 3.3). The use of electrostatic chucks necessitates the deposition of electrically conductive films to the backsides of EUV masks. Mask backsides are discussed further in Chapter 4.

3.2 Illumination Systems

The configuration of the illumination and projection optics of a 0.33-NA EUV exposure system are shown in Fig. 3.4. The layout is similar in concept to optical exposure tools, except that all optical elements are reflective. Because of the need to maximize overall optical transmission, significant engineering effort has been directed at minimizing the number of optical elements.

As in optical exposure tools, the illumination optics serve dual purposes. First, illumination must be applied uniformly across the exposure slit, and second, capability should be provided for shaping the illumination for the purposes of resolution enhancement and source-mask optimization. These are accomplished with two sets of mirror arrays, as shown in Fig. 3.5. The light

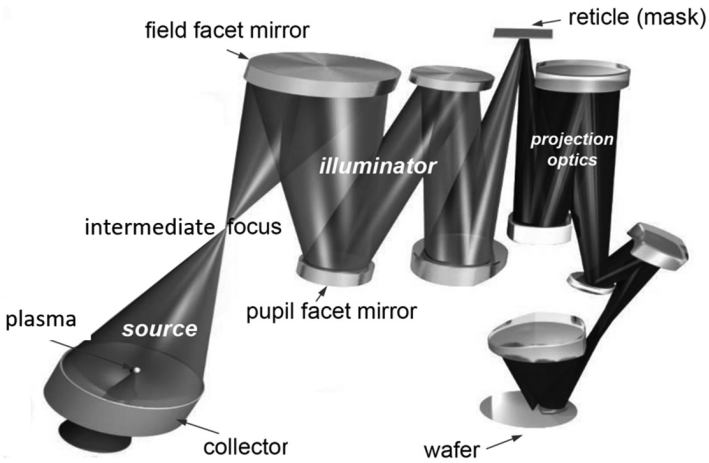

Figure 3.4 Schematic of the illumination and projection optics for the ASML NXE:3400B exposure tool.[27]

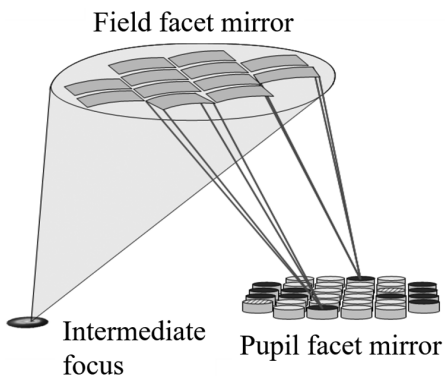

Figure 3.5 The mirror system used in EUV illuminators to enable flexible illumination.[27]

from each field facet mirror is projected across the illumination slit, resulting in reasonably uniform light (Fig. 3.6), analogous what is accomplished by a fly's eye array in an optical exposure tool.

The capabilities of illumination systems on optical exposure tools were improved over the course of several decades, such that inverse lithography technology (ILT) [also referred to as source-mask optimization (SMO)] for optical lithography is now well supported with highly flexible, programmable illumination. Fine adjustment of the illumination is possible, with thousands of mirrors available to shape the illumination.[29] With the ability to make fine adjustments on optical exposure tools, actual illumination shapes can be made in very close approximation to ideal ones.

Programmable illumination is also available on EUV exposure systems but with an order of magnitude fewer pixels[30] (see Fig. 3.7). As can be seen in

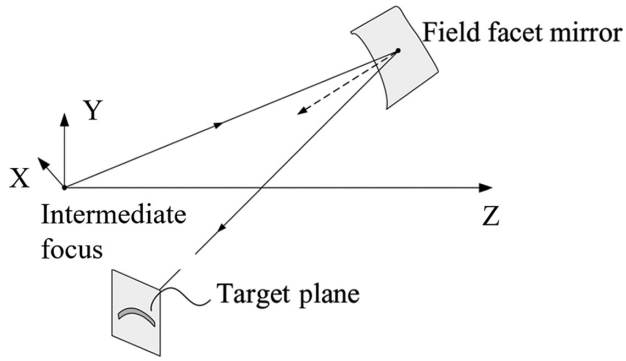

Figure 3.6 Schematic of projection of light from the field facet mirror onto the illumination slit of the scanner. Between the field facet mirror and the reticle are the intermediate optics shown in Fig. 3.4.[28]

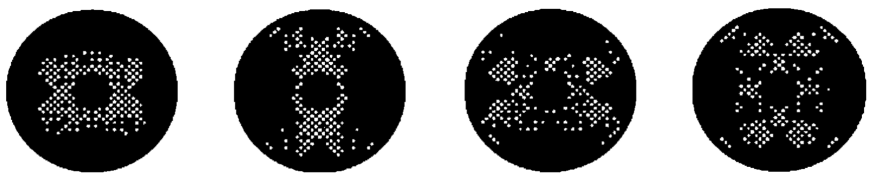

Figure 3.7 Examples of illumination tested for optimization of 7-nm-node metal layers using an ASML NXE:3300B EUV exposure tool.[31]

Figs. 3.4–3.6, the field facet and pupil facet mirrors are necessarily shaped optical elements. As with all optical elements associated with EUV lithography, the mirror surfaces need to be of very high quality. This greatly increases the cost of making such arrays for EUV lithography systems, compared to the planar micro-mirror arrays used for creating programmable illumination in optical exposure tools. Consequently, there are fewer mirrors in arrays for EUV systems than for optical tools. With the coarser adjustment found in EUV exposure tools, it is important to model lithographic performance and calculate optical proximity corrections based on actual illumination shapes, rather than ideal ones, in order to achieve accuracy.

As noted in the prior chapter, illumination stability is a challenge for EUV lithography. The collector mirror in the source can become contaminated over time, particularly by tin, and this will cause changes in illumination uniformity. Moreover, it is known from earlier work in optical lithography that not only must total light intensity be uniform across the slit but also the details of the light distribution within the pupil can affect imaging.[32] For example, when using quadrupole illumination, it is important that the total light intensity is well balanced among all four quadrants.

In EUV exposure systems, light beams from the condenser optics illuminate a reflective mask that has areas that are either of high or low

reflectance, according to the pattern to be printed, much as a conventional mask for optical lithography has areas of high and low transmission. The resulting optical pattern is imaged by a lens comprising several mirrors. Early, experimental low-NA (≤0.1) EUV lenses usually had two or four mirrors, while current 0.33-NA systems have six mirrors. The image is focused by the projection optics onto a wafer.

Because EUV optical systems are all-reflective, including the mask, the light incident on the reticle must necessarily be off axis, that is, at non-normal angles of incidence. Because of the finite numerical aperture of lenses, there will be a range of angles from which light is incident on the mask and collected (Fig. 3.8). Finite angles are needed for mechanical clearances, and the range of angles through the numerical aperture must be accommodated. Reflectivity from surfaces is typically a function of the angle of incidence, and this is particularly true for multilayer mirrors, where reflectance falls off steeply at angles away from where the maximum reflectance occurs (Fig. 3.9).

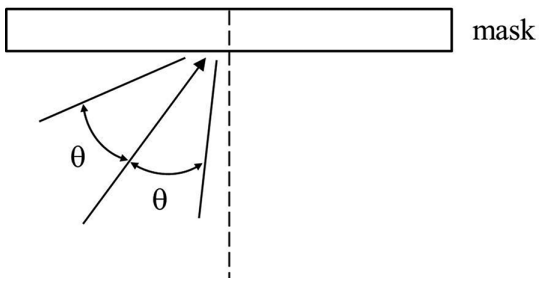

Figure 3.8 Light incident on an EUV mask.

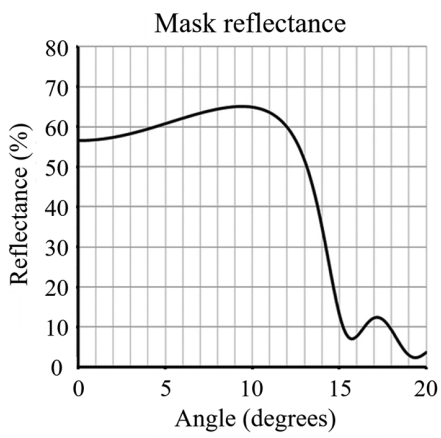

Figure 3.9 Calculated reflectance from a Mo/Si multilayer.[33] The multilayer was optimized for masks to be used on an exposure tools with a 6° chief ray angle, such as ASML's NXE:3400B with *NA* = 0.33.

The mean angle of incidence on the mask—the chief ray angle—is 6° for 0.33-NA EUV systems. All light rays must be incident from the same side of the normal to the mask, and all light rays are collected on the other side of the normal. The chief ray angle is a function of the numerical aperture (at the mask) and increases with a larger NA (assuming a fixed lens reduction). Reducing the angles of incidence nearer to normal requires a lower NA (at the wafer) or larger lens reduction. Without increasing the lens reduction, the mask 3D effects described in Chapter 6 will become more significant with an increased NA. This consideration affected system architectural choices for high-NA EUV exposure tools, discussed in more detail in Chapter 10.

3.3 Projection Optics

During the very early days of EUV lithography development, it became understood that the projection optics would have very stringent requirements for surface figure and roughness, and would therefore be difficult to fabricate. For example, early immersion exposure tools had aberration levels <1 nm, or <5 mλ.[34] To achieve a similar level of aberrations for EUV lithography in terms of milliwaves, the absolute level of aberrations would need to be <0.07 nm! While this level of aberrations has not yet been achieved, a very impressive level of aberrations of <0.2 nm (rms) has been reported.[35]

Aberrations are typically described in terms of Zernike polynomials, and the impact on imaging considered relevant in optical lithography has generally been accounted for adequately by the first 36 Zernike polynomials. These are relatively low spatial frequency concerns, and they are affected by the surface figure of lens optical elements, where surface figure deviations from the ideal are averaged over dimensions on millimeter scale. The impact of lens aberrations on imaging in EUV lithography is described by the same theory that applies to optical lithography, modified by a change of wavelength.

In addition to the image degradation due to aberrations caused by mirror figure error, it was also understood by early researchers in EUV lithography that surface roughness of lens mirrors at very high spatial frequencies would scatter light. Initially, this roughness was thought to scatter light only at wide angles, outside of the exit pupil of the projection optics. The primary effect of such roughness is a reduction in the total amount of light that would reach the wafer, but otherwise it would have little impact on imaging. However, wafer patterning using early tools revealed significant image contrast degradation (~35%) due to high levels of scattered light (flare) that were transferred to the wafer plane[36,37] at a much higher level than had been observed in optical lithography.[38]

The problem of light scattering is illustrated in Fig. 3.10. For mirror surfaces that deviate from the ideal at very low spatial frequencies, light will be reflected specularly but perhaps at the wrong angle, thus resulting in aberrations. For

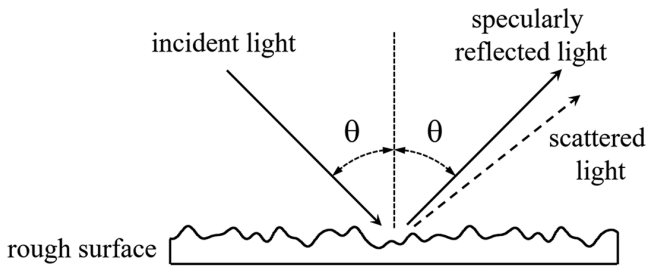

Figure 3.10 Illustration of light reflected and scattered from a rough surface.

Table 3.1 Mirror surface parameters, requirements and recent results for EUV mirrors.

Spatial frequency range	Range values	Lithographic impact	Requirements (pm, rms)[30,39,40]	Current status (pm, rms)[40,41]
Figure (low spatial frequency)	<1 mm^{-1}	Aberrations	50	~30
Mid-spatial-frequency roughness	1 mm^{-1} to 1 μm^{-1}	Flare	100	~80
High-spatial-frequency roughness	1 μm^{-1} to 50 μm^{-1}	Light loss	100	~70

roughness that is comparable to the wavelength of light, some of the reflected light will scatter over a range of angles. For very high spatial frequency roughness, the scattering angles will be very large, and the scattered light will not be transmitted through the exit pupil of the optics. This results in an effective loss of light intensity. At intermediate spatial frequencies, light will be scattered but will transferred to the wafer, albeit not necessarily at the intended location. This latter type of scattered light will degrade image formation. Mirror surface requirements for use in EUV projection optics are summarized in Table 3.1.

Even with great care in polishing, and with only a few elements in the lenses, flare in EUV systems is usually much higher than encountered in conventional optical lithography. An initial set of optics for an early full-field exposure tool had approximately 40% long-range flare, and improved optics still had 17% flare.[42,43] The next generation of full-field exposure tools had 7–10% flare,[44] while the long-range flare in tools today is ~3%.[45] This is in contrast to state-of-the-art KrF and ArF lenses, where long-range flare <1% is routine. Corrections for flare are now a routine component of the OPC for EUV lithography and typically account for flare as a function of distance.[46]

However, high levels of flare will degrade process windows that cannot be ameliorated by OPC (see Problem 3.3).[47]

The reason for the greater level of flare in EUV lenses is the short wavelength involved and the use of mirrors. Consider a surface which produces an rms level of phase variation rms_{phase} in light reflected from the surface. The total integrated scattered (TIS) light from such a surface is given by[48]

$$TIS = 4\pi^2 \left[\frac{rms_{phase}}{\lambda}\right]^2. \tag{3.5}$$

For a given level of surface roughness, a mirror will produce greater phase error than a refracting surface, as the light passes twice past surface roughness from a reflector but only once with a refracting surface. Because of the very short EUV wavelength, compared to DUV light, the amount of scatter is much greater for EUV optical systems for a given level of surface roughness. [Note the denominator of Eq. (3.5).]

Further complicating the polishing of mirror surfaces is the need to use aspheric mirrors in order to minimize the number of mirrors in the lens. With less than 70% reflectance per mirror, each pair of mirrors added reduces light intensity at the wafer by over half, so aspheric optical elements are necessary for EUV lithography. Polishing tools with small surface areas are used to make aspheric mirrors, and care needs to be taken to avoid mirror roughness on a length scale equal to the size of the polishing tool. In addition, the multilayer deposition process can be tuned to have the effect of smoothing roughness in the underlying substrate,[49] but this must be balanced with maximizing total reflectance. Because of the very stringent requirements for mirror-surface figure, the deposited multilayer films must be low stress so that they do not deform the carefully polished glass substrates.

The total amount of light that is scattered by mirror roughness in the projection optics depends directly upon the total amount of light that is reflected from the mask. Consequently, the impact of flare is highly dependent on mask absorber density and details of the layouts. The amount of reflective area on masks depends on the tone (positive or negative) of the resists used. For EUV lithography, it is desirable to minimize the amount of reflective area to have low levels of flare, and masks covered mostly with absorber are also less sensitive to mask blank defects, as will be discussed further in the next chapter. Hence, contact, via, and cut layers benefit from the use of positive tone resists, while negative resists might be better for gate layers. For contact, via, and cut masks, which typically have <10% reflective area when using positive tone resists, only a small amount of light is transmitted into the lens, and therefore the overall level of flare will be small. Metal layers typically

have 40–60% reflective area, so flare will be significant regardless of the tone of the resist.

With a proper characterization of flare, it is possible to calculate the impact of scattered light on optical images, and optical proximity corrections can be adjusted accordingly. Flare has often been considered as a constant background level of light, but this is only the long-range flare. Because light can be scattered over distances of microns, calculating the impact of flare accurately requires taking local pattern density into account. This increases the complexity of correcting the optical proximity corrections, but methodologies have been developed for doing this. In fact, such layout dependent corrections for flare were applied to the first fabrication of an integrated circuit using EUV lithography.[50] Computational corrections for flare are discussed further in Chapter 6.

Lens heating has long been a characteristic of i-line and ArF lenses, where the glass used for lens elements absorbs a small amount of light. In EUV systems, mirrors absorb a considerably higher percentage of light (>30%), leading inevitably to significant lens heating. Consequently, the mirrors used for the optics of EUV exposure tools are fabricated from ultra-low expansion glass, which has an extremely small coefficient of thermal expansion[51] (see Figs. 3.11 and 3.12). As can be seen in Fig. 3.12, for ULE®, an ultra-low expansion glass made by Corning, the coefficient of thermal expansion is zero at a single temperature and non-zero at temperatures higher or lower than the point of zero expansion. The coefficient of thermal expansion for ULE® can be contrasted with that of fused silica (0.5 ppm/°C), which is generally considered to be a low-expansion material.

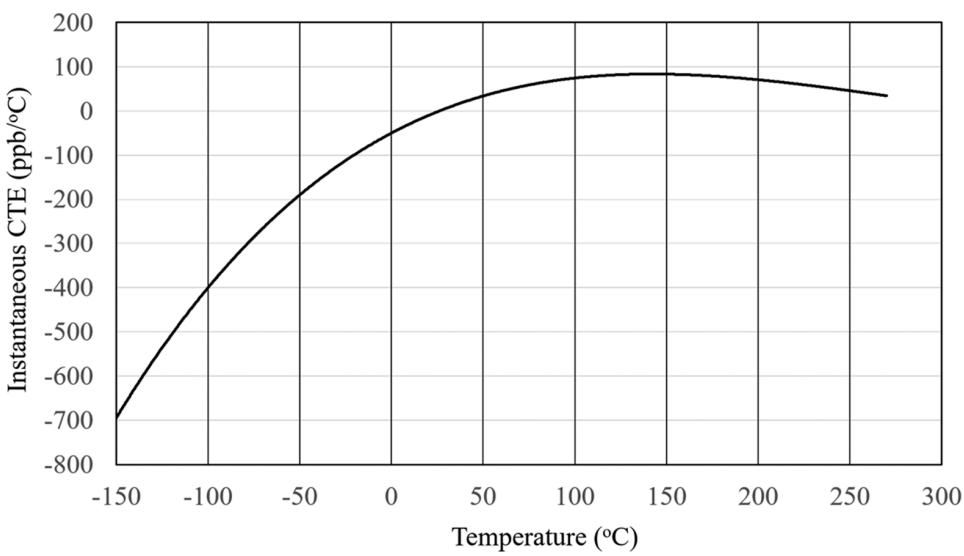

Figure 3.11 Coefficient of thermal expansion for ULE® 7973.[52]

One interesting consequence of the use of all-reflective optics is the shape of the slit in scanning-exposure tools. In KrF and ArF reduction scanners with dioptric lenses, the slit is rectangular. In these situations, the imaging is done through the center of the lens, where aberrations are usually smallest. The slit remains rectangular in shape when optical scanners have catadioptric lenses, but the slit height is necessarily reduced, and the slit can be offset from center, due to the central obscuration found in catadioptric lenses (Fig. 3.13). In reflective optics, aberrations can often be minimized in a slit that is curved, a property that was exploited in the first generation of projection exposure tools several decades ago.[53] By imaging in such a curved slit, fewer optical elements are required to correct for aberrations. Since minimizing the number of

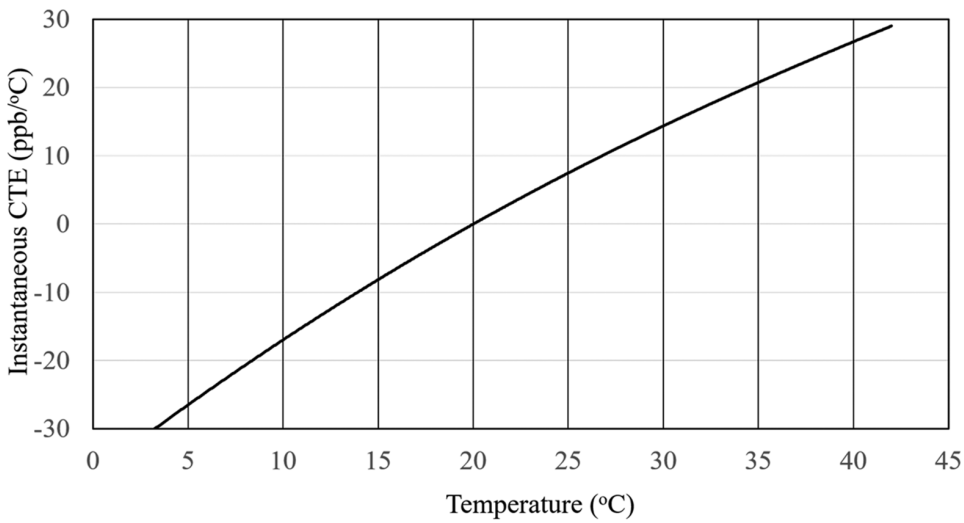

Figure 3.12 Coefficient of thermal expansion for ULE® 7973 near room temperature.[52]

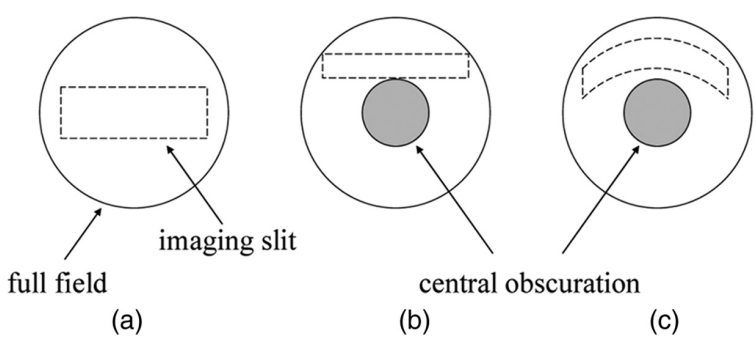

Figure 3.13 Examples of slits for different types of lenses: (a) refractive lens, such as is typically found in non-immersion optical scanners; (b) catadioptric lens, such as is found in immersion optical scanners or very-high-NA non-immersion scanners; and (c) ring field, as is usually used in EUV exposure systems.

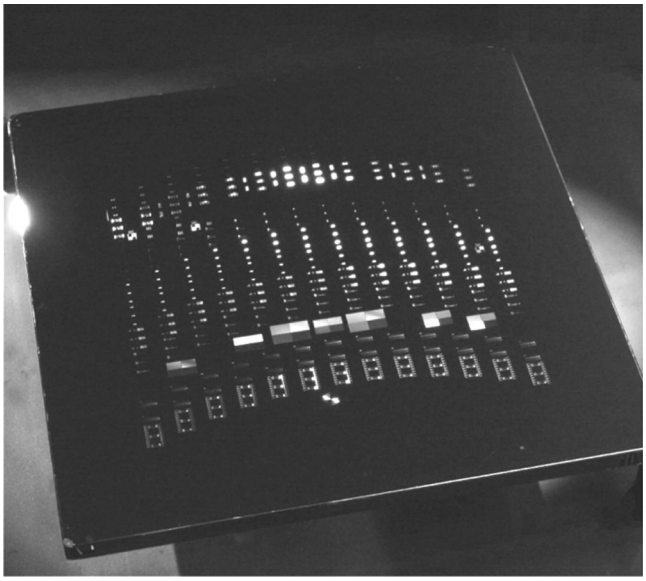

Figure 3.14 An EUV mask with features arranged to follow a curved slit to enable static as well as scanning exposures.

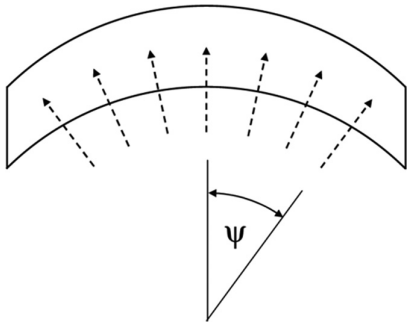

Figure 3.15 The illumination is incident on the mask with an azimuthal angle ψ across the slit. Systems designed to emulate ASML's 0.33-NA systems use a range of azimuthal angles of ±18.6°.[55]

reflections to maximize throughput is an important consideration for EUV lithography, EUV scanners have curved slits.[54] Shown in Fig. 3.14 is a mask that was fabricated so it could be exposed in a static as well as a scanning mode. Consequently, sections of the mask were arranged to follow the slit, and the curvature is evident in Fig. 3.14.

The ring-field configuration increases the complexity of OPC, because the direction of the light incident on the mask changes across the slit. While the angle of incidence relative to the normal of the mask plane remains constant, it acquires an azimuthal component, as illustrated in Fig. 3.15. Consequently, the light may not be strictly perpendicular or parallel to horizontal or vertical

features on the mask. As will be discussed in Chapter 6, aerial images depend on the angle at which light is incident on the mask. To compensate for the resulting variation in the printing, OPC needs to vary across the slit to achieve full accuracy.

3.4 Alignment Systems

For the most part, alignment systems for EUV exposure tools are very similar to their optical counterparts, with some care taken to fabricate the alignment optics using low-outgassing materials. One component that must necessarily be different for EUV exposure tools is the sensor on the wafer stage that is used to reference the wafer stage to the reticle, which must be done through the lens at the exposure wavelength. This is shown schematically in Fig. 3.16. On the wafer stage is an artifact comprising two primary features. One is a mark whose position can be measured using the systems that precisely locate the positions of wafer alignment marks. The other is a sensor that can detect the image of reticle alignment marks that are projected through the optics of the exposure tool. The distance between these two features is predetermined to a high degree of accuracy. On dual-stage exposure tools, the positions of wafer alignment marks are measured during wafer metrology, as is the position of the alignment mark on the wafer stage. When the wafer stage is moved under the lens, the positions of the reticle alignment marks can be measured, enabling alignment between wafer and reticle. As with all EUV sensors, there is always concern over contamination of the sensor used to align the mask, but this is particularly true for sensors on the wafer stage, where resist-coated wafers can be placed and can outgas.

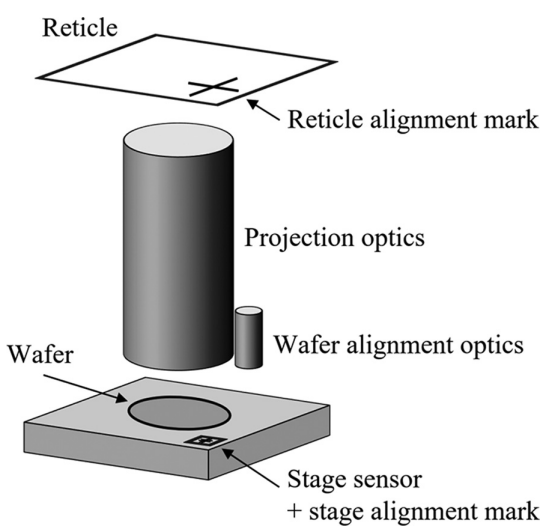

Figure 3.16 Schematic of wafer and reticle alignment.

3.5 Stages in EUV Lithography Systems

The requirement for good vacuum in EUV exposure systems has consequences for the stages of scanners. In optical lithography systems, air bearings have long been used for wafer and mask stages to enable smooth scanning motions. It is possible to construct air bearings for the stages that can be used in a vacuum by using configurations where the air can be removed locally.[56,57,58] However, magnetic bearings have obvious advantages for EUV applications [59,60,61] and are used in the EUV exposure systems from ASML.[62] Stages with magnetic bearings are often referred to as mag-lev stages.

In a typical arrangement involving magnetic bearings, there is an array of magnets on the bottom of the stage (see Fig. 3.17). Stage motion is achieved by driving current through the windings of static stators that are below the stage. This configuration is advantageous, because it eliminates the need for attaching power cables to the moving stage, and it also reduces the problem of controlling the stage temperature. Magnet arrays are often in the Halbach configuration,[63] which is an arrangement of permanent magnets that produces a strong field on one side of the array and a very weak magnetic field on the other. This is achieved by creating a spatially rotating magnetic field. Such an array is illustrated in Fig. 3.18.

3.6 Focus Systems

Good focus control is extremely important for EUV lithography. Although the Rayleigh depth of focus for 0.33-NA optics is 124 nm, there are considerations in EUV lithography that compel very tight focus control, beyond the familiar focus-driven variations in critical dimensions that arise in optical lithography. Moreover, for high-NA (NA = 0.55) EUV lithography, the Rayleigh depth of focus is only 45 nm. The aforementioned additional considerations compelling good focus control will be discussed in more detail in subsequent chapters.

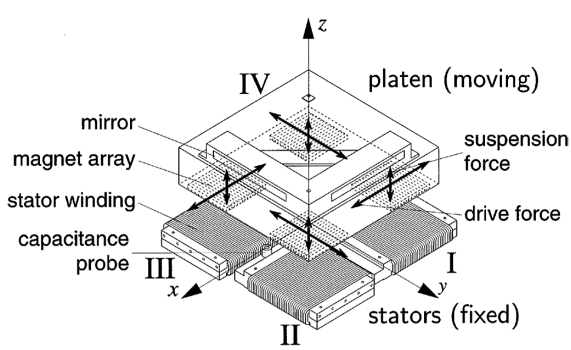

Figure 3.17 Schematic of a magnetically levitated stage.[64] The arrows indicate the directions in which motor forces are exerted on the magnetic arrays.

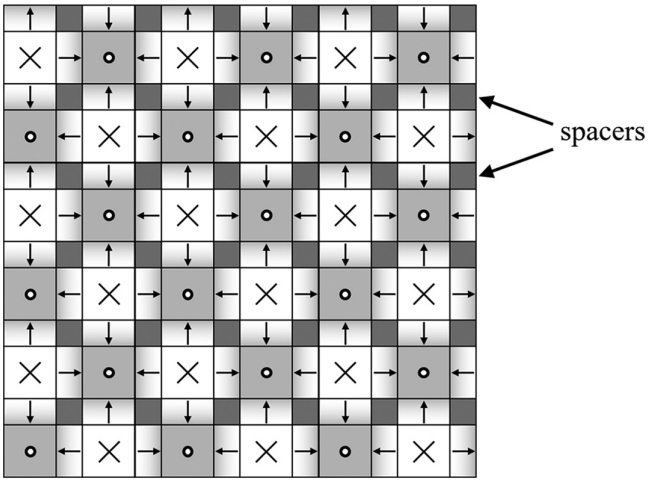

Figure 3.18 Halbach arrangement of magnets.[65] The arrows point in the direction of the magnetic field from north to south. Circles indicate that the magnetic field has the north pole coming out of the page, while the X indicates a field pointing into the page.

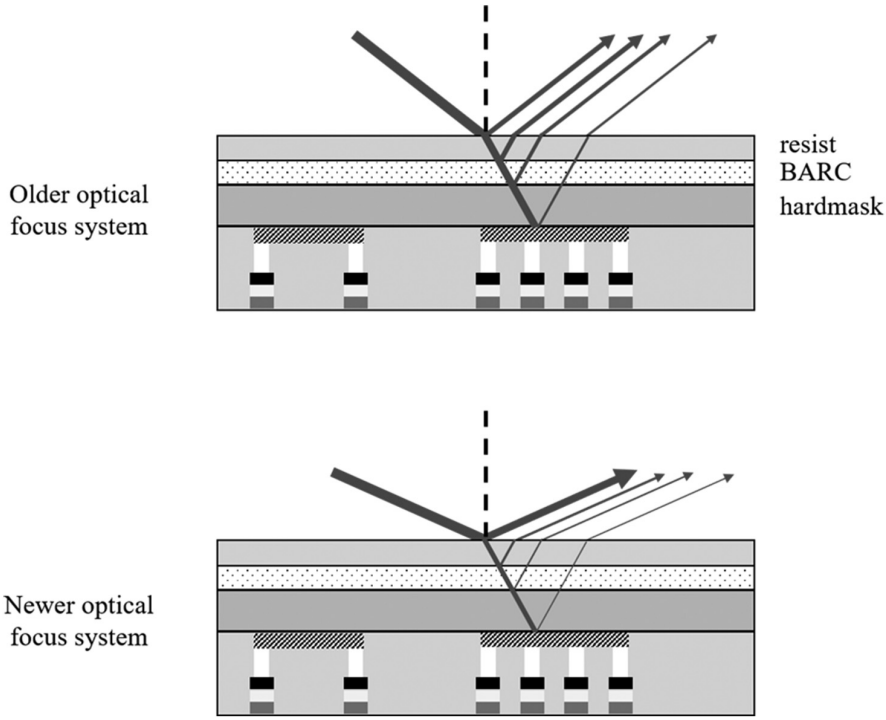

Figure 3.19 Optical focus systems. With more oblique incident light, along with shorter wavelengths over a broad band, a stronger signal is produced by the top layers of the pattern stack relative to signals produced by reflections from underlayers.

To establish wafer focus and leveling, optical techniques are often used, but it has long been known that such methods are affected by films and patterns that may already exist on the wafers.[66,67,68] To address this problem, ASML introduced an air gauge to calibrate their optical focus and leveling systems.[69] For EUV exposure systems, compatibility with the vacuum environment is an important consideration, making it difficult to use air gauge focus metrology. Consequently, ASML developed an optical focus system that is less sensitive to films and patterns on the wafer.[70] This reduced sensitivity was achieved by using ultraviolet wavelengths over a broad band instead of using optical and infrared wavelengths over narrow bandwidths, as well as using a more glancing angle of incidence for the optical beams (see Fig. 3.19). Low levels of light must be used to avoid exposing resists with the ultraviolet light. Process engineers can also reduce the difference in focus measurement among chip areas of varying pattern density by using dummy features where possible.

Problems

3.1 Show that the Rayleigh resolution of an EUV (λ = 13.5 nm) lithography system with an NA = 0.33 is 20.5 nm and that the Rayleigh depth of focus is 124 nm. Show that the resolution and depth of focus are 12.3 nm and 44.6 nm, respectively, for an EUV lens with a 0.55 NA.

3.2 The attenuation length of carbon for light of wavelength 13.5 nm is 155 nm. Show that the transmission of light through a six-mirror lens where each mirror is coated with 1 nm of carbon is 92.6% of an identical lens for which the mirrors have no carbon coating. (Remember that the light will travel twice through the carbon coating on each mirror.)

3.3 The change in linewidth ΔL when the dose $E(x)$ is changed proportionally $E(x) \rightarrow (1+\Delta)E(x)$ is given by

$$\Delta L = 2\Delta(ILS)^{-1},$$

where ILS is the image log slope.[71] Show that the same relationship holds for an added dose $E(x) \rightarrow E(x) + \Delta$, where Δ is independent of position.

References

1 http://www.engineeringtoolbox.com/convective-heat-transfer-d_430.html
2 http://web.mit.edu/16.unified/www/FALL/thermodynamics/notes/node136.html
3 H. Lee, S. Lee, J. Park, and H, "Extreme ultraviolet pellicle cooling by hydrogen gas flow (Conference Presentation)," *Proc. SPIE* Vol. **10809**, p. 108091B, 2018.

4 M. Kang, S. Lee, E. Park, and H, "Thermo-mechanical behavior analysis of extreme-ultraviolet pellicle cooling with H_2 flow, *Proc. SPIE* Vol. 10450, 2017.
5 J. van Schoot, "High NA EUV lithography: Enabling Moore's Law in the next decade," *EUVL Workshop*, 2017, https://www.euvlitho.com/2017/P22.pdf
6 K. Boller, R. Haelbich, H. Hogrefe, W. Jark, and C. Kunz. "Investigation of carbon contamination of mirror surfaces exposed to synchrotron radiation." *Nuclear instruments and methods in physics research* **208**, no. 1-3 273–279 (1983).
7 T. Koide, S. Sato, T. Shidara, M. Niwano, M. Yanagihara, A. Yamada, A. Fujimori, A. Mikuni, H. Kato, and T. Miyahara. "Investigation of carbon contamination of synchrotron radiation mirrors." *Nuclear Instruments and Methods in Physics Research Section A: Accelerators, Spectrometers, Detectors and Associated Equipment* **246**, no. 1-3, 215–218, (1986).
8 J. Chen, Characterization of EUV induced contamination on multilayer optics. PHD Thesis, University of Twente, 2011.
9 This figure was provided by Dr. Andrea Wüest.
10 S. B. Hill, I. Ermanoski, C. Tarrio, T. B. Lucatorto, T. E. Madey, S. Bajt, M. Fang, and M. Chandhok. "Critical parameters influencing the EUV-induced damage of Ru-capped multilayer mirrors," *Proc. SPIE* Vol. **6517**, p. 65170G, 2007.
11 M. E. Malinowski, P. A. Grunow, C. Steinhaus, W. M. Clift, and L. E. Klebanoff. "Use of molecular oxygen to reduce EUV-induced carbon contamination of optics," *Proc. SPIE* Vol. **4343**, pp. 347–356, 2001.
12 L. E. Klebanoff, M. E. Malinowski, P. A. Grunow, W. M. Clift, C. Steinhaus, A. H. Leung, and S. J. Haney, "First environmental data from the EUV engineering test stand," *Proc. SPIE* Vol. **4343**, pp. 342–34.
13 A. S. Kuznetsov, M. A. Gleeson, R. W. E. Van de Kruijs, and F. Bijkerk. "Blistering behavior in Mo/Si multilayers," *Proc. SPIE* Vol. **8077**, p. 807713, 2011.
14 A. S. Kuznetsov, M. A. Gleeson, and Frederik Bijkerk. "Hydrogen-induced blistering mechanisms in thin film coatings." *Journal of physics: Condensed matter* **24**, no. 5, 052203 (2011).
15 R.A.J.M. Van den Bos, C. J. Lee, J. P. H Benschop, and F. Bijkerk, "Blister formation in Mo/Si multilayered structures induced by hydrogen ions," *Journal of physics D: applied physics*, **50**(26), p. 265302, 2017.
16 Y. Ekinci, M. Vockenhuber, B. Terhalle, M. Hojeij, L. Wang, and T. R. Younkin, "Evaluation of resist performance with EUV interference lithography for sub-22-nm patterning," *Proc. SPIE* Vol. **8322**, p. 83220W, 2012.

17 M. P. Kanouff and A. K. Ray-Chaudhuri, "Wafer chamber having a gas curtain for extreme-UV lithography," U.S. Patent No. 6, 198, 792B1 (2001).
18 M. P. Kanouff and A. K. Ray-Chaudhuri, "A gas curtain for mitigating hydrocarbon contamination of EUV lithographic optical components," *Proc. SPIE* **3676**, pp. 735–742 (1999).
19 V. V. Banine and J. H. J. Moors, "Lithography Apparatus and Device Manufacturing Method," US Patent 8, 094, 288 B2 (2012).
20 P. W. H. De Jager, H. G. C. Werij, and P. Van Zuylen. "Lithographic device." U.S. Patent 6, 459, 472, issued October 1, 2002.
21 M. van de Kerkhof, H. Jasper, L. Levasier, R. Peeters, R. van Es, J. Bosker, A.r Zdravkov et al. "Enabling sub-10nm node lithography: presenting the NXE: 3400B EUV scanner," *Proc. SPIE* Vol. **10143**, p. 101430D, 2017.
22 Y. Fan, L. Yankulin, P. Thomas, C. Mbanaso, A. Antohe, R. Garg, Y. Wang, et al. "Carbon contamination topography analysis of EUV masks," *Proc. SPIE* Vol. **7636**, p. 76360G 2010.
23 L. Shi, F. Sarubbi, S. N. Nihtianov, L. K. Nanver, T. L. M. Scholtes, and F. Scholze. "High performance silicon-based extreme ultraviolet (EUV) radiation detector for industrial application," *2009 35th Annual Conference of IEEE Industrial Electronics*, pp. 1877–1882. IEEE, 2009.
24 G. A. Wardly, "Electrostatic wafer chuck for electron beam microfabrication." *Review of Scientific Instruments* **44**, no. 10, pp. 1506–1509 (1973).
25 Electrostatic chucks may be of Coulomb or Johnsen-Rahbek type, as described further in M. Sogard, A. Mikkelson, M. Nataraju, K. Turner and R. Engelstad, "Analysis of Coulomb and Johnsen-Rahbek electrostatic chuck performance for EUV lithography," *J. Vac. Sci. Technol. B* **25**(6), pp. 2155–2161 (2007).
26 M.R. Sogard, A.R. Mikkelson, V. Ramaswamy, and R.L. Engelstad, "Analysis of Coulomb and Johnsen-Rahbek elecrostatic chuck performance in the presence of particles for EUV lithography," *Proc. SPIE* **7271**, 72710H (2009).
27 W. Kaiser, presented at Semicon Korea, 2018.
28 J. Jiang, Q. Mei, Y. Li, and Y. Liu. "Illumination system with freeform fly's eye to generate pixelated pupil prescribed by source-mask optimization in extreme ultraviolet lithography." *Optical Engineering* **56**, no. 6 (2017): 065101.
29 M. Mulder, A. Engelen, O. Noordman, R. Kazinczi, G. Streutker, B. van Drieenhuizen, S. Hsu, K. Gronlund, M. Degünther, D. Jürgens, J. Eisenmenger, M. Patra, and A. Major, "Performance of a Programmable Illuminator for generation of Freeform Sources on high NA immersion systems," *Proc. of SPIE* Vol. **7520**, 75200Y, 2009.

30 M. Lowisch, P. Kuerz, O. Conradi, G. Wittich, W. Seitz, and W. Kaiser. "Optics for ASML's NXE: 3300B platform," *Proc. SPIE* Vol. **8679**, p. 86791H, 2013.
31 Y. Chen, L. Sun, Z. J. Qi, S. Zhao, F. Goodwin, I. Matthew, and V. Plachecki. "Tip-to-tip variation mitigation in extreme ultraviolet lithography for 7 nm and beyond metallization layers and design rule analysis," *Journal of Vacuum Science & Technology B, Nanotechnology and Microelectronics: Materials, Processing, Measurement, and Phenomena* **35**, no. 6 (2017): 06G601.
32 D. G. Flagello, B. Geh, R. Socha, P. Liu, Y. Cao, R. Stas, O. Natt, and J. Zimmermann. "Understanding illumination effects for control of optical proximity effects (OPE)," *Proc. SPIE* Vol. **6924**, p. 69241U, 2008.
33 S. Raghunathan, O. R. Wood, P. Mangat, E. Verduijn, V. Philipsen, E. Hendrickx, R. Jonckheere, K. A. Goldberg, M. P. Benk, P. Kearney, Z. Levinson, B. W. Smith, et al. "Experimental measurements of telecentricity errors in high-numerical-aperture extreme ultraviolet mask images." *J. Vac. Sci. Tech. B*, Vol **32**, no. 6 (2014): 06F801.
34 J. de Klerk, C. Wagner, R. Droste, L. Levasier, L. Jorritsma, E. van Setten, H. Kattouw, J. Jacobs, and T. Heil. "Performance of a 1.35 NA ArF immersion lithography system for 40-nm applications," *Proc. SPIE* Vol. **6520**, p. 65201Y, 2007.
35 M. van de Kerkhof, H. Jasper, L. Levasier, R. Peeters, R. van Es, J. Bosker, A. der Zdravkov, et al. "Enabling sub-10nm node lithography: presenting the NXE: 3400B EUV scanner," *Proc. SPIE* Vol. **10143**, p. 101430D, 2017.
36 B. La Fontaine, D. P. Gaines, D. R. Kania, G. E. Sommargren, S. L. Baker, and D. Ciarlo. *Performance of a two-mirror, four-reflection, ring-field optical system at* λ = 13 nm. No. UCRL-JC-123013; CONF-960493-17. Lawrence Livermore National Lab., CA (United States), 1996.
37 B. La Fontaine, T. P. Daly, H. N. Chapman, D. P. Gaines, D. G. Stearns, D. W. Sweeney, and D. R. Kania. *Measuring the effect of scatter on the performance of a lithography system*. No. UCRL-JC-123064; CONF-960493-12. Lawrence Livermore National Lab., CA (United States), 1996.
38 Joseph P. Kirk, "Scattered light in photolithographic lenses," *Proc. SPIE* Vol. **2197**, pp. 566–572, 1994.
39 B. Wu and A. Kumar, "Extreme ultraviolet lithography: a review," *J. Vac. Sci. Technol. B* **25**(6), pp. 1743–1761 (2007).
40 B. Geh, "EUVL: the natural evolution of optical microlithography," *Proc. SPIE* Vol. **10957**, p. 1095705, 2019.
41 K. Murakami, T. Oshino, H. Kondo, H. Chiba, H. Komatsuda, K. Nomura, and H. Iwata, "Development status of projection optics and illumination optics for EUV1," *Proc. SPIE* **6921**, 69210Q (2008).

42 D. A. Tichenor, W. C. Replogle, S. H. Lee, W. P. Ballard, A. H. Leung, G. D. Kubiak, L. E. Klebenoff, S. Graham, J. E. M. Goldsmith, K. L. Jefferson, J. B. Wronsky, T. G. Smith, T. A. Johnson, H. Shields, L. C. Hale, H. N. Chapman, J. S. Taylor, D. W. Sweeney, J. A. Folta, G. E. Sommargren, K. A. Goldberg, P. Naulleau, D. T. Attwood, and E. M. Gullikson, "Performance upgrades in the EUV engineering test stand," *Proc. SPIE* **4688**, pp. 72–86 (2002).
43 S. H. Lee, P. Naulleau, C. Krautschik, M. Chandbok, H. N. Chapman, D.J. O'Connell, and M. Goldstein, "Lithographic flare measurements of EUV full-field projection optics," *Proc. SPIE* **5037**, pp. 103–111 (2003).
44 T. Miura, K. Murakami, K. Suzuki, Y. Kohama, K. Morita, K. Hada, Y. Ohkubo, and H. Kwai, "Nikon EUVL development progress update," *Proc. SPIE* **6921**, 69210M (2008).
45 V. W. Guo, F. Jiang, A. Tritchkov, S. Jayaram, S. Mansfield, L. Zhuang, Y. Sun, X. Zhuang, and T. Bailey. "SRAF requirements, relevance, and impact on EUV lithography for next-generation beyond 7nm node," *Proc. SPIE* Vol. **10583**, p. 105830N (2018).
46 B. La Fontaine, Y. Deng, M. Dusa, A. Acheta, A. Fumar-Pici, H. Bolla, B. Cheung, B. Singh, and H. J. Levinson, "Characterization, modeling, and impact of scattered light in low-k1 lithography," *Proc. SPIE* Vol. **5754**, pp. 285–293 (2005).
47 M. Lowisch, U. Dinger, U. Mickam, and T. Heil, "EUV imaging—an aerial image study," *Proc. SPIE* **5374**, pp. 53–63 (2004).
48 E. M. Gullikson, S. L. Baker, J. E. Bjorkholm, J. Bokor, K. A. Goldberg, J. E. Goldsmith, C. Montcalm, P. P. Naulleau, E. A. Spiller, D. G. Stearns, J. S. Taylor, and J. H. Underwood, "EUV scattering and flare of 10X projection cameras," *Proc. SPIE* **3676**, pp. 717–723 (1999).
49 E. Spiller, S.L. Baker, P.B. Mirkarimi, V. Sperry, E.M. Gullikson, and D.G. Stearns, "High-performance Mo-Si multilayer coatings for extreme-ultraviolet lithography by ion-beam deposition," *Appl. Opt.* **42**(19), pp. 4049–4058 (2003).
50 B. La Fontaine, Y. Deng, R. Kim, H. J. Levinson, S. McGowan, U. Okoroanyanwu, R. Seltmann, C. Tabery, A. Tchikoulaeva, T. Wallow, O. Wood, J. Arnold, D. Canaperi, M. Colburn, K. Kimmel, C. Koay, E. McLellan, D. Medeiros, S. P. Rao, K. Petrillo, Y. Yin, H. Mizuno, S. Bouten, M. Crouse, A van Dijk, Y. van Dommelen, J. Galloway, S. Han, B. Kessels, B. Lee, S. Lok, B. Niekrewicz, B. Pierson, R. Routh, E. Schmitt-Weaver, K. Cummings, and J. Word, "The use of EUV lithography to produce demonstration devices," *Proc. SPIE* **6921**, 69210P (2008).
51 https://www.corning.com/media/worldwide/csm/documents/7973%20Product%20Brochure_0919.pdf

52 https://www.corning.com/worldwide/en/products/advanced-optics/product-materials/optical-materials.html
53 A. Offner, "Unit power imaging catoptric anastigmat," U.S. Patent No. 3, **748**, 015 (1973).
54 D. M. Williamson, "Evolution of ring field systems in microlithography," *Proc. SPIE* **3482**, pp. 369–376 (1998).
55 R. Capelli, A. Garetto, k. Magnusson, and T. Scherübl, "Scanner arc illumination and impact on EUV photomasks and scanner imaging," *Proc. SPIE* Vol. **9231**, p. 923109 (2014).
56 K. Suzuki, T. Fujiwara, K. Hada, N. Hirayanagi, S. Kawata, K. Morita, K. Okamoto, T. Okino, S. Shimizu, and T. Yahiro, "Nikon EB stepper: its system concept and countermeasures for critical issues," *Proc. SPIE* **3997**, pp. 214–224 (2000).
57 T. Novak, D. Watson, and Y. Yoda, "Nikon electron projection lithography system: mechanical and metrology issues," *Am. Soc. Precis. Eng. Proc.* (2000). http://www.aspe.net/publications/Annual_2000/Annual_00.html
58 T. H. Bisschops, et al., "Gas bearings for use with vacuum chambers and their application in lithographic projection apparatuses," U.S. Patent No. 6603130 (2003).
59 A. T. A. Peijnenburg, J.P.M. Vermeulen, and J. van Eijk, "Magnetic levitation systems compared to conventional bearing systems," *Microelectron. Eng.* **83**(4–9) pp. 1372–1375 (2006).
60 P. T. Konkola, "Magnetic bearing stages for electron beam lithography," *MS Thesis*, Massachussetts Institute of Technology (1998). http://hdl.handle.net/1721.1/9315
61 M. Williams, P. Faill, P. M. Bischoff, S.P. Tracy, and B. Arling, "Six degrees of freedom Mag-Lev stage development," *Proc. SPIE* **3051**, pp. 856–867 (1997).
62 F. de Jong, B. van der Pasch, T. Castenmiller, B. Vleeming, R. Droste, and F. van de Mast. "Enabling the lithography roadmap: an immersion tool based on a novel stage positioning system," *Proc. SPIE* Vol. **7274**, p. 72741S, 2009.
63 K. Halbach, "Design of permanent multipole magnets with oriented rare earth cobalt material." *Nuclear instruments and methods* **169**, no. 1 (1980): 1–10.
64 W. Kim and D. L. Trumper. "High-precision magnetic levitation stage for photolithography." *Precision Engineering* **22**, no. 2 (1998): 66–77.
65 D. A. Markle, "Magnetically positioned XY stage having six degrees of freedom." U.S. Patent 6, 072, 251, issued June 6, 2000.
66 T. O. Herndon, C. E. Woodward, K. H. Konkle, and J. I. Raffel, "Photocomposition and DSW autofocus correction for wafer-scale lithography," *Proc. Kodak Microelectron. Sem.* pp. 118–123 (1983).

67 G. Zhang, S. DeMoor, S. Jessen, Q. He, W. Yan, S. Chevacharoenkul, V. Vellanki, P. Reynolds, J. Ganeshan, J. Hauschild, and M. Pieters, "Across wafer focus mapping and its applications in advanced technology nodes." *Proc. SPIE* **6154**, 61540N (2006).
68 B. M. La Fontaine, J. Hauschild, M.V. Dusa, A. Acheta, E.M. Apelgren, M. Boonman, J. Krist, A. Khathuria, H.J. Levinson, A. Fumar-Pici, and M. Pieters, "Study of the influence of substrate topography on the focusing performance of advanced lithography scanners." *Proc. SPIE* **5040**, pp. 570–581 (2003).
69 F. Kahlenberg, R. Seltmann, B. M. La Fontaine, R. Wirtz, A. Kisteman, R. N. M. Vanneer, and M Pieters, "Best focus determination: bridging the gap between optical and physical topography," *Proc. SPIE* **6520**, 65200Z (2007).
70 W. P. de Boeij, R. Pieternella, I. Bouchoms, M. Leenders, M. Hoofman, R. de Graaf, H. Kok, et al. "Extending immersion lithography down to 1x nm production nodes," *Proc. SPIE* **8683**, p. 86831L, 2013.
71 H. J. Levinson, *Principles of Lithography*, 4th Edition, SPIE, 2019.

Chapter 4
EUV Masks

As discussed previously, there are no high-transmission optical materials at EUV wavelengths due to limitations imposed by atomic absorption. As a consequence, all optical elements in the lens must be reflective for EUV lithography.[1] Similarly, EUV masks must be either reflective or stencil-type. The semiconductor industry has made reflective masks standard, as they were seen as more practical than stencil masks. This means that masks for EUV lithography are fundamentally different from those used for optical lithography. An extensive amount of engineering effort was directed at determining what the format should be for reflective EUV masks, and additional effort was required to make them suitable for use in high-volume manufacturing.

4.1 Structure of EUV Masks

A typical configuration for an EUV mask blank is shown in Fig. 4.1. A multilayer reflector is deposited on the front side of a flat, glass substrate. A capping layer, typically ruthenium, is deposited on the multilayer, and then the absorber is deposited on the capping layer. Because the absorber is typically metallic, optical contrast is low between the absorber and multilayer, making defect inspection difficult. Consequently, a thin film is often deposited on top of the absorber to increase the contrast at DUV wavelengths. An electrically conductive backside film is also deposited to enable the mask to be secured on electrostatic chucks in exposure tools. Electron micrographs of an early EUV reflection mask are shown in Fig. 4.2.

As in optical binary masks, EUV binary masks are divided into "dark" and "light" areas, but for EUV lithography, the light areas are reflective rather than transmissive, while the dark areas are covered by absorbers to prevent reflection. For early EUV masks, gold was often used as an absorber, as also used for many 1× x-ray masks, even though lift-off processes were required for fabrication, due to the absence of a process for dry etching gold. Potential absorber materials that could be dry-etched were considered, such as chromium, which was a standard absorber material for optical masks, and TiN.

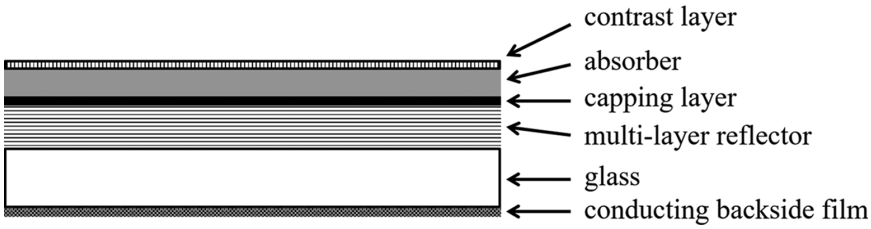

Figure 4.1 Schematic of an EUV mask blank. This figure is not to scale, as the deposited films are nanometers or tens of nanometers in thickness, while the glass substrate on which the films are deposited is nominally 6.35 mm thick. The purpose of the contrast layer is to improve defect inspection of the mask and not enhancement of imaging on wafers.

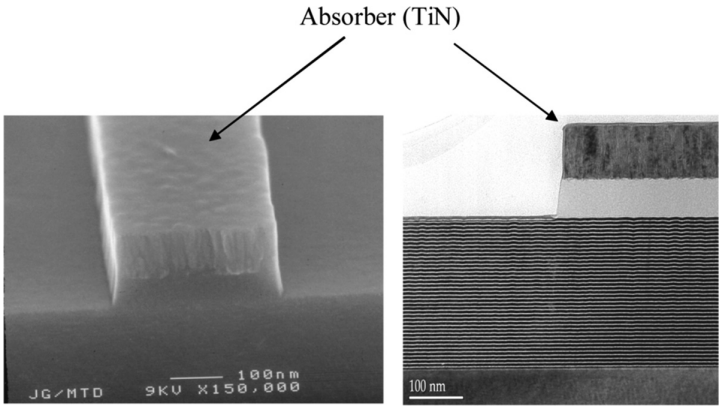

Figure 4.2 Micrographs of an early EUV mask fabricated at Advanced Micro Devices. The TiN absorber sits on a thick SiO_2 buffer layer that had been deposited directly onto a MoSi multilayer. Ruthenium buffer layers on the EUV mask blanks used currently are much thinner (~2 nm).[2] The left micrograph is a tilt SEM, while the right picture is a TEM, showing the multilayer reflector.

In addition to the desired optical properties, there are many requirements that materials must meet in order to be suitable for use as absorbers on EUV masks. A number of the important characteristics are listed in Table 4.1. Please note that these materials requirements pertain to absorbers for binary masks as well as attenuated phase-shifting EUV masks.

Eventually, TaN[3,4] and TaBN[5] emerged as absorber materials, because they have higher absorbance than TiN, thereby enabling the use of thinner absorbers,[6,7,8] can be dry-etched,[9,10,11] and are also durable during cleaning processes. These tantalum-based materials can also be etched in absorber repair tools,[12] which is another important consideration. The absorbers on EUV masks used currently in high-volume manufacturing are composed of these materials. The attenuation lengths at λ = 13.5 nm for elements considered for EUV mask absorbers are given in Table 4.2. The importance of

Table 4.1 Requirements for materials used as absorbers on EUV masks.

Deposition characteristics	Single phase
	Amorphous films
	Low surface roughness
	Low residual stress
Processing characteristics	Cleaning durability
	Etchable
	Repairable
	Inspectable
Additional characteristics	Good adhesion to the capping layer
	Ultrahigh vacuum compatible
	Stable to maximum processing temperatures
	Hydrogen resistant with and without EUV light

Table 4.2 Attenuation lengths for materials that can be used for EUV mask absorbers.[13]

Material	Attenuation length (nm)
TaN	24.9
TaBN	24,8
TiN	56.9
Co	16.2
Ni	14.8
Cr	28.0
Te	14.7

having high absorption for the absorbers of binary masks for advanced nodes will be discussed in Chapter 6.

The nontelecentricity of EUV exposure systems has certain implications for EUV masks. Even though the angle of incidence of the illumination on the mask is small (6° mean for 0.33-NA systems), it does result in differences in the imaging of features that are parallel to the plane of incidence relative to those that are perpendicular.[14,15] This is because features perpendicular to the plane of incidence partially shadow the incident light (Fig. 4.3). The nature of the 3D aspects of EUV imaging are explored in further detail in Chapter 6.

Because of the need to minimize effects due to non-telecentricity, thin absorbers are desirable. This characteristic needs to be balanced with the amount of light reflecting from portions of the mask covered by absorbers. Reflection results from light that has gone through the absorber and been reflected back from the multilayer mirror. Because of the combination of

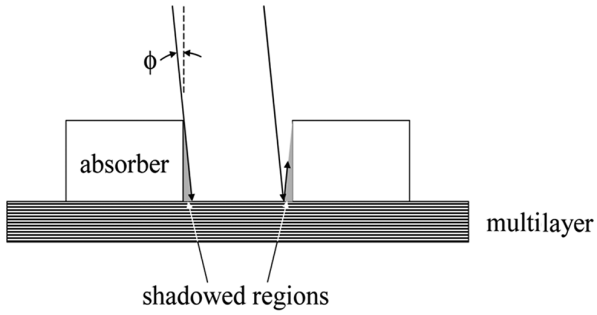

Figure 4.3 Lines that run perpendicular to the plane of incidence of the obliquely incident light are shadowed. For *NA* = 0.33, the mean ϕ = 6°.

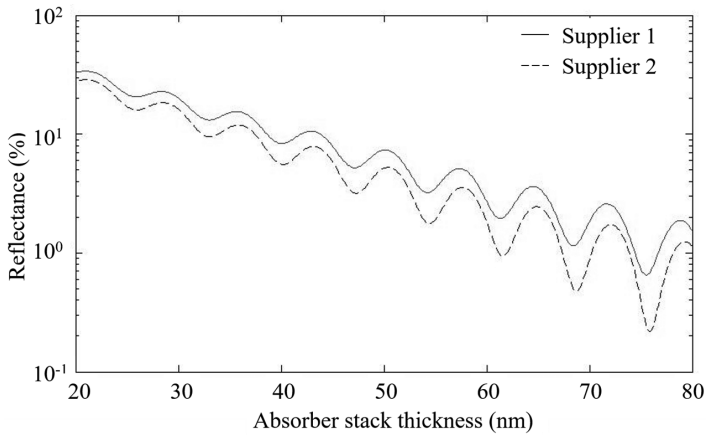

Figure 4.4 Calculated reflectance from absorbers from two different mask blank suppliers, as a function of absorber thickness.

moderate optical absorption and the thinness of the absorber, some light is reflected from areas on the mask covered by absorber. A swing curve of reflection versus absorber thickness results[16] (Fig. 4.4). Absorber thickness is typically chosen at an absorber minimum, since this leads to small reflectance, and it also minimizes the changes to reflectance with absorber thickness variation. Tantalum-based absorber stacks, which include the contrast coating, commonly have a ~60-nm total thickness and reflectance of 1–2%. The thickness of this absorber is several times the wavelength of EUV light, in contrast to the situation in optical lithography, where the thicknesses of mask absorbers are fractions of the wavelengths. This is another reason why mask 3D effects are more significant for EUV than for optical lithography.

Throughout most of the exposure field, the impact on imaging of reflections from absorbers can be included in OPC calculations, but problems occur at the edges of exposure fields. Generally, aperture blades are used to block light from portions of the mask not intended for exposure, but the true

edge of the exposure area is typically defined in optical lithography by absorbers on the masks. This is necessary for the edges of exposure areas to be sharp in the optical image, because only features on the front of the mask will provide a distinct edge to the exposure area. The aperture blades are far from the focal plane of the lens, resulting in gradual edges for the images of the aperture blades in the wafer plane. Moreover, the placement of the aperture blades lacks the micron accuracy needed to be able to apply a shadow correction at the edges of exposure fields by means of OPC.

A common solution for providing a truly dark edge to the exposure area for EUV lithography is to etch the multilayer, as illustrated in Fig. 4.5, thereby eliminating the primary reflector just outside of the exposure area. This etched area is often referred to as the "black border." While etching the multilayer does effectively eliminate reflection of EUV light,[17] the glass at the bottom of the black border can reflect DUV light (see Problem 4.4), which must be taken into account for systems that do not incorporate spectral purity filters to eliminate light at DUV wavelengths.[18]

During the early years of EUV lithography development, it was not obvious what the substrate material or physical format should be for masks. It was understood that whatever material was chosen, very low defects and extreme flatness were important qualities (discussed further below). A great deal of effort had been expended over many years to produce very-low-defect and very-flat silicon crystal surfaces, so serious consideration was given to using silicon as the substrate material. Many early EUV masks were indeed fabricated on silicon wafers.

Eventually, it was decided to use ultra-low thermal expansion materials (ULTEM) for the substrates of EUV masks. Because EUV masks are ~30% absorbing in the reflecting areas and nearly 100% in the areas with an absorber, EUV masks will heat up during exposure. Such heating and subsequent cooling will lead to overlay errors due to thermal expansion and contraction of the mask unless EUV masks are fabricated on substrates with extremely low coefficients of thermal expansion. Glass materials with very low coefficients of thermal expansion are available and have been characterized

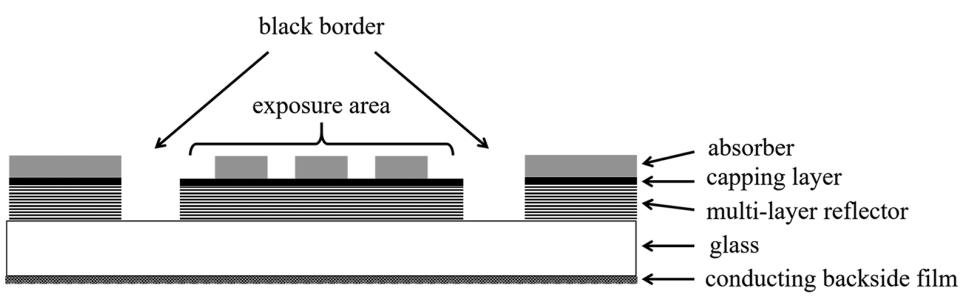

Figure 4.5 EUV mask structure with an etched multilayer for the black border.

for use as EUV mask substrates.[19,20] Examples of such glass materials are ULE® from Corning, Inc. (described in Chapter 3) and Zerodur® from Schott. Because of concerns regarding thermal expansion and surface defects and flatness, one early proposal was to bond a silicon wafer onto a ULTEM substrate, thereby providing good thermal as well as surface properties.[21] Eventually, there was sufficient confidence that very flat and low defect ULTEM substrates could be fabricated, and multilayer mirrors for EUV masks are now deposited directly on the glass. Note that it is possible to use ULTEM substrates for EUV masks, unlike the situation in optical lithography, where glass transmission is a significant consideration. This is one instance where the reflection geometry for EUV lithography is an advantage.

Another important decision was for EUV masks to have the same mechanical form factor as conventional 6" optical masks. This enabled the use of much of the existing mask-making infrastructure, some without any modification and some with only minor modifications, to fabricate EUV masks. EUV mask requirements are detailed in SEMI Standards P37 (Specification for Extreme Ultraviolet Lithography Mask Substrates), P38 (Specification for Absorbing Film Stacks and Multilayers on Extreme Ultraviolet Lithography Mask Blanks), and P40 (Specification for Mounting Requirements and Alignment Reference Locations for Extreme Ultraviolet Lithography Masks).

To create the reflector for the mask, Mo/Si multilayers are deposited on the glass substrate. For multiple reasons, it was found useful to deposit a thin layer between the absorber and the multilayer reflector. First, a material with good etch selectivity relative to the absorber is useful, and second, it is helpful for this to be a material that is fairly stable in the environment of the scanner and in tools for mask cleaning. It is also important for this capping layer not to be highly absorbing in order to maintain good reflectivity in regions where the absorber has been etched away.

As described in Chapter 3, electrostatic chucks are used to hold masks in EUV exposure tools. This necessitates that the backsides of the masks be electrically conducting, and this requirement is incorporated in the SEMI P38 standard for mask blanks. In additional to the need to be electrically conducting, the backside films also need to be sufficiently mechanically durable to withstand multiple cycles for mounting and demounting on the reticle chuck. Thus, backside films have hardness requirements as well as a need to be electrically conductive.

Since EUV masks are fabricated on electrically insulating glass substrates, there are effects associated with electrical charging of EUV masks, similar to those encountered with optical masks. One problem that arises from electrical charging is beam deflection during mask writing using electron beam tools,[22,23] although means have been identified to mitigate this effect.[24]

Electrostatic damage (ESD), observed on optical masks,[25] is also a concern for EUV masks. Because EUV photons have energies well above the work functions of the materials that compose mask film stacks, photoelectrons will be emitted when masks are irradiated with EUV light, causing the mask absorber to become charged electrically. This is a condition that can lead to ESD. One advantage with patterned EUV masks is that features on the masks are not electrically isolated, as they are on optical masks, because the underlying capping layer and multilayer are electrically conductive. It should be noted that the conductivity of the multilayer has semiconductor (rather than metallic) characteristics, but it is still electrically conductive.[26] There is also susceptibility to charging when mask features are measured using scanning electron microscopes, particularly when such measurements are performed after the mask pattern is isolated electrically by an etched black border.

4.2 Multilayer and Mask Substrate Defects

A problem with defects in the substrate or the multilayer film for the mask configuration shown in Fig. 4.1 was recognized by early researchers. The pictures shown in Fig. 4.6 are from one of Dr. Obert Wood's laboratory notebooks from 1992. On the left is an SEM of a pattern in resist. Part of the pattern corresponds to programmed features on the mask, while one line that printed repeatedly was not part of the design. Dr. Wood eventually determined that this printing defect resulted from a scratch in the glass on which the mask had been fabricated.

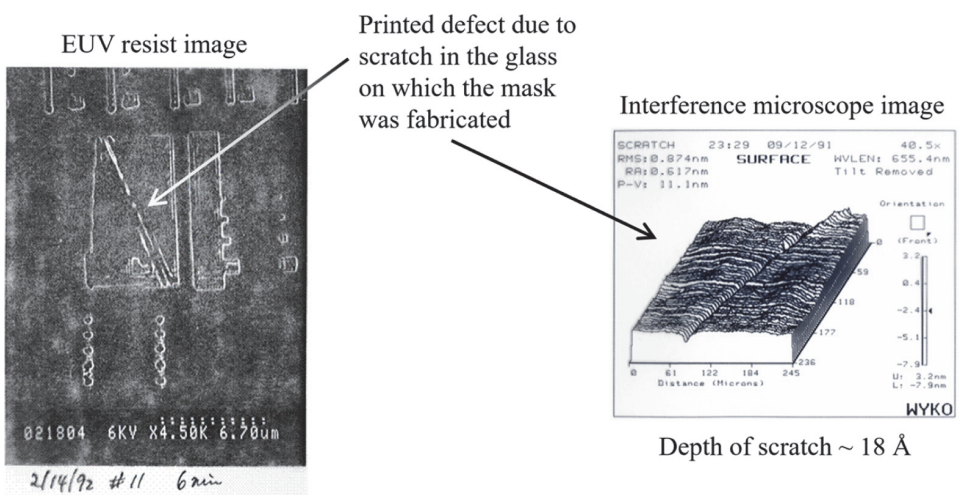

Figure 4.6 The picture on the left is a micrograph of a pattern in 60-nm-thick PMMA exposed on an EUV exposure tool with 0.08-NA Schwarzschild optics at an exposure wavelength of 13.8 nm. On the right is an image from an interference microscope that revealed that a printing feature that was not programmed in the mask was due to a scratch in the glass on which the mask was fabricated.

The printed defect shown in Fig. 4.6 is an example of a phase defect. There was no extraneous absorber or missing multilayer, but instead the height of the multilayer film was modified by the scratch in the substrate on which the film was deposited. This resulted in variations in the phase of the light reflected across the scratch. When the depth of the scratch is h, the phase difference between the light reflected from the bottom of the scratch and the rest of the multilayer is

$$\frac{4\pi h}{\lambda \cos \phi}, \tag{4.1}$$

where ϕ is the angle of incidence for light illuminating the mask, and λ is the wavelength of the light (see Fig. 4.7). When the depth h of the scratch is given by

$$h = N\frac{\lambda \cos \phi}{4}, \tag{4.2}$$

where N is an odd integer, then the light reflected from the bottom of the scratch will interfere destructively from the surrounding multilayer. From experience with optical phase shifting masks, this type of feature is printable. For 0.33-NA exposure tools, the chief ray angle is 6°, so

$$\frac{\lambda \cos \phi}{4} = 3.4 \text{ nm}, \tag{4.3}$$

indicating that phase defects can result from very small changes in height. Phase defects can result from flaws other than scratches, such as small pits in the substrate and small particles. This is illustrated in Fig. 4.8, and an example is shown in Fig. 4.9.

Since multilayer defects cannot be effectively repaired,[27] the existence of such defects has many implications for EUV lithography. First and foremost is the need for mask blanks with very few multilayer defects. Moreover, what

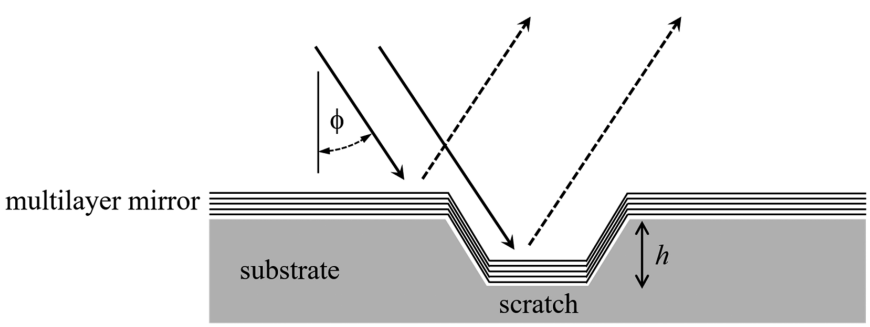

Figure 4.7 Reflection from a multilayer film deposited on a substrate that is scratched.

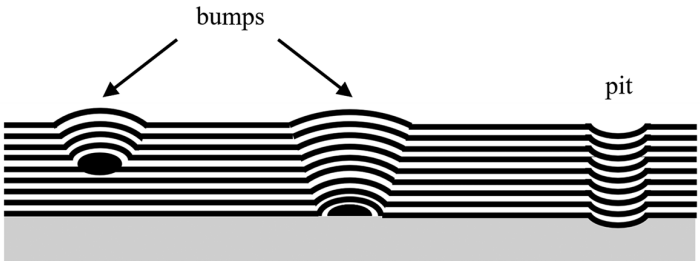

Figure 4.8 Illustration of EUV mask blank defects. The pit defect on the right can result in a phase defect, while the bump defect on the left due to the embedded particle can affect both the amplitude and phase of the aerial image. The bump defect in the middle will primarily affect the phase.

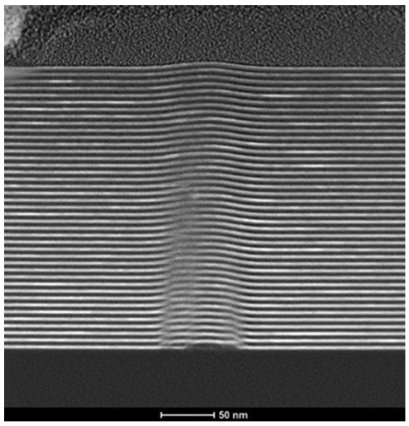

Figure 4.9 TEM of a phase defect from a small particle on the surface on which the multilayer film was deposited.

constitutes a defect can be something very small in size. This, in turn, makes for significant challenges for defect inspection, which will be discussed further in Chapter 8. Mask defect printability has been studied since it was initially recognized that the range of sizes over which defects print depends on the proximity of the defects to other features.[28] The situation is more complicated for EUV lithography, since there are mask blank defects as well as absorber defects that are significant concerns.

Mask blank defects can consist of multiple types, as illustrated in Fig. 4.8. Bump-type defects result from particles on the glass substrate on which the mask blank is fabricated or particles embedded in the multilayer, while pit-type defects often originate from small divots in the glass on which the multilayer is deposited. Because the formation of printable multilayer defects can be initiated by very small particles or pits in the glass substrate, such substrates need to be exceedingly defect free. Using optical inspection tools,

detection of these defects on substrates that are composed of glass is very challenging, because there will often be very little optical contrast.

Because it is nearly impossible to make EUV mask blanks that are 100% defect free, methods for mitigating the impact of the defects that do exist are needed. One of the most useful is pattern-shift. In this approach, the locations of defects on the mask blank are determined relative to fiducial marks that have been formed on the blank (Fig 4.10). Prior to exposing the resist on the mask blank, the mask writer aligns to these same fiducial marks, and the pattern is written so that the defects are covered by absorber and hence will not print.

As can be seen in Fig. 4.10, the defect must be smaller than the width of the absorber in order for the pattern shift method to be effective. Moreover, because of uncertainties in measuring the size and location of the defect, and errors in alignment by the mask writer prior to electron beam exposure, the absorber must be even larger than the defect, with a guardband of width β about the defect[29] (Fig. 4.11). In one instance, using an actinic inspection tool for locating the defects and measuring their sizes, an estimated value of $\beta = 80$ nm (mean $+ 2\sigma$) was obtained.[30] With this value for β, an absorber that has a lateral dimension at the mask level of $2 \times 80 + 40$ nm = 200 nm is needed to cover a 40-nm defect. There are development activities to reduce this value, primarily by improving the accuracy of determining the location of the defects, in order to enable defects to be covered effectively by minimum sized features at the 7-nm node and beyond.

As with optical lithography, the printability of defects has been studied extensively for EUV masks, and both absorber and substrate defects have been investigated. For EUV lithography, mask defect printability studies have

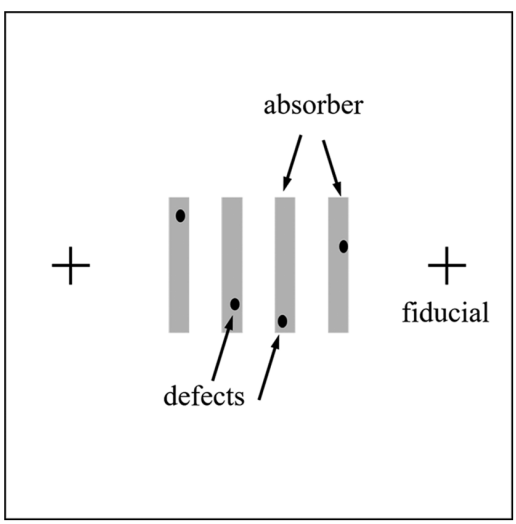

Figure 4.10 Illustration of pattern shift to cover multilayer defects with absorber.

been convolved with assessments of mask inspection capability, which has long been a particular problem for EUV, because actinic patterned mask inspection tools have only recently become commercially available. Moreover, LER has made it difficult to identify small changes in critical dimensions due to mask defects, and multilayer roughness has made it difficult to detect small bump or pit defects. The problem of multilayer roughness is illustrated in Fig. 4.12, where a noisy background is clearly apparent.

In one example of determining mask defect printability, shallow trenches were etched into the glass substrate on which an EUV mask was fabricated.[32] The absorber was patterned into lines and spaces that were oriented perpendicular to the trenches in the glass. A resist-coated wafer was subsequently exposed using this mask, and representative printed defects are shown in Fig. 4.13. The printability of defects is shown in Table 4.3. As can be

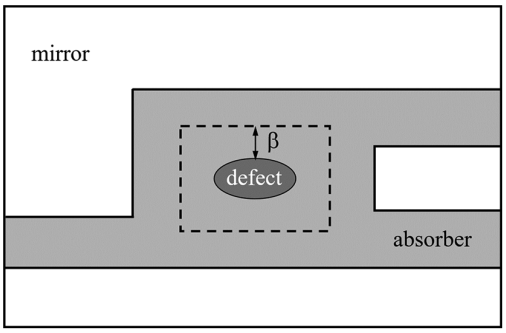

Figure 4.11 Illustration of the need for absorbers with larger lateral extent than the defects in order for the pattern shift approach to be effective at mitigating mulitlayer defects.

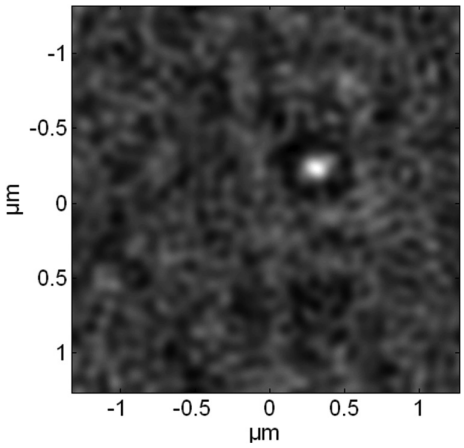

Figure 4.12 Image of a silicon-capped multilayer with a detected pit defect, using a 193-nm inspection tool.[31]

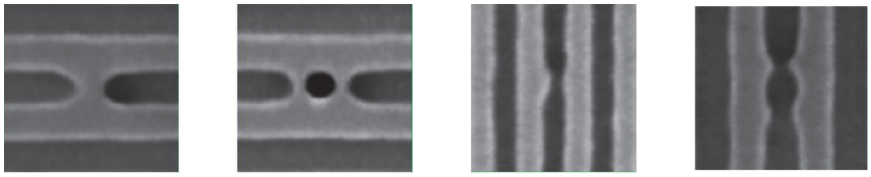

Full-bridge defects Partial-bridge defect Partial-hole defect

Figure 4.13 Scanning electron micrographs of patterns printed in resist when using a test mask with programmed substrate defects.[32]

Table 4.3 Defect printability from the study of Ref. 32. All dimensions are at wafer-scale, except for the trench depth, which is the actual depth on the mask. Values in the cells are coded as follows: 0 – no defect, 1 – partial bridging, 2 – full bridging, 3 – partial hole.

		1X defect size (nm)				
Trench depth (nm)	**Pattern pitch (nm)**	**15**	**20**	**25**	**30**	**35**
14	56	0	1	2	2	2
14	80	2	2	2	3	2
14	104	1	1	2	3	3
10	56	0	1	2	2	2
10	80	2	2	2	2	2
10	104	1	2	2	2	3
6	56	0	2	2	2	2
6	80	1	2	2	2	2
6	104	1	1	2	2	2

seen, a shallow depth does not ensure that defects do not print, although defects with the smallest lateral width print the least. There are also several more conventional studies of the printability of mask absorber defects.[33]

As seen in Fig 4.9, phase defects can arise from small particles (or pits) on the surface of the glass substrate on which the mask blank is fabricated. The extent to which such substrate defects propagate through the multilayer is dependent upon the deposition method. While some data indicate that substrate defects can be smoothed over with ion-beam deposition techniques,[34] depositions that lead to high reflectance and do not produce additional defects are typically conformal. Consequently, smoothing of defects during the deposition process has not proven to be a useful approach for defect reduction.

An interesting approach for mitigating mask defects is "vote-taking," where multiple copies of a mask design are used to expose each wafer, each

exposed with a fraction of the total dose. This idea was originally introduced for optical 1× stepper lithography as a way of mitigating reticle defects,[35] and was reconsidered in the context of EUV lithography.[36] Experimental results showed that the use of three or four copies were effective at mitigating many mask defects. Also of interest was a measured 17% reduction in critical dimension variation of contact holes when four masks were used,[37,38] indicating that mask critical dimension variation has a significant impact on overall process control.

As noted, printable phase defects can be created by extremely small particles, which may be smaller than can be detected with optical (visible or DUV) light. Indeed, defects have been detected using actinic inspection tools that could not be found with conventional visible-light defect inspection tools.[39] Consequently, it is necessary to inspect masks with tools that use EUV light to provide sensitivity to printable defects.[40,41,42] Mask inspection will be discussed further in Chapter 8.

4.3 Mask Flatness and Roughness

The use of reflective masks also imposes requirements on mask flatness. As can be seen in Fig. 4.14, mask nonflatness will result in image-placement errors. For consistency with the overlay requirements of 16-nm ½-pitch logic technology, EUV masks must be flat to within 24 nm (peak to valley),[43,44] unless techniques are implemented to compensate for the pattern placement errors caused by mask nonflatness. One means of compensating for mask nonflatness is to modify pattern placement on the mask when writing the mask pattern, so as to counterbalance the mask nonflatness. An example of this approach is grid-matching correction for thickness variation (GMC-TV), provided by NuFlare for their beam writers.[45,46] Additional means of

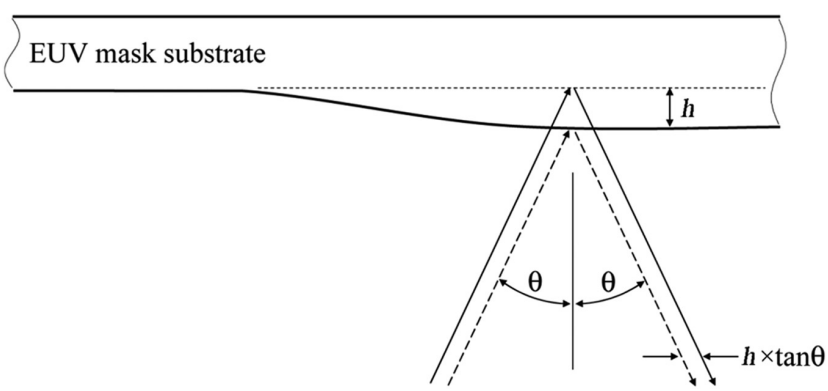

Figure 4.14 Mask nonflatness leads to image-placement errors. The lateral displacement $h \times \tan\theta$ is reduced on the wafer by the reduction of the projection optics.

compensating for mask nonflatness in order to reduce overlay errors are discussed in Chapter 7.

To ensure good overlay, flatness of very low magnitudes must be maintained while the masks are in use, which means that EUV mask chucks must also be very flat, and great care must be taken to avoid particles on the back side of the masks that can lead to front-side mask nonflatness after chucking (see Fig. 4.15).[47] Backside defect measurement capability is needed to ensure backside cleanliness, as will be discussed further in Chapter 8.

The issue of multilayer mirror height variation over very short distances is significant for masks, just as it is for the mirrors in EUV projection optics. Very high spatial-frequency roughness will cause light-loss, reducing system throughput. If such roughness is non-uniform across the mask, it will appear as an effective exposure dose variation. Mask mirror roughness has additional significance compared to the multilayer films on mirrors in the projection optics, because the mask mirror is in the object plane of the projection optics. Consequently, roughness on the mask will affect the image at the wafer plane.

EUV mask roughness measured on a patterned mask using an atomic force microscope (AFM) is shown in Fig. 4.16, illustrating two types of roughness, multilayer roughness and absorber sidewall roughness. Both types of roughness can be transferred to resist patterns.[48] Multilayer roughness produces phase variations, and these will lead to variations in light intensity at the wafer plane.[49] Such variations have been measured using EUV imaging

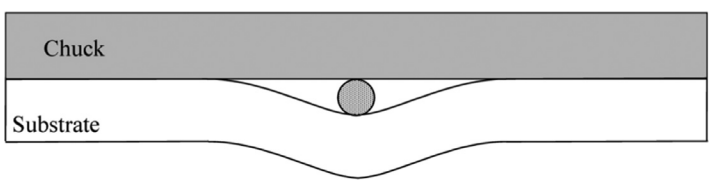

Figure 4.15 Mask deformation due to a particle between the mask substrate and the chuck.

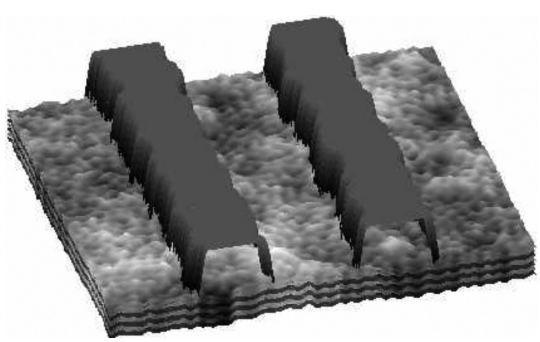

Figure 4.16 Measurement of mask roughness using an AFM.[49]

microscopes, including an aerial image measurement system (AIMS) that emulates the imaging of an exposure tool such as ASML's NXE:3400B.[50] Such intensity variations due to roughness, by themselves, were found to contribute an effect dose variation of ~0.5% (3σ) at best focus and approximately twice that at ±60-nm defocus (Fig. 4.17). Since the normalized image slope will be smaller under out-of-focus conditions, the larger effective dose variations will have an even greater impact on LER in resist patterns imaged out of focus than what occurs at best focus. This again illustrates the importance of good focus control for EUV lithography.

As can be seen in Fig. 4.16, the absorber can also have line-edge roughness. Such roughness can transfer to the wafer, although the high-frequency components of the mask LER will be filtered according to the resolution of the optics. The fraction of the power spectral density (PSD) for the mask absorber LER that is transferred to the wafer is given by an LER transfer function (LTF), shown in Fig. 4.18 across spatial frequencies.

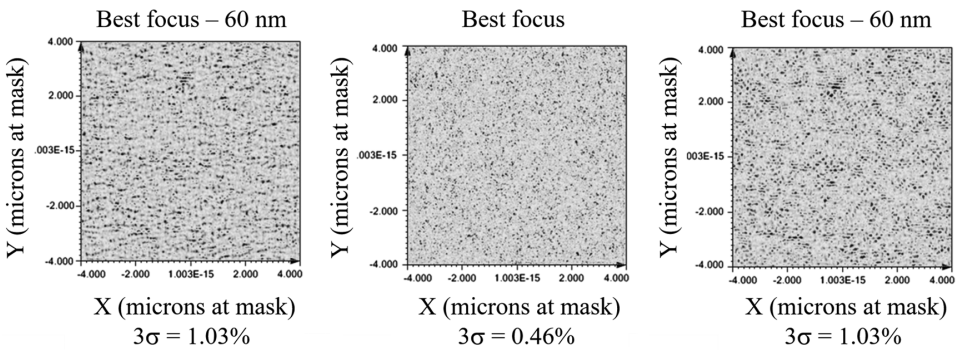

Figure 4.17 Measurement of reflected light intensity from the multilayer of an EUV mask, using an EUV AIMS tool.[50]

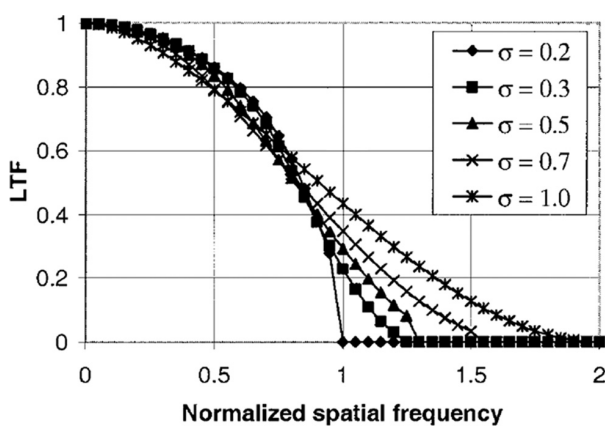

Figure 4.18 LER transfer function as a function of spatial frequency, normalized to NA/λ.[51]

Naturally, the high-frequency LER from the mask is filtered by the lens.[51,52] As can be seen in Fig. 4.18, the LER transfer from the mask to reticle is greatly reduced for spatial frequencies $>NA/\lambda$. Since this ratio is 3.5 times larger for 0.33-NA EUV exposure tools than for 1.35-NA ArF immersion tools, the LER of absorbers on EUV masks needs to be much less than on leading-edge optical masks.

4.4 EUV Mask Fabrication

EUV masks are fabricated using the same electron beam exposure tools that are used to pattern advanced optical photomasks. As noted in Section 4.3, LER must be much less on EUV masks than for optical photomasks. This necessitates high doses of electrons to avoid LER that results from electron shot noise. Accordingly, multi-beam writers are typically used for writing EUV masks, in order to achieve high doses for reducing LER, while maintaining reasonable write times.[53,54]

Another important difference between writing optical and EUV masks involves electron backscatter (Fig. 4.19), which results in proximity-dependent patterning.[55] Software is used to compensate for these proximity effects, but the amount of backscattering is dependent on the substrate materials. For optical masks, the range for backscattered electrons is ~10 μm for 50-keV incident beams. Since the absorbers on optical masks are typically only about 100 nm thick, this implies that most of the backscattering occurs in the glass substrate. For EUV masks, the Mo/Si multilayer thickness is ~280 nm thick and can therefore contribute significantly to the backscattering. Moreover, electron scattering tends to be stronger from scattering atoms of higher atomic numbers (see Table 4.4). Electron scattering by molybdenum is greater than by silicon or oxygen, and tantalum scatters more than the absorber materials used in optical masks. Consequently, proximity corrections for EUV masks

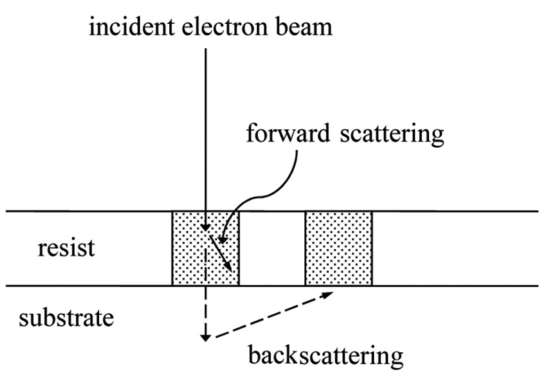

Figure 4.19 Illustration of resolution degradation and proximity effects in electron-beam lithography. The shaded areas are intended for exposure, but electrons will scatter into the resist where exposure is not intended.

Table 4.4 Atomic numbers for elements commonly used in EUV mask blanks.

Element	Atomic number
Silicon	14
Oxygen	8
Molybdenum	42
Chromium	24
Tantalum	72

Table 4.5 Thicknesses and probability for electron backscatter from materials commonly used to fabricate masks.[55]

	Optical mask materials			EUV mask materials		
Material	SiO_2	Cr	MoSi	SiO_2	TaBN	Mo/Si
Thickness (nm)	∞	103	70	∞	51	280
Backscattering probability (%)	8.2	0.4	0.3	8.2	1.1	1.5

will differ in detail from those used for optical masks, because the electrons will scatter differently from the multilayers and absorbers of EUV masks than from the absorbers of optical masks (see Table 4.5).

Besides the writing of mask patterns, there are many other operations required for fabricating masks, such as etch, cleans and defect repair, along with substantial metrology for critical dimensions, registration, defect detection, and assessment of defect printability. As noted in Section 4.1, absorber materials that are selected for EUV masks can be etched, repaired and cleaned, although the specific chemistries involved may be somewhat different from those for processing optical masks. It has been common practice in mask shops to perform inspections at or near the same wavelengths as used for exposing wafers. In this regard, inspection tools for EUV masks, with sources and optics for EUV light, rather than DUV, are substantially different from those used in optical lithography. EUV mask inspection tools are discussed further in Chapter 8.

4.5 EUV Pellicles

The absence of highly transparent materials at EUV wavelengths implies that conventional polymer-based pellicles cannot be used (see Problem 4.2). The transparency requirement for EUV lithography is high because light needs to pass twice through a pellicle for a reflection mask. However, because of material limitations, a target of 90% transmission has been set, far below the transmission of DUV pellicles. Even so, pellicles for EUV lithography

Table 4.6 Requirements for EUV pellicles.[60] It is expected that these requirements will evolve over time.

Parameter	Targets
EUV average transmission (single pass)	≥90%
EUV transmission uniformity	≤0.4% half range
EUV reflectivity	<0.04%
EUV scattering	<0.25%
DUV average transmission	>50%
Mechanical stability (deflection at 2 Pa)	<0.5 mm over 110 × 140 mm^2
Compatible with use in EUV scanner	≥250 W, in the presence of hydrogen

need to be very thin in order to reach the target of 90% transmission. The use of very thin membranes for EUV pellicles was proposed in 2003,[56] but creating large-area (>110 mm × 144 mm) thin-film membranes was not seen as possible for many years. Consequently, very little effort was expended to develop pellicles for EUV lithography until fairly recently, and alternative approaches to address the issue of reticle contamination were pursued.

Without a pellicle, it was clear that the reticle environment in the exposure tools needed to be very clean. However, studies at GLOBALFOUNDRIES[57] and Intel[58] revealed a contamination rate of one particle per 20–25 reticle load/unload cycles, and additional contamination during wafer exposures. With concern that alternative approaches might not be adequately effective to ensure good yield, activities were belatedly initiated to develop full-field thin-membrane EUV pellicles.[59] Target requirements for EUV pellicles are summarized in Table 4.6.

One possible EUV pellicle film material that seemed to have good potential was polysilicon,[60] and considerable work has been invested in further developing such films. That development not only brought about improvements in polysilicon pellicles but also led to better appreciation of the challenges in making a pellicle that is truly suitable for high-volume manufacturing. For example, in addition to the requirement of a high (≥90%) average transmission, for good process control, such transmission has to be sufficiently uniform.

Polysilicon pellicles are often capped with silicon nitride, because of concerns with oxidation of the silicon, which would reduce transparency. The potential for changes to the pellicle films during exposure is greater for EUV lithography than for ArF lithography, due substantially to the greater energy of EUV photons, and because even small changes to the chemical composition of EUV pellicles can have a large impact on transmission.

Another issue that has received attention is pellicle heating. Although only 10–30% of the EUV light is absorbed by the pellicle, heat is dissipated inefficiently. Because the pellicle is extremely thin, conduction of the heat

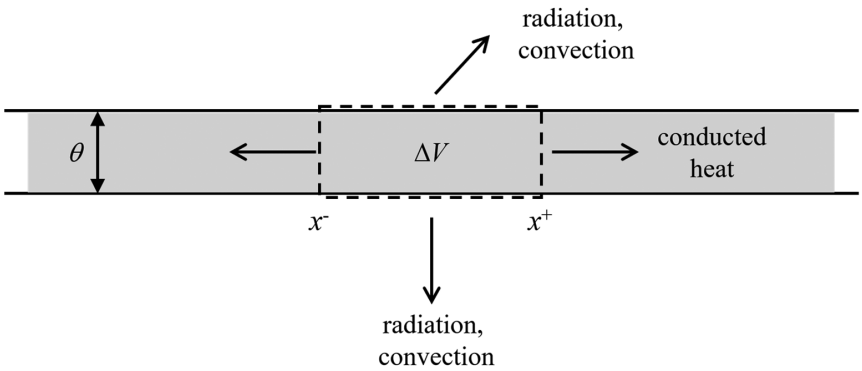

Figure 4.20 Volume of a pellicle of thickness θ that is being heated by incident EUV light.

away from the illuminated section is limited by the small cross-section for heat conduction (see Fig. 4.20). The temperature of a volume ΔV of the pellicle is described by[61]

$$\rho C_p \Delta V \frac{dT}{dt} = H_{EUV}\Delta V + \sigma_B A\left(\varepsilon_{pell}T^4 - \varepsilon_{amb}T_{amb}^4\right) + k_T T\theta\left(\frac{dT(x^+)}{dt} - \frac{dT(x^-)}{dt}\right) - H_{diff}A, \tag{4.4}$$

where ρ is the mass density, C_p is the specific heat of the pellicle, H_{EUV} is the rate at which heat is absorbed in ΔV, T is the temperature of the volume ΔV, T_{amb} is the temperature of the chamber ambient, t is time, σ_B is the Boltzmann constant, k_T is the thermal conductivity of the pellicle material, H_{diff} is heat transfer rate by convection to any surrounding gas, and ε_{pell} and ε_{amb} are the emissivities of the pellicle and ambient, respectively. $\Delta V = A\theta$, with A being the area of the top or bottom of ΔV. The second term on the right side of Eq. (4.4) represents radiative heat transfer, and the third term is the heat conducted away from ΔV. The final term represents the heat removed by convection if there is any gas surrounding the reticle.

The temperature of a pellicle composed of SiNx was calculated, with the results shown in Fig. 4.21. For this calculation, it was assumed that the incident energy at the pellicle was 0.29 W/cm^2, which was an estimate assuming a 60-W EUV source. The reticle scan speed was assumed to be 400 mm/sec. As can be seen, the temperature in the area being exposed can reach very high temperatures, even for a rather weak light source. These high temperatures are very localized, thus leading to large thermally induced stresses. Since EUV pellicles are very thin, pellicle materials must have good mechanical strength; the issue of thermally induced stress makes this requirement even more critical. Moreover, this problem becomes more problematic as the light source power is increased.

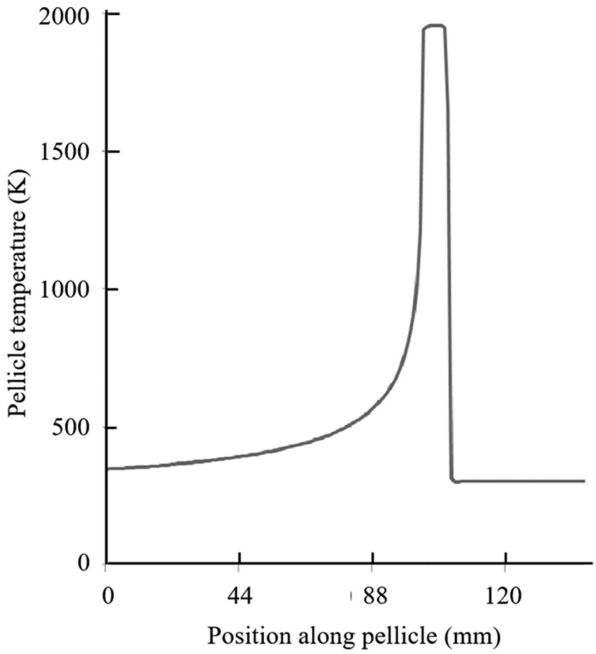

Figure 4.21 Temperature of a SiNx pellicle 0.25 s into a scan.[62]

The (infrared) emissivity value for the SiNx pellicle is low (0.0035), partly because of material and partly due to dimensional effects, where emissivity for thin films can be substantially lower than for bulk solids. Consequently, for the data shown in Fig. 4.21, the heat loss due to radiation was moderate, even with a very large difference in temperature between the pellicle and its surroundings. More recently, work has been done to identify materials with high emissivities to cap the pellicle. Emissivity is related to optical absorption and reflection, so materials that are reflecting at infrared wavelengths, such as metals, might be considerd poor capping layer materials for enhancing radiative cooling based on bulk optical properties, but thin metal films are suitable.[62]

Local heating can be very large if a particle falls on the pellicle.[63] Such particles can comprise elements that are highly absorbing at EUV wavelengths and can have dimensions much larger than the pellicle's thickness. In addition to being concerned about the cost of replacing broken pellicles and possibly masks that are contaminated with debris from the ruptured pellicles, there is also strong potential for contamination of the projection optics, because there is a direct path between the mask and the first mirror of the lens.

As noted in Chapter 3, the necessity of vacuum limits the use of air flows to cool pellicles and masks. However, there is some low level of hydrogen in the space surrounding the reticle stage, and this can be exploited to provide

some level of convection cooling.[64] One reason for this hydrogen is to prevent a build-up of carbon contamination on EUV masks, which had been observed in early EUV tools and testing[65] (see Fig. 4.22). Carbon contamination can affect imaging in multiple ways. Multilayer reflectivity is reduced if there is carbon on top of the mirror.[66] Carbon can also be deposited on the sidewalls of absorbers, effectively widening the line.[67] Hydrogen, which is used to control carbon contamination, can also provide some level of convection cooling for the pellicle, although the effectiveness is limited by the need to maintain low pressures. Note that having a pellicle attached to the mask may limit the amount of hydrogen that reaches the mask surface and could reduce the efficacy for controlling carbon contamination of the mask surface.

Achieving adequate pellicle transmission remains a challenge. A pellicle with a total thickness of 53 nm, composed of polysilicon with silicon nitride capping layers on both sides, had a transmission of 86%.[59] Although very thin, it still had transmission less than the goal of 90%. Even with transmission as high as 90%, it has been questioned whether or not the benefits of pellicles outweigh the loss of throughput that results from using them.[69]

Because it has been difficult to fabricate EUV pellicles composed of polysilicon and silicon nitride[70,71] that meet requirements for transmission and durability, alternative materials have been explored. Thin films of silicon carbide were used for x-ray masks, because they were resistant to radiation damage and had good mechanical properties, and this material is being studied to make EUV pellicles.[72]

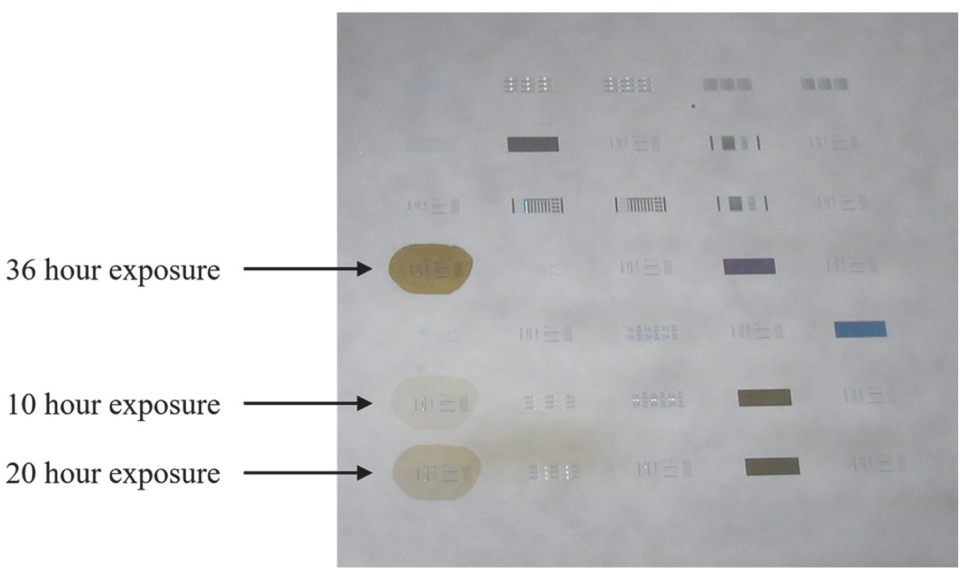

Figure 4.22 Photograph of an EUV mask that was intentionally contaminated with 10^{-4} Torr of methyl methacrylate (MMA) and exposed to EUV radiation for varying durations. Carbon contamination is clearly visible in the exposed areas.[68]

A very interesting type of material for pellicles that has been given serious consideration are membranes composed of carbon nanotubes.[73,74] Such membranes have several advantages. Because of the porosity of the films (Fig. 4.23), their mass density is low, enabling high transmission. Transmissions as high as 96% have been reported.[76] Another advantage of the porous nature of the membranes is insensitivity to changes in air pressure that could rupture continuous films, which contributes to durability on top of the strength of the films. However, porosity has a couple of disadvantages. It is possible for small particles to pass through the spaces between nanotubes, and such was indeed observed to occur in tests involving 30-nm-diameter polystyrene latex spheres. However, the contamination rate of the mask was significantly reduced by the pellicle.[76]

The spacing between nanotubes (~tens of nanometers) is on a scale at which scattering of EUV light can occur. With bare carbon nanotubes, this is not a problem, but it can be problematic if the nanotubes are coated. One reason for coating the nanotubes is to improve emissivity, as discussed above. Another reason has to do with the significant amount of hydrogen in the chamber of EUV exposure tools. Hydrogen can react with the carbon which comprise the nanotubes, with reaction rates enhanced by EUV light, forming volatile methane. Accelerated tests of this erosion of the nanotubes by hydrogen showed that molybdenum was an effective coating for prevent preventing material loss. However, nanotube pellicles coated with molybdenum resulted in a level of light scattering that would degrade imaging unless the molybdenum layer is exceedingly thin, and very thin layers are less effective at protecting the nanotubes from ambient hydrogen.[76]

Another characteristic of polysilicon relevant to it being a film for EUV pellicles is its high absorption at DUV wavelengths.[77] This makes it impossible to inspect for defects through a polysilicon pellicle when using a

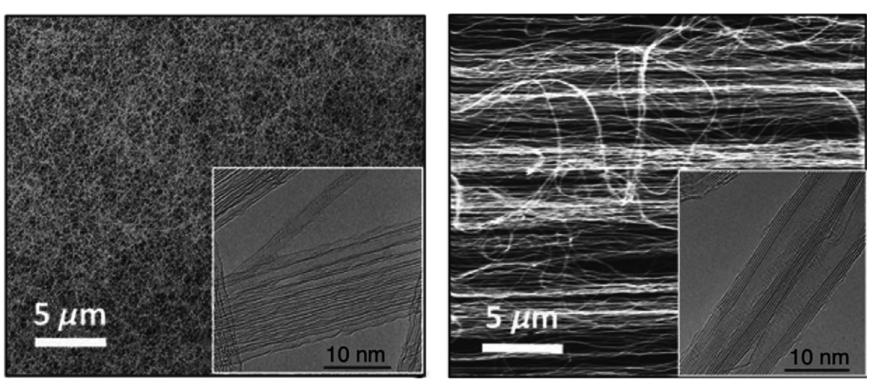

Figure 4.23 The SEMs on the left are from thin films fabricated from single-walled carbon nanotubes, while the one on the right was from a film made from multiwalled carbon nanotubes.[75]

mask defect inspection tool that operates at DUV wavelengths. Consequently, ASML proposed a fixture so that pellicles could be mounted and demounted from masks,[78] in contrast to the common practice of gluing pellicles to optical masks (Fig. 4.24).

In this approach, studs (Fig. 4.25) are glued to the mask, and the pellicle is then clipped to the studs (Fig. 4.26). The studs may not be compatible with particular pieces of inspection and cleaning equipment, and therefore it may be necessary to remove the studs for those operations. Because of the need for extreme cleanliness during the processing of EUV masks, fully automated tools are needed to apply the studs onto masks, remove such studs, and mount and demount pellicles onto the studs. ASML has built such tools, as have others.[79]

Should pellicles composed of films other than polysilicon and have good transmission at DUV wavelengths become available, it remains to be seen whether or not this mountable/demountable approach to pellicles will be used. The introduction of actinic patterned mask inspection tools also obviates this

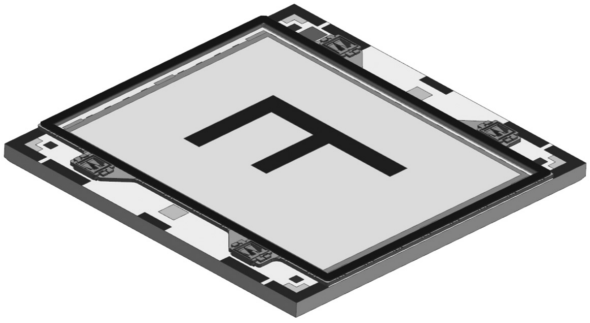

Figure 4.24 The proposed mountable/demountable pellicle proposed by ASML.[79]

Figure 4.25 A picture of a pellicle stud.[80]

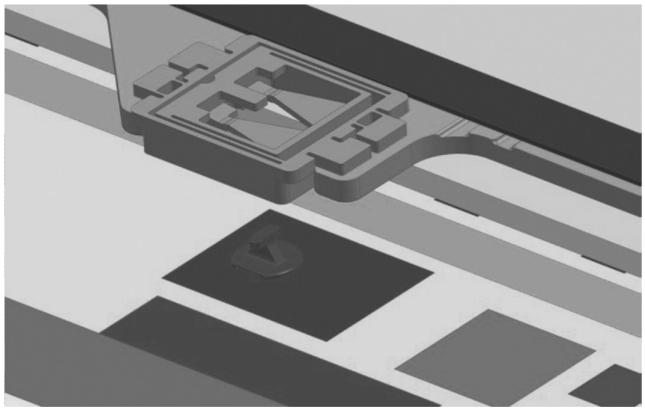

Figure 4.26 Clip that is attached to the pellicle frame. This clip attaches to the stud shown in Fig. 4.25.[79]

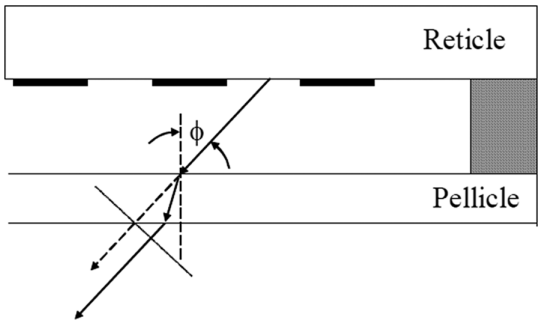

Figure 4.27 Light refraction from a pellicle.

approach for pellicles. In this regard, other suppliers are pursuing approaches for EUV pellicles that are glued to masks more conventionally.[81,82]

In optical lithography, the introduction of hyper-NA immersion lithography resulted in light rays with angles far from normal being captured by the lens (Fig. 4.27). It was soon recognized that such geometries would lead to apodization, aberrations,[83] and changes in critical dimensions through pitch, due to refraction by the pellicle and angle-dependent transmission. Hence, accurate determinations of OPC required that calculations of aerial images included the effects induced by the pellicles, and the masks used for OPC calibration needed to have pellicles attached.

The situation in EUV lithography is different for several reasons:

1. The real parts of the indices of refraction of the pellicle materials for EUV lithography are very close to 1.0.
2. EUV pellicles are substantially thinner than optical pellicles.
3. The NA for EUV tools is much smaller than for immersion lithography.

This can be understood quantitatively by considering the change in the optical path difference (OPD) due to the pellicle. Light propagating through the space of the pellicle has an optical path length of $t/\cos\phi$ in the absence of the pellicle. With a pellicle, the light traverses a different optical path length to reach the line perpendicular to the straight light ray. The resulting OPD is

$$\mathrm{OPD} = t\left[\frac{-1}{\cos\phi} + \frac{n}{\cos\left[\arcsin\left(\frac{\sin\phi}{n}\right)\right]} + \left(\sin\phi\tan\phi - \frac{\sin^2\phi}{n\sqrt{1-\frac{\sin^2\phi}{n^2}}}\right)\right], \tag{4.5}$$

where t is the thickness of the pellicle, and n is the index of refraction of the pellicle material. In this analysis, the imaginary part of the refractive index is neglected. While this is not a strong assumption for EUV lithography, it will be seen that the optical effects due to the pellicle are so small that minor corrections do not affect the conclusion. The first term is the optical path for a ray traveling straight in air. The second term is for the refracted ray in the pellicle, and the third term is the optical path of the refracted light from the pellicle to the point where it meets the line normal to the rays, shown in Fig. 4.27. To the second order, this gives an OPD of

$$t\left[n - 1 + \frac{\phi^2}{2}\left(1 - \frac{1}{n}\right)\right]. \tag{4.6}$$

As can be seen from Eq. (4.6), the OPD due to the pellicle depends on three parameters: the thickness of the pellicle, the difference in refractive index relative to air or vacuum, and the largest angle ϕ. Typical values for these parameters are given in the following table for 1.35-NA optical lithography and 0.33-NA EUV lithography. For this table, it is assumed that the optical pellicles are made from Teflon AF,[84] while the EUV pellicles are fabricated from polysilicon. As can be seen in the table, optical pellicles are about five times thicker than EUV pellicles, and there are over two orders of magnitude difference in $n - 1$. There is a smaller difference (between optical and EUV lithography) in the maximum incident angle, in spite of a large difference in numerical aperture, in part because of the off-axis illumination configuration in EUV lithography, which results in an additional 6° for the maximum incident angle.

Even if EUV pellicles are composed of materials other than polysilicon, there will still be a small impact of EUV pellicles on imaging. For example, carbon nanotubes pellicles are promising, but the nanotubes require coatings in order to remain intact with ambient hydrogen, and some of these coating materials have lower values than silicon for the real parts of the indices of refraction. If we take one example, molybdenum, with a particularly low

value (0.923) for the real part of the index of refraction, and if we assume that the full 50-nm thickness of the pellicle is made of molybdenum, the maximum OPD for 0.33-NA EUV lithography is still only ~0.02 waves.

The impact of having a non-flat pellicle is also smaller for EUV lithography than for optical lithography (Fig. 4.28). If a pellicle is not perfectly flat, normally incident light refracts and is displaced by a distance of δ given by

$$\delta = t\left(1 - \frac{1}{n}\right)\sin\phi. \tag{4.7}$$

For thin pellicles, the displacement of light rays by refraction is small, even for moderate amounts of pellicle nonflatness.

Although refraction effects by EUV pellicles are expected to be small, very small variations in thickness will change the pellicle transmission, an effect resulting from light absorption by the pellicle material. For example, silicon has an attenuation length of 0.588 microns at a wavelength of 13.5 nm.[85] For a polysilicon pellicle, a 52-nm-thick pellicle will have 0.3% less transmission than a 50-nm-thick transmission. This is within the requirements listed in Table 4.7.

Because it seemed that EUV pellicles would not be possible at the time that 0.33-NA exposure tools were being designed, little room was available for

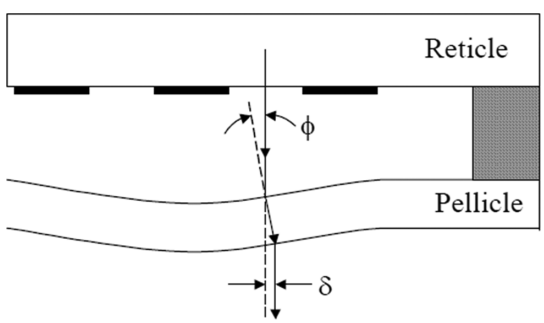

Figure 4.28 Geometry placement errors because of nonflat pellicles.

Table 4.7 Parameters for optical and EUV pellicles.

	1.35-NA optical lithography	**0.33-NA EUV lithography**
t	284 nm	50 nm
$n - 1$	0.35	−0.001
Maximum ϕ	19.7°	~11°
Maximum OPD	0.54 waves	−0.0037 waves

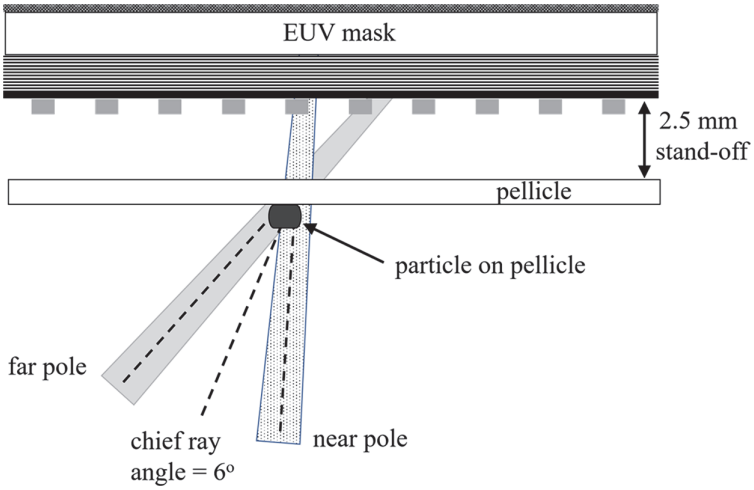

Figure 4.29 Light from dipole source attenuated by a particle on a pellicle.[87]

pellicles once they started to receive serious consideration. Consequently, the maximum standoff distance is 2.5 mm, which is much less than the standoff of many pellicles for optical lithography. The effect on imaging of particles on EUV pellicles has been studied. Since particles on pellicles are far from the focal plane of the optics, their principal impact is the attenuation of light,[86] primarily affecting critical dimensions. Although only the effect of the particle on incident light is illustrated in Fig. 4.29, particles can also affect the light diffracted by the mask and directed towards the projection optics, due to the reflection geometry. Studies have shown that particles ≤ 10 μm in size have a tolerable impact on imaging for a standoff distance of 2.5 mm.

4.6 Reticle Pods for EUV Masks

Once a standard was established for the EUV mask physical format, attention turned to the mask carrier. Because it was long thought that it would not be possible to fabricate thin membranes sufficiently large to serve as pellicles, extra steps were taken to protect EUV masks in such carriers from particle contamination. What resulted was the dual pod carrier, originally proposed jointly by Canon and Nikon,[88] which has both an inner and outer shell, illustrated in Fig. 4.30. A SEMI standard (E152) for this pod was also created.[89] When used within a tool, a reticle can be kept in the inner shell, providing additional protection against contamination. When EUV pellicles began to appear possible, dual reticle pod designs were modified to provide the mechanical clearance for pellicles.[90,91] A picture of a dual pod carrier is shown in Fig. 4.31.

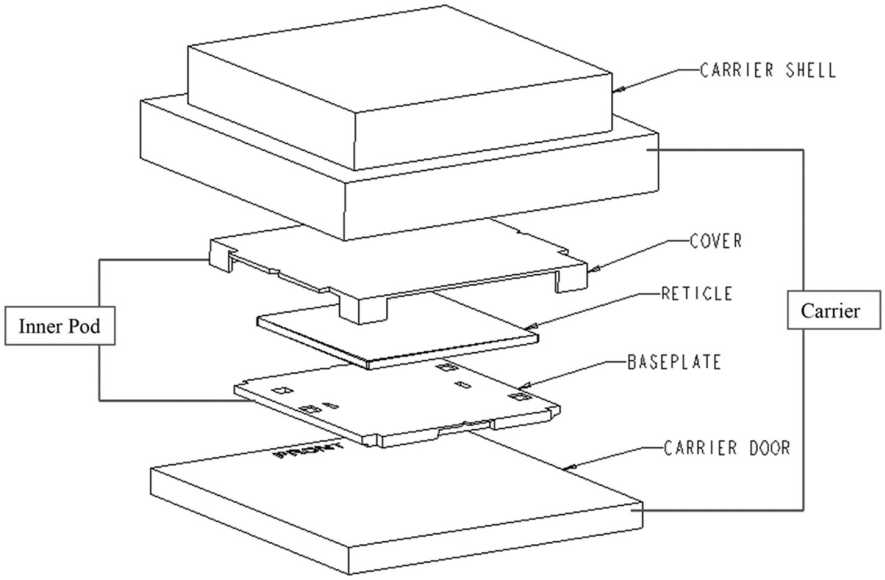

Figure 4.30 Schematic of an EUV reticle dual pod.[92]

Figure 4.31 Picture of an Entegris EUV reticle pod.[93] The outer pod is shown on the upper left, while the inner pod is on the bottom right.

4.7 Alternative EUV Absorbers and Mask Architectures

Absorber materials other than TaN and TaBN are being pursued for use in binary masks because of the advantages of thin absorbers, coupled with the need to have greater absorptivity to maintain low reflectance from mask areas

covered by thin absorbers. The materials shown in Fig. 4.32 with large values of k are good candidates from an optical perspective for absorbers on binary masks. However, there are many other requirements for absorbers other than optical properties that must be met (listed in Table 4.1). For example, nickel has been considered as an absorber material,[94,95,96,97] but the lack of identified volatile nickel compounds has made it difficult to pattern this material using reactive ion etching.[98]

Because of issues due to mask 3D effects, such as the shadowing illustrated in Fig. 4.3, as well as the desire to enable EUV phase shifting masks,[99,100] different mask architectures have been considered.[101,102,103,104] One of the earliest types of phase-shifting masks to be investigated was the attenuated phase-shifting mask. In optical lithography, the absorbers of attenuated phase-shifting masks are less than 100% absorbent, and the light transmitted through the absorber is phase shifted ~180° from the light transmitted through the clear apertures in the mask. Attenuated phase-shifting masks for EUV lithography are conceptually similar, where an appreciable fraction of EUV light is reflected from the multilayer reflector and transmitted back through the absorber (Fig. 4.33).

If the complex index of refraction of the absorber is $n + ik$, then the fraction of light R reflected from the absorber, relative to that reflected from the clear regions, is given by[105]

$$R = e^{-\frac{4\pi k(2t)}{\lambda_0}}, \tag{4.8}$$

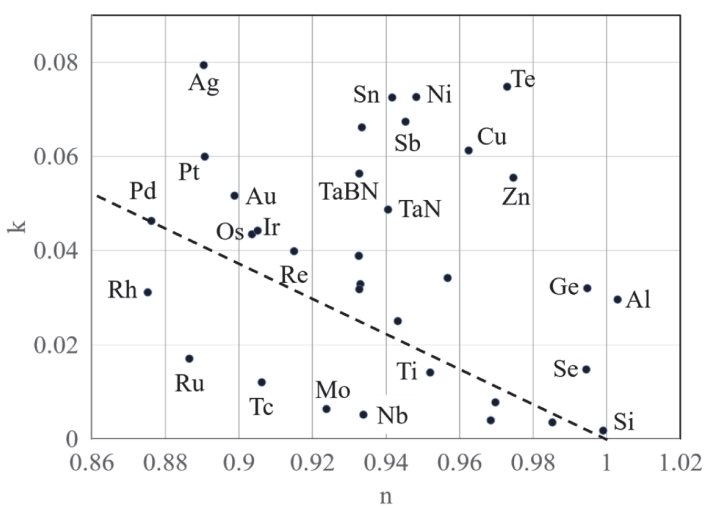

Figure 4.32 Values of n and k for various elements and mask-making materials. For materials below the dashed line, the reflectance of light is >6% in areas on masks covered by absorber, and the phase change = 1.2π.

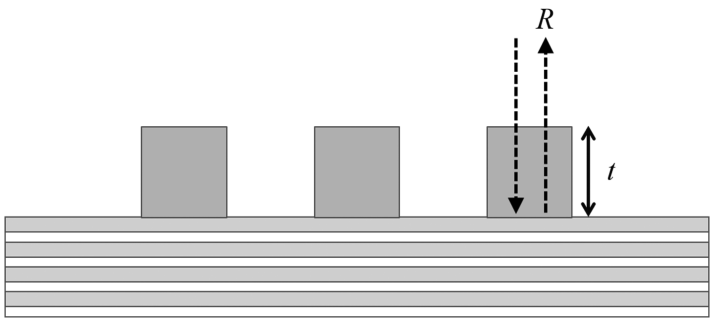

Figure 4.33 Schematic of an EUV attenuated phase-shifting mask.

where λ_0 is the wavelength of EUV light in vacuum. If we assume an infinitely thin reflector, the phase of this light, relative to that reflected from the regions of the mask without absorber, is given by

$$\Delta\phi = 2\pi\left(\frac{2t}{\lambda_o} - \frac{2tn}{\lambda_o}\right) \tag{4.9}$$

$$= \frac{4\pi t}{\lambda_o}\left(1 - n\right). \tag{4.10}$$

This results in the following relationship:

$$k = \frac{(n-1)\ln(R)}{2\Delta\phi}. \tag{4.11}$$

For optical attenuated phase-shifting masks, $\Delta\phi \approx \pi$, but for EUV lithography, the optimum has been found to be $\Delta\phi \approx 1.2\pi$, when mask 3D effects are taken into account.[106] (Mask 3D effects are discussed in more detail in Chapter 6.) Equation (4.11) can be rewritten:

$$t = \frac{\lambda_o \Delta\phi}{4\pi(1-n)}. \tag{4.12}$$

The absorbers will be thinner when the real part of the refractive index n deviates significantly from 1.0. As will be discussed further in Chapter 6, thin absorbers are very desirable from an OPC and RET perspective.

Values for n and k and been compiled by the Center for X-Ray Optics, and values for various solids are shown in Fig. 4.32. For elements below the dashed line the "transmission" R will be greater than 6%, which is generally considered a minimum value for getting benefits from phase shifting. This significantly reduces the number of elements that can be used for fabricating attenuated phase-shifting masks for EUV lithography. Among the elements with $n < 0.92$, rhemium is an extremely rare element, while all isotopes of

technetium are radioactive. This leaves ruthenium and palladium as the only elements suitable for fabricating attenuated phase-shifting masks. Since one of the functions of the Ru capping layer[107] found on current EUV masks is as an etch stop layer, a replacement capping layer will be needed if mask absorbers are made from ruthenium. Alternatively, an additional film consisting of a material other than ruthenium could be deposited between the capping layer and the attenuating absorber. This additional layer can also serve to provide an extra degree of freedom to balance total absorption and phase.

From an optical perspective, palladium is a potential absorber for attenuated phase-shifting masks. However, as a Group VIII metal, there may be challenges for etching, similar to what has been experienced for nickel. Moreover, imaging simulations indicated a lower NILS for palladium-based attenuated phase-shifting masks compared to those based on ruthenium.[107]

Alternating phase-shifting masks for EUV lithography have also been explored. The most common approach for this involves partial etch of the multilayers, as illustrated in Fig. 4.34. The depth of this partial etch can produce ~180° phase shifting for application to line/space patterns, while ~90° phase shifting can be used for focus monitors. Binary masks created by etching the multilayers down to the glass substrate have also been considered[100,108] (Fig. 4.35). Exposures with such masks showed reduced mask 3D effects, such as horizontal–vertical bias,[109] but this approach was not pursued because of concern over pinhole defects in the resist or hardmask used to define the pattern of the etched multilayer, because the resulting defects cannot be repaired.

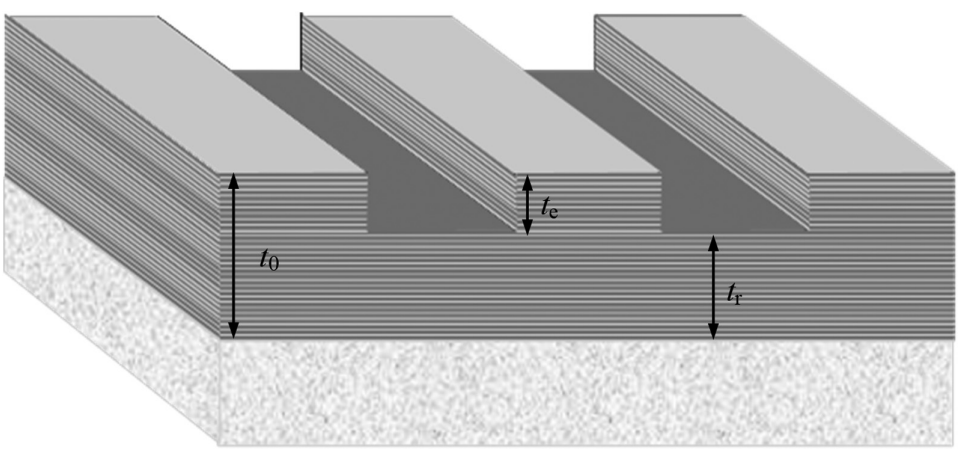

Figure 4.34 Schematic of an alternating phase-shifting mask for EUV lithography. The depth of the etched trench t_e controls the phase of the reflected light.[101]

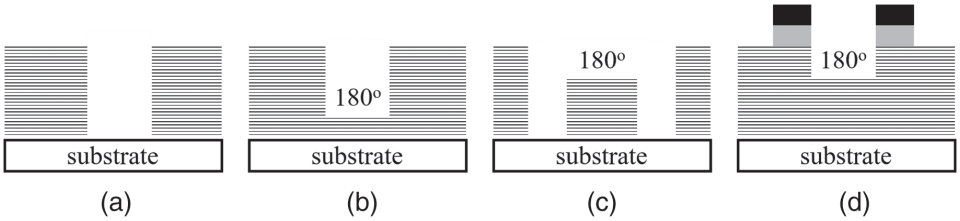

Figure 4.35 Different types of etched multilayer masks: (a) binary mask, (b) attenuated phase shifting mask (PSM), (c) alternating PSM double etched, and (d) alternating PSM with absorbers.[109]

Problems

4.1 With a coefficient of thermal expansion (CTE) of 0.52 ppm/°C for fused silica, show that the separation between of features on a mask that are originally 100 mm apart changes by 104 nm for a 2°C increase in temperature, assuming that mask is fabricated on a fused silica substrate. Based on the data shown in Fig. 3.7, for ULE®

$$CTEppb/°C = 1.55T - 31.0,$$

where T is in units of °C. Show that the separation between of features on a mask that are originally 100 mm apart changes by 0.31 nm for a 2°C increase in temperature, assuming the mask substrate is composed of ULE®.

4.2 Use the CXRO website (http://www.cxro.lbl.gov/) to obtain the extinction coefficient for teflon, a common material used for making DUV pellicles. Using this value, show that a pellicle made of teflon would need to be <6 nm thick in order to have 90% transmission. Is this a practical thickness?

4.3 Show that 50-nm mask nonflatness contributes wafer-level pattern placement errors of 1.3 nm for systems that illuminate the mask at a chief ray angle of 6° and have projection optics with a reduction ratio of 4:1.

4.4 Assuming that the index of refraction of ULE at DUV wavelengths is 1.5, show that 4% of normally incident DUV light is reflected from ULE.

References

1 Zone plate lenses at EUV wavelengths are often used for metrology applications, but are not suitable for large field, high resolution projection optics.

2 P. Yan, G. Zhang, S. Chegwidden, E. A. Spiller, and P. B. Mirkarimi. "EUVL mask with Ru ML capping," *Proc. SPIE* Vol. **5256**, pp. 1281–1286, 2003.
3 P. Yan, "Impact of EUVL mask buffer and absorber material properties on mask quality and performance," *Proc. SPIE* Vol. **4688**, pp. 150–160 (2002).
4 P. Yan, G. Zhang, A. Ma, and T. Liang, "TaN EUVL mask fabrication and characterization," *Proc. SPIE* Vol. **4343**, pp. 409–14 (2001).
5 P. Yan, G. Zhang, R. Nagpal, E. Y. Shu, C. Li, P. Qu, and F. T. Chen. "EUVL mask patterning with blanks from commercial suppliers," *Proc. SPIE* Vol. **5567**, pp. 774–780, 2004.
6 M. Takahashi, T. Ogawa, E. Hoshino, H. Hoko, B.T. Lee, A. Chiba, H. Yamanashi, and S. Okazaki, "Tantalum nitride films for the absorber material of reflective-type EUVL mask," *Proc. SPIE* **4343**, pp. 760–770 (2001).
7 P. Yan, G. Zhang, P. Kofron, J. Powers, M. Tran, T. Liang, A. Stivers, and F. C. Lo, "EUV mask absorber characterization and selection," *Proc. SPIE* **4066**, pp. 116–123 (2000).
8 T. Shoki, T. Kinoshita, N. Sakaya, M. Hosoya, R. Ohkubo, Y. Usui, H. Kobayashi, and O. Nagarekawa, "Damage-free extreme ultraviolet mask with TaBN absorber," *J. Vac. Sci. Technol. B* **21**(6), pp. 3021–3026 (2003).
9 Y. Du, C. J. Choi, G. Zhang, S. Park, P. Yan, and K. Baik, "TaN-based EUV mask absorber etch study," *Proc. SPIE* Vol. **6283**, p. 62833D, 2006.
10 H. Seitz, M. Renno, T. Leutbecher, N. Olschewski, T. Reichardt, R. Walter, H. Popp, et al. "EUVL mask blanks: Recent results on substrates, multilayers and the dry-etch process of TaN-absorbers," *Proc. SPIE* Vol. **6151**, p. 615109, 2006.
11 F. Letzkus, J. Butschke, M. Irmscher, H. Sailer, U. Dersch, and C. Holfeld. "EUVL mask manufacturing: technologies and results," *Proc. SPIE* Vol. **5992**, p. 59922A, 2005.
12 T. Liang, E. Frendberg, D. J. Bald, M. Penn, and A. R. Stivers. "E-beam mask repair: fundamental capability and applications," *Proc. SPIE* Vol. **5567**, pp. 456–466, 2004.
13 The Center for X-Ray Optics (CXRO) at Lawrence Berkeley National Laboratory has a convenient database of optical properties at EUV and x-ray wavelengths. http://cxro.lbl.gov/
14 K. Otaki, "Asymmetric properties of the aerial image in extreme ultraviolet lithography," *Jpn. J. Appl. Phys. Pt.* 1, **39**(12B), pp. 6819–6826 (2000).
15 S.B. Bollepalli, M. Khan, and F. Cerrina, "Image formation in extreme ultraviolet lithography and numerical aperture effects," *J. Vac. Sci. Technol. B* **17**(6), pp. 2992–2997 (1999).

16 E. van Setten, D. Oorschot, C. Man, M. Dusa, R. de Kruif, N. Davydova, K. Feenstra, et al. "EUV mask stack optimization for enhanced imaging performance," *Proc. SPIE* Vol. **7823**, p. 78231O, 2010.
17 T. Kamo, K. Tawarayama, Y. Tanaka, Y. Arisawa, H. Aoyama, T. Tanaka, and O. Suga. "Light-shield border impact on the printability of extreme-ultraviolet mask." *Journal of Micro/Nanolithography, MEMS, and MOEMS* **10**, no. 2 (2011): 023001.
18 G. Watanabe, N. Fukugami, T. Komizo, Y. Kodera, and T. Nishi. "EUV mask with advanced hybrid black border suppressing EUV and DUV OOB light reflection," *Proc. SPIE* **10807**, p. 108070N, 2018.
19 R.E. Hrdina, B.Z. Hanson, P.M. Fenn, and R. Sabia, "Characterization and characteristics of an ULE glass tailored for the EUVL needs," *Proc. SPIE* **4688**, pp. 454–461 (2002).
20 I. Mitra, M. J. Davis, J. Alkemper, R. Müller, L. Aschke, E. Mörsen, S. Ritter, H. Hack, and W. Pannhorst, "Thermal expansion behavior of proposed EUVL substrate materials," *Proc. SPIE* **4688**, pp. 462–468 (2002).
21 H. J. Levinson and K. B. Nguyen. "Extreme ultraviolet lithography reflective mask." U.S. Patent 6, 159, 643, issued December 12, 2000.
22 J. Choi, D.S. Nam, B.G. Kim, S-G. Woo, and H.K. Cho, "Resist charging effect in photomask: its impact on pattern placement error and critical dimension," *J. Vac. Sci. Technol. B* **26**(6), pp. 2345–2350 (2008).
23 T. Kamo, Y. Tanaka, T. Tanaka, I. Nishiyama, O. Suga, T. Abe, T. Takikawa, H. Mohri, T. Shoki, and Y. Usui. "Thin-absorber extreme-ultraviolet lithography mask with light-shield border for full-field scanner: flatness and image placement change through mask process." *Journal of Micro/Nanolithography, MEMS, and MOEMS* **9**, no. 2 (2010): 023005.
24 N. Nakayamada, S. Wake, T. Kamikubo, H. Sunaoshi, and S. Tamamushi, "Modeling of charging effect and its correction by EB mask writer EBM-6000," *Proc. SPIE* **7028**, 20280C (2008).
25 G. C. Rider, "Current understanding of the electrostatic risk to reticles used in microelectronics and similar manufacturing processes." *Journal of Micro/Nanolithography, MEMS, and MOEMS* **17**, no. 2 (2018): 020901.
26 J. G. Hartley, S. Raghunathan, and A. Govindaraju, "Electrical characterization of multilayer masks for extreme ultraviolet lithography," *Journal of Vacuum Science & Technology B: Microelectronics and Nanometer Structures Processing, Measurement, and Phenomena* **23**, no. 6 (2005): 2891–2895.
27 S. Hau-Riege, A. Barty, P. Mirkarimi, S. Baker, M. A. Coy, M. Mita, V. E. Robertson, T. Liang, and A. Stivers, "Repair of phase defects in extreme-ultraviolet lithography mask blanks," *J. Appl. Phys.*, pp. 6812–6821 (2004).
28 H.J. Levinson, "Impact of reticle imperfections on integrated circuit processing," *Proc. Third Annual Sym. Bay Area Chrome Users Soc.*

(BACUS), September 14 and 15, 1983, Sunnyvale, California, as described in Semicond. Int., pp. 22–23 (December, 1983).

29 Z. J. Qi, J. Rankin, E. Narita, and M. Kagawa, "Viability of pattern shift for defect-free EUV photomasks at the 7nm node," *Proc. SPIE* **9635**, p. 96350N, 2015.

30 R. Jonckheere, T. Yamane, Y. Morikawa, and T. Kamo, "Blank defect coverage budget for 16nm half-pitch single EUV exposure," *Proc. SPIE* **10807**, p. 108070H, 2018.

31 S. Stokowski, J. Glasser, G. Inderhees, and P. Sankuratri, "Inspecting EUV mask blanks with a 193nm system," *Proc. SPIE* **7636**, p. 76360Z, 2010.

32 E. Verduijn, P. Mangat, O. Wood, J. Rankin, Y. Chen, F. Goodwin, R. Capelli, et al., "Printability and actinic AIMS review of programmed mask blank defects," *Proc. SPIE* **10143**, p. 101430K, 2017.

33 K. D. Badger, Z. J. Qi, E. Gallagher, K. Seki, and G. McIntyre. "Illuminating EUVL mask defect printability," *Proc. SPIE* 8522, p. 85220I, 2012.

34 C.C. Walton, P.A. Kearney, P.B. Mirkarimi, J.M. Bowers, C. Cerjan, A.L. Warrick, K. Wilhelmsen, E. Fought, C. Moore, C. Larson, S. Baker, S.C. Burkhart, and S.D. Hector, "Extreme ultraviolet lithography–reflective mask technology," *Proc. SPIE* 3997, pp. 496–507 (2000).

35 C. Fu, D. H. Dameron, and A. McCarthy. "Elimination of mask-induced defects with vote-taking lithography." *In Optical Microlithography V*, vol. **633**, pp. 270–277, 1986.

36 T. A. Brunner, M. Ozlem, G. Han, J. Rankin, O. Wood, and E. Verduijn. "Vote-taking for EUV lithography: a radical approach to mitigate mask defects," *Proc. SPIE* Vol. **10143**, p. 1014313, 2017.

37 J. Bekaert, P. De Bisschop, C. Beral, E. Hendrickx, M. A. van de Kerkhof, S. Bouten, M. Kupers, G. Schiffelers, E. Verduijn, and T. A. Brunner. "EUV vote-taking lithography: crazy... or not?," *Proc. SPIE* **10583**, p. 105830I, 2018.

38 J. Bekaert, P. De Bisschop, C. Beral, E. Hendrickx, M. A. van de Kerkhof, S. Bouten, M. Kupers, G. Schiffelers, E. Verduijn, and T. A. Brunner. "EUV vote-taking lithography for mitigation of printing mask defects, CDU improvement, and stochastic failure reduction," *Journal of Micro/Nanolithography, MEMS, and MOEMS* **17**, no. 4 (2018): 041013.

39 S. Jeong, L. Johnson, Y. Lin, S. Rekawa, P. Yan, P. Kearney, E. Tejnil, J. Underwood, and J. Bokor, "Actinic EUVL mask blank defect inspection system," *Proc. SPIE* **3676**, pp. 298–308 (1999).

40 Y. Tezuka, M. Ito, T. Terasawa, and T. Tomie, "Actinic detection of multilayer defects on EUV mask blanks using LPP light source and dark-field imaging," *Proc. SPIE* **5374**, pp. 271–280 (2004).

41 T. Kamo, T. Terasawa, T. Yamane, H. Shigemura, N. Takagi, T. Amano, K. Tawarayama, et al. "Evaluation of EUV mask defect using blank inspection, patterned mask inspection, and wafer inspection." *Proc. SPIE*, vol. **7969**, p. 79690J. 2011.
42 A. Tchikoulaeva, H. Miyai, K. Takehisa, T. Suzuki, Haruhiko Kusunose, H. Watanabe, I. Mori, and S. Inoue. "EUV actinic blank inspection: from prototype to production," *Proc. SPIE*, vol. **8679**, p. 86790I. 2013.
43 S.D. Hector, "EUVL masks: requirements and potential solutions," *Proc. SPIE* **4688**, pp. 134–149 (2002).
44 International Technology Roadmap for Semiconductors (2013).
45 S. Yoshitake, S. Tamamushi, and M. Ogasawara. "Desired IP control methodology for EUV mask in current mask process." *European Mask and Lithography Conference (EMLC)* (2008).
46 Y. Tanaka, T. Kamo, K. Ota, H. Tanaka, O. Suga, M. Itoh, and S. Yoshitake. "Overlay accuracy of EUV1 using compensation method for nonflatness of mask," *Proc. of SPIE* Vol, vol. **7969**, pp. 796936–1. 2011.
47 V. Ramaswamy, R.L. Engelstad, K.T. Turner, A.R. Mikkelson, and S. Veeraraghavan, "Distortion of chucked extreme ultraviolet reticles from entrapped particles," *J. Vac. Sci. Technol. B* **24**(6), pp. 2829–2833 (2006).
48 Y. Arisawa, T. Terasawa, and H. Watanabe, "Impact of EUV mask roughness on lithography performance," *Proc. SPIE* **8679**, p. 86792S, 2013.
49 P. P. Naulleau, S. A. George, and B. M. McClinton, "Mask roughness and its implications for LER at the 22-and 16nm nodes," *Proc. SPIE* **7636**, p. 76362H, 2010.
50 X. Chen, E. Verduijn, O. Wood, T. Brunner, R. Capelli, D. Hellweg, M. Dietzel, and G. Kersteen, "Evaluation of EUV mask impacts on wafer line-edge roughness using aerial and SEM image analyses," *Proc. SPIE* **10583**, p. 105830J, 2018.
51 P.P. Naulleau and G.G. Gallatin, "Line-edge roughness transfer function and its application to determining mask effects in EUV resist characterization," *Appl. Optic.* **42**(17), pp. 3390–3397 (2003).
52 H. Tanabe, G. Yoshizawa, Y. Liu, V.L Tolani, K. Kojima, and N. Hayashi, "LER transfer from a mask to wafers," *Proc. SPIE* **6607**, 66071H (2007).
53 C. Klein, H. Loeschner, and E. Platzgummer. "MBMW-201: The next generation multi-beam mask writer (Conference Presentation)," *Proc. SPIE* **10958**, p. 109580K, 2019.
54 H. Hiroshi, H. Kimura, T. Tamura, and K. Ohtoshi. "Multi-beam mask writer MBM-1000," *Proc. SPIE* **10958**, p. 109580J, 2019.
55 H. Tanabe, T. Abe, Y. Inazuki, and N. Hayashi, "Short-range electron backscattering from EUV masks," *Proc. SPIE* **7748**, p. 774823, 2010.

56 H. J. Levinson and C. F. Lyons, Advanced Micro Devices, Inc., "Pellicle for use in EUV lithography and a method of making such a pellicle," U.S. Patent 6, 623, 893 (2003).
57 H. J. Levinson, "EUV Lithography at the Threshold of High Volume Manufacturing," *EUVL Workshop*, 2018, https://www.euvlitho.com/2018/2018%20EUVL%20Workshop%20Proceedings.pdf
58 B. Turkot, "EUVL readiness for high volume manufacturing," *in Int. Workshop on EUV Lithography.* 2016.
59 C. Zoldesi, K. Bal, B. Blum, G. Bock, D. Brouns, F. Dhalluin, N. Dziomkina, J. D. A. Espinoza, J. de Hoogh, S. Houweling, M. Jansen, M. Kamali, A. Kempa, R. Kox, R. de Kruif, J. Lima, Y. Liu, H. Meijer, H. Meiling, I. van Mil, M. Reijnen, L. Scaccabarozzi, D. Smith, B. Verbrugge, L. de Winters, X. Xiong, and J. Zimmerman, "Progress on EUV pellicle development," *Proc. SPIE* **9048**, 90481N (2014).
60 C. Zoldesi, K. Bal, B. Blum, G. Bock, D. Brouns, F. Dhalluin, N. Dziomkina, et al. "Progress on EUV pellicle development," *Proc. SPIE* **9048**, p. 90481N, 2014.
61 D. L. Goldfarb, M. O. Bloomfield, and M. Colburn. "Thermomechanical behavior of EUV pellicle under dynamic exposure conditions," *Proc. SPIE* **9776**, p. 977621, 2016.
62 P. J. Van Zwol, M. Nasalevich, W. Pim Voorthuijzen, E. Kurganova, A. Notenboom, D. Vles, M. Peter, et al., "Pellicle films supporting the ramp to HVM with EUV," *Proc. SPIE* **10451**, p. 104510O, 2017.
63 H. Shin and H. Oh, "Extreme-ultraviolet pellicle durability comparison for better lifetime," *Proc. SPIE* **11147**, p. 111470U, 2019.
64 M. Kang, S. Lee, E. Park, and H. Oh, "Thermo-mechanical behavior analysis of extreme-ultraviolet pellicle cooling with H2 flow," *Proc. SPIE* **10450**, p. 104501N, 2017.
65 U. Okoroanyanwu, K. Dittmar, T. Fahr, T. Wallow, B. La Fontaine, O. Wood, C. Holfeld, K. Bubke, and J. Peters, "Analysis and characterization of contamination in EUV reticles," *Proc. SPIE* **7636**, p. 76361Y, 2010.
66 J. Doh, C. Y. Jeong, S. Lee, J. U. Lee, H. Cha, J. Ahn, D. G. Lee, S. S. Kim, H. K. Cho, and S. Rah, "Determination of the CD Performance and Carbon Contamination of an EUV Mask by Using a Coherent Scattering Microscopy/In-situ Contamination System," *Journal of the Korean Physical Society 57*, no. 6 (2010): 1486–1489.
67 Y. Fan, L. Yankulin, P. Thomas, C. Mbanaso, A. Antohe, R. Garg, Y. Wang, et al., "Carbon contamination topography analysis of EUV masks," *Proc. SPIE* **7636**, p. 76360G, 2010.
68 U. Okoroanyanwu, E. Langer, T. Wallow, O. Wood, B. La Fontaine, C. Holfeld, J. H. Peters, M. Bender, M. Rossinger, S. Trogisch, F. Goodwin, G. Denbeaux, Y. Fan, A. Antohe, L. Yankulin, R. Garg,

K. Goldberg, and P. Naulleau, "EUV reticle contamination and cleaning," *presented at the 2008 International Symposium on Extreme Ultraviolet Lithography*.

69 Y. Hyun, J. Kim, K. Kim, S. Koo, S. Kim, Y. Kim, C. Lim, and N. Kwak, EUV mask particles adders during scanner exposure, *Proc. SPIE* **9422**, 94221U-1 - 94221U–7 (2015).

70 Y. Ono, K. Kohmura, A. Okubo, D. Taneichi, H. Ishikawa, and T. Biyajima, "Development of a novel closed EUV pellicle for EUVL manufacturing," *Proc. SPIE*, pp. 99850B–99850B (2016).

71 D. L. Goldfarb, "Fabrication of a full-size EUV pellicle based on silicon nitride," *Proc. SPIE Photomask Technology*, pp. 96350A–96350A (2015).

72 M. Goldstein, Y. Shroff, and D. Tanzil, "Pellicle, methods of fabrication and methods of use for extreme ultraviolet lithography." U.S. Patent 7, **666**, 555 (2010).

73 E. E. Gallagher, J. Vanpaemel, I. Pollentier, H. Zahedmanesh, C. Adelmann, C. Huyghebaert, R. Jonckheere, and J. U. Lee, "Properties and performance of EUVL pellicle membranes," *Proc. of SPIE* **9635**, 96350X-1 - 96350X–8 (2015).

74 U. Okoroanyanwu and R. Kim. "EUV pellicle and method for fabricating semiconductor dies using same." *U.S. Patent* 7, 767, **985** (2010).

75 I. Mochi, M. Timmermans, E. Gallagher, M. M. Juste, I. Pollentier, R. Rajeev, P. Helfenstein, S. Fernandez, D. Kazazis, and Y. Ekinci, "Experimental evaluation of the impact of EUV pellicles on reticle imaging," *Proc. SPIE* **10810**, p. 108100Y, 2018.

76 M. Y. Timmermans, I. Pollentier, J. U. Lee, J. Meersschaut, O. Richard, C. Adelmann, C. Huyghebaert, and E. E. Gallagher, "CNT EUV pellicle: moving towards a full-size solution" *Proc. SPIE* **10451**, p. 104510P, 2017.

77 D. E. Aspnes, A. A. Studna, and E. Kinsbron. "Dielectric properties of heavily doped crystalline and amorphous silicon from 1.5 to 6.0 eV." *Physical Review B* **29**, no. 2 (1984): 768.

78 D. Brouns, A. Bendiksen, P. Broman, E. Casimiri, P. Colsters, D. de Graaf, H. Harrold, et al., "NXE pellicle: development update," *Proc. SPIE* **9985**, p. 99850A, 2016.

79 S. Moon, S. Y. Chu, D. Y. Shin, S. Jeon, and J. D. You, "Fully Automated EUV Pellicle Mask Shop Tools for HVM," *presented at SPIE Photomask Technology Conference*, 2019.

80 D. Smith, "ASML NXE pellicle update," http://ieuvi.org/TWG/Mask/2016/20160221/1_Pellicle_TWG2016_NXE_Pellicle_fx.pdf

81 Y. Ono, K. Kohmura, A. Okubo, D. Taneichi, H. Ishikawa, and T. Biyajima, "Development of closed-type EUV pellicle," *Proc. SPIE* **10807**, 108070I, 2018.

82 A. Ishikawa, H. Tanaka, Y. Ono, A. Okubo, and K. Kohmura, "Development of the breathable frame for closed EUV pellicle," *Proc. SPIE* **11178**, p. 111780N, 2019.
83 K. Bubke, B. Alles, E. Cotte, M. Sczyrba, and C. Pierrat, "Pellicle-induced aberrations and apodization in hyper-NA optical lithography," *Proc. SPIE* **6283**, 628318 (2006).
84 M.K. Yang, R.H. French, and E.W. Tokarsky, "Optical properties of Teflon® AF amorphous fluoropolymers," *J. Micro/Nanolith, MEMS, MOEMS* **7**(3), 033010 (2008).
85 Many optical properties of materials can be found on the CRXO database at http://www.cxro.lbl.gov
86 P. Evanschitzky and A. Erdmann. "Efficient simulation of EUV pellicles," *Proc. SPIE* **10450**, p. 104500B, 2017.
87 H-R. No, S.-G. Lee, S.-H. Oh, and H.-K. Oh. "Pattern degradation with larger particles on EUV pellicle," *Proc. SPIE* **10809**, p. 108091G, 2018.
88 K. Ota, M. Yonekawa, T. Taguchi, and O. Suga. "Evaluation results of a new EUV reticle pod based on SEMI E152," *Proc. SPIE* **7636**, p. 76361F, 2010.
89 SEMI Standard E152 - Specification for Mechanical Features of EUV Pod for 150 mm EUVL Reticles.
90 Entegris White Paper, "Enabling Advanced Lithography: The Challenges of Storing and Transporting EUV Reticles," www.entegris.com
91 http://www.gudeng.com/index.php/en/euv-pod-4
92 L. He, S. Wurm, P. Seidel, K. Orvek, E. Betancourt, and J. Underwood, "Status of EUV reticle handling solution in meeting 32 nm hp EUV lithography," *Proc. SPIE* **6921**, p. 69211Z, 2008.
93 This figure was provided by Mr. Preston Williamson of Entegris.
94 O. Wood II, S. Raghunathan, P. Mangat, V. Philipsen, V. Luong, P. Kearney, E. Verduijn, et al., "Alternative materials for high numerical aperture extreme ultraviolet lithography mask stacks," *Proc. SPIE* **9422**, p. 94220I, 2015.
95 S. K. Patil, S. Singh, U. Okoroanyanwu, and P. J. S. Mangat. "Mask structures and methods of manufacturing." U.S. Patent 9, 195, 132, issued November 24, 2015.
96 V. Luong, V. Philipsen, E. Hendrickx, K. Opsomer, C. Detavernier, C. Laubis, F. Scholze, and M. Heyns. "Ni-Al alloys as alternative EUV mask absorber." *Applied Sciences* **8**, no. 4 (2018): 521.
97 V. Jindal, H. N. G. Fong, B. Varghese, S. Liu, and A. Rastegar. "Extreme Ultraviolet Mask Absorber Materials." U.S. Patent Application 16/512, 693, filed January 23, 2020.
98 K. Rook, N. Srinivasan, V. Ip, M. Lee, and T. Henry. "Ion beam etch for the patterning of advanced absorber materials for EUV masks," *Proc. SPIE* **11178**, p. 111780G, 2019.

99 O. R. Wood, D. L. White, J. E. Bjorkholm, L. E. Fetter, D. M. Tennant, A. A. MacDowell, B. LaFontaine, and G. D. Kubiak. "Use of attenuated phase masks in extreme ultraviolet lithography." *J. Vac. Sci. Technol.* **B15**, no. 6 (1997): 2448–2451.
100 B. La Fontaine, A. R. Pawloski, O. Wood, Y. Deng, H. J. Levinson, P. Naulleau, P. E. Denham, et al. "Demonstration of phase-shift masks for extreme-ultraviolet lithography," *Proc. SPIE* **6151**, p. 61510A, 2006.
101 B. La Fontaine, A. R. Pawloski, Y. Deng, C. Chovino, L. Dieu, O. R. Wood II, and H. J. Levinson, "Architectural choices for EUV lithography masks: patterned absorbers and patterned reflectors," *Proc. SPIE* **5374**, pp. 300–310, 2004.
102 S. Schwarzl, F. Kamm, S. Hirscher, K. Lowack, W. Domke, M. Bender, S. Wurm, et al. "Comparison of EUV mask architectures by process window analysis," *Proc. SPIE* **5751**, pp. 435–445, 2005.
103 T. Schmoeller, J. K. Tyminski, J. Lewellen, and W. Demmerle, "The impact of mask design on EUV imaging," *Proc. SPIE* **7379**, p. 73792H, 2009.
104 A. R. Pawloski, B. La Fontaine, H. J. Levinson, S. Hirscher, S. Schwarzl, K. Lowack, F. Kamm, et al. "Comparative study of mask architectures for EUV lithography," *Proc. SPIE* **5567**, pp. 762–773, 2004.
105 M. Burkhardt, "Investigation of alternate mask absorbers in EUV lithography," *Proc. SPIE* **10143**, p. 1014312, 2017.
106 M. van Lare, F. J. Timmermans, and J. Finders, "Alternative reticles for low-k1 EUV imaging," *Proc. SPIE* **11147**, 111470D, 2019.
107 T. Shoki, M. Ootsuka, M. Sakamoto, T. Asakawa, R. Sakamoto, H. Kozakai, K. Hamamoto, et al. "Improvement of defects and flatness on extreme ultraviolet mask blanks," *Journal of Micro/Nanolithography, MEMS, and MOEMS* **12**, no. 2 (2013): 021008.
108 L. Van Look, V. Philipsen, E. Hendrickx, G. Vandenberghe, N. Davydova, F. Wittebrood, R. de Kruif, et al., "Alternative EUV mask technology to compensate for mask 3D effects," *Proc. SPIE* **9658**, p. 96580I, 2015.
109 Y. Deng, B. M. La Fontaine, H. J. Levinson, and A. R. Neureuther. "Rigorous EM simulation of the influence of the structure of mask patterns on EUVL imaging," *Proc. SPIE* **5037**, pp. 302–313, 2003.

Chapter 5
EUV Resists

To date, most resists used for EUV lithography are chemically amplified resists, based on KrF and ArF resist platforms (although new concepts are also being given serious consideration). However, the demands for EUV resists differ from those of photoresists used at optical wavelengths in some critical ways. Because EUV lithography is intended to be used to produce features and pitches beyond the resolution limits of ArF lithography, EUV resists must be capable of very high resolution and have low line-edge roughness. There is also an enhanced need for sensitivity because of the low output of EUV light sources compared to excimer lasers, a problem described in Chapter 2. For DUV resists, sensitivity has been obtained through chemical amplification, and the greater the extent to which photoacids can diffuse and produce deprotection, the fewer photons are required to expose the resist. However, substantial diffusion will effectively blur the image, reducing resolution. To maintain a high-resolution image after post-exposure bake, there is a rule of thumb that the diffusion length of the photoacids in chemically amplified resists should be less than ~16% of the pitch.[1] Using this estimate as a guide, for 20-nm half-pitch technology, the diffusion length will need to be less than ~6 nm and must be even smaller for later nodes. In addition to having much tighter requirements for resolution and LER, the mechanisms of the radiation chemistry of EUV resists are different from those of optical resists, and these mechanisms for EUV resists are discussed in the first section of this chapter.

5.1 Exposure Mechanisms of Chemically Amplified EUV Resists

In KrF and ArF chemically amplified resists, incident photons are absorbed by photoacid generators, with acids produced as a direct consequence of this photoabsorption.[2] The radiation chemistry in EUV resists involves a somewhat different mechanism. EUV photons are highly energetic (~92 eV), so photoabsorption typically results in the generation of a photoelectron. Acids are produced as the result of collisions between electrons and

photoacid generators.[3,4,5,6] These electrons can be unscattered photoelectrons or elastically scattered electrons, but they can also be electrons of lower energy produced by inelastic collisions. As shown schematically in Fig. 5.1, the photoabsorption of EUV photons of energy $h\nu$ will result in a photoelectron of energy $h\nu - I_e$, where I_e is the ionization energy of the resist molecule from which the photoelectron originates. The photoelectron can scatter inelastically, where some energy is lost during the scattering process. Such scattering can create more ions and electrons, with this process continuing until the electrons produced have energies less than a threshold E_{th}, below which further ionization events will not result. Importantly, encounters between sufficiently energetic electrons and photoacid generators can result in the production of photoacids.

As depicted in Fig. 5.1, a photoelectron will propagate from its point of origin and subsequently scatter, which can result in the generation of additional energetic electrons. Many of these secondary electrons also have the potential to induce chemical reactions. As a consequence, the quantum yield for EUV resists can actually exceed 1.0,[9] where

$$\text{quantum yield} = \frac{\text{number of photoacids generated}}{\text{number of photons absorbed}}. \tag{5.1}$$

This is different from DUV lithography, where the quantum yield is typically less than 1.0.

The photoelectrons and secondary electrons will travel some distances before being scattered. The average distance before scattering is known as the mean free path. As a result, there is blur of the original optical image in the resist, even prior to post-exposure bake. Although the mean free path in

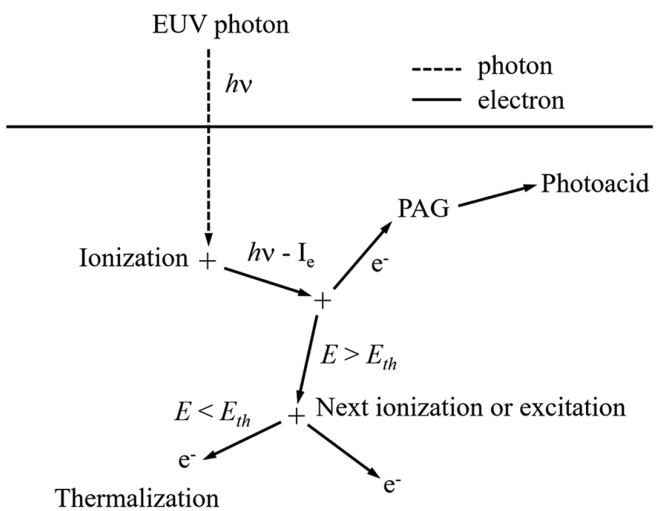

Figure 5.1 Schematic of the radiation chemistry mechanisms of EUV resists.[7,8]

organic materials for electrons with energy ~100 eV is <1 nm,[10,11] there can be multiple scattering events, leading to ranges for photoacid generation potentially much larger than 1 nm from the point of initial photon absorption. The situation is complicated, since electrons in EUV resists are created by ionization events, and the resulting positive ions can attract the electrons, thereby reducing their ranges. The determination of actual photoelectron ranges in EUV resists is still an area of active research,[12,13] and the answer will have implications for the ultimate resolution capability of EUV lithography. Insight into the nature of photoelectron and secondary electron blur could lead to methods for limiting the impact on resolution.

Although existing data are incomplete, an upper boundary for photoelectron-limited resolution has been determined from exposures using EUV interferometric lithography. Interferometric lithography provides higher-contrast aerial images (NILS = π for all pitches) than typically achieved with projection lithography, but such images enable determination of limits imposed by processes in the resist, separate from the image contrast. With interferometric lithography, line/space patterns with 10-nm half-pitches have been obtained, indicating that EUV lithography can be extended to such dimensions without being limited by photoelectron blur.[14]

Another issue that can arise due to the higher energy of EUV photons, relative to DUV photons, is polymer cross-linking, which occurs to a greater extent with the more energetic radiation. As a consequence, resists can simultaneously exhibit positive resist behavior at low to moderate doses, along with negative resist behavior at higher doses. This is illustrated in Fig. 5.2 and is another resist concern associated with EUV lithography of which practitioners need to be mindful. Shown in Fig. 5.2 are experimental characteristic curves for a resist exposed with KrF and EUV light. When exposed with KrF light, the resist shows positive resist characteristics throughout the entire exposure range. On the other hand, with EUV exposure the resist behaves with positive characteristics at low and medium doses but shows clear negative resist behavior at higher doses. This negative resist behavior has been attributed to cross-linking of the polymers that form the resist.

The details of EUV resist radiation chemistry are important because phenomena at the quantum level affect the characteristics of the resist that are significant for EUV lithography, which is applicable at features sizes of 20 nm and below. The first of these quantum-level characteristics that was recognized as important was line-edge roughness (LER), which affects linewidth control and can limit the applicability of EUV lithography to critical layers, such as transistor gate and metal layers. As the LER problem was studied in detail for EUV lithography, it became recognized that the underlying physical mechanisms that vary probabilistically and thereby lead to LER can also induce defects.[16] Physical processes that vary

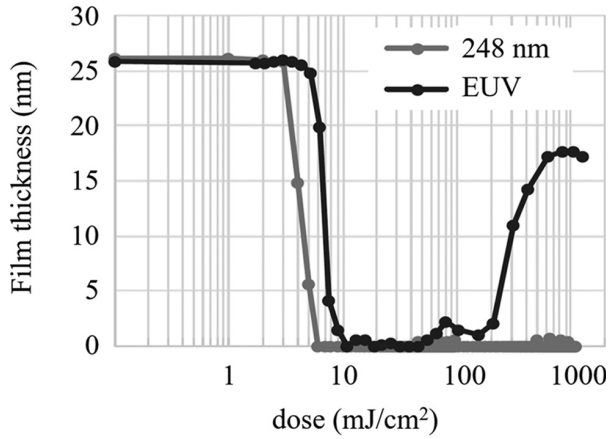

Figure 5.2 Characteristic curves of a single-type resist exposed separately with KrF (248-nm-wavelength) and EUV (13.5-nm-wavelength) light.[15]

probabilistically are often referred to as *stochastic* phenomena. Stochastic phenomena are discussed in more detail in the next section. (Metrics for characterizing LER are discussed at length in Chapter 3 of *Principles of Lithography*.[17])

Resolution is another characteristic of resists where quantum-level phenomena are relevant. During the development of EUV lithography, it was found that the resolution obtained in developed resist patterns fell far short of the optical resolution. Further study of the problem led to the realization that the resolution in resist patterns was being limited by photoacid diffusion during the post-exposure bake.[18] To address this problem, suppliers of EUV resists modified resist compositions by using photoacid generators that produced photoacids with shorter diffusion lengths,[19] and the amount of base quencher was increased.[20] The result was a significant improvement in the resolution achieved using EUV lithography.

However, decreasing photoacid diffusion, although it enabled better resolution, was not without drawbacks. With lessened diffusion, the amount of deprotection per photoacid decreased, resulting in a need for higher exposure doses. Moreover, diffusion in resists contributed to the mitigation of line-edge roughness, an effect which had already been recognized in KrF [21] and ArF lithography.[22] With less photoacid diffusion, there could be greater LER. This experience led to recognition that there are trade-offs among resolution, line-edge roughness, and resist exposure dose sensitivity, which became referred to as the RLS triangle[23] (Fig 5.3). It is generally desirable to reduce all three quantities in the triangle, but reducing the parameter in one corner of the triangle often necessitates increases in one or both of the others.

The interactions among resolution, LER, and sensitivity has been expressed in a single metric, the Z-factor:[24]

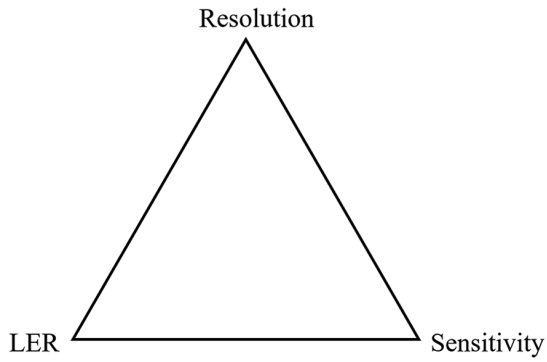

Figure 5.3 The RLS triangle, where R = resolution, L = LER, and S = sensitivity.

$$Z\,(\mathrm{mJ{-}nm^3}) = R^3 \times L^2 \times S. \tag{5.2}$$

where R represents the resolution in terms of half-pitch (nm), L represents the LER (in nm), and S is the exposure dose in units of mJ/nm^2. With the Z-factor, trade-offs among resolution, LER, and exposure dose are taken into account in a single parameter. Small values of Z are desirable, with values ~2×10^{-8} mJ-nm^3 being typical.[25]

Note that the three parameters composing the Z-factor cannot be adjusted arbitrarily. Lithographic technologies are targeted to specific nodes, so the resolution is fixed for a given node. Moreover, the requirements of the integrated technology will impose maximum useable values for LER, leaving dose sensitivity as the only parameter not fixed by the circuit-level technology. As will be discussed further in Chapter 9, exposure dose is a concern with respect to wafer cost.

5.2 Stochastic Effects in EUV Lithography

Although line-edge roughness has long been studied in the context of optical lithography,[21] it has been of significantly greater concern for EUV lithography. One reason is simply the feature sizes of interest, which are much smaller for EUV lithography than for optical lithography, and LER requirements typically scale with feature size. This can be put into perspective by considering relevant dimensions. Resists are composed of molecules, which introduce a granularity to features created in resists by lithographic processes. For example, the diameter of a molecule of 10,000-amu molecular weight has been estimated to be approximately 3 nm.[26] Creating resists from molecules of that size leads to textured surfaces in resist patterns, although this may be mitigated somewhat by conformation changes of the polymers after development. Resists have long consisted of molecules of such sizes, but with a 20-nm half-pitch at the 7-nm node, molecular dimensions are a significant

fraction of nominal size for features of interest for EUV lithography. Although the small sizes of features of interest for EUV lithography has increased the concern over LER, it has been the low power output of EUV light sources that has made the LER problem particularly significant for EUV lithography.

Weak light sources lead to photon shot noise, which is the fluctuation in the number of photons in a beam of light. Photon shot noise results from basic quantum statistics, where the root-mean-square (rms) variation in the number of photons σ_n is related to the average number of photons $\langle n \rangle$ by the following expression:[27]

$$\frac{\sigma_n}{\langle n \rangle} = \frac{1}{\sqrt{\langle n \rangle}}. \tag{5.3}$$

The variability in the number of photons, expressed in Eq. (5.3), can be considered as an effective fluctuation in dose, which in turn can lead to variations in the position of the line-edge on the nanometer scale, i.e., LER. Changes in line-edge positions Δx have long been connected to the aerial image $I(x)$ through the relationship[28]

$$\Delta x = \frac{\Delta E}{E}\left(\frac{1}{I}\frac{dI}{dx}\right)^{-1} \tag{5.4}$$

$$= \frac{1}{NIS}\frac{\Delta E}{E}, \tag{5.5}$$

where $\Delta E/E$ is the fractional change in the dose E, and NIS is the normalized image-slope. If photon shot noise is considered as an effective fluctuation in dose (ΔE), the edge of the resist feature will vary according to Eqs. (5.4) and (5.5). From these equations it can also be seen that a larger edge acuity can reduce the impact of photon shot noise on LER.

Photon shot noise also appears to be more significant for EUV than for optical lithography, because it is typical in lithography to characterize the intensity of light beams in units of mJ/cm^2. The energy E of a single photon of wavelength λ is

$$E = hc/\lambda, \tag{5.6}$$

which equals 1.471×10^{-14} mJ for an EUV photon. If the energy of a beam is 10 mJ/cm^2, the number of photons that would pass through a 1 cm $\times$ 1 cm cross-sectional area is 6.8×10^{14}. However, in lithography, areas of interest are much smaller. For example, the number of EUV photons passing through a 2 nm $\times$ 2 nm cross-sectional area is only ~27 for a 10 mJ/cm^2 dose. Thinking of this from a lithographic perspective, it means that the exposure

dose that goes into a 2 nm $\times$ 2.nm $\times$ t volume, where t is the resist thickness, fluctuates:

$$\frac{\sigma_n}{\langle n \rangle} = \frac{1}{\sqrt{27}} = 0.19. \tag{5.7}$$

This is a very large dose fluctuation, and it is the reason that photon shot noise is a significant contributor to LER in EUV lithography.

Because exposure doses are typically measured in units of mJ/cm^2, photon beams with highly energetic photons have fewer photons per mJ/cm^2 compared to beams of less energetic photons. Since photon energy scales inversely with wavelength, a beam of ArF light will have 193/13.5 $\approx$ 14 times more photons for a given energy per unit area, than a beam of EUV light (see Fig. 5.4). As can be seen in Fig. 5.4, EUV photons are absorbed sparsely at a dose of 10 mJ/cm^2. With large spaces between exposed portions of the resist, roughness results.

In addition to photon shot noise, there are many other components of the lithographic process that fluctuate. Many of these mechanisms have always existed in lithographic processes, but they have become significant after decades of scaling. For example, LER = 8 nm is 3.2% of a 250-nm feature, while a much smaller LER = 4 nm is 20% of 20-nm features in technologies where EUV lithography was first used for HVM. At the level of 3.2%, it was a curiosity, and it had a small (though non-negligible) impact on device performance, while 20% is quite significant.

Another way to look at this is by considering the length scales. Carbon–carbon bond lengths are ~0.14 nm, which is 0.7% of 20 nm, while molecules, even small ones, are a much greater percentage (see Fig. 5.5).

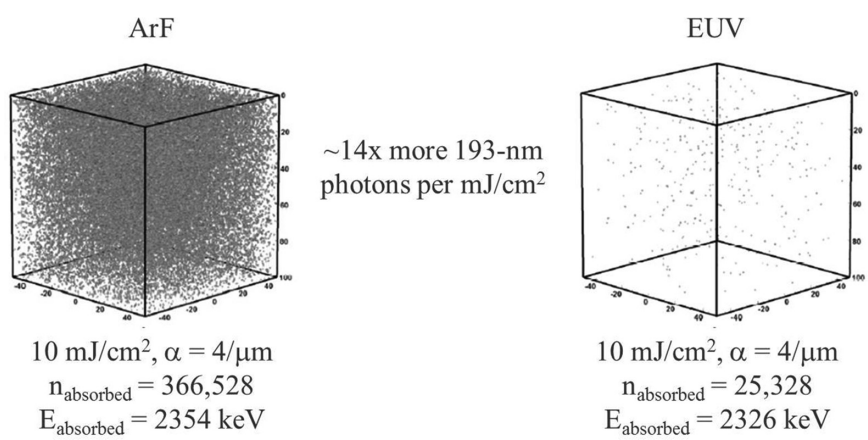

Figure 5.4 Results of a Monte Carlo simulation of absorbed photons, assuming equivalent absorption and dose between ArF and EUV exposures.[29] The sparser absorption sites for EUV lithography result in higher LER than for ArF lithography.

Achieving LER of a few percent of 20-nm critical dimensions requires considerations at the molecular level.

Sources of LER other than photon shot noise also became recognized when researchers looked at plots of LER versus exposure dose (Fig. 5.6). If the only source of LER is photon shot noise, then LER should be proportional to $1/\sqrt{dose}$. As can be seen in Fig. 5.6, this proportionality

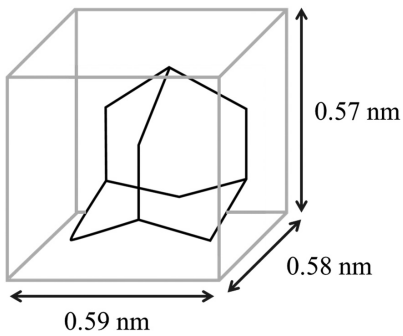

Figure 5.5 Illustration of the finite size of molecules. The molecule in this figure is adamantane, which is often found in chemically amplified resists to improve etch resistance.[30]

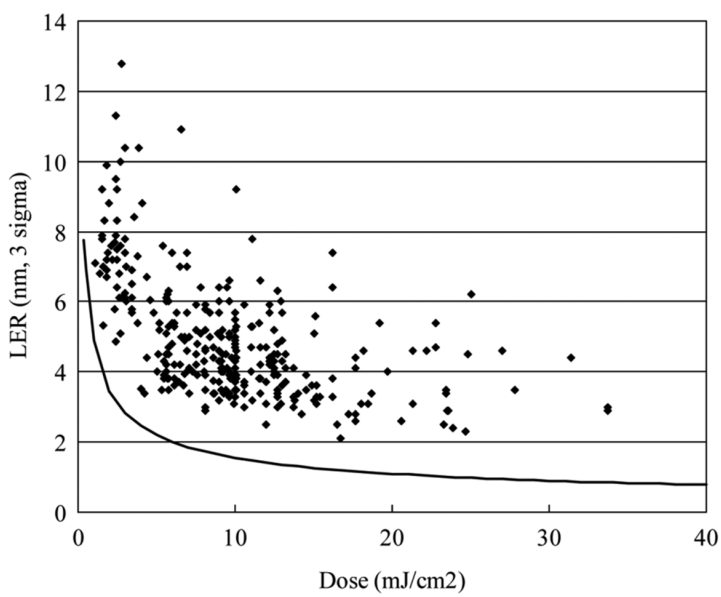

Figure 5.6 Line-edge roughness vs. exposure dose for various EUV resists exposed on a 0.3-NA microexposure tool at Lawrence Berkeley National Laboratory. The diamonds are measured results for individual resists[17] and corrected for mask absorber and multilayer-roughness contributions to LER,[31] while the solid curve was produced by a model of LER resulting purely from shot noise.

appears to be the case at low doses, but at higher doses the actual LER reaches a floor and does not decrease below a certain level. This suggests that LER is dominated by photon shot noise at low doses, while other mechanisms become significant at high doses, where the photon shot noise becomes small.

In recent years, factors that contribute to LER, in addition to photon shot noise, have been included in lithographic models, both analytical ones and Monte Carlo simulations. A number of such contributors for chemically amplified resists are listed in Table 5.1. In various modeling exercises, sometimes only a subset of the parameters in Table 5.1 are actually varied statistically. For example, photoacid diffusion is often considered as an overall blur rather than a true random walk. Nevertheless, such simulations have provided useful insight and learning, even though incomplete. Statistical resist models are available in commercially available simulation packages, such as Prolith[29] and Sentaurus Lithography (S-Litho).[32]

At the molecular level, components in resist, such as photoacid generators and base quenchers, are not distributed uniformly. With a high loading of photoacid generators (PAGs), the mean spacing between PAGs is ~1.7 nm, which sets a scale on which LER can occur. Variation results from simple statistical fluctuation in the spacings between PAG molecules (Fig. 5.7), which increases LER. Moreover, both aggregation and segregation (Fig. 5.8) in chemically amplified resists has been observed. Aggregation is the tendency for molecular constituents of resists to form clusters, while segregation involves gradients in the local densities of components. Because of their polar character, photoacid generators are particularly susceptible to aggregation (Fig. 5.9).

PAG aggregation in chemically amplified resists has been observed experimentally with massive-cluster secondary ion mass spectroscopy,[33] where resist films were bombarded with clusters of gold atoms (see Fig. 5.10). When

Table 5.1 Factors that vary statistically in chemically amplified resists.

Photon shot noise
Photon absorption
Photoacid generator concentration/distribution
Quencher concentration/distribution
Electron scattering, elastic and inelastic
Photoacid generation
Quencher decomposition
Photoacid diffusion
Quencher diffusion
Deprotection reactions

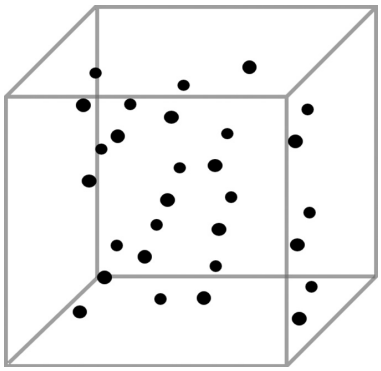

Figure 5.7 Illustration of the nonuniform distribution of the constituents of multi-component resists.

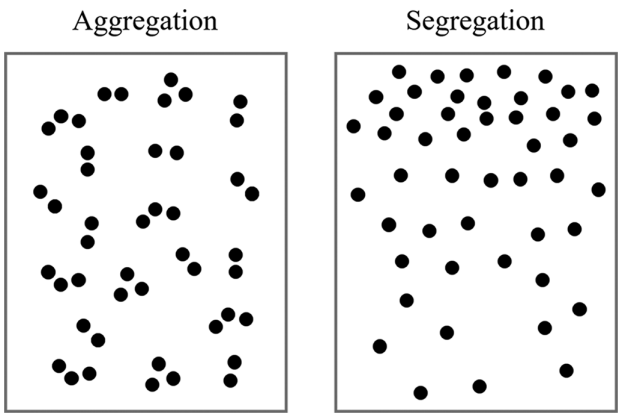

Figure 5.8 Illustration of aggregation and segregation in resists.

PAG molecules are distributed uniformly, a low level is expected of events in which multiple PAG molecules are detected in the emission from the sputtered films. However, a significant number of PAG–PAG co-emission events were observed, indicating aggregation. Modeling has shown that aggregation increases LER.[34] As a consequence, photoacid generators are often bonded to resist polymers, which suppresses aggregation and reduces LER.[35]

It was long speculated that segregation occurs in chemically amplified resists because of characteristics observed in patterned thin resist films. There is typically 10–15 nm of top loss in line/space patterns, suggesting a higher concentration of PAGs in the top of the resist, an hypothesis found to be consistent with modeling.[36] Moreover, a large increase in LER was observed as resist films became very thin.[37] The situation involving patterning of resist films during wafer processing can be further complicated by the substrate, which can be a source of amines that deplete photoacids at the bottom of resist films. Recently, there have been measurements of segregation in a

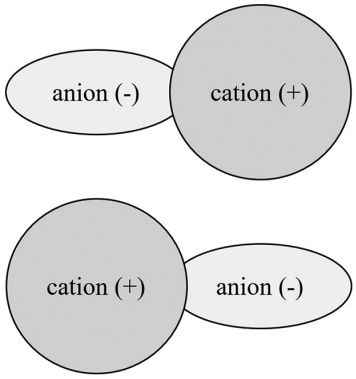

Figure 5.9 The polar characteristic of photoacid generators that can lead to aggregation.

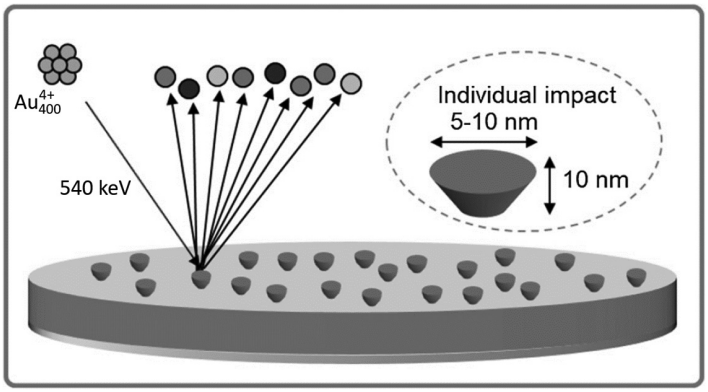

Figure 5.10 Massive-cluster secondary ion mass spectroscopy.[33]

chemically amplified resist, immediately after coating, in the direction perpendicular to the wafer surface using resonant soft x-ray reflectivity.[38,39] Good fits to data could not be obtained assuming a single film of uniform composition, nor with a two-film assumption, but good fits were achieved by using a three-layer model (Fig. 5.11). This indicates material segregation, particularly at the top and bottom of the resist film.

Optical absorption is a phenomenon that can also affect the distribution of photoacids after exposure. For resists in which components are distributed uniformly, more photo-initiated events will take place at the top of the resist, because the light is attenuated as it propagates from the top to the bottom of the resist film.

Optical absorption also has an impact on stochastic effects. Consider an exposure of energy E_0. The amount of light energy absorbed by a resist film of thickness T is

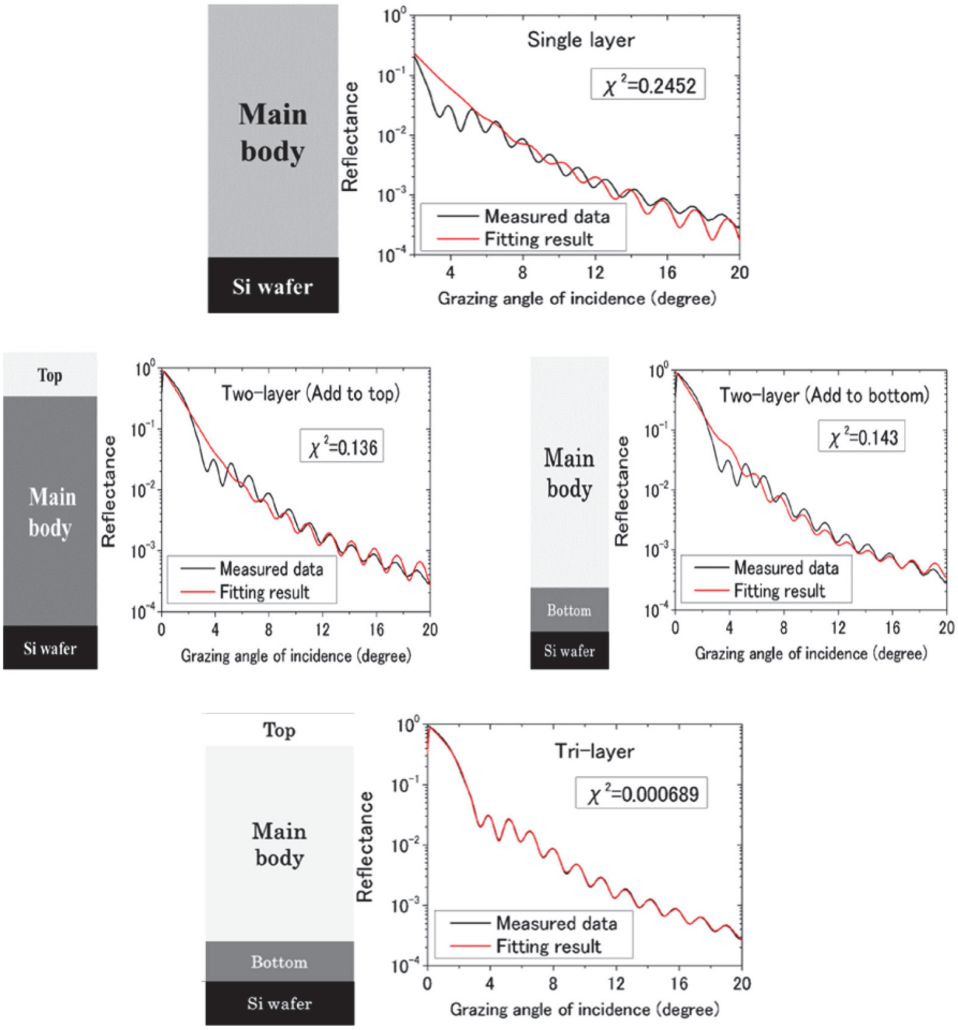

Figure 5.11 Measurements using resonant soft x-ray reflectivity. Good fits to the data could not be obtained when it was assumed that the resist film comprises only one or two layers.[39]

$$E_0\left(1 - e^{-\alpha T}\right) = E_0\left(\alpha T - \frac{1}{2}(\alpha T)^2 + \ldots\right). \tag{5.8}$$

Considering Eq. (5.9) to first order, there is a direct trade-off between the exposure dose and the absorptivity of the resist. While the detailed relationship among exposure dose, absorption, and stochastics is generally complex, Eq. (5.8) indicates that the impact of photon shot noise can be offset by increasing the absorption by the resist.

The solubility of chemically amplified resists depends on the density of photoacids, which will fluctuate roughly in proportion to

$$\frac{1}{\sqrt{\langle n_{photoelectrons} \rangle}}, \tag{5.9}$$

where $n_{photoelectrons}$ is the density of photoelectron generation. This photoelectron density depends upon both the photon flux and absorption, with statistical variations reduced by increasing the optical absorption of the resist materials. This enables LER to be reduced without simply increasing the exposure dose. Consequently, it is beneficial to use elements with high optical absorption at $\lambda = 13.5$ nm for the formulation of EUV resists. As can be seen in Fig. 1.3, certain metals and iodine have high absorption at EUV wavelengths, so they are good candidates for use in EUV resists.

Increasing the optical absorption of EUV resist needs to be done with care. If highly absorbing components are added but dispersed sparsely throughout the resist film, the net result will be centers of high optical absorption that are widely separated. This will increase stochastic variation. On the other hand, incorporating elements that strongly absorb EUV light and having them distributed evenly throughout the resist film will reduce stochastic effect. This is another example where EUV resists need to be considered at molecular scale.

In the early days of EUV lithography development, low optical absorption was considered desirable for EUV resists, since high absorption can lead to sloped sidewalls of developed resist features. This concern changed, as the target node for introduction of EUV lithography into HVM shifted from the 45 nm node to the 7 nm node. With smaller feature sizes, the resist was thinned to avoid pattern collapse. For the resist to continue to absorb the same fraction of incident light, the absorption of the resist necessarily needed to increase. With scaling, LER increasingly became a concern, which provided additional motivation to increase the absorptivity of the resist.

In addition to roughness, stochastic effects can induce defects, examples of which are shown in Fig. 5.12. Such defects limit lithographic capability. For example, 36-nm pitch represents at k_1 of 0.44 for $NA = 0.33$, which is high by the standards of optical lithography, but considerable work was required to yield line/space patterns at that pitch.

One of the reasons that stochastic defects limit lithographic capability so significantly is the exponential dependence of defect density on feature size, shown in Fig. 5.13. As the average dimension gets smaller by only a few nanometers, the defect density increases by several orders of magnitude. With advanced logic circuits, the defect density required to yield complex logic circuits is very low. For example, consider AMD's Ryzen 9 3900X microprocessor, which has ~9.9 billion transistors. With typically three

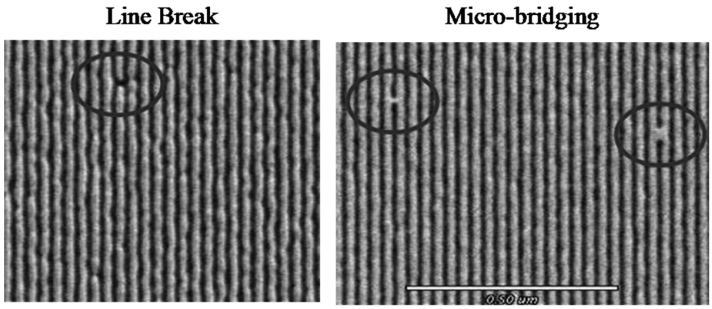

Figure 5.12 Stochastics-induced defects in 30-nm-pitch lines and spaces, patterned using EUV lithography.[40]

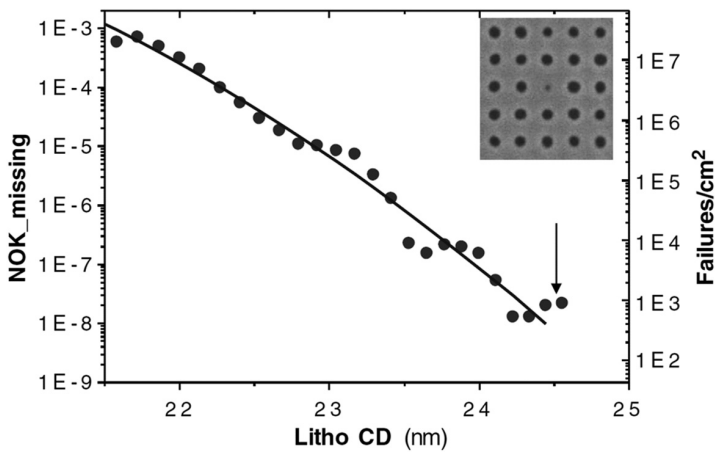

Figure 5.13 Changes in defect density (right vertical axis) as a function of contact size for contacts on a 48-nm pitch.[41] The metric NOK_missing is the ratio of closed (plus nearly closed) contacts to the total number measured. The circular markers represent measurements on the wafer after etch, although the CDs are post-lithography. The solid line is a fit of the data to $\log_{10}(\text{NOK}) = a + b\text{CD} + c\text{CD}^2$.

contacts per transistor, the contact failure rate required to yield such a microprocessor is $<3 \times 10^{-11}$. As will be discussed in Chapter 7, stochastic defects have a significant impact on process control considerations.

Insight into the exponential dependence of defect density on feature size has been provided by Dr. Hiroshi Fukuda, who noted that photoelectron and secondary electron trajectories can align towards a single direction, rather than have scattering localized around the point of initial photoexcitation (Fig. 5.14).[72,73,74,75] There are similar considerations for photoacid diffusion. If the probability of an electron scattering (or a photoacid diffusing) in a certain direction is p, then the probability of scattering in N sequential steps is p^N. If Δx is the average distance for a single scattering event, then the probability to travel a distance x is

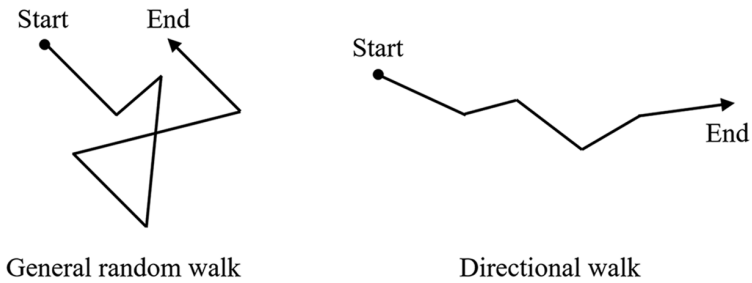

Figure 5.14 Different types of scattering events. Sequential scattering events and diffusion that go towards one direction can lead to defects.

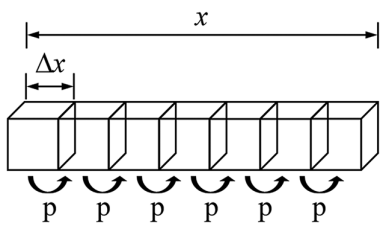

Figure 5.15 Scattering or diffusion towards a single direction.

$$p^N = p^{x/\Delta x} \tag{5.10}$$

(see Fig. 5.15). This is a quantity that varies exponentially with distance. When events such as electron scattering and photoacid diffusion extend across a line, a defect can be generated. For example, along a directional walk in a positive resist, a path of deprotected polymer will be generated, leading to a line break.

The addition of stochastic phenomena as sources of defects increases the complexity of defect reduction, since it makes identifying the origin of defects more difficult. Many types of defects that arise in resist processing, such as residues left on wafer following develop and rinse, as well as particles in the resist, occur with EUV resists, and reducing these types of defects requires that they be distinguished from defects resulting from stochastic effects. It has been noted that stochastics-induced defects are of very small size and almost always affect only a single feature.[42] Hence, defects that involve multiple line bridges or multiple closed holes are indicative of defects with origins other than resist stochastics. This will be discussed in more detail in Chapter 7.

Attempts have been made to understand what fraction of LER is due to photon shot noise and what amount is due to the resist materials.[43,44] Much depends on the exposure dose. As noted previously, LER is dominated by photon shot noise at low doses, but resist materials contribute substantially to LER at high exposure doses. In one interesting set of simulations, effects from aerial image profiles were eliminated by using a step-function aerial

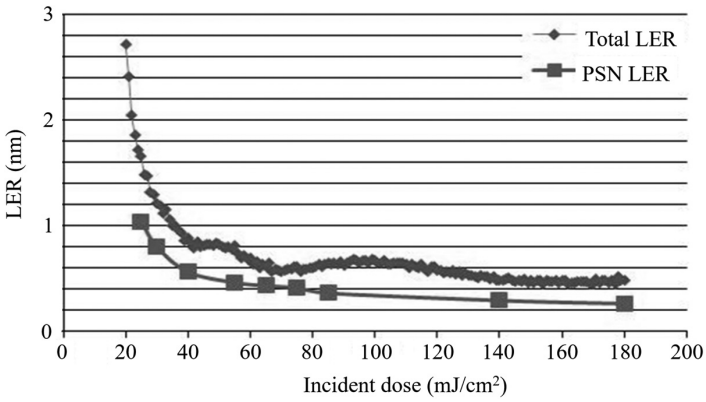

Figure 5.16 LER from simulations using an infinitely sharp aerial image.[43] Plotted are the total LER and the LER resulting only from photon shot noise (PSN). The nonmonotonic behavior is due to statistical noise resulting from a finite number of simulations for each dose.

image. Although such an aerial image is physically unrealizable, it could be adopted in simulations. Even with an infinitely sharp aerial image, LER that varied with exposure dose was observed in the simulations. As can be seen in Fig. 5.16, even at the highest doses, the LER due to photon shot noise is comparable to that from other contributions, at least within the dose range shown. Material optimization is also important. Reduction of photon shot noise does not necessarily ensure low LER.

The negative resist behavior shown in Fig. 5.2 may become a complication at higher doses, offsetting the reduction of photon shot noise, although such behavior may not be characteristic of all resist chemical platforms. It could be that such negative resist behavior is occurring in some resists at lower doses, with photon shot noise creating localized regions of high dose, resulting in micro-bridges.

5.3 New Concepts for Chemically Amplified Resists

Because of the problems described in the previous section, alternatives to conventional chemically amplified resists are being explored for EUV lithography. The objective is to create resists that meet dimensional uniformity and LER requirements, while avoiding extremely high exposure doses. Some of these alternative concepts still involve chemical amplification, and these are discussed in this section.

One new concept that that has been explored involves multitrigger resists.[45] This is illustrated in Fig. 5.17. With traditional chemically amplified resists, the photoacid generator directly produces photoacids when induced by electrons created through EUV exposure. In multi-trigger resists, there are two components that undergo radiation-induced chemical reactions. The by-products of this radiation chemistry, by themselves, do not cause

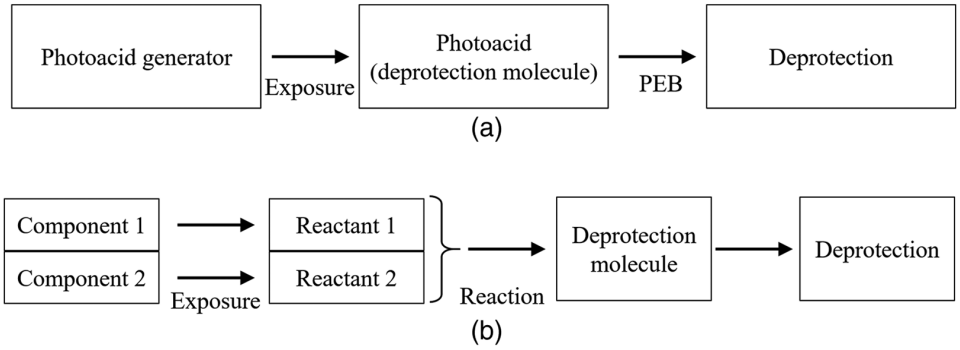

Figure 5.17 (a) Exposure and reaction path for traditional chemically amplified resists; (b) Exposure and reaction path for multitrigger resists. In areas of high exposure, reactants 1 and 2 will combine, while they will be too far apart for this to occur in areas of low exposure.

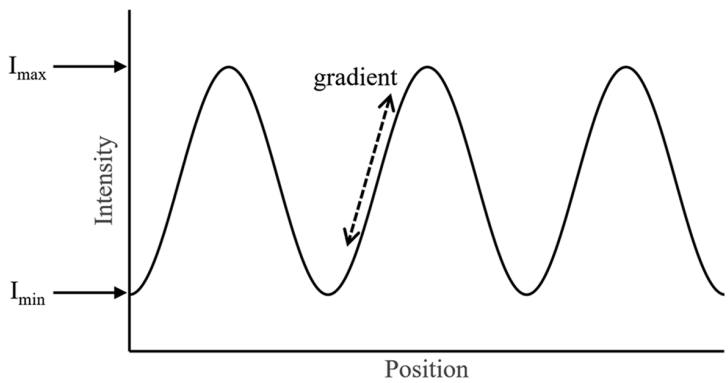

Figure 5.18 Illustration of contrast in an aerial image.

deprotection in the resist. However, if densities are high enough, these two by-products react with each other to create the molecules that will ultimately cause deprotection.

One characteristic of multitrigger resists is that they have high contrast (Fig. 5.18), defined as

$$\text{contrast} = \frac{I_{\max} - I_{\min}}{I_{\max} + I_{\min}}. \tag{5.11}$$

Many years ago, contrast was replaced as an important characteristic of aerial images and chemical profiles with gradient metrics predominately. While gradients are important, the consequences of inadequate contrast can be seen in Fig. 5.12. A large value for $I_{\min}$ increases the likelihood of line breaks (for positive resists), since there is higher probability that the threshold dose will be exceeded locally, due to photon shot noise, in portions of resist that are meant to be retained after develop.

Pattern exposure	PAG	----------→	acid
	PDB	----------→	deactivated
	PP	----------→	PP
	polymer	----------→	polymer
1st post-exposure bake	PAG	----------→	PAG
	acid + PDB	----------→	PAG
	acid + PP	----------→	photosensitizer + acid
	acid + polymer	----------→	deprotected polymer + acid
Ultraviolet flood exposure	photosensitizer + PAG	----------→	photosensitizer + acid
	photosensitizer + PDB	----------→	photosensitizer
	PP	----------→	PP
	polymer	----------→	polymer
2nd post-exposure bake	PAG	----------→	PAG
	acid + PDB	----------→	PAG
	acid + PP	----------→	photosensitizer + acid
	acid + polymer	----------→	deprotected polymer + acid

Figure 5.19 Outline of PSCAR process, showing the significant reactants and by-products.[48] The following acronyms are used: photoacid generator (PAG), photodecomposable base (PDB), and photosensitizer precursor (PP).

Another new concept is *Photo-Sensitized Chemically Amplified Resist*™ (PSCAR™).[46,47] In this approach, the number of photoacids in the exposed areas is increased in a way that provides a sharper image than would be obtained by simply increasing the amount of photoacid generator in the resist. This is accomplished by adding a component, a photosensitive precursor, to the resist. The PSCAR process is outlined in Fig. 5.19. During the exposure step, the PSCAR resist behaves in the same way as a conventional chemically amplified resist: photoacid generators (PAGs) are converted to photoacids, and the photodecomposable bases (PDBs) are effectively neutralized.

There are two post-exposure bake steps. During the first post-exposure bake, there is some polymer deprotection, and, importantly, photodecomposable bases (primarily in the unexposed areas) neutralize acids and sharpen the chemical distribution of the acids. Also during this first post-exposure bake, the photosensitive precursors are converted to photosensitizers by the acids. Hence, the distribution of photosensitizers follows the partially sharpened distribution of acids.

Then follows an ultraviolet (UV) flood exposure step at a sufficiently long wavelength (350–420 nm) that the PAGs do not respond photochemically to the light. Flood exposure modules providing uniform UV light are available from Tokyo Electron, so the entire process can be done in a continuous flow when using resist processing equipment from this supplier. In the flood exposure step, the photosensitizers react with the remaining PAGs and

thereby create more photoacids. This process essentially amplifies the photoacids, and it does this preferentially in regions of high exposure. The net results are steeper acid chemical gradients and higher chemical contrast. As discussed previously, higher contrast is useful to reduce stochastics-induced defects. Note that the additional photoacids are generated using inexpensive ultraviolet photons instead of expensive EUV photons.

The PSCAR process does require the addition of another chemical component, which can potentially increase the contribution of resist chemical stochastics to LER. Further development work will confirm if the improvement in chemical contrast will offset the increased stochastics due to additional components in the resist.

5.4 Metal-Oxide EUV Resists

Because of the many issues associated with chemically amplified resists, resists based on different types of radiation chemistry are being considered. One class of new resists, based on metal oxides, has received significant attention. Such resists have metal oxide cores with organic ligands attached. Secondary electrons or photons directly convert these ligands to active sites, thereby enabling two adjacent cores to bond chemically (Fig. 5.20). Eventually, a network of bonded products is formed that isn't soluble in organic solvents. This is clearly a negative resist, so it is not well suited for imaging contacts and vias, but there is considerable interest in using such resists for line and space patterns. For the metal in the core, tin is often used,[49] but zirconium and hafnium have also been considered.[50] Such metals have high optical absorption (Fig. 1.3), which is an advantageous characteristic. The incorporation of metals into the resist formulation may also decrease electron scattering mean free paths, thereby reducing image blur by the electrons and also reducing stochastic defects due to the mechanisms described in Section 5.2.

Incorporating metals is helpful for etch selectivity. However, such high selectivity can be a source of defects, since very small amounts of residual resist that does not dissolve in developer can inhibit etch. Higher levels of defects are seen after etch in metal-oxide resists than post-develop, and this has delayed the use of this class of resists in high-volume manufacturing.

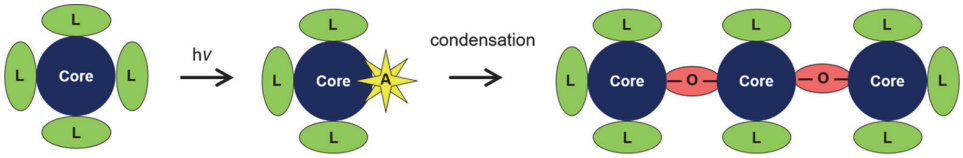

Figure 5.20 Illustration of the condensation mechanism of metal-oxide resists.[51]

In one study, measurements of overlay were high when metal-oxide resists were used, in comparison to the situation where chemically amplified resists were used.[52] It was determined that grains had formed in the patterned metal-oxide resists, which led to noise in the optical overlay measurements.

5.5 Scissioning Resists

Another class of positive resists is based on the physical mechanism of polymer chain scissioning by high-energy radiation, whereby high-molecular-weight polymers are converted to small molecules that are more soluble in developers. The most commonly used resist in this class is poly (methyl methacrylate) (PMMA). PMMA has not been used in HVM, because it is very insensitive and has poor plasma etch resistance, but it provides good resolution. making it useful for exploratory studies in lithography.

Since it has been recognized that exposures in EUV resists are mediated by electrons, it seems reasonable to consider modifying electron-beam (e-beam) resists for use in EUV lithography, and this has been done with a scissioning e-beam resist. While e-beam resists are frequently chemically amplified platforms, Nippon Zeon produces a positive-tone e-beam resist, ZEP520A,[53] that consists of copolymers made up of acrylate and styrene monomers (Fig. 5.21). Under exposure to radiation, these copolymers undergo scissioning, which alters the material's solubility in organic solvent developers. The use of styrene monomers also improves etch resistance. This e-beam resist has been modified for use in EUV lithography.[54] Because these scissioning resists have few components, there is potential for less stochastic variation at the molecular level.

5.6 Vacuum-Deposited Resists

Recently, patterns have been created in EUV resists deposited by chemical vapor deposition (CVD) and developed using dry methods.[55] Such resist processes have potential advantages, such as much lower susceptibility to

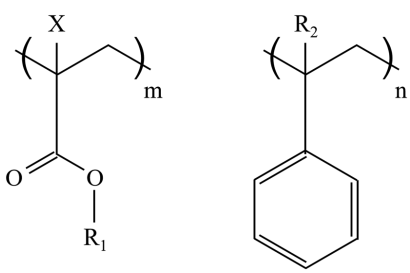

Figure 5.21 Chemical structure of the two polymers forming ZEP520A resist.[53] The polymer on the left side of the figure is acrylate based, while that on the right side is styrene based.

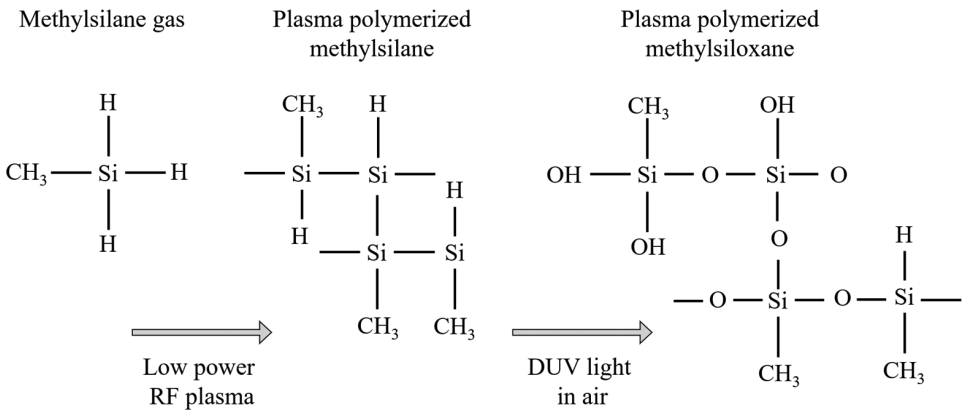

Figure 5.22 Outline of the process for an organo-silicon-based vacuum-deposited resist process.[56]

pattern collapse following resist develop, and vacuum deposition may lead to more homogeneous resist films on wafers than achieved by spin coating. Dry resist processes, based primarily on organo-silicon[56,57] or chalcogenide chemistries,[58,59] have been explored in the past, but such resists have been used to only a limited degree, such as where conformal coating of the resist over substantial topography—something difficult to achieve with spin-coating—is needed.[60] However, with the resolution and LER limitations of other types of EUV resists, deposited resists are being revisited.

The chemistry of an earlier vacuum-deposited resist, based on organo-silicon chemistry and intended for use with DUV exposures, is illustrated below (Fig. 5.22). Such resists were negative tone, and the resulting oxide formation required the presence of oxygen and/or water. Dry develop was possible using halogen chemistries, providing selectivity between a resist that has incorporated oxygen and one that has not. Adapting this approach to EUV lithography, involving an oxidation step, would require careful introduction of gases into the exposure systems, or it could perhaps rely on activation of the resist during exposure, with oxidation occurring in a subsequent step, outside of the exposure chamber.

More recently, results have been presented on EUV exposures of vacuum-deposited resists.[55] Although specific constituents of these EUV deposited resists have not yet been published or presented, from moderate-exposure doses (35–50 mJ/cm^2) it can be inferred that an element that is highly optically absorbing at EUV wavelengths (Fig. 1.3) is a constituent (see Fig. 5.23).

5.7 Underlayers

The patterning of semiconductor devices using optical lithography has long involved complex stacks comprising multiple layers, including planarizing

	32 nm pitch		26 nm pitch	
Develop	Wet	Dry	Wet	Dry
Dose (mJ/cm^2)	47	42	39	39
EL_{max}(%)	24	35	20	26
LWR (nm)	3.4	3.0	2.9	3.0
Z-factor (10^{-8} mJ/nm^3)	2.3	1.6	0.72	0.77
CD (nm)	16.3	16.1	13.1	12.9
	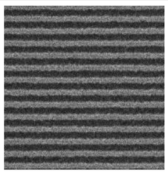	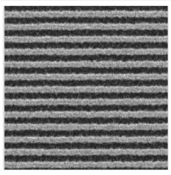	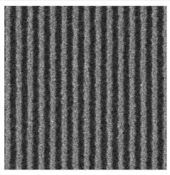	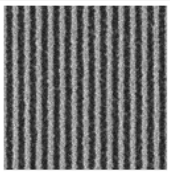

Figure 5.23 Patterns formed in 20-nm-thick resists that were vacuum deposited on a spin-on carbon underlayer and exposed on a 0.33-NA NXE:3400.[55] The exposure latitude (EL) is for ±10% critical dimension control. note that the 32-nm pitch and 26-nm pitch are for different orientations, so the impact of mask 3D effects is different (see Chapter 6).

films and anti-reflection coatings. For EUV lithography, there is typically very little reflection from the layers under the resist, so antireflection coatings are not needed for EUV lithography. (Only carefully engineered film stacks, such as the Mo/Si multilayer reflectors used on EUV masks and optics, have appreciable reflectance at EUV wavelengths.) However, it has been recognized that the films immediately under the resist do affect the patterning in significant ways. For example, chemically amplified resists used for EUV lithography are susceptible to amine poisoning, as was found earlier for DUV lithography. Consequently, it is important that the film immediately under the resist not be a source of amines, and it may even need to serve as an impermeable chemical barrier to contamination from films below. The degree to which underlayers are sources of bases or acids can affect the exposure dose, and the dose-to-size ratio has been found to be dependent on underlayer material composition.[61,62,63] Even HMDS (hexamethyldisilazane)[17] priming has been found to reduce the develop rate of resist near the substrate.[64] The level of stochastics-induced defects is also dependent on the underlayer (see Fig. 5.24).

As described above, photoacid generators can segregate during the spin-coating process.[36] If this segregation results in a layer of resist depleted of PAG molecules near the resist/substrate interface, scumming will occur after develop.[62] The degree to which this happens is dependent on the energetics of the interactions between PAG molecules and the substrate, which can vary widely through ranges of PAGs and substrates.[61] This implies that the engineering of EUV resist processes requires a co-optimization of resist materials and substrates, greatly increasing the complexity of process development.

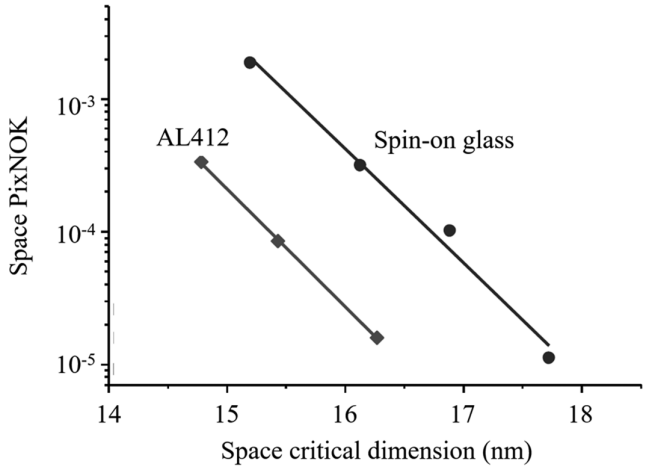

Figure 5.24 Variations in the metric for micro-bridges, PixNOK, as a function of space dimensions for 36-nm-pitch patterns of a positive, chemically amplified resist patterned on two different types of substrates.[41] AL412 is a spin-on underlayer that is commercially available from Brewer Science.[65]

In the past, measures of line-edge roughness often showed a substantial dependence on the substrates. It was eventually recognized that SEM measurement noise contributed significantly to these apparent variations in measured roughness. Using methods that address the issue of SEM noise enable a proper interpretation of the substrate-dependence of LER, a factor that continues to be seen, albeit with smaller ranges than seen previously.[66,67]

It is essential that resists adhere well to the substrate. In addition to addressing traditional concerns related to adhesion, such as undercut during etch, it has been found that improved adhesion reduces pattern collapse, which is very relevant for EUV lithography.

It has also been found that the composition of spin-on-carbon used under metal-oxide resist films has a significant impact on defect levels after etch.[68] This is due, in large measure, to the large differences in etch rates between organic materials and the inorganic compounds of the resist. For metal-oxide resists, it is essential to avoid the chemical reaction or adsorption of metal-containing compounds to underlayers in exposed regions, since even a very small amount of residual resist can block the etch of underlayers.

It has been proposed to incorporate elements that are highly absorbing at EUV wavelengths into the film immediately below the resist (Fig. 5.25), the idea being that photoelectrons or secondary electrons from the underlayer will propagate into the bottom of the resist film, leveling the gradients in chemical reactions between the top and bottom of exposed resist.[69,70] However, the benefits of this approach are limited to the bottom few nanometers of the resist film, because of short mean free paths for electrons. Incorporating photoacid generators and EUV sensitizers into the underlay is another

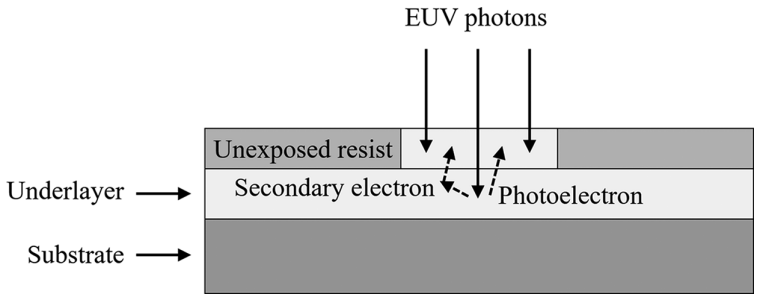

Figure 5.25 Photoelectrons and secondary electrons generated in the underlayer propagating into the resist film.

method for harvesting EUV photons.[71] This approach also benefits from high optical absorption in the underlayer.

Problems

5.1 Assume that the edge position x of a developed line/space pattern in resist of thickness T occurs when the total light energy that reaches the bottom of the resist is E_0. Ignoring the effects of resist bleaching during exposure, show that the position of the resist moves to $x + \Delta x$ according to

$$\Delta x = \frac{1}{NIS}\alpha\Delta T, \tag{5.12}$$

where $NIS = \frac{1}{E_0}\frac{dE}{dx}$, and α is the absorption coefficient of the resist.

References

1 U. Okoroanyanwu, "Resist road to the 22 nm node," *Future Fab Int.* **17** (2004).
2 J. F. Cameron, N. Chan, K. Moore, and G. Pohlers, "Comparison of acid generating efficiencies in 248 and 193 nm photoresists," *Proc. SPIE* **4345**, pp. 106–118 (2001).
3 R. L. Brainard, C. Henderson, J. Cobb, V. Rao, J. F. Mackevich, U. Okoroanyanwu, S. Gunn, J. Chambers, and S. Connolly, "Comparison of the lithographic properties of positive resists upon exposure to deep- and extreme-ultraviolet radiation," *J. Vac. Sci. Technol. B* **17**(6), pp. 3384–3389 (1999).
4 R. L. Brainard, G.G. Barclay, E.H. Anderson, and L.E. Ocola, "Resists for next-generation lithography," *Microelectron. Eng.* 61–62, pp. 707–715 (2002).
5 T. Kozawa, Y. Yoshida, M. Uesaka, and S. Tagawa, "Study of radiation induced reactions in chemically amplified resists for electron beam and x-ray lithography," *Jpn. J. Appl. Phys.* **31**, pp. L1574–L1576 (1992).

6 R. Brainard, E. Hassanein, J. Li, P. Pathak, B. Thiel, F. Cerrina, R. Moore, M. Rodriguez, B. Yakshinskiy, E. Loginova, T. Madey, R. Matyi, M. Malloy, A. Rudack, P. Naulleau, A. Wüest, and K. Dean, "Photons, electrons, and acid yields in EUV photoresists: a progress report," *Proc. SPIE* **6932**, 693215 (2008).
7 T. Kozawa, S. Tagawa, H.B. Cao, H. Deng, and M.J. Leeson, "Acid distribution in chemically amplified extreme ultraviolet resist," *J. Vac. Sci. Technol. B* **25**(6), pp. 2481–2485 (2007).
8 Kozawa, Takahiro, and Seiichi Tagawa. "Radiation chemistry in chemically amplified resists." *Japanese Journal of Applied Physics* **49**, no. 3R (2010): 030001.
9 R.L. Brainard, P. Trefonas, J.H. Lammers, C.A. Cutler, J.F. Mackevich, A. Trefonas, and S.W. Robertson, "Shot noise, LER and quantum efficiency of EUV photoresists," *Proc. SPIE* **5374**, pp. 74–85 (2004).
10 S. Tanuma, C.J. Powell, and D.R. Penn, "Calculations of electron inelastic mean free paths V: data for 14 organic compounds over the 50-2000 eV range," *Surf. Interface Anal.* **21**, pp. 165–176 (1994).
11 P. Pianetta in X-Ray Data Booklet, https://xdb.lbl.gov/xdb-new.pdf
12 S. Grzeskowiak, J. Kaminsky, S. Gibbons, A. Narasimhan, R. L. Brainard, and G. Denbeaux. "Electron trapping: a mechanism for acid production in extreme ultraviolet photoresists." *Journal of Micro/Nanolithography, MEMS, and MOEMS* **17**, no. 3 (2018): 033501.
13 I. Pollentier, Y. Vesters, J. Jiang, P. Vanelderen, and D. de Simone. "Unraveling the role of secondary electrons upon their interaction with photoresist during EUV exposure," *Proc. SPIE* Vol. **10450**, p. 104500H (2017).
14 O. Yildirim, E. Buitrago, R. Hoefnagels, M. Meeuwissen, S. Wuister, G. Rispens, A. van Oosten, et al. "Improvements in resist performance towards EUV HVM," *Proc. SPIE* Vol. **10143**, p. 101430Q (2017).
15 I. Pollentier, Y. Vesters, J. Jiang, P. Vanelderen, and D. de Simone. "Unraveling the role of secondary electrons upon their interaction with photoresist during EUV exposure," *Proc. SPIE* **10450**, p. 104500H, 2017.
16 P. De Bisschop, "Stochastic effects in EUV lithography: random, local CD variability, and printing failures." *Journal of Micro/Nanolithography, MEMS, and MOEMS* **16**, no. 4 (2017): 041013.
17 H. J. Levinson, *Principles of Lithography*, 4th Edition, SPIE Press, 2019.
18 T. I Wallow, R. Kim, B. La Fontaine, P. P. Naulleau, C. N. Anderson, and R. L. Sandberg. "Progress in EUV photoresist technology," *Proc. 23rd European Mask and Lithography Conference*, pp. 1–9. VDE, 2007.
19 J. W. Thackeray, R. A. Nassar, R. Brainard, D. Goldfarb, T. Wallow, Y. Wei, J. Mackey, P. Naulleau, B. Pierson, and H. H. Solak. "Chemically amplified resists resolving 25 nm 1: 1 line: space features with EUV lithography," *Proc. SPIE* **6517**, p. 651719, 2007.

20 T. Kozawa, S. Tagawa, J. Joseph Santillan, and T. Itani. "Quencher effects at 22 nm pattern formation in chemically amplified resists," *Japanese Journal of Applied Physics* **47**, no. 7R (2008): 5404.
21 S. C. Palmateer, S. G. Cann, J. E. Curtin, S. P. Doran, L. M. Eriksen, A. R. Forte, R. R. Kunz, T. M. Lyszczarz, M. B. Stern, and C. M. Nelson-Thomas. "Line-edge roughness in sub-0.18-um resist patterns," *Proc. SPIE* **3333**, pp. 634–642, 1998.
22 T. Azuma, K. Chiba, M. Imabeppu, D. Kawamura, and Y. Onishi, "Line-edge roughness of chemically amplified resists," *Proc. SPIE* **3999**, pp. 264–269, 2000.
23 G. M. Gallatin, P. Naulleau, and R. Brainard. "Fundamental limits to EUV photoresist," *Proc. SPIE* **6519**, p. 651911, 2007.
24 T. Wallow, C., R. Brainard, K. Petrillo, W. Montgomery, C. Koay, G. Denbeaux, O. Wood, and Y. Wei, "Evaluation of EUV Resist Materials for use at the 32 nm half-pitch node," *SPIE* **6921** (2008).
25 X. Wang, Z. Tasdemir, I. Mochi, M. Vockenhuber, L. van Lent-Protasova, M. Meeuwissen, R. Custers, G. Rispens, R. Hoefnagels, and Y. Ekinci, "Progress in EUV resists towards high-NA EUV lithography," *Proc. SPIE* **10957**, p. 109570A, 2019.
26 T. Yamaguchi, H. Namatsu, M. Nagase, K. Kurihara, and Y. Kawai, "Line-edge roughness characterized by polymer aggregates in photoresists," *Proc. SPIE* **3678**, pp. 617–624 (1999).
27 F. Reif, *Fundamentals of Statistical and Thermal Physics*, McGraw-Hill, New York (1965).
28 H. J. Levinson and W. H. Arnold. "Focus: the critical parameter for submicron lithography." *Journal of Vacuum Science & Technology B: Microelectronics Processing and Phenomena* **5**, no. 1 (1987): 293–298.
29 J. J. Biafore, M. D. Smith, C. A. Mack, J. W. Thackeray, R. Gronheid, S. A. Robertson, T. Graves, and D. Blankenship. "Statistical simulation of resist at EUV and ArF," *Proc. SPIE* 7273, p. 727343, 2009.
30 S. Takechi, A. Kotachi, K. Nozaki, E. Yano, K. Watanabe, T. Namiki, M. Igarashi, Y. Makino, and M. Takahashi. "Chemically amplified resist compositions and process for the formation of resist patterns," U.S. Patent 6, 329, 125, issued December 11, 2001.
31 Dr. Patrick Naulleau has estimated that 1.43 nm of LER results from the mask absorber LER, and this has been factored out of the data by assuming that the measured LER is the root sum of squares of the mask LER and the LER due to all other factors. It is the LER due to nonmask sources that is plotted. See P.P. Naulleau, D. Niakoula, and G. Zhang, "System-level line-edge roughness limits in extreme ultraviolet lithography," *J. Vac. Sci. Technol. B* **26**(4), pp. 1289–1293 (2008).
32 W. Gao, A. Philippou, U. Klostermann, J. Siebert, V. Philipsen, E. Hendrickx, T. Vandeweyer, and G. Lorusso. "Calibration and

verification of a stochastic model for EUV resist," *Proc. SPIE* 8322, p. 83221D, 2012.

33 X. Hou, M. Li, M. J. Eller, S. V. Verkhoturov, E. A. Schweikert, and P. Trefonas. "Understanding photoacid generator distribution at the nanoscale using massive cluster secondary ion mass spectrometry." *Journal of Micro/Nanolithography, MEMS, and MOEMS* **18**, no. 3 (2019): 033502.

34 R. A. Lawson and C. L. Henderson. "Mesoscale kinetic Monte Carlo simulations of molecular resists: the effect of PAG homogeneity on resolution, LER, and sensitivity," *Proc. SPIE* **7273**, p. 727341, 2009.

35 C. Lee, C. L. Henderson, M. Wang, K. E. Gonsalves, and W. Yueh, "Effects of photoacid generator incorporation into the polymer main chain on 193 nm chemically amplified resist behavior and lithographic performance," *Journal of Vacuum Science & Technology B: Microelectronics and Nanometer Structures Processing, Measurement, and Phenomena* **25**, no. 6 (2007): 2136–2139.

36 B. Rathsack, K. Nafus, S. Hatakeyama, Y. Kuwahara, J. Kitano, R. Gronheid, and A. Vaglio Pret. "Resist fundamentals for resolution, LER, and sensitivity (RLS) performance tradeoffs and their relation to micro-bridging defects," *Proc. SPIE* **7273**, p. 727347, 2009.

37 G. R. Amblard, R. D. Peters, J. L. Cobb, and K. Edamatsu. "Development and characterization of 193-nm ultra-thin resist process," *Proc. SPIE* **4690**, pp. 287–298, 2002.

38 C. Wang, T. Araki, B. Watts, S. Harton, T. Koga, S. Basu, and H. Ade, "Resonant soft X-ray reflectivity of organic thin films." *Journal of Vacuum Science & Technology A: Vacuum, Surfaces, and Films* **25**, no. 3 (2007): 575–586.

39 T. Ishiguro, J. Tanaka, T. Harada, and T. Watanabe, "Resonant Soft X-ray Reflectivity for the Chemical Analysis in Thickness Direction of EUV Resist," *J. Photopolym. Sci. Technol.*, **32**, 333-337 (2019).

40 H. J. Levinson, "EUV Lithography at the Threshold of High Volume Manufacturing," *EUVL Symposium*, 2018, https://www.euvlitho.com/2018/P1.pdf

41 P. De Bisschop and E. Hendrickx, "Stochastic printing failures in EUV lithography," *Proc. SPIE* **10957**, p. 109570E, 2019.

42 Y. Kamei, S. Kawakami, M. Tadokoro, Y. Hashimoto, T. Shimoaoki, M. Enomoto, K. Nafus, A. Sonoda, and P. Foubert, "Improvement of CD stability and defectivity in resist coating and developing process in EUV lithography process," *Proc. SPIE* **10809**, p. 1080924, 2018.

43 A. Chunder, A. Latypov, J. J. Biafore, H. J. Levinson, and T. Bailey. "Systematic assessment of the contributors of line edge roughness in EUV lithography using simulations," *Proc. SPIE* **10583**, p. 105831N, 2018.

44 C. A. Mack, "Metrics for stochastic scaling in EUV lithography," *Proc. SPIE* **11147**, p. 111470A, 2019.
45 C. Popescu, G. O'Callaghan, A. McClelland, J. Roth, T. Lada, and A. P. G. Robinson, "Performance enhancements with the high opacity multi-trigger resist," *Proc. SPIE* **11326**, p. 1132611, 2020.
46 S. Tagawa, S. Enomoto, and A. Oshima. "Super high sensitivity enhancement by photo-sensitized chemically amplified resist (PS-CAR) process." *Journal of Photopolymer Science and Technology* **26**, no. 6 (2013): 825–830.
47 S. Nagahara, M. Carcasi, H. Nakagawa, E. Buitrago, O. Yildirim, G. Shiraishi, Y. Terashita, et al. "Challenge toward breakage of RLS trade-off for EUV lithography by Photosensitized Chemically Amplified Resist (PSCAR) with flood exposure," *Proc. SPIE* **9776**, p. 977607, 2016.
48 S. Nagahara, C. Q. Dinh, G. Shiraishi, Y. Kamei, K. Nafus, Y. Kondo, M. Carcasi, et al. "PSCAR optimization to reduce EUV resist roughness with sensitization using Resist Formulation Optimizer (RFO)," *Proc. SPIE* **10960**, p. 109600A, 2019.
49 J. Stowers, J. Anderson, B. Cardineau, B. Clark, P. De Schepper, J. Edson, M. Greer, et al. "Metal oxide EUV photoresist performance for N7 relevant patterns and processes," *Proc. SPIE* Vol. **9779**, p. 977904 (2016).
50 L. Wu, M. Baljozovic, G. Portale, D. Kazazis, M. Vockenhuber, T. Jung, Y. Ekinci, and S. Castellanos. "Mechanistic insights in Zr-and Hf-based molecular hybrid EUV photoresists," *Journal of Micro/Nanolithography, MEMS, and MOEMS* **18**, no. 1 (2019): 013504.
51 W. D. Hinsberg and S. Meyers. "A numeric model for the imaging mechanism of metal oxide EUV resists," *Proc. SPIE* Vol. **10146**, p. 1014604 (2017).
52 R. Gronheid, S. Higashibata, O. Demirer, Y. Tanaka, D. Van den Heuvel, M. Mao, M. Suzuki, S. Nagai, W. Li, and P. Leray. "Overlay error investigation for metal containing resist (MCR)," *Proc. SPIE* **10959**, p. 1095905, 2019.
53 M. A. Mohammad, K. Koshelev, T. Fito, D. A. Z. Zheng, M. Stepanova, and S. Dew, "Study of Development Processes for ZEP-520 as a High-Resolution Positive, and Negative Tone Electron Beam Lithography Resist," *Jpn. J. Appl. Phys.* **51** 06FC05 (2012).
54 A. Shirotori, Y. Vesters, M. Hoshino, A. Rathore, D. De Simone, G. Vandenberghe, and H. Matsumoto, "Development of main chain scission type photoresists for EUV lithography," *Proc. SPIE* **11147**, p. 111470J, 2019.
55 M. Alvi, D. Dries, R. Gottscho, K. Gu, B. Kam, S. Kanakasabapathy, D. Li, J. Marks, K. Nardi, T. Nicholson, Y. Pan, D. Peters, A. Schoepp, N. Shamma, E. Srinivasan, S. Tan, C. Thomas, B. Volosskiy,

T. Weidman, R. Wise, W. Wu, J. Xue, J. Yu, C. Fouquet, R. Custers, J. G. Santaclara, M. Kubis, G. Rispens, L. van Lent-Protasova, M. Dusa, P. Jaenen, and A. Pathak, "Lithographic performance of the first entirely dry lithographic process, presented at the EUVL Workshop, 2020.

56 O. P. Joubert, D. Fuard, C. Monget, P. Schiavone, O. Toublan, A. Prola, J. M. Temerson, et al. "Process optimization of a negative-tone CVD photoresist for 193-nm lithography applications," *Proc. SPIE* **3678**, pp. 1371–1380, 1999.

57 C. Y. Lee, S. Das, J. W. Yang, T. W. Weidman, D. Sugiarto, M. P. Nault, D. Mui, and Z. A. Osborne. "Feasibility of a CVD-resist-based lithography process at 193-nm wavelength," *Proc. SPIE* **3333**, pp. 625–63, 1998.

58 A. P. Kovalskyy, J. Cech, M. Vlcek, C. M. Waits, M. Dubey, W. R. Heffner, and H. Jain. "Chalcogenide glass e-beam and photoresists for ultrathin grayscale patterning." *Journal of Micro/Nanolithography, MEMS, and MOEMS* **8**, no. 4 (2009): 043012.

59 V. Dan'ko, I. Indutnyi, V. Myn'ko, M. Lukaniuk, and P. Shepeliavyi, "The nanostructuring of surfaces and films using interference lithography and chalcogenide photoresist." *Nanoscale Research Letters* **10**, no. 1 (2015): 1–6.

60 S. Yoshida, M. Esashi, T. Kobayashi, and M. Kumano. "Conformal coating of poly-glycidyl methacrylate as lithographic polymer via initiated chemical vapor deposition." *Journal of Micro/Nanolithography, MEMS, and MOEMS* **11**, no. 2 (2012): 023001.

61 A. De Silva, K. Petrillo, L. Meli, J. C. Shearer, G. Beique, L. Sun, I. Seshadri, et al. "Single-expose patterning development for EUV lithography," *Proc. SPIE* **10143**, p. 101431G, 2017.

62 D. L. Goldfarb, M. Glodde, A. De Silva, I. Sheshadri, N. M. Felix, K. Lionti, and T. Magbitang. "Fundamentals of EUV resist-inorganic hardmask interactions." *Proc. SPIE* **10146**, p. 1014607, 2017.

63 A. De Silva, I. Seshadri, A. Arceo, K. Petrillo, L. Meli, B. Mendoza, Y. Yao, M. Belyansky, S. Halle, and N. M. Felix, "Study of alternate hardmasks for extreme ultraviolet patterning." *J. Vac. Sci. Techno*. **B34**, no. 6 (2016): 06KG03.

64 R. Gronheid, A. Vaglio Pret, B. Rathsack, J. Hooge, S. Scheer, K. Nafus, H. Shite, and J. Kitano, "EUV RLS performance tradeoffs for a polymer bound PAG resist," *Proc. SPIE* **7639**, p. 76390M, 2010.

65 T. Ouattara, C. Washburn, A. Collin, V. Krishnamurthy, D. Guerrero, and M. Weigand, "EUV assist layers for use in multilayer processes," *Proc. SPIE* **8322**, p. 83222E, 2012.

66 V. Constantoudis, G. Papavieros, G. Lorusso, V. Rutigliani, F. Van Roey, and E. Gogolides. "Line edge roughness metrology: recent challenges and

advances toward more complete and accurate measurements." *Journal of Micro/Nanolithography, MEMS, and MOEMS* **17**, no. 4 (2018): 041014.

67 V. Rutigliani, G. F. Lorusso, D. De Simone, F. Lazzarino, G. Papavieros, E. Gogolides, V. Constantoudis, and C. A. Mack. "Setting up a proper power spectral density and autocorrelation analysis for material and process characterization." *Journal of Micro/Nanolithography, MEMS, and MOEMS* **17**, no. 4 (2018): 041016.

68 E. Gallagher, "EUV Lithography and Materials that Propel if Forward," *presented at the EUVL Workshop*, 2020.

69 M. P. Belyansky, R. K. Bonam, A. Desilva, and S. Halle. "Resist having tuned interface hardmask layer for EUV exposure." U.S. Patent 9, 929, 012, issued March 27, 2018.

70 A. De Silva, J. Church, D. Metzler, L. Meli, N. M. Felix, P. Friddle, B. Nagabhirava, S. Kanakasabapathy, and R. Wise, "High-Z metal-based underlayer patterning for improving EUV stochastics (Conference Presentation)," *Proc. SPIE* **11323**, p. 113230M, 2020.

71 H. Xu, J. M. Blackwell, and T. R. Younkin, and K. Min. "Underlayer designs to enhance the performance of EUV resists," *Proc. SPIE* **7273**, p. 72731J., 2009.

72 H. Fukuda, "Localized and cascading secondary electron generation as causes of stochastic defects in extreme ultraviolet projection lithography." *Journal of Micro/Nanolithography, MEMS, and MOEMS* **18**, no. 1 (2019): 013503.

73 H. Fukuda, "Cascade and cluster of correlated reactions as causes of stochastic defects in extreme ultraviolet lithography." *Journal of Micro/Nanolithography, MEMS, and MOEMS* **19**, no. 2 (2020): 024601.

74 H. Fukuda, "Stochastic defect generation in EUV lithography analyzed by spatially correlated probability model, reaction-limited and scattering-limited?." *In International Conference on Extreme Ultraviolet Lithography 2019*, **vol. 11147**, p. 1114716. International Society for Optics and Photonics, 2019.

75 H. Fukuda, "Impact of asymmetrically localized and cascading secondary electron generation on stochastic defects in EUV lithography," *Proc. SPIE* **10957**, 2019.

Chapter 6
Computational Lithography for EUV

Early work on EUV lithography primarily involved patterning at large values of k_1, at least in comparison to what had been routine for optical lithography for many years. For example, EUV lithography was introduced into high-volume manufacturing at the 7-nm node, with ~20-nm half-pitch, giving $k_1 = 0.49$, while k_1 has been considerably less than 0.4 for logic using optical lithography since the 32-nm node. Although there were some early studies indicating that an accurate description of imaging for EUV lithography was necessarily complex, most of the complications were seen to occur at low values of k_1, so the computational aspects of EUV lithography required to address many issues received much less attention than other aspects of the technology for a number of years. However, in order to meet the requirements of the 5-nm node and beyond, many computational aspects of EUV lithography need to be considered, and there has been much recent work.

There are several reasons why computational lithography for advanced EUV lithography is more complex than it is for optical lithography. To begin, OPC for EUV lithography still has all of the requirements of conventional, optical OPC, such as the need to ensure good targeting of dimensions at the best operating point and good dimensional control throughput the process window, which includes variations on the mask. Because EUV lithography is applied at the most advanced nodes, accuracy requirements are necessarily tighter than they are for optical lithography. There are some differences between the conventional OPC for EUV lithography and that for optical lithography. For example, it is important for both lithographic technologies to ensure that the image log-slope maintains a certain minimum, but this metric may get greater emphasis in EUV lithography. As noted in Chapter 5, the impact of resist stochastics can be reduced by maintaining a large normalized image slope, so more weight may be given to this image metric during OPC optimization.

In addition to the considerations of conventional OPC with tight tolerances, the oblique illumination and the particular structure of EUV masks combine to necessitate consideration of rigorous of models to a much greater degree than for optical lithography in order to calculate aerial images with the necessary accuracy. Flare and aberrations are more significant for EUV lithography than for optical lithography and thus need more attention. These additional factors are important for EUV lithography and are discussed in this chapter. In practice, there is a need to account for all of these various physical phenomena simultaneously, which is very challenging.

6.1 Conventional OPC Considerations

The purpose of OPC is the adjustment of dimensions on masks in order to compensate for nonlinear and proximity-dependent imaging to thereby achieve the desired dimensions on the wafer. In EUV lithography, this is still an important goal for OPC, but it is more complex than for optical lithography. As noted in Chapter 4, features on the mask that are oriented perpendicular to the plane of illumination are shadowed by the absorbers, while those parallel to the plane of incidence are not, leading to different horizontal and vertical print biases. Correcting for horizontal–vertical dimensional differences was recognized early as an important function of OPC specific to EUV lithography.

The situation is somewhat more complex than simple horizontal–vertical dimensional differences, because the plane of incidence varies across the slit, as described in Chapter 3. The result is that plane of incidence is neither strictly perpendicular nor strictly horizontal to Manhattan patterns, except for features in the center of the slit (Fig. 6.1). Consequently, horizontal–vertical corrections will vary across the slit.

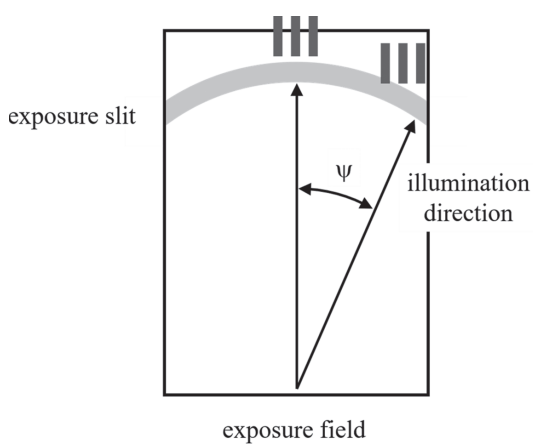

Figure 6.1 The azimuthal component of illumination, varying across the exposure slit.

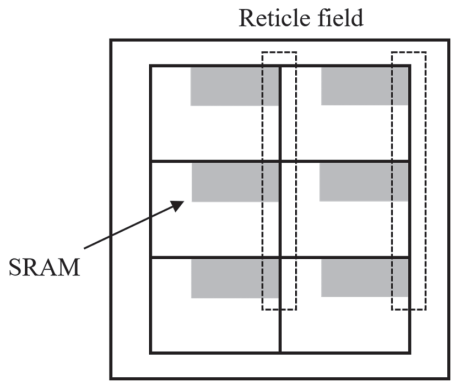

Figure 6.2 Illustration of the breaking of hierarchy because of variations across the slit.

For OPC, an important consequence of these variations across the slit is the breaking of hierarchy. This is illustrated in Fig. 6.2. Consider the fabrication of microprocessors that are arrayed across a reticle field in two columns and three rows. Suppose that each microprocessor has SRAM in the upper-right corner of the die. For SRAMs in the dies on the left side of the reticle field, the illumination will be nearly normal or parallel to the features. For the dies on the right side of the reticle field, the illumination will be at an oblique angle. This means that OPC generated for dies on the left side of the reticle field cannot be applied directly to the dies on the right side of the field. This is a very different situation from that encountered in optical lithography. This breaking of hierarchy increases OPC runtimes in situations where obtaining accurate OPC is essential.

Over the course of several decades, the lenses of optical exposure tools improved considerably. As a consequence, for optical lithography lens aberrations and flare have been of consequence only for very low k_1 (<0.3). The situation for EUV lithography is quite different. Aberrations result when the light rays forming images are not all in proper phase, with the scale for this being set by the wavelength. For EUV lithography to have the same effective level of aberrations as for optical lithography means that EUV lenses would need to improve over optical lenses on an absolute (nanometer) level by a factor of 193/13.5 = 14.3. Lens makers have made remarkable improvements, but not quite to this level. Hence, aberrations are non-negligible for EUV lithography, even for processes with $k_1 > 0.3$.

An example of the impact of coma aberration on imaging, which has long been know to affect the dimensions of lines in a finite array,[1] is shown in Fig. 6.3. The total aberration levels for EUV exposure tools are 10–15 mλ rms.[2] If we assume that the levels of Z8 are ~½ of the total rms level, then it can be seen from Fig. 6.3 that coma will contribute 0.2–0.3-nm CD variation across a finite array. To put this level of variation into context, the control requirement for critical dimensions for metal layers is projected in

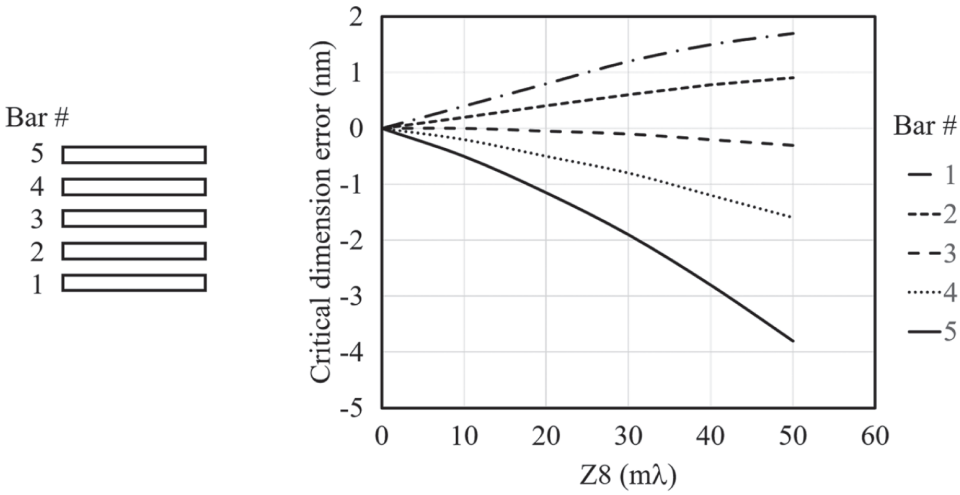

Figure 6.3 Calculated critical dimension errors as a function of Z8 (coma) aberration error for a 5-bar structure (left side of figure) consisting of 16-nm lines and spaces that was imaged with a 0.33 NA and quadrupole illumination.[6]

the IRDS to be 1.8 nm (3σ) in 2025.[3] The CD variation due to aberrations is a small, but not inconsequential, fraction of the total requirement. Aberrations can vary as much as 5× across the slit,[4] so correcting for the dimensional shifts induced by aberrations through OPC will need to take this variation across the slit into account. Since aberrations vary tool to tool, such an approach will necessarily produce solutions that are unique to individual exposure tools, and each mask will be corrected only for a specific tool.[5] An inability to use masks on multiple exposure tools is certainly inconvenient.

Aberrations affect pattern placement as well as critical dimensions[7] as illustrated in Fig. 6.4. With very tight overlay requirements, pattern placement is an important consideration for EUV lithography. Compensation for pattern placement errors using OPC is discussed in the next chapter.

As described in Chapter 3, EUV lenses have substantial flare relative to optical lenses. For the 7-nm node, where the primary application of EUV lithography is for contact and via layers, the impact of flare is small. However, for later nodes, for which EUV lithography will be applied to line/space patterns with much greater bright area, and compensation for flare will be required. Importantly, accurate computation of aerial images must take mask layouts into account.

As illustrated in Fig. 3.10, flare in optical systems is a consequence of the scattering of light from rough mirror surfaces. Because this scattering can occur over a range of angles, the resulting flare will occur over a range of distances. Large-angle scattering will result in long-range flare, often considered as a uniform background of light on which the images of individual features are superimposed. The total amount of long-range flare is

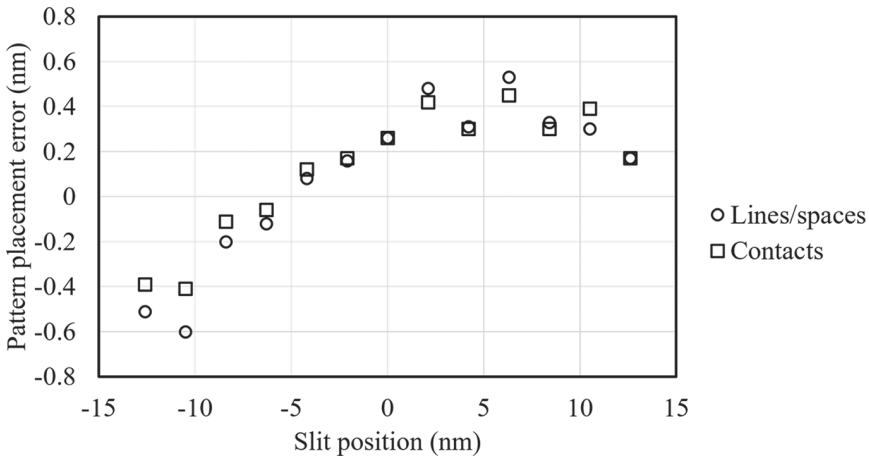

Figure 6.4 Calculated across-slit pattern placement errors based on measured aberrations in an NXE:3300B EUV exposure tool, assuming annular illumination.[8] The line/space patterns were on a 40-nm pitch in the *y* direction, while the contacts were on a 40-nm pitch in the *y* direction and a 56-nm pitch in the *x* direction.

a function of the total amount of reflective area on the mask. Shorter-range scattering will depend on the mask layout at a more detailed level, as the amount of short-range and mid-range scattering will be functions of the percentage of mask area covered locally by absorber. This dependence of flare on range and pattern density has long been recognized, and corrections were made for it in the first fabrication of an integrated circuit using EUV lithography.[9]

One means of estimating flare I_S is the convolution of aerial image intensity I without flare over the image field with a series of Gaussians:

$$I_S(x, y) = I_{DC} + \sum_{i=1}^{N} \frac{a_i}{r_i^2} \iint_{Field} I(x', y') e^{-\frac{(x-x')^2 + (y-y')^2}{r_i^2}} dx'dy', \qquad (6.1)$$

where I_{DC} is a constant flare background, and N is the number of spatial ranges over which flare is considered. In a study of flare in ArF lithography, three ranges were chosen, and the spatial ranges r_i spanned 3 μm to 6800 μm.[10] This method can also be applied to EUV lithography. In the absence of spectral filtering, DUV light may be transmitted from the source to the wafer. Such light acts as additional flare and needs to be included when calculating flare compensation.[11] Since tantalum-based absorbers reflect ~15% at DUV wavelengths,[12] there can be a significant DUV contribution even when most of the mask is covered by absorber.

Compensation of flare over a range of spatial distances requires corresponding measurements. Various methods for measuring flare have been proposed,[13] which are most commonly variants of the method proposed

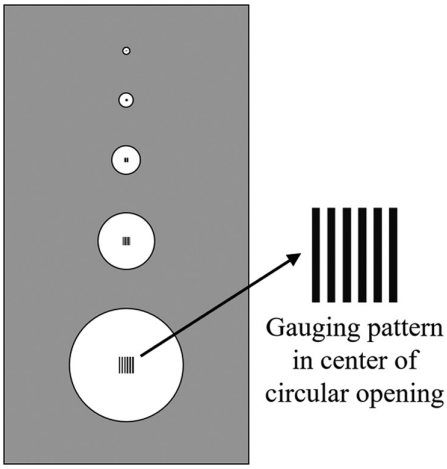

Figure 6.5 Illustration of a zonal ring approximation structure for measuring flare as a function of distance. The diameters of the rings vary logarithmically.[16]

by Joe Kirk,[14] where resist is exposed at high doses. The amount of flare can be measured by determining the dose level required to clear positive-tone resist (after develop) in areas that correspond to absorber features on a mask, relative to clear areas. This method has worked well for optical lithography,[15] but it is more difficult to apply to EUV lithography, because of the negative resist behavior that can occur at high doses in positive resists, as discussed in Chapter 3. An example of an alternative method suitable for EUV lithography is the zonal ring approximation method (ZRAM), in which the dimensions of flare sensing features surrounded by varying amounts of clear areas are measured (Fig. 6.5).[16]

Flare reduces the normalized image slope (see Problem 6.2) and increases process variation.[17,18] Even if critical dimensions are corrected by OPC at best dose and focus, flare will also increase process variability bands (PVbands), particularly when stochastics are taken into consideration, and this needs to be taken into account when performing process window OPC.

The mask error enhancement factor (MEEF) is an important consideration when mask critical dimension variation is taken into account to determine process windows. With EUV lithography there is a return to single patterning, and MEEF can be high for dense patterns. Certain features, such as the tip-to-tip between lines (Fig. 6.6), have long been constructed with optical lithography using cut or block masks, so the large values of MEEF for these features when using single exposure patterning has not been of consequence. An optimization study was performed for various features in the layout shown in Fig. 6.6,[19] with the results summarized in Table 6.1. It should be noted that the patterning of tip-to-tip features is challenging, and process windows are often limited by the ability to print such features.[20]

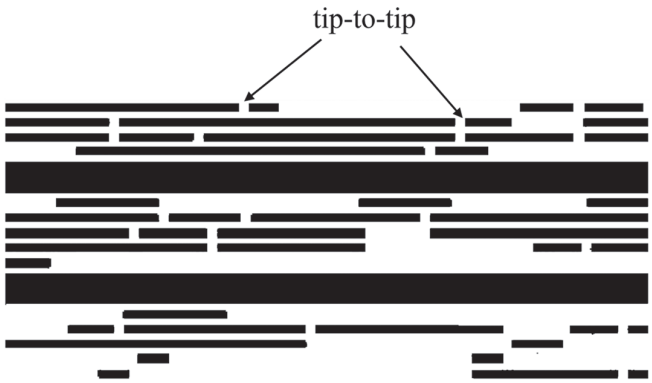

Figure 6.6 Clip of foundry metal 2 layer at the 5-nm node, with 32-nm pitch and 25-nm tip-to-tip dimensions.[19]

Table 6.1 Ranges for MEEF for the geometries in Fig. 6.6.

Feature type	MEEF without SRAFs	MEEF with SRAFs
Lines/spaces	1.0–2.7	0.7–2.7
Tip-to-tip	2.0–8.0	1.8–4.8

Notably, process windows were enlarged substantially by including SRAFs in the source-mask optimization (SMO). SMO and inverse lithography technology (ILT) will be discussed further in Section 6.4.

As discussed in this section, the issues familiar in OPC for optical lithography also need to be addressed for EUV lithography, although the factors may be weighted differently, and greater accuracy is needed when applying EUV lithography at the more advanced nodes. The topic of the next section is more significant for EUV lithography than for optical lithography.

6.2 The 3D Aspects of EUV Masks

A key difference between aerial image modeling for optical and EUV lithography is the degree to which mask three-dimensional (3D) effects have an impact on imaging. While such effects are known to affect optical lithography, the magnitude of the difference between images calculated using a thin-absorber model for the mask and a full 3D model are small, and it is generally possible to account for the 3D effects with efficient approximations. On the other hand, mask 3D effects are quite significant for EUV lithography, and ideal mask models with infinitely thin absorbers and reflectors are far from accurate. It is often not possible to treat mask 3D effects simply as perturbations on top of a generally sound imaging model based on infinitely thin mask absorbers and reflectors. The actual and more complex situation is

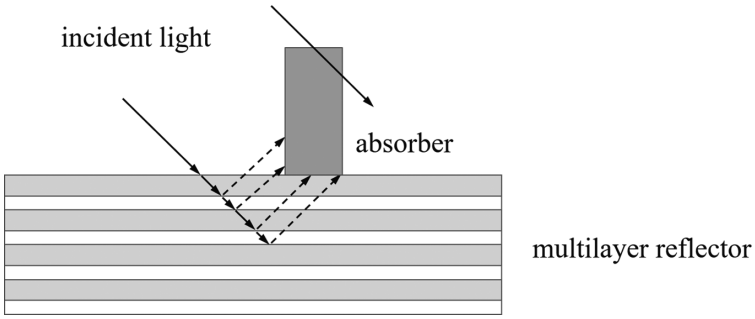

Figure 6.7 Illustration of the 3D character of EUV imaging.

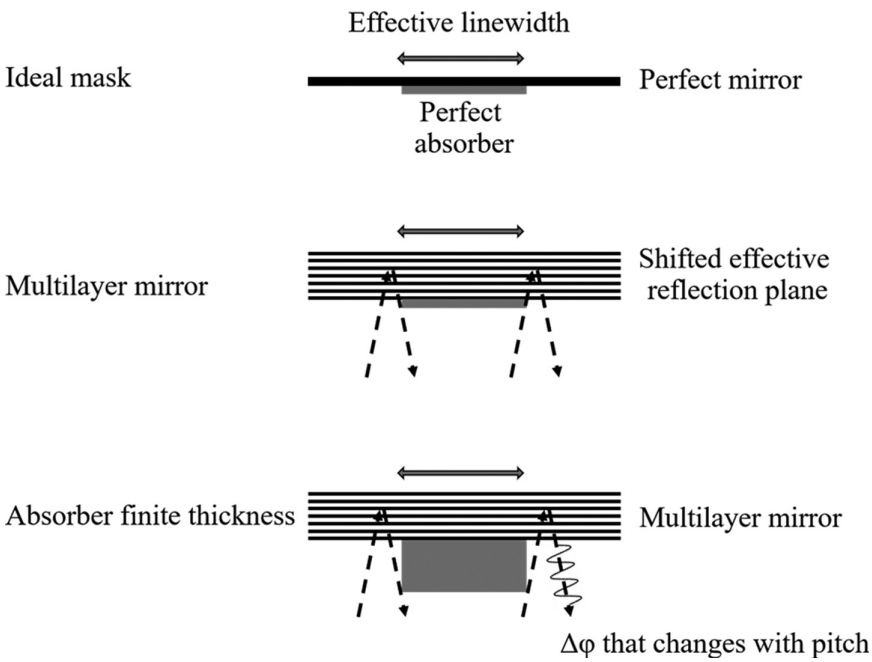

Figure 6.8 Illustration of the effects of the finite thicknesses of absorbers and multilayer mirrors.

depicted in Figs. 6.7 and 6.8. Because the absorber materials are not completely opaque, some light passes through the absorbers. (As noted in Chapter 4, the attenuation length for tantalum-based absorbers is ~25 nm.) For the multilayer mirror, there are reflections from every interface in the multilayer stack, which leads to complex interactions at the mask.

As will be seen later in this chapter, there are manifestations of the 3D character of the interactions between obliquely incident EUV light and the mask structures that produce variations in best focus with pitch, imaging blurring, and pattern placement shifts. These undesirable effects can be

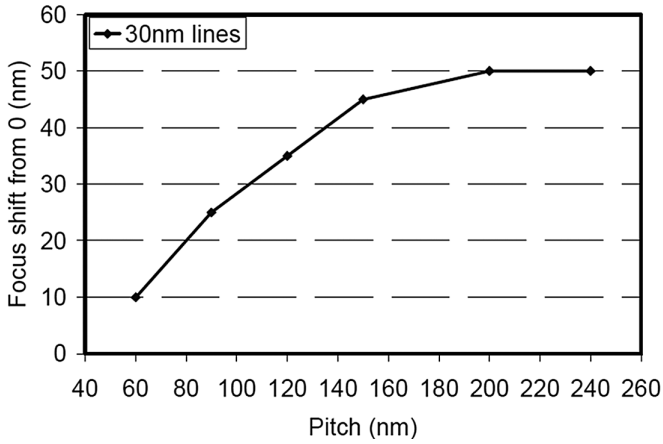

Figure 6.9 Simulated focus vs. pitch for 30-nm lines. For this simulation, the mask absorber was assumed to consist of 100-nm-thick TaN on a 28-nm SiO_2 buffer layer. The NA was 0.25.[21]

reduced by using alternative multilayer reflectors and absorbers that have greater optical absorption, but 3D models are required for calculating aerial images.

Accounting for the 3D nature of the interactions of EUV light with masks involves more than applying complex models for calculating aerial images accurately and then adjusting mask dimensions on the basis of the same considerations as used for optical OPC. An early rigorous simulation study of EUV lithography showed that the plane of best focus is a function of pitch, even in the absence of spherical aberrations.[21] Results from this study can be seen in Fig. 6.9, showing a 40-nm focus range through pitch. Such a large dependence of focus on pitch is not something encountered in aberration-free optical lithography. Without steps taken to mitigate the variations in focus through pitch, such a physical effect would significantly reduce the useable process window. At the time the data shown in Fig. 6.9 were initially generated, it was thought that EUV lithography might be introduced for 160-nm minimum pitch technology,[22,23] in which case the range of the focus shifts would have been considerably less than 40 nm, because most of the focus variation occurs at smaller pitches. Note that a 160-nm pitch represents an extremely large k_1 ($\approx$1.5 @ $NA = 0.25$). As the actual insertion point for EUV lithography occurred with small pitches (40-nm pitch, $k_1 = 0.49$ @ $NA = 0.33$), this pitch-dependent focus is an issue for the use of EUV lithography in high-volume manufacturing.

Another situation in which the plane of best focus is affected by EUV mask 3D effects is the 2-bar structure shown in Fig. 6.10. When symmetric dipole illumination is used for patterning, the top and bottom lines of the pair have different planes of best focus. For the case of a 32-nm pitch structure, the

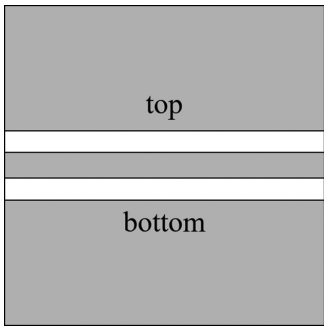

Figure 6.10 A 2-bar structure consisting of two lines on a tight pitch but relatively isolated from other features.

best focus planes were found in simulation to be separated by more than 50 nm (Fig. 6.11). This situation can be improved by adjusting the illumination. Using re-engineered symmetric illumination, the two lines can have the same plane of best focus. With this modified symmetric illumination, there is some difference in critical dimensions even at best focus, but this can be corrected by adjusting dimensions on the mask, i.e., through OPC. Alternatively, the use of asymmetric illumination can improve the situation significantly, bringing the planes of best focus into coincidence, as well as providing equal dimensions.[24] In this example, although the mask pattern is symmetric, the overall symmetry has been broken by the oblique angle of the illumination, resulting in top and bottom lines that have different planes of best focus or differences in dimensions. OPC and SMO solutions for EUV lithography need to address these effects and to find global solutions that work across a broad range of feature types and pitches.

The lateral shifting of features with changes in wafer focus is another EUV mask 3D-effect related to focus that was identified early.[25,26,27] Because of the dependence of pattern placement on focus, this is usually referred to as a wafer telecentricity error. It should be distinguished from nontelecentricity on the mask side of the projection optics, where pattern placement varies with the plane of the mask, as described in Chapter 4. Since the amount of pattern shift varies linearly over typical ranges of defocus, wafer telecentricity error can be expressed as a dimensionless number, equal to the amount of pattern shift divided by the magnitude of defocus, with both quantities measured in nanometers. Consider the contour plot shown in Fig. 6.12. The centroid position, i.e., the pattern placement, varies with focus. This variation is approximately linear. A measure of the magnitude of this effect is θ, an angle. Hence, the unit for telecentricity is often mrad.

The pattern shift through focus due to mask 3D effects differs among pitches, as illustrated in Fig. 6.13. Note that the overlay requirement in the 2020 IRDS for logic in the year 2025 is 2.0 nm, so the largest placement shifts

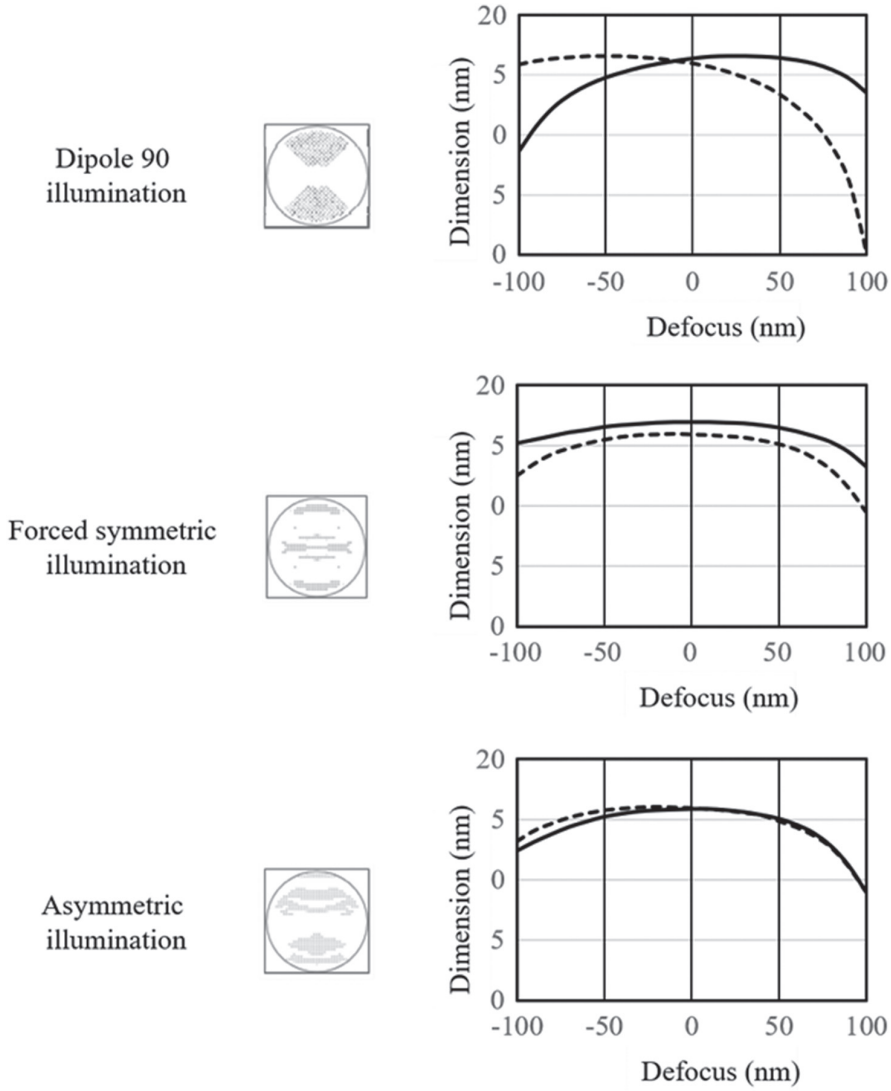

Figure 6.11 Critical dimensions of a 2-bar structure with symmetric and asymmetric illumination. The solid line is the simulated printed dimension of the bottom line for a 32-nm pitch (dark field structure).[24]

due to defocus represent a significant fraction of the total overlay budget. Since the biggest shifts occur at large defocus, the impact of nontelecentricity can be minimized by having very good focus control. Moreover, the largest pattern shifts involve the largest pitches, so these shifts can also be reduced through the use of SRAFs.

Measuring the absolute pattern shift on wafers is not straightforward. However, wafer telecentricity errors vary through pitch, so it is possible to

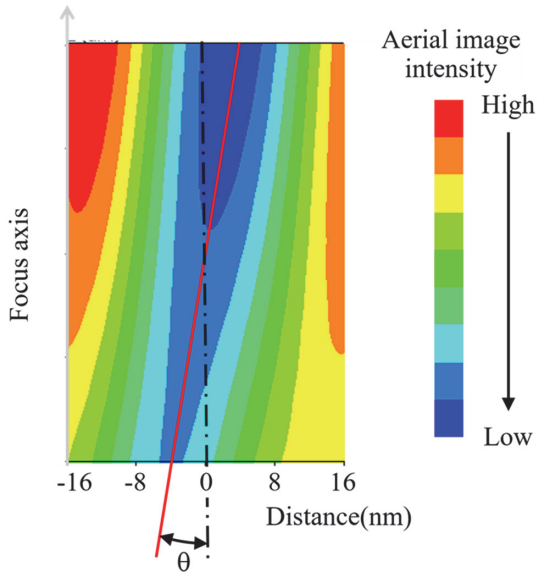

Figure 6.12 Contour plot of simulated aerial image intensity, assuming 32-nm-pitch lines/spaces and 0.42 NA.[25]

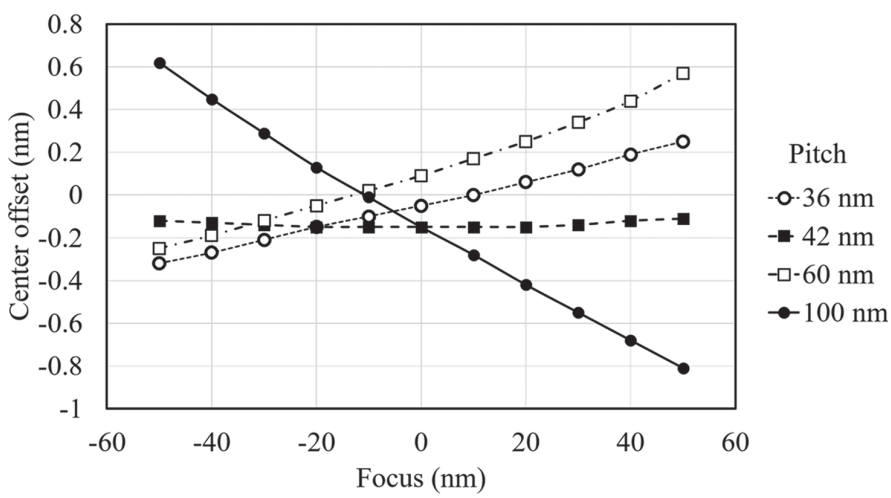

Figure 6.13 Pattern shift through focus for various pitches.[28]

measure the differences in pattern shifts among pitches. In one study, differences in telecentricity among pitches for 0.33-NA optics was found to be as large as 11 mrad (see Fig. 6.14).[29] For 0.33-NA optics, the Rayleigh depth of focus is ±62 nm. At the limits of this focus range, the induced relative pattern placement errors would be

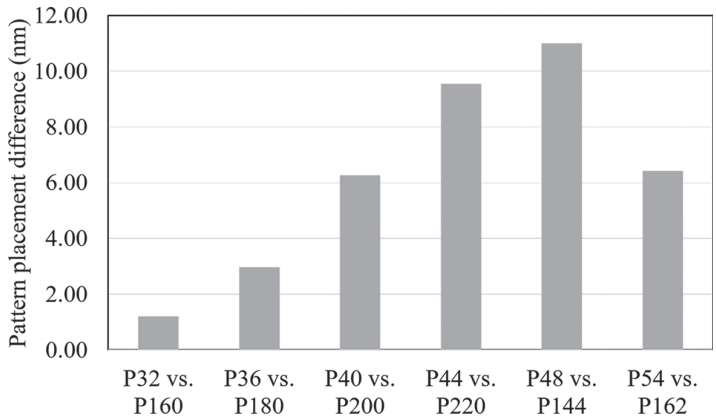

Figure 6.14 Measured telecentricity differences between pairs of difference pitches for horizontal line/space patterns, exposed on a 0.33-NA EUV exposure tool. The mask absorber was 70-nm-thick TaN.[29]

$$11 \times 10^{-3} \times 62 \text{ nm} = 0.68 \text{ nm}, \tag{6.2}$$

which is a large fraction of overlay budgets for the 7-nm node and beyond. For EUV lithography, this means that focus needs to be controlled much more tightly on the basis of overlay considerations than by regarding linewidths alone.

This lateral shifting with changes in focus has a significant effect on process-window OPC, which will need to account for shifts in the centerlines of features, as well as edges. This is an example where EUV lithography cannot be viewed simply as optical lithography at a very short wavelength, since such centerline shifts are generally not significant in optical lithography.

The lateral shifting of features can affect image quality as well as overlay. Consider the situation depicted in Fig. 6.15, where the image of a grating illuminated by a monopole source will be formed by the interference between two diffracted rays of light. The amplitude of two rays illustrated in Fig. 6.15 is given by

$$A = A_0 e^{ik_x x + i\phi_0} + A_1 e^{-ik_x x + i\phi_1}. \tag{6.3}$$

This resulting intensity is given by

$$I = A_0^2 + A_1^2 + 2A_0 A_1 \sin(k_x x + \Delta\phi), \tag{6.4}$$

where

$$\Delta\phi = \phi_1 - \phi_0. \tag{6.5}$$

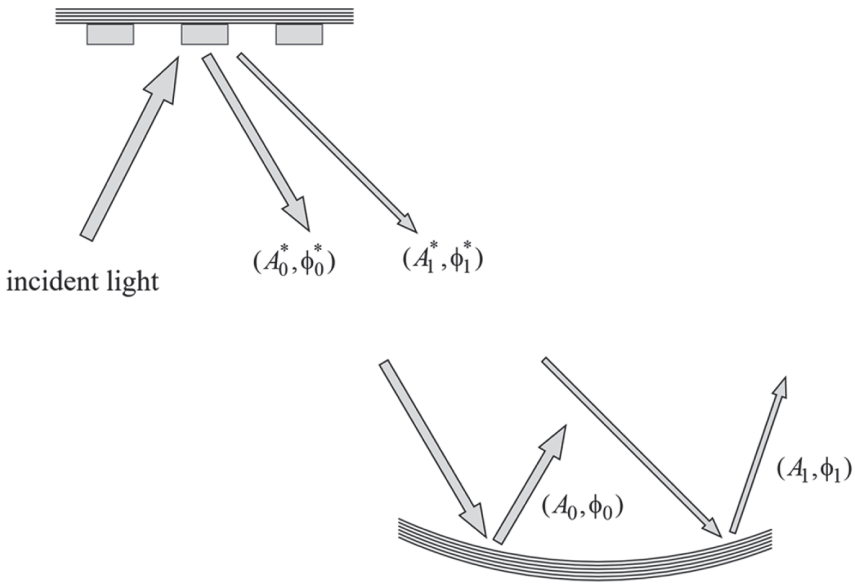

Figure 6.15 Diffracted light rays with different intensities (A_1) and phase (ϕ_1).

In optical lithography, the intensities of ±first-order diffracted rays are balanced, and they are of equal phase at the wafer plane when using aberration-free projection optics. For EUV lithography, the rays travel different amounts through absorbers and multilayers, resulting in an imbalance. The resulting contrast is

$$C = \frac{I_{\max} - I_{\min}}{I_{\max} + I_{\min}} \tag{6.6}$$

$$= \frac{2(A_1/A_0)}{1 + (A_1/A_0)^2}. \tag{6.7}$$

From Eq. (6.7), it can be seen that there is a loss of contrast when $A_0 \neq A_1$ (see Problem 6.1). Moreover, the image is shifted as a consequence of $\Delta\phi$ (Eq. (6.4)). For monopole illumination, this shift could be corrected through OPC, but monopole illumination is not typically used, because it leads to large telecentricity errors, i.e., pattern placement shifts with variations in focus. If dipole illumination is used, the resulting intensity is the sum of expressions such as Eq. (6.4) for monopole illumination but with a difference in the sign of the phase difference. The intensity for symmetric dipole illumination is therefore[30]

$$\frac{I + I'}{2} = A_0^2 + A_1^2 + A_0 A_1 \sin(k_x x + \Delta\phi) + A_0 A_1 \sin(k_x x - \Delta\phi) \tag{6.8}$$

$$= A_0^2 + A_1^2 + 2A_0A_1 \sin(k_x x)\cos(\Delta\phi). \tag{6.9}$$

The contrast is further reduced by pole intensity imbalance and a factor $\cos(\Delta\phi)$, a consequence of the total image being the sum of two images shifted in opposite directions:

$$C = \frac{I_{\max} - I_{\min}}{I_{\max} + I_{\min}} \tag{6.10}$$

$$= \frac{2(A_1/A_0)}{1 + (A_1/A_0)^2}\cos(\Delta\phi). \tag{6.11}$$

In this example, the image placement differed between two points in the illumination and resulted in a blurred combined image with reduced contrast. Since all practical sources have finite extent, image blur that is induced by mask 3D effects is a fundamental problem for EUV lithography.[31] This blur can be moderated by the use of very thin absorbers on the mask, but this will require the use of materials that are more absorbing that those used currently, TaN and TaBN. Attenuated phase-shifting masks may also be beneficial. The multilayer also contributes to these pattern shifts, which can be reduced somewhat (but not eliminated) by the use of alternative multilayers, such as Ru/Si.[32,33,34] The intentional introduction of some aberrations into the projections optics has even been proposed to reduce the image blurring.[35] Since the blurring gets worse at out-of-focus conditions, very tight focus control is beneficial.[30]

Since the nontelecentric nature of the illumination on EUV masks is a major reason why images are strongly affected by the 3D characteristics of the electromagnetic interactions of the light with the mask, the dependence of the multilayer reflector on angle is significant. As discussed in Chapter 1, multilayer reflectors are often nonideal, with intermixing of molybdenum and silicon. As shown in Fig. 1.9, such intermixing reduces the overall reflectivity of the multilayer mirror, and it has also been found to modify the dependence of reflectance on the angle of incidence on the mask. This is shown in Fig. 6.16, where reflectance from an ideal multilayer varies little for angles up to $\sim 9°$ but then falls off steeply at larger angles. On the other hand, the multilayer stack with intermixing has much less variation in reflectance up to the maximum angle $\sim 10.7°$ for 0.33-NA systems. Since the reflectance can vary significantly with the angle of incidence, there can be substantial apodization in the imaging.[36] The magnitude of such apodization depends critically on the degree to which the Mo/Si multilayers approximate ideal ones, so accurate calculations of EUV imaging require detailed knowledge of the reflectance properties of the multilayer mirrors on the masks.

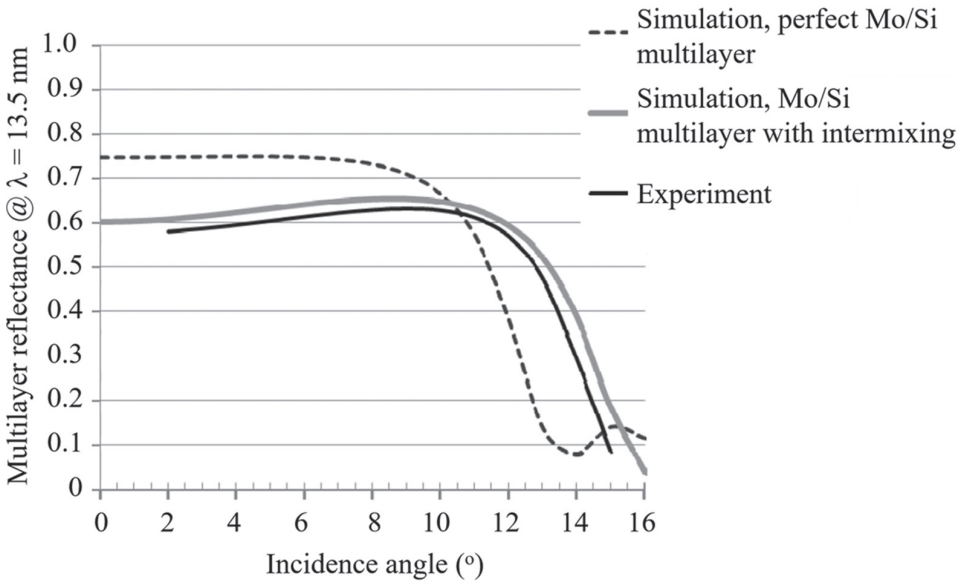

Figure 6.16 Reflectance from a Mo/Si multilayer mirror. The simulations are performed with and without the assumption of Mo–Si intermixing.[37]

The variation in reflectance at the largest angles is critical, since the light rays that form the images of small features emanate at large angles.

Accounting for 3D mask effects requires the application of rigorous simulations. The authors of references cited above used various simulators, such as Panoramic Technology's HyperLith and EM-Suite simulations tools[38] and Dr.LiTHO.[39,40] However, rigorous simulators[41] that directly apply methods such as finite-difference time-domain (FDTD) and rigorously coupled wave analysis (RCWA) perform calculations slowly, making them unsuitable for direct OPC computations. Consequently, methods have been developed to increase computational speed that employ some approximations but are still able to capture the essential physics; these methods have been used in simulators such as Tachyon M3D[42] and FastLitho.[43]

6.3 Resist Physics

Whether performing rigorous simulations to achieve accuracy or applying model-based OPC, resist models need to be able to account for the essential physics of the resist in order to obtain useful results. The "resist models" of early OPC engines were small adjustments applied to aerial images to improve the fit to measured data. Over time, such fits have evolved in order to account better for the actual physics of resists. As described in Chapter 3, the photochemistry of chemically amplified resists is very complex. Since chemically amplified resists have long been used in optical lithography, much

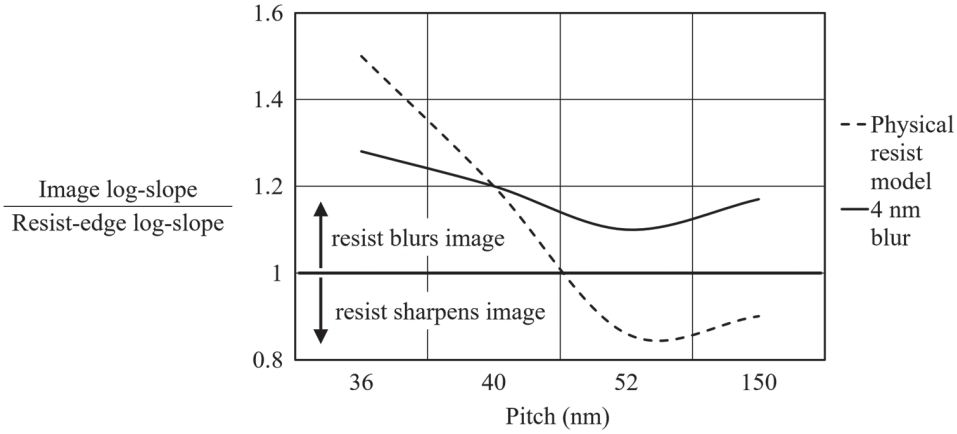

Figure 6.17 Ratio of image slopes and chemical gradients from rigorous simulations of 18-nm trenches in chemically amplified resists.[45]

of this photochemistry is far from unique to EUV lithography, so the modeling of chemically amplified resists will not be discussed in detail here. However, there is one aspect that merits attention.

When chemical gradients following post-exposure bakes were first compared to the normalized slopes of the aerial images that formed patterns, it was observed that photoacid diffusion generally led to chemical gradients that were less steep than the slopes of the aerial images.[44] This meant that the resist-edge log-slopes (RELSs) were smaller than the image log-slopes (ILSs), and the impact of diffusion has generally been considered as a blurring of the image. More recently, detailed modeling of chemically amplified resists that include photo-decomposable bases has revealed more complex behavior. When the bases have short diffusion lengths, such blur was seen across a range of pitches in rigorous simulations, but when base diffusion lengths are long, there can be pitches at which the image is effectively sharpened following post-exposure bake (Fig. 6.17). In this case, the effect of diffusion during the post-exposure bake cannot be described adequately by a simple blur. This behavior is not unique to EUV lithography, but it does add to the complexity of computational problems for EUVL. Proper accounting of the diffusion of photoacids and bases is important to achieve accurate OPC in optical lithography, but it is more important in EUV lithography because of the need for greater accuracy (in terms of nanometers) and the fact that concentrations of photoacid generators and photodecomposable bases are higher in EUV resists, relative to optical materials.

As discussed in Chapter 3, alternatives to chemically amplified resists are being considered for use in EUV lithography. For some of them, such as metal-oxide resists, the physical models seem to be simpler than those of chemically amplified resists. Without diffusion of multiple components, such

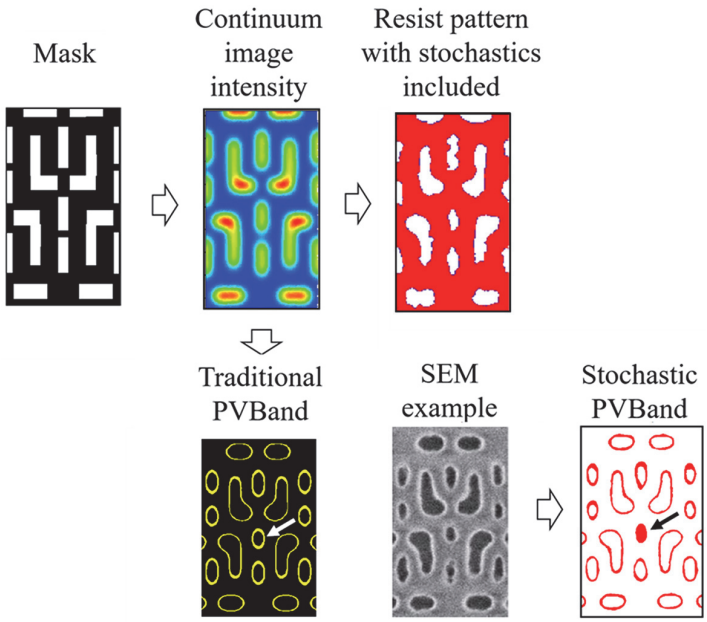

Figure 6.18 Illustration of changes in calculated PVbands when stochastics are included. The calculations were performed using Prolith™. The SEM was of resist patterned on a 0.25-NA EUV exposure tool.[46]

as photoacids and photodecomposable bases, during a post-exposure bake, the chemical distributions following exposure closely approximate the original aerial images.

Resist stochastics are also far more significant for EUV lithography, and their impact needs to be taken into account when determining OPC. One of the most apparent manifestations of resist stochastics is an increase in the widths of process variability bands (PVbands). In some instances, this increase leads to process failures.[46] This is illustrated in Fig. 6.18, where a traditional PVband calculation, which includes variability over focus, dose, and mask dimensions, indicates good printing over the range of process variations. Inclusion of stochastics shows a failing feature, even at best focus and dose.

Monte Carlo methods, which can involve hundreds of thousands of iterations,[47] are appropriate for calculating stochastic PVbands for small areas, such as shown in Fig. 6.18, but are impractical for application to full-chip process-window OPC. A first step for addressing the problem of stochastics has been to maintain large image log-slopes when generating the OPC, since a large ILS can help to mitigate LER, particularly the component resulting from photon shot noise. If we consider the photon shot noise to be an effective dose variation, line-edge variations can be reduced by increasing the ILS, because of the well-known increase in exposure latitude with larger image log-slopes.[48] Ensuring that the ILS doesn't get too small has been done

routinely for optical OPC, but the acceptable minimum ILS for EUV lithography needs to be bigger than for optical lithography and weighted more heavily. Stochastic contributions to PVbands have been estimated using more complex functions of the ILS or NILS.[45] This is particularly useful at low exposure doses, where the photon shot noise is a large contributor to stochastic variations. As will be described in more detail in the next chapter, stochastic variations frequently have non-normal distributions, which makes it complicated to apply analytical solutions to estimate the impact of stochastics on PVbands. This is an area of active research.

6.4 Imaging Optimization for EUV Lithography

Several 3D mask effects were described in Section 6.2. These, along with other issues that are relevant for OPC and process window optimization, such as complex resist physics and stochastics, are summarized in Table 6.2. Control of each parameter is possible, but in practice, they all need to be addressed simultaneously. Thus, the determination of OPC and the optimization for EUV lithography is very complex.

One method for reducing variations through pitch is through the use of sub-resolution assist features (SRAFs).[49] These have long been found to be beneficial in optical lithography, particularly at low values of k_1. Since EUV lithography through the 7-nm nodes has involved relatively high values of $k_1 \geq 0.49$, so the use of SRAFs for EUV lithography has been limited, even though some benefit from the use of SRAFs was observed (Fig. 6.19).

Table 6.2 Summary of the parameters that need to be considered when computing OPC or optimizing the mask and source.

Phenomena	Requirements
Conventional OPC considerations	CDs within specifications over a suitably large process window MEEF < 4
Mask 3D effects	Small differences in best focus through pitch End-of-array (2-bar) focus differences Imaging blurring Pattern placement shifts with focus
Resist models	Capturing complex physics into computational efficient models
Stochastics	Need to maintain large NILS Include in PVband
Aberrations	Address across slit, tool to tool
Out-of-band light and flare	Incorporate into OPC models

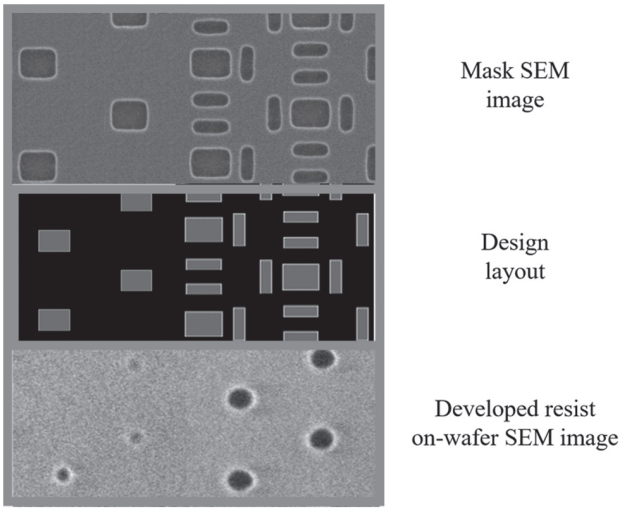

Figure 6.19 Mask, design, and wafer patterns for 48-nm and 34-nm contact holes on a 64-nm pitch. The patterns in resist were exposed on a 0.25-NA EUV exposure tool using SEVR-165 resist.[50]

With EUV lithography being applied to the patterning of pitches ≤32 nm ($k_1 \leq 0.39$), SRAFs been increasing in use. SRAF printing into resist has long been a problem, even in optical lithography, and the situation is worse with EUV lithography. Typically, this printing does not go through the full depth of the photoresist, which makes prediction difficult for models that are based on thresholds,[51] and the problem is made even more challenging by stochastics, which can lead to intermittent SRAF printing. Nevertheless, SRAFs are often important to address many of the EUV 3D mask issue, particularly for line/space patterns.[52]

It has proven difficult to realize the full resolution potential of EUV lithography, due to the resist issues described in Chapter 5, as well as the imaging problems discussed in this chapter. Consequently, inverse lithography technology (ILT) and a related approach, source-mask optimization (SMO), for EUV lithography are being developed that offer opportunities to optimize imaging performance. With conventional OPC, images of features for a design are calculated, and modifications to the mask layout are made based on those calculations. This is essentially a deterministic problem in physics: for a given mask layout, there is only one possible solution, within computation errors and within the context of a specific optical model. Mathematically, this can be expressed as[53]

$$\omega = f(\psi), \tag{6.12}$$

where ψ is the mask pattern, ω is the wafer pattern, and f is an operator that incorporates the physics of the optics and resist. On the other hand, the inverse problem,

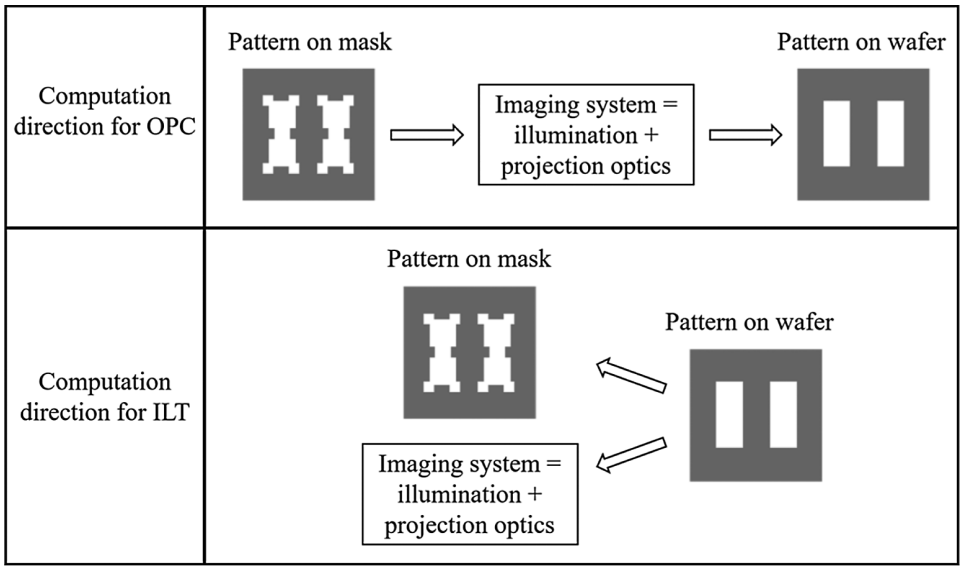

Figure 6.20 Differing directions of the computations for OPC and ILT.

$$\psi^* = f^{-1}(\phi), \tag{6.13}$$

where ψ^* is the optimal mask function and Φ is the target wafer pattern, is multivalued. Consequently, the inverse problem is not deterministic, and it is possible to end up with a local, rather than global, optimization (Fig. 6.20). Moreover, the computation times are lengthy for inverse lithography.

The foundation for inverse lithography was established in the 1980s,[54,55] and has been applied to optical lithography for over a decade.[56,53] Because of the long computation times, ILT has typically been applied only to memory cells or a few logic cells with small process windows obtained using conventional OPC techniques. In principle, mask layouts can be divided into small partitions, and ILT can be applied to the many sections by using arrays of servers. However, this can lead to mismatch between ILT solutions at the boundaries between partitions (Fig. 6.21), necessitating additional computation time to address whenever ILT is applied to an area larger than a single partition. Alternatively, full-chip, stitchless ILT can be accomplished using co-optimized GPU-based computing platforms and associated software.[57]

The optimum shapes for mask features obtained using ILT were often found to have curved features. For many years, this was problematic for mask-making, since it was not efficient to make curved patterns with vector shaped-beam (VSB) writing tools. The introduction of multi-beam mask writers has solved this particular problem. The desirability of using multi-beam mask writers for patterning EUV masks in order to improve mask linewidth control and LER was noted in Chapter 4, so these tools address

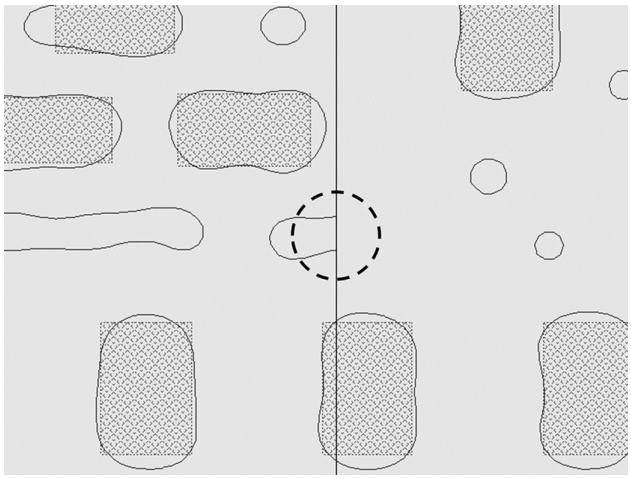

Figure 6.21 Example of a stitching problem involving an SRAF at the boundary between two sections of a layout where the inverse lithography was performed separately.[58]

two concerns for EUV masks.[59] Recent studies have shown that curved features—primary as well as sub-resolution—significantly improve process windows,[60] particularly when mask dimensional variation is included.[61]

As discussed in Section 6.2, several of the consequences of mask 3D effects can be mitigated by adjusting the illumination. However, it is challenging to find a solution that will work for the varying pitches and layouts of random logic. The use of SRAFs helps by effectively reducing the range of pitches over which optimization needs to be performed.

Problems

6.1 In Eq. (6.1), show that the contrast is maximized when $A_0 = A_1$.

6.2 Suppose that flare is a fraction f of the dose to size for a given feature. Show that the image log-slope for this feature is reduced by flare by the factor $1 - f$.

References

1 T. A. Brunner, "Impact of lens aberrations on optical lithography." *IBM Journal of Research and Development* **41**, no. 1.2 (1997): 57–67.
2 J. Miyazaki and A. Yen. "EUV Lithography Technology for High-volume Production of Semiconductor Devices." *Journal of Photopolymer Science and Technology* **32**, no. 2 (2019): 195–201.
3 https://irds.ieee.org/
4 M. Lam, C. Clifford, A. Raghunathan, G. Fenger, and K. Adam. "Enabling full field physics based OPC via dynamic model generation," *Proc. SPIE* **10143**, p. 1014316, 2017.

5 L. Yin, A. Raghunathan, G. Fenger, S. Shang, N. Lafferty, and J. Sturtevant, "Impact of aberrations in EUV lithography: metal to via edge placement control," *Proc. SPIE* **10583**, p. 105830Q, 2018.
6 J. Hwang, I. Kim, G. Kim, H. No, B. Kim, and H. Oh. "CD error caused by aberration and its possible compensation by optical proximity correction in extreme-ultraviolet lithography," *Proc. SPIE* **10143**, p. 101431U, 2017.
7 A. Raghunathan, G. Fenger, M. Lam, C. Clifford, K. Adam, and J. Sturtevant, "Edge placement errors in EUV from aberration variation," *Proc. SPIE* **10451**, p. 104510W, 2017.
8 Y. Chen, L. Liebmann, L. Sun, A. Gabor, S. Zhao, F. Luo, O. Wood II, et al., "Holistic analysis of aberration induced overlay error in EUV lithography," *Proc. SPIE* **10583**, p. 105830D, 2018.
9 B. La Fontaine, Y. Deng, R. Kim, H. J. Levinson, S. McGowan, U. Okoroanyanwu, R. Seltmann, C. Tabery, A. Tchikoulaeva, T. Wallow, O. Wood, J. Arnold, D. Canaperi, M. Colburn, K. Kimmel, C. Koay, E. McLellan, D. Medeiros, S. P. Rao, K. Petrillo, Y. Yin, H. Mizuno, S. Bouten, M. Crouse, A. van Dijk, Y. van Dommelen, J. Galloway, S. Han, B. Kessels, B. Lee, S. Lok, B. Niekrewicz, B. Pierson, R. Routh, E. Schmitt-Weaver, K. Cummings, and J. Word, "The use of EUV lithography to produce demonstration devices," *Proc. SPIE* **6921**, 69210P (2008).
10 J. Word, J. Belledent, Y. Trouiller, W. Maurer, Y. Granik, E. Sahouria, and Olivier Toublan. "Full-chip model-based correction of flare-induced linewidth variation," *SPIE* Vol. **5567**, pp. 700–710, 2004.
11 S. A. George, P. P. Naulleau, C. D. Kemp, P. E. Denham, and S. Rekawa, "Assessing out-of-band flare effects at the wafer level for EUV lithography," *SPIE* Vol. **7636**, p. 763626, 2010.
12 G. F. Lorusso, N. Davydova, M. Eurlings, C. Kaya, Y. Peng, K. Feenstra, T. H. Fedynyshyn, et al., "Deep ultraviolet out-of-band contribution in extreme ultraviolet lithography: predictions and experiments," *Proc. SPIE* **7969**, p. 79692O, 2011.
13 L. Sun, O. R. Wood, E. A. Verduijn, M. Singh, W. Wang, R. Kim, P. J. Mangat, H. P. Koh, and H. J. Levinson. "Review of resist-based flare measurement methods for extreme ultraviolet lithography," *Journal of Micro/Nanolithography, MEMS, and MOEMS* **12**, no. 4 (2013): 042001.
14 J. P. Kirk, "Scattered light in photolithographic lenses," *Proc. SPIE* **2197**, pp. 566–572, 1994.
15 B. M. La Fontaine, M. V. Dusa, A. Acheta, C. Chen, A. Bourov, H. J. Levinson, L. C. Litt, M. Mulder, R. Seltman, and J. van Praagh. "Flare and its impact on low-k1 KrF and ArF lithography," *Proc. SPIE* **4691**, pp. 44–56, 2002.

16 I. Kim, H. Kang, C. Park, J. Park, J. Lee, J. Park, D. Goo, J. Yeo, S. Choi, and W. Han. "Methodology of flare modeling and compensation in EUVL." *Proc. SPIE* **7140**, p. 714009, 2008.
17 L. Dong, R. Chen, T. Fan, R. Zhao, Y. Wei, J. Jia, Z. Levinson, et al. "Impact of flare on source mask optimization in EUVL for 7 nm technology node," *Proc. SPIE* **11323**, p. 113232E, 2020.
18 S. H. Lee, Y. Shroff, and M. Chandhok. "Flare and lens aberration requirements for EUV lithographic tools," *Proc. SPIE* **5751**, pp. 707–714, 2005.
19 A. Armeanu, V. Philipsen, F. Jiang, G. Fenger, N. Lafferty, W. Gillijns, E. Hendrickx, and J. Sturtevant, "Enabling enhanced EUV lithographic performance using advanced SMO, OPC, and RET," *Proc. SPIE* **10809**, p. 108090G, 2019.
20 Y. Chen, L. Sun, Z. J. Qi, S. Zhao, F. Goodwin, I. Matthew, and V. Plachecki, "Tip-to-tip variation mitigation in extreme ultraviolet lithography for 7 nm and beyond metallization layers and design rule analysi." *Journal of Vacuum Science & Technology B, Nanotechnology and Microelectronics: Materials, Processing, Measurement, and Phenomena* **35**, no. 6 (2017): 06G601.
21 P. Yan, "Understanding Bossung curve asymmetry and focus shift effect in EUV lithography," *SPIE* Vol. **4562**, pp. 279–287, 2002.
22 P. J. Silverman, "The Intel Lithography Roadmap." *Intel Technology Journal* **6**, no. 2, pp. 55–61 (2002).
23 C. W. Gwyn and P. J. Silverman. "EUVL: transition from research to commercialization," *SPIE* Vol. **5130**, pp. 990–1004, 2003.
24 T. Last, L. de Winter, P. van Adrichem, and J. Finders. "Illumination pupil optimization in 0.33-NA extreme ultraviolet lithography by intensity balancing for semi-isolated dark field two-bar M1 building blocks." *Journal of Micro/Nanolithography, MEMS, and MOEMS* **15**, no. 4 (2016): 043508.
25 S. Raghunathan, O. R. Wood, P. Mangat, E. Verduijn, V. Philipsen, E. Hendrickx, R. Jonckheere, et al. "Experimental measurements of telecentricity errors in high-numerical-aperture extreme ultraviolet mask images," *J. Vac Sci. Technol.* Vol. **B32**(6), (2014): 06F801.
26 A. Erdmann, T. Schmöller, and P. Evanschitzky. "Mask induced imaging artifacts in extreme ultraviolet lithography." In *2nd International SEMATECH EUVL Symposium*. 2003.
27 O. Wood II, Y. Chen, P. Mangat, K. Goldberg, M. Benk, B. Kasprowicz, H. Kamberian, J. McCord, and T. Wallow, "Measurement of through-focus EUV pattern shifts using the SHARP actinic microscope," *SPIE* Vol. **10450**, p. 1045008, 2017.
28 L. Van Look, I. Mochi, V. Philipsen, E. Gallagher, E. Hendrickx, G. McIntyre, F. Wittebrood, K. Lyakhova, L. de Winter, T. Last,

T. Fliervoet, G. Schiffelers, J. Finders, P. van Adrichem, A. Lyons, B. Laenens, J. Liddle, and J. T. Neumann, "Mask 3D Effect Mitigation by Source Optimization and Assist Feature Placement," *Proceedings from the International Symposium on Extreme Ultraviolet Lithography*, Hiroshima (2016) http://euvlsymposium.lbl.gov/pdf/2016/Oral/Mon_S3-5.pdf

29 V. Philipsen, E. Hendrickx, E. Verduijn, S. Raghunathan, O. Wood II, V. Soltwisch, F. Scholze, N. Davydova, and P. Mangat, "Imaging impact of multilayer tuning in EUV masks, experimental validation," *SPIE* Vol. **9235**, p. 92350J, 2014.

30 M. Burkhardt, "Investigation of alternate mask absorbers in EUV lithography," *SPIE* Vol. **10143**, p. 1014312, 2017.

31 J. Finders, E. van Setten, P. Broman, E. Wang, J. McNamara, and P. van Adrichem, "EUV source optimization driven by fundamental diffraction considerations," *SPIE* Vol. **10450**, p. 104500C, 2017.

32 M. Singh, "EUV mask for use during EUV photolithography processes." U.S. Patent 9, 075, 316, issued July 7, 2015.

33 O. Wood II, S. Raghunathan, P. Mangat, V. Philipsen, V. Luong, P. Kearney, E. Verduijn, et al. "Alternative materials for high numerical aperture extreme ultraviolet lithography mask stacks," *Proc. SPIE* **9422**, p. 94220I, 2015.

34 H. Mesilhy, P. Evanschitzky, G. Bottiglieri, E. van Setten, T. Fliervoet, and A. Erdmann, "Pathfinding the perfect EUV mask: the role of the multilayer," Proc. SPIE 11323, Extreme Ultraviolet (EUV) Lithography XI, 1132316 (23 March 2020); doi: 10.1117/12.2551870

35 J. Franke, J. Bekaert, V. Blanco, L. Van Look, F. Wahlisch, K. Lyakhova, P. van Adrichem, M. J. Maslow, G. Schiffelers, and E. Hendrickx, "Improving exposure latitudes and aligning best focus through pitch by curing M3D phase effects with controlled aberrations," *SPIE* Vol. **11147**, p. 111470E, 2019.

36 N. Davydova, E. van Setten, S. Han, M. van de Kerkhof, R. de Kruif, D. Oorschot, J. Zimmerman, et al. "Mask aspects of EUVL imaging at 27 nm node and below," *Proc. SPIE* **8166**, p. 816624, 2011.

37 V. Philipsen, E. Hendrickx, R. Jonckheere, N. Davydova, T. Fliervoet, and J. T. Neumann, "Actinic characterization and modeling of the EUV mask stack," *Proc. SPIE* **8886**, p. 88860B, 2013.

38 Panoramic Technology, http://www.panoramictech.com

39 T. Fühner, T. Schnattinger, G. Ardelean, and A. Erdmann, "Dr. LiTHO: a development and research lithography simulator," *Proc. SPIE* **6520**, p. 65203F, 2007.

40 A. Erdmann, D. Xu, P. Evanschitzky, V. Philipsen, V. Luong, and E. Hendrickx, "Characterization and mitigation of 3D mask effects in extreme ultraviolet lithography," *Advanced Optical Technologies* **6**, no. 3-4 (2017): 187–201.

41 Erdmann, Andreas, and Peter Evanschitzky. "Rigorous electromagnetic field mask modeling and related lithographic effects in the low k1 and ultrahigh numerical aperture regime." *Journal of Micro/Nanolithography, MEMS, and MOEMS* **6**, no. 3 (2007): 031002.
42 P. Liu, "Accurate prediction of 3D mask topography induced best focus variation in full-chip photolithography applications," *Proc. SPIE* **8166**, p. 816640, 2011.
43 M. Yeung and E. Barouch, "Development of fast rigorous simulator for large-area EUV lithography simulation," *SPIE* Vol. **10957**, p. 109751D, 2019.
44 A.R. Pawloski, A. Acheta, I. Lalovic, B. La Fontaine, and H.J. Levinson, "Characterization of line edge roughness in photoresist using an image fading technique," *Proc. SPIE* **5376**, pp. 414–425 (2004).
45 S. G. Hansen, "Photoresist and stochastic modeling." *Journal of Micro/Nanolithography, MEMS, and MOEMS* **17**, no. 1 (2018): 013506.
46 P. De Bisschop, "Stochastic effects in EUV lithography: random, local CD variability, and printing failures." *Journal of Micro/Nanolithography, MEMS, and MOEMS* **16**, no. 4 (2017): 041013.
47 A. V. Pret, T. Graves, D. Blankenship, K. Bai, S. Robertson, P. De Bisschop, and J. J. Biafore. "Comparative stochastic process variation bands for N7, N5, and N3 at EUV," *Proc. SPIE* **10583**, p. 105830K, 2018.
48 H. J. Levinson and W. H. Arnold, "Focus: the critical parameter for submicron lithography," *J. Vac. Sci. Technol. B* **5**, pp. 293–298 (1987).
49 R. Kim, W. Gillijns, Y. Drissi, J. U. Lee, D. Trivkovic, V. M. Blanco Carballo, S. Larivière, et al. "EUV single patterning for logic metal layers: achievement and challenge (conference presentation)," *Proc. SPIE* **10450**, p. 1045004, 2017.
50 D. Civay, E. A. Verduijn, C. H. Clifford, P. J. Mangat, and T. I. Wallow, "Subresolution assist features in extreme ultraviolet lithography." *Journal of Micro/Nanolithography, MEMS, and MOEMS* **14**, no. 2 (2015): 023501.
51 P. De Bisschop, "Optical proximity correction: a cross road of data flows." *Japanese Journal of Applied Physics* **55**, no. 6S1 (2016): 06GA01.
52 R. Sejpal, V. Philipsen, A. Armeanu, C. Wei, W. Gillijns, N. Lafferty, G. Fenger, and E. Hendrickx, "Exploring alternative EUV mask absorber for iN5 self-aligned block and contact layers," *Proc. SPIE* **11148**, p. 111481B, 2019.
53 D. S. Abrams and L. Pang. "Fast inverse lithography technology," *Proc. SPIE* **6154**, p. 61541J, 2006.
54 B. E. A. Saleh and S. I. Sayegh, "Reduction of errors of microphotographic reproductions by optimal corrections of original masks," *Optical Engineering* **20**, no. 5 (1981): 205781.

55 K. M. Nashold and Bahaa EA Saleh, "Image construction through diffraction-limited high-contrast imaging systems: an iterative approach." *JOSA A* **2**, no. 5 (1985): 635–643.
56 A. E. Rosenbluth, S. J. Bukofsky, C. A. Fonseca, M. S. Hibbs, K. Lai, A. F. Molless, R. N. Singh, and A. K. K. Wong, "Optimum mask and source patterns to print a given shape." *Journal of Micro/Nanolithography, MEMS, and MOEMS* **1**, no. 1 (2002): 13–31.
57 L. L Pang, P. J. Ungar, A. Bouaricha, L. Sha, M. Pomerantsev, M. Niewczas, K. Wang, B. Su, R. Pearman, and A. Fujimura, "TrueMask ILT MWCO: full-chip curvilinear ILT in a day and full mask multi-beam and VSB writing in 12 hrs for 193i," *Proc. SPIE* **11327**, p. 113270K, 2020.
58 L. L. Pang, E. V. Russell, B. Baggenstoss, M. Lee, J. Digaum, M. Yang, P. J. Ungar, et al. "Study of mask and wafer co-design that utilizes a new extreme SIMD approach to computing in memory manufacturing: full-chip curvilinear ILT in a day." *Proc. SPIE* **11148**, p. 111480U, 2019.
59 Efficient algorithms for generating curvilinear masks for optical lithography have been developed in recent years. See Pang, Ungar, Bouaricha, et al.
60 K. Hooker, A. Kazarian, X. Zhou, J. Tuttle, G. Xiao, Y. Zhang, and K. Lucas, "New methodologies for lower-K1 EUV OPC and RET optimization," *Proc. SPIE* **10143**, p. 101431C, 2017.
61 R. Pearman, J. Ungar, N. Shirali, A. Shendre, M. Niewczas, L. Pang, and A. Fujimura, "How curvilinear mask patterning will enhance the EUV process window: a study using rigorous wafer+ mask dual simulation," *Proc. SPIE* **11178**, p. 1117809, 2019.

Chapter 7
Process Control for EUV Lithography

There are several sources of process variation that are unique to EUV lithography or of significantly greater significance than in optical lithography. The issues for overlay, linewidth control, and defects relevant to EUV lithography are discussed in this chapter. Recently, attention has been given to the subject of edge placement errors, which result from a combination of critical dimension and overlay errors.[1] Although edge placement is the fundamental quantity of interest, overlay and critical dimension control will be considered separately in this chapter so that the causes of process variations can be understood more clearly. Metrology is an important consideration for process control and is the topic of the next chapter.

The application of EUV lithography only to very advanced nodes (7 nm and beyond) means that process control requirements are always very tight. Selected dimensions and control requirements from the 2020 International Roadmap for Devices and Systems (IRDS) are shown in Table 7.1. As can be seen, control is expected to be required at the nanometer and sub-nanometer

Table 7.1 Values for selected critical dimensions and control requirements for logic from the 2020 International Roadmap for Devices and Systems (IRDS).

Logic industry "Node" labeling (nm)	"7"	"5"	"3"	"2.1"	"1.5"	"1.0"
Year of production	2018	2022	2022	2025	2028	2031
MPU/ASIC minimum metal half-pitch (nm)	18.0	15.0	12.0	10.5	8.0	8.0
Metal LWR	2.7	2.3	1.8	1.5	1.2	1.2
Metal CD control (3σ) (nm)	2.7	2.3	1.8	1.5	1.2	1.2
Gate LER	0.8	0.7	0.6	0.5	0.5	0.5
Physical gate length for HP Logic (nm)	20	18	16	14	12	12
Gate CD control (3σ) (nm)	1.1	1.0	0.9	0.7	0.6	0.6
Overlay (mean + 3σ)	3.6	3.0	2.4	2.1	1.6	1.6

level, that is, at the molecular scale (see Chapter 5). Meeting these requirements is challenging, particularly because there are mechanisms that induce process variations for which there are no counterparts in optical lithography, as will be seen in this chapter. Improvements of just a few tenths of a nanometer are significant for advanced nodes. For example, reducing the overlay by only 0.5 nm at the 5-nm node is a 17% improvement relative to the target.

7.1 Overlay

For overlay, all of the issues that are relevant for optical lithography pertain to EUV lithography. These include matters such as alignment and overlay measurement mark quality, overlay modeling, and mask and wafer heating. Some contributions to overlay errors, such as aberrations, are relevant for optical lithography but are more significant for EUV lithography. There are also some additional contributions to overlay errors for EUV lithography for which there are no counterparts in optical lithography, and these will be discussed in this section.

As noted in Chapter 4, mask nonflatness causes overlay errors in EUV lithography. For optical photomasks, an overall flatness of 100 nm is a typical requirement for leading-edge masks, driven by focus control considerations, with tighter flatness adding to blank costs. For EUV masks, much tighter flatness is required because of the impact on overlay. For example, only 50-nm nonflatness will lead to 1.3-nm overlay error at the wafer level (see Problem 4.3). This is a substantial fraction of the total overlay budget at the 7-nm node and beyond (Table 7.1). Without some method of compensation, for mask nonflatness to contribute an overlay error that is only 10% of the total overlay budget for the 5-nm node, mask flatness would need to be <10 nm. This would lead to extremely expensive masks, particularly since the additional polishing needed to attain such flatness would increase defects.

There are also overlay errors that can result from mask backside nonflatness, even if the frontside of a chucked EUV mask is flat (see Fig. 7.1). When the mask is chucked, there will be in-plane distortion that is proportional to the backside slope ϕ:[2,3]

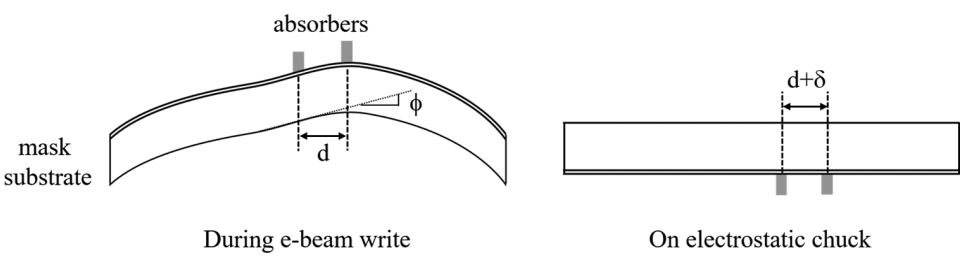

Figure 7.1 Mask shape during e-beam write and when on the electrostatic chuck.

$$\delta \approx \frac{1}{8}\phi T, \tag{7.1}$$

where T is the thickness of the mask. If the deviation from planar of the backside at position x is $z(x)$, then

$$\phi = \frac{dz}{dx}. \tag{7.2}$$

As with frontside nonflatness, backside nonflatness of tens of nanometers will cause pattern placement errors that are significant (see Problem 7.1).

Fortunately, a substantial fraction of the overlay error induced by mask nonflatness can be compensated by overlay adjustments on the exposure tool.[4] For example, if the backside nonflatness consists entirely of bow (second-order nonflatness), then the resulting mask placement errors consist of an overall magnification error. Accordingly, compensating for bow is straightforward.

The following is ASML's general intrafield overlay model up to third order:

$$\begin{aligned}\delta x = {} & k_1 + k_3 * x + k_5 * y + k_7 * x^2 + k_9 * xy + k_{11} * y^2 \\ & + k_{13} * x^3 + k_{15} x^2 y + k_{17} * xy^2 + k_{19} y^3,\end{aligned} \tag{7.3}$$

$$\begin{aligned}\delta y = {} & k_2 + k_4 * y + k_6 * x + k_8 * y^2 + k_{10} * xy + k_{12} * x^2 \\ & + k_{14} * y^3 + k_{16} y^2 x + k_{18} * yx^2 + k_{20} x^3.\end{aligned} \tag{7.4}$$

For EUV exposure tools, the k_{13} and k_{20} terms are not adjustable,[5] but considerable adjustment capability is still available to compensate for the overlay errors induced by mask nonflatness.[4] For example, in one study it was projected that the overlay error from masks blanks with 30-nm range nonflatness and 80-nm range thickness variation could be reduced to 0.2 nm (3σ) by the application of third-order overlay models.

Correcting for mask nonflatness in a practical way requires repeatable clamping of the mask to the reticle chuck to allow such nonflatness to occur consistently for each mask. One way to ensure this is to clamp the substrate initially in its center and subsequently clamp the outer portions.[6] It is also important that no particles are introduced between the mask and chuck that will change the clamping characteristics over time.

Appropriate overlay measurement sampling is necessary in order to benefit fully from the use of third-order (or higher) models. If there are N parameters in a model, then more than N pieces of data are needed for fitting the model. Since overlay measurements typically provide overlay errors in both the x and y directions, the number of measurement sites needs to be

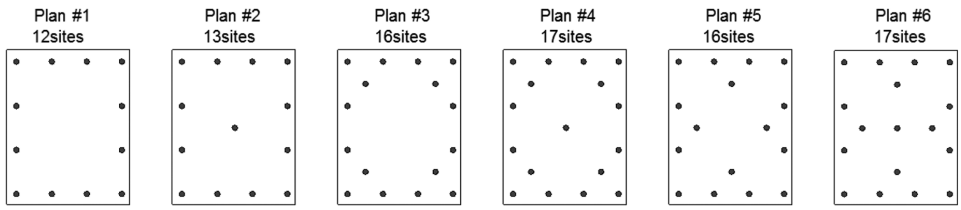

Figure 7.2 Some of the intrafield sampling plans used in a Monte Carlo simulation to produce the results in Fig. 7.3.

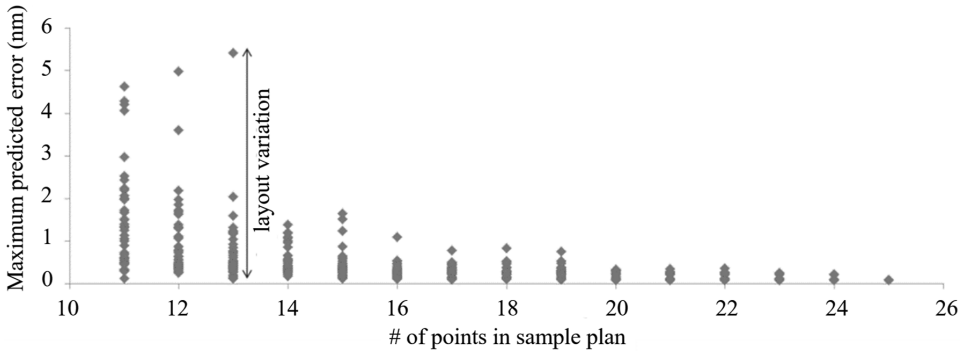

Figure 7.3 Results of a Monte Carlo simulation, showing the need for a sufficient number of measurement sites per field that are properly distributed.

greater than $N/2$. Even with a sufficient number of sites, they need to be distributed properly to get accurate coefficients for each order.

This was studied by a Monte Carlo simulation.[5] Some of the sampling plans are shown in Fig. 7.2, and the results of the simulation are shown in Fig. 7.3, illustrating the value of having a sufficient number of properly distributed measurement sites. Naturally, the best results are obtained with the largest number of overlay measurements, but there is a point of diminishing returns. In the study from which Figs. 7.2 and 7.3 came, greatly reduced improvement was obtained by increasing the number of measurement sites per field above 20.

Another consequence of the oblique illumination of the mask is pattern placement shifting through focus (Fig. 6.12),[7] a consequence of pole imbalance in the ±1 diffraction orders (Fig. 7.4). This pole imbalance is the consequence of variation in the reflectivity of mask multilayer reflectors as a function of the angle of incidence. Over the ranges of defocus typical of EUV lithography, the pattern shift varies linearly with defocus to a good approximation, so a measure of this effect, referred to as the nontelecentricity, is the pattern shift divided by defocus.

Nontelecentricity contributes negligibly to overlay errors in optical lithography, while in EUV lithography it adds to the overlay errors from

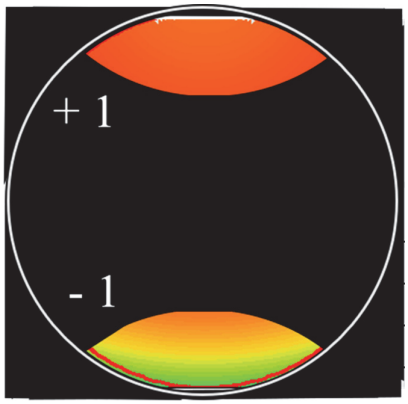

Figure 7.4 The dipole order imbalance due to mask-induced apodization, used to calculate the aerial image intensities of Fig. 6.12.[7]

more conventional sources of error, such as misalignment by the exposure tools, reticle misregistration, etc. Because it is difficult to reduce these more typical overlay errors by more than required from linear scaling, the impact of nontelecentricity needs to be minimized. One way in which this may be accomplished is through good focus control. Normally, the use of short wavelengths relaxes focus control requirements, but this assumes that the primary impact of defocus is on dimensional control. Nontelecentricity imposes tighter focus requirements.

As noted in Chapter 3, temperature control is difficult in vacuum. EUV masks are susceptible to heating, since they are ≥30% absorbent even in the areas covered by multilayer reflectors not covered by absorber. Fortunately, the use of ultra-low thermal expansion materials, such as ULE™, for the mask substrate makes requirements for mask temperature control reasonable (see Problem 7.2) even when such temperatures are not allowed to be unconstrained.

As wafers and masks heat and therefore expand, there is potential for them to slip on their chucks, which can occur in unpredictable ways. Measures have been taken in the physical design and control software for mask and wafer chucks to minimize this problem.[8] Strong friction forces between chucks and clamped substrates can also minimize slippage.[9]

Since temperature control is critical for good overlay, time is needed to ensure that masks and wafers brought into EUV systems reach thermal equilibrium with the scanner environment prior to exposure. This can reduce productivity, but it will typically not be a major issue in high-volume manufacturing, where there is a steady stream of materials going in and out of the exposure tools. As noted in Chapter 3, time is also needed for exposure systems to stabilize thermally following any events that could result in the loss of temperature control. This includes maintenance that requires opening vacuum systems.

In Chapter 3, it was noted that aberrations are effectively higher for EUV lithography than for optical lithography, in spite of mirrors with very low figure error. It is well known that aberrations can affect pattern placement, so these aberrations will have an impact on overlay. Because these vary across the slit and differ tool to tool, compensation is difficult. While it is possible to modify pattern placement on the mask to compensate for aberration-induced pattern shifts, the amount of compensation would vary across the slit. Moreover, because aberrations vary tool to tool, this would necessitate that each mask be for use specifically on a particular scanner. Compensation for certain aberrations can be corrected between fleets of EUV and immersion scanners, and this will be discussed shortly.

For i-line and ArF lithography, glass lens elements absorb a small fraction of the light, which causes heating and induces changes in the imaging. Since this effect was first identified,[10] control systems internal to the exposure tools have been implemented. Over time, such control methods have been extended to compensate for lens aberrations beyond focus and field magnification, which were the two parameters first identified as being changed by lens heating.[11] For EUV lenses, there is greater potential for heating, since EUV mirrors absorb >30% of incident light, a far greater amount than occurs in optical systems. Fortunately, there are also some methods to offset this greater absorption of light. First, EUV mirrors can be fabricated from ultra-low-thermal-expansion materials, such as ULE™ and Zerodur™, thereby reducing changes to the shapes of EUV mirrors that accompany changes in temperature. Second, the full backside of the mirror is accessible for contact, providing a large area for conducting heat from the mirror. As in optical lenses, mechanical elements can be fabricated from low-expansion materials, such as Invar. Moreover, it is possible to apply mechanical forces across the backside in order to compensate, at least partially, for changes in mirror shape due to heating. Such an approach has already been adopted for catadioptric immersion lenses.[11]

As noted in Chapter 5, there are significant benefits to using higher exposure doses to reduce photon shot noise. However, higher doses will increase the overlay problems associated with mask and wafer heating, and will also increase lens heating. Only in 2019 did EUV light sources installed on exposure tools in wafer fabs reach 250-W power levels,[12] and exposure doses for initial EUV processes used in HVM have typically been less than 50 mJ/cm^2. With low doses, it could be expected that heating might not be significant, but there can be substantial infrared light from the CO_2 laser transmitted to the reticle and through the optics. Thus, wafer heating is a concern even at low source power and low exposure doses.

There are several factors of importance for mix-and-match between immersion and EUV scanners (Table 7.2). The first of these, reticle gravitational sag, results from reticles on optical exposure tools being supported on the reticle table only along the edges of the mask, as is necessary for transmission masks.

Table 7.2 Parameters pertinent to mix-and-match overlay between immersion and EUV exposure tools.

Reticle gravitational sag
Lens distortion
Optical pellicle out-of-plane distortions during scan
Uncorrectable overlay terms in higher-order model

As a consequence of this mechanical configuration, the centers of optical reticles are unsupported and will therefore sag due to the force of gravity. There are resulting pattern placement shifts due to the out-of-plane distortion of the masks, quite similar to what is shown in Fig. 7.1. This sag tends to be the same from reticle to reticle and from tool to tool (with some small differences dependent on absorber film stress levels and percentage of absorber that is etched).[13] Consequently, the resulting pattern placement errors are nearly the same for all wafers exposed on optical tools and therefore do not contribute to overlay among such layers. The situation is different when one of the layers is patterned using EUV lithography, as the EUV mask is clamped across most of its width. Fortunately, it is possible to compensate for most of the mismatch due to differences in clamping between optical and EUV masks since the gravitational sag of optical reticles is fairly reproducible.

Another reproducible signature that is different between optical EUV scanners is related to lens distortion. For many years, lenses on wafer steppers had characteristic third- and fifth-order distortion signatures that were inherent in the designs. As lenses improved, these distortions become small. Moreover, since they are built into the lens design, these distortion errors will not contribute to layer-to-layer overlay errors when both layers are exposed on exposure tools that have the same lens design. On the other hand, for mix-and-match situations involving optical and EUV lithography, the distortions will lead to overlay errors, a significant fraction of which cannot be corrected using the higher-order overlay models, such as Eqs. (7.3) and (7.4).

It is possible to compensate for overlay errors due to reticle sag and lens distortion by adjusting the pattern placement when writing the EUV masks, correcting for the fixed differences between optical and EUV exposures. Such corrections need to be at the angstrom level at the wafer plane, so they are typically <2 nm at the mask level, often sub-nanometer. For the most part, these adjustments are within the control capabilities of advanced mask writing tools.

It has been observed that optical pellicles can deform during high-speed scans in air. Due to refraction of light, this deformation can cause patterns to shift by an amount δ:

$$\delta = t\left(1 - \frac{1}{n}\right) \sin \phi, \tag{7.5}$$

where t and n are the thickness and refractive index of the pellicle, respectively (see Fig. 4.28). This deformation can be minimized by using pellicles that are tightly stretched across the frame. Because EUV pellicles scan in vacuum, such deformations are not an issue for EUV lithography. Moreover, as noted in Chapter 4, EUV pellicles are much thinner than optical pellicles, and the index of refraction $n \approx 1$ for EUV pellicles. Hence, the placement errors induced by EUV pellicles are small (see Eq. (4.7)).

In the higher-order overlay models of Eqs. (7.3) and (7.4), certain terms in the polynomial expansion are not adjustable on scanners, according to the make and model of the exposure tool. For ASML's most advanced immersion scanners, all terms are correctable except k_{20}, while both k_{13} and k_{20} are not correctable on EUV exposure tools. Making changes on tools for which a term may be adjustable could lead to a situation where overlay subsequently cannot be corrected when using a tool on which that particular term, such as k_{13}, is not adjustable. This is clearly a problem that arises only when using optical and EUV for separate layers and when overlay between the layers is critical.

7.2 Critical Dimension Control

As with overlay, there are counterparts in optical lithography for most causes of dimensional variation in EUV lithography. Some factors, such as aberrations and flare, are more significant for EUV lithography than for optical lithography, but their impact has been well studied and characterized. Mask 3D contributions are unique to EUV lithography and were discussed in the previous chapter.

Focus is a source of dimensional variation for any type of projection lithography, but there are a couple of aspects of focus control that are notable for EUV lithography. On ASML's exposure systems, optical focus sensors are used to detect the top surface of the wafer, and such optical systems are influenced by substrate films and topography.[14,15,16,17,18] For optical exposure tools, ASML addressed this problem by introducing an air gauge sensor (AGILE) to calibrate the optical focus sensor.[19] Adapting an air gauge for vacuum systems proved difficult, so ASML improved their level sensor to be less sensitive to substrate films, as described in Section 3.6, but some sensitivity remains.[20]

The fraction of the focus budget consumed by the thickness of the resist is greater for EUV lithography than for optical lithography. It was noted many years ago that the refraction of light at the air-resist interface reduces the fraction of the focus budget taken up by the resist from the full film thickness to the thickness divided by the index of refraction of the resist.[21] For optical lithography, the index of refraction of the resist ~1.7, so this refraction has a significant impact. For EUV lithography, $n \approx 1$, so essentially the full

thickness of the resist goes into the focus budget. This becomes ever more significant as the NA is increased.

As noted in Chapter 2, the collector mirrors of LPP EUV light sources are susceptible to tin contamination, and this can affect illumination uniformity. Not only can this affect the uniformity of light intensity across the slit, but it can also modify the illumination across the pupil. Such variations across the pupil can lead to dimensional variations.

Line-edge roughness will induce linewidth variations in the absence of any other sources of dimensional variation. This has been quantified using Monte Carlo simulations[22] and analytically, under the assumption that the power spectral density (PSD) has the functional form

$$PSD(f) = \frac{2\sigma_{LER}^2 L_C}{(1 + (2\pi f L_C)^{0.5+\alpha})}, \tag{7.6}$$

where σ_{LER} and L_C are the standard deviation and correlation length of the roughness, respectively, and f is the spatial frequency. When $\alpha = 0.5$, the dimensional variation of a feature of extent W (see Fig. 7.5) due to LER that is uncorrelated between the two sides of the feature is given by[23,24]

$$\sigma_L^2 = \frac{4L_C\sigma_{LER}^2}{W}\left[1 - \frac{L_C}{W}(1 - e^{-W/L_C})\right]. \tag{7.7}$$

Consequently, LER will cause critical dimension variation, as well as affect characteristics such as transistor drive and leakage currents and electrical resistance. Correlation lengths have been found to be ≈10.0–12.5 nm in chemically amplified resists,[25] while ~6.5 nm in a scissioning resist.[26] As can be seen in Eq. (7.7), linewidth variation is less with smaller correlation lengths.

The sources of stochastic variation that lead to LER have also been found to product defects, as discussed in Section 5.2.[27] This has made it difficult to

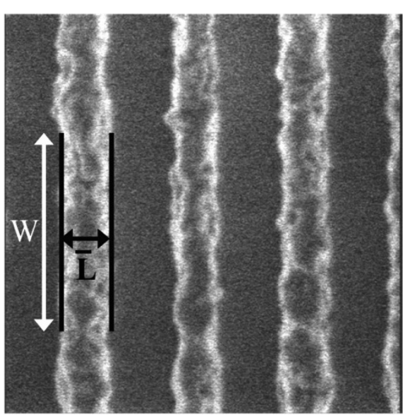

Figure 7.5 The dimension L, averaged along W, will vary line to line due to LER.

consider edge-placement errors separately from yield, as had been done for many years in optical lithography.[28] This will be discussed further, following a description of yield issues in EUV lithography in the next section.

7.3 Yield

Yield losses with lithographic origins can result from random defects, as well as parameters such as critical dimensions and overlay that are outside the specifications (particularly for layouts that have small process windows). These conventional yield problems are exacerbated by stochastic phenomena, which are significant for EUV lithography. Moreover, the statistics of edge placement variations due to critical dimension variation or overlay differ critically from the statistics of defects. This can be appreciated through the following considerations. Overlay and critical dimensions are usually controlled to the 3σ or 4σ level. A process with a mean on target and controlled to $\pm 4\sigma$ has 63 ppm out of specifications. At this level, it would be impossible to yield devices with billions of transistors if the instances when overlay or critical dimensions are out of specifications occurred randomly.

Fortunately, overlay and critical dimensions do not vary randomly. Consider, for example, overlay errors due to a wafer scaling error. In this situation, the mean overlay will vary gradually from one side of the wafer to the other. There will be large areas where overlay is within specifications everywhere, while there are other parts of the wafer where overlay is out of specifications for many features (Fig. 7.6). Similarly, for dimensional variation caused by hotplate temperature nonuniformity, the variations will typically occur over length scales of millimeters or tens of millimeters. Thus, it is possible to yield circuits that have billions of transistors even when control of overlay and critical dimensions is only to the 3σ or 4σ level, as there will be some circuits for which there are many instances when parameters are out of specifications, while all parameters will be in specifications for many other circuits.

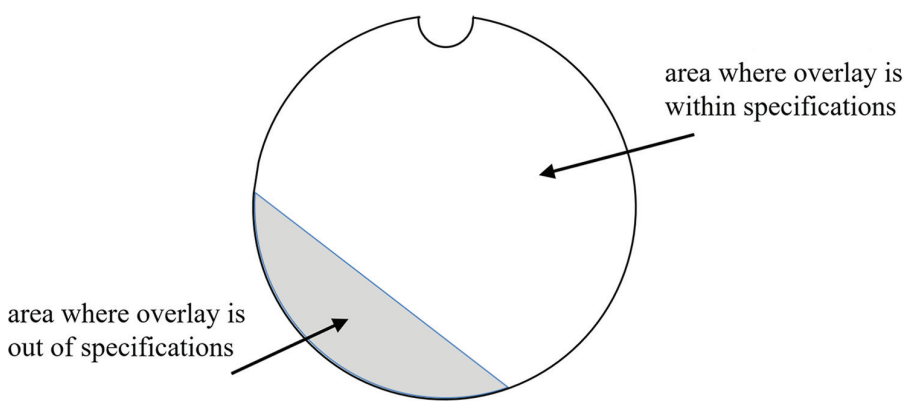

Figure 7.6 Illustration of the nonrandom variation for overlay.

On the other hand, defects due to stochastics occur locally and are generally random. The appropriate statistical requirements for random defects are very different than those with systematic characteristics. Defects at the 63-ppm ($\pm 4\sigma$) level are not adequate; levels need to be well below 1 ppb in order to yield devices with billions of transistors. This can be considered as a control level between $\pm 6\sigma$ and $\pm 7\sigma$, considerably tighter than is needed for overlay or critical dimensions (Table 7.3).

Although the emphasis thus far has been on stochastic defects, as these are of particular significance for EUV lithography, there are defects with origins similar to those that occur in optical lithography, although in EUV lithography these have more stringent requirements due to the smaller feature sizes being printed with EUV lithography and the generally higher levels of integration for integrated circuits made at the advanced nodes where EUV lithography is used. Smaller features typically necessitate improvements in filtration and the resist pumps where the point-of-use filtration takes place, and these have proven necessary for EUV lithography.[29] Although chemically amplified resists based on ArF and KrF platforms are often used for EUV lithography, their properties are somewhat different from the resists used in optical lithography. Even where the same chemical constituents are used, optimization for the use in EUV lithography has led to higher concentrations of photoacid generators and base quenchers. As a consequence, the surface properties of EUV resists are different from those used in optical lithography, necessitating optimization of rinses following development. Substantial defect reduction has been achieved by changing the filter, with the best filter sometimes varying from resist to resist.[30,31]

Yield improvement is facilitated by an understanding of the origins of defects. This makes important the ability to distinguish between defects that are caused by resist processing or poor filtering and defects originating in resist stochastics or photon shot noise. The results of a careful analysis showing how defects can largely be differentiated are summarized in Fig. 7.7. Defects consisting of residues following resist development extend over multiple features, as can some of the defects caused by in-film particles, while

Table 7.3 Control levels and failure rates, assuming that defects occur according to a normal distribution.

Control level	Failure rate
$\pm 3\sigma$	2700 ppm
$\pm 4\sigma$	63 ppm
$\pm 5\sigma$	0.57 ppm
$\pm 6\sigma$	2.0 ppb
$\pm 7\sigma$	0.0026 ppb

Defect mode		Residue	One closed hole	Multiple closed holes	Embedded	Solution in coater-developer
Image (ADI)		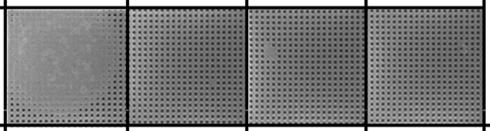				
Probable sources	Resist residue on the pattern after developing and rinse processes	✓				Optimization of rinse process
	In-film particles (resist/SOG/SOC)		✓	✓	✓	Optimization of material supply system
	Stochastic failures		✓			Searching

Figure 7.7 Defects in contacts patterned with EUV lithography. For most defects, it is possible to distinguish between those caused by resist stochastics and those with different causes.[29] SOG is spin-on-glass, and SOC is spin-on-carbon.

defects caused by stochastics are limited in extent to single features and do not show evidence of embedded particles during SEM review. This study showed that the origin of many of the defects could be identified.

Another way to distinguish defects is to look at defect density as a function of feature size (Fig. 7.8). As trenches or contacts get smaller than a certain threshold, there is an increase in bridges or closed contacts, with a

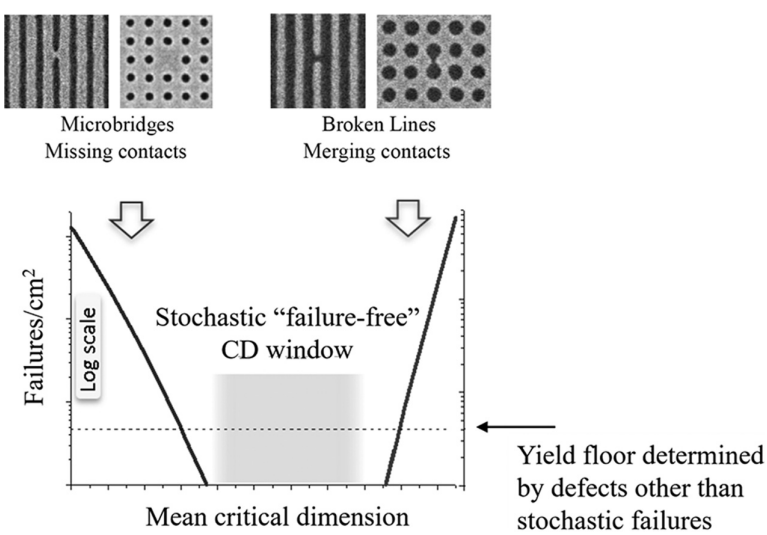

Figure 7.8 Illustration of patterning failures for dense features. The vertical axis has a logarithmic scale.[32]

trend that approximately depends exponentially on feature size. Similarly, as lines get narrow and contacts get large, there is a tendency towards line breaks and merging contacts. In between these "stochastic failure cliffs" there is a window where the level of stochastic defects should be small, so defects in this window should usually have origins other than resist stochastics.

The emergence of stochastics-induced defects has added another factor to be considered for establishing process windows. In addition to limits on the values of dose and focus determined by critical dimensions, it is also essential to constrain the ranges of these quantities to ensure levels of stochastic failures that are sufficiently low to meet yield targets.[33,34]

The analysis of yield for EUV lithography has been made more complex by the non-normal (non-Gaussian) nature of the distributions of critical dimensions.[35] An example of this is shown in Fig. 7.10, where deviations from normality are evident, particularly for small features.

The reason for this behavior can be understood as follows. Many sources of critical dimension variation can be considered as effective variations in dose.[37] This is particularly true for situations in which photon shot noise is a significant source of variation. Suppose that the distribution of effective doses is Gaussian. The resulting distribution of critical dimensions will not also be Gaussian, because critical dimension is a nonlinear function of exposure dose. A functional form that describes the relationship between dimensions and dose is[38]

$$CD = CD_0 + a\left(1 - \frac{E_0}{E}\right). \tag{7.8}$$

The resulting distribution of dimensions, due to a Gaussian distribution in dose, is shown in Fig. 7.10. As can be seen, the distribution is skewed towards smaller dimensions, similar to the result of rigorous simulation (Fig. 7.9).

In order to maximize the value of wafers, layouts with very tight process windows are often used, in order to get the most dies possible on each wafer. This often results in situations where particular layouts, often referred to as "hot spots," may have sufficiently large failure rates to affect yield at undesirable levels. In the early phases of technology development, hot spot failures may not be noticed, as there may be other, more significant sources of yield loss. As technologies mature and overall yield improves, the yield loss due to hot spots may become apparent. Since these failures do not occur regularly, they are sometimes referred to as "soft" failures.[39] Resist stochastics also contribute to the irregular occurrence of such defects, as shown in Fig. 6.18.

Several steps are useful for reducing yield losses from hot spots. The inclusion of stochastic variation in the calculations of PVbands enables many potential hot spots to be identified during the layout process, and they can be modified. If layout modifications result in logic or memory cell sizes that are

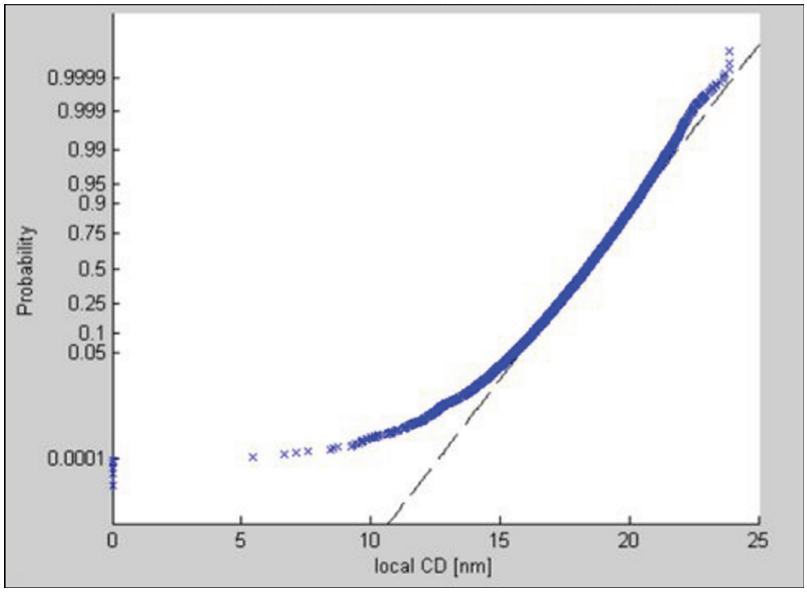

Figure 7.9 Simulated distribution of printed critical dimensions of a nominal 17.5-nm line, for 0.33-NA exposure and quadrupole illumination, using a stochastic resist model.[36]

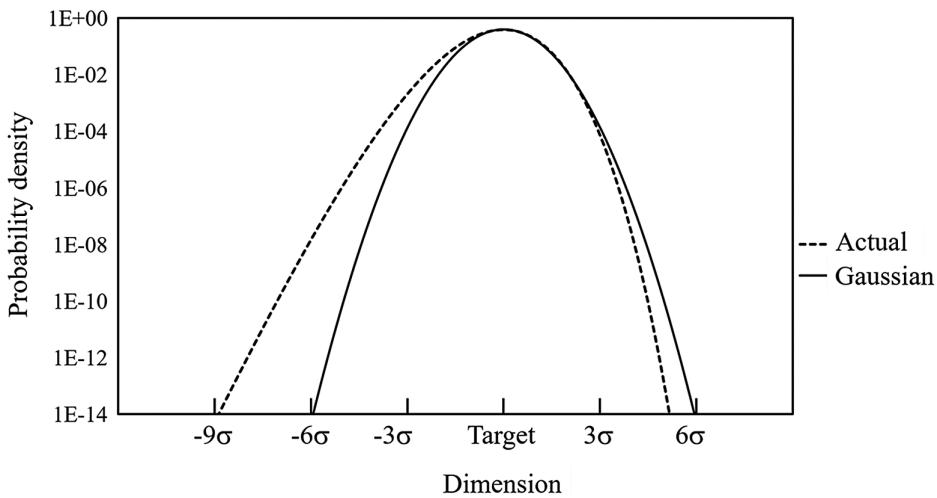

Figure 7.10 Probability density functions, illustrating the skewed distribution of dimensions due to the nonlinear relationship between dose and dimension.

unacceptably big, the use of different resists that have lower levels of stochastics may be necessary. This may require higher exposure doses. The inverse lithography techniques described in the previous chapter are often effective at enlarging process windows, thereby reducing the number of instances when defects form at such "hot spots."

Problems

7.1 Suppose that mask backside nonflatness is given by

$$z(x) = A\cos^2\frac{\pi x}{W}, \tag{7.e}$$

where $A = 20$ nm, and $W = 10$ mm. Show that the maximum pattern placement error after the mask is chucked is 5 nm.

7.2 The coefficient of thermal expansion (CTE) of ULE is approximately at linear function of temperature for temperatures near 20°C:

$$\mathrm{CTE}(T) = 1.67T - 33.4, \tag{7.f}$$

where the temperature T is measured in Celsius, and the CTE is in units of ppb/°C. Show that two features separated by 100 mm on a mask fabricated by ULE will move apart by ~0.4 nm when the mask is heated by 2°C.

7.3 Suppose the projection optics has six mirrors, each of which reflects 65% of the incident light. Suppose also that the multilayer reflector also has 65% reflectance. Show that the power incident on the wafer is ~2.5% of that incident on the mask, assuming that the pattern density on the mask is 50% absorber.

References

1 A. H. Gabor, A. C. Brendler, T. A. Brunner, X. Chen, J. A. Culp, and H. J. Levinson. "Edge placement error fundamentals and impact of EUV: will traditional design-rule calculations work in the era of EUV?" *Journal of Micro/Nanolithography, MEMS, and MOEMS* **17**, no. 4 (2018): 041008.

2 S. Raghunathan, O. Wood, P. Vukkadala, R. Engelstad, B. Lee, S. Bouten, T. Laursen, J. Zimmerman, J. Sohn, and J. Hartley. "A study of reticle nonflatness induced image placement error contributions in EUV lithography," *Proc. SPIE* Vol. **7636**, p. 76360W, 2010.

3 M. Chandhok, S. Goyal, S. Carson, S. Park, G. Zhang, A. M. Myers, M. L. Leeson, et al. "Compensation of overlay errors due to mask bending and nonflatness for EUV masks," *Proc. SPIE* Vol. **7271**, p. 72710G, 2009.

4 X. Chen, C. Turley, J. Rankin, T. Brunner, and A. Gabor. "Minimizing wafer overlay errors due to EUV mask nonflatness and thickness variations for N7 production," *Proc. SPIE* Vol. **10143**, p. 101431F, 2017.

5 X. Chen, A. Gabor, P. Samudrala, S. Meyers, E. Hosler, R. Johnson, and N. Felix. "Mix-and-match considerations for EUV insertion in N7 HVM," *Proc. SPIE* Vol. **10143**, p. 101430F, 2017.

6 H. Levinson and T. White. "Method and system for flattening a reticle within a lithography system." U.S. Patent 7, 199, 994, issued April 3, 2007.
7 S. Raghunathan, O. R. Wood, P. Mangat, E. Verduijn, V. Philipsen, E. Hendrickx, R. Jonckheere, et al. "Experimental measurements of telecentricity errors in high-numerical-aperture extreme ultraviolet mask images," *J. Vac Sci. Technol.* Vol. **B32**(6), (2014): 06F801.
8 P. Kochersperger, "Overlay correction by reducing wafer slipping after alignment." U.S. Patent 7, 542, 263, issued June 2, 2009.
9 C. J. Martin, A. R. Mikkelson, R. O. Tejeda, R. L. Engelstad, E. G. Lovell, K. L. Blaedel, and A. A. Claudet. "Mechanical modeling of the reticle and chuck for EUV lithography," *Proc. SPIE* Vol. **4688**, pp. 194–204, 2002.
10 T. A. Brunner, J. G. Lewis, and M. P. Manny. "Stepper self-metrology using automated techniques," *Proc. SPIE* Vol. **1261**, pp. 286–297, 1990.
11 Y. Yoda, A. Hayakawa, S. Ishiyama, Y. Ohmura, I. Fujimoto, T. Hirayama, Y. Shiba, K. Masaki, and Y. Shibazaki, "Next-generation immersion scanner optimizing on-product performance for 7 nm node," *Proc. SPIE* Vol. **9780**, p. 978012, 2016.
12 M. Mastenbroek, "Progress on 0.33 NA EUV systems for High-Volume Manufacturing," *Proc. SPIE* Vol. **11147**, p. 1114703, 2019.
13 A. R. Mikkelson, R. L. Engelstad, E. G. Lovell, Theodore M. Bloomstein, and M. E. Mason, "Mechanical distortions in advanced optical reticles," *Proc. SPIE* **3676**, pp. 744–755, 1999.
14 T.O. Herndon, C.E. Woodward, K.H. Konkle, and J.I. Raffel, "Photo-composition and DSW autofocus correction for wafer-scale lithography," *Proc. Kodak Microelectron. Sem*. pp. 118–123 (1983).
15 B. La Fontaine, J. Hauschild, M. Dusa, A. Acheta, E. Apelgren, M. Boonman, J. Krist, A. Khathuria, H. Levinson, A. Fumar-Pici, and M. Pieters, "Study of the influence of substrate topography on the focusing performance of advanced lithography scanners," *Proc. SPIE* **5040**, pp. 570–581 (2003).
16 J. E. van den Werf, "Optical focus and level sensor for wafer steppers," *J. Vac. Sci. Tech.* **10**(2), pp. 735–740 (1992).
17 T. Tojo, M. Tabata, Y. Ishibashi, H. Suzuki, and S. Takahasi, "The effect of intensity distribution in the reflected beam on the detection error of monochromatic optical autofocus systems," *J. Vac. Sci. Tech. B* **8**(3), pp. 456–462 (1990).
18 M. A. van den Brink, J.M.D. Stoeldraijer, and H. F. D. Linders, "Overlay and field-by-field leveling in wafer steppers using an advanced metrology system," *Proc. SPIE* **1673**, pp. 330–344 (1992).
19 F. Kahlenberg, R. Seltmann, B. M. La Fontaine, R. Wirtz, A. Kisteman, R. N. M. Vanneer, and M. Pieters, "Best focus determination: bridging

the gap between optical and physical topography," *Proc. SPIE* **6520**, p. 65200Z, 2007.

20 W. P. de Boeij, R. Pieternella, I. Bouchoms, M. Leenders, M. Hoofman, R. de Graaf, H. Kok, P. Broman, J. Smits, J. J. Kuit, and M. McLaren, "Extending immersion lithography down to 1x nm production nodes." *Proc. SPIE* **8683**, p. 86831L, 2013.

21 W. H. Arnold and H. J. Levinson. "Focus: the critical parameter for submicron optical lithography: part 2," *Proc. SPIE* Vol. **772**, pp. 21–34, 1987.

22 Y. Ma, H. J. Levinson, and T. Wallow, "Line edge roughness impact on critical dimension variation," *Proc. SPIE* **6518**, 651824 (2007).

23 G. F. Lorusso, P. Leunissen, M. Ercken, C. Delvaux, F. Van Roey, N. Vandenbroeck, H. Yang, A. Azordegan, and T. DiBiase, "Spectral analysis of line width roughness and its application to immersion lithography," *J. Microlith. Microfab. Microsyst.* **5**(3), 033003-1– 03003–6 (2006).

24 C. A. Mack, "Analytical expression for the impact of linewidth roughness on critical dimension uniformity," *J. Micro/Nanolith. MEMS MOEMS*, 020501-1– 020501–3 (2014).

25 R. Fallica, E. Buitrago, and Y. Ekinci, "Comparative study of line roughness metrics of chemically amplified and inorganic resists for extreme ultraviolet." *Journal of Micro/Nanolithography, MEMS, and MOEMS* **15**, no. 3 (2016): 034003.

26 A. Shirotori, Y. Vesters, M. Hoshino, A. Rathore, D. De Simone, G. Vandenberghe, and H. Matsumoto, "Development of main chain scission type photoresists for EUV lithography," *Proc. SPIE* **11147**, p. 111470J, 2019.

27 P. De Bisschop, "Stochastic effects in EUV lithography: random, local CD variability, and printing failures," *Journal of Micro/Nanolithography, MEMS, and MOEMS* **16**, no. 4 (2017): 041013.

28 A. H. Gabor, A. C. Brendler, T. A. Brunner, X. Chen, J. A. Culp, and H. J. Levinson, "Edge placement error fundamentals and impact of EUV: will traditional design-rule calculations work in the era of EUV?" *Journal of Micro/Nanolithography, MEMS, and MOEMS* **17**, no. 4 (2018): 041008.

29 Y. Kamei, S. Kawakami, M. Tadokoro, Y. Hashimoto, T. Shimoaoki, M. Enomoto, K. Nafus, A. Sonoda, and P. Foubert, "Improvement of CD stability and defectivity in resist coating and developing process in EUV lithography process," *Proc. SPIE* Vol. **10809**, p. 1080924, 2018.

30 A. Dauendorffer, T. Shiozawa, K. Yoshida, N. Nagamine, Y. Kamei, S. Kawakami, S. Shimura, K. Nafus, A. Sonoda, and P. Foubert. "CLEAN TRACK solutions for defectivity and CD control towards 5 nm and smaller nodes," *Proc. SPIE* **11323**, p. 113232A, 2020.

31 L. D'Urzo, H. Bayana, J. Vandereyken, P. Foubert, A. Wu, J. Jaber, and J. Hamzik. "Continuous improvements of defectivity rates in immersion photolithography via functionalized membranes in point-of-use photochemical filtration," *Proc. SPIE* **10146**, p. 101462A (2017).
32 P. De Bisschop, "Stochastic printing failures in extreme ultraviolet lithography." *Journal of Micro/Nanolithography, MEMS, and MOEMS* **17**, no. 4 (2018): 041011.
33 P. De Bisschop and E. Hendrickx, "On the dependencies of the stochastic patterning-failure cliffs in EUVL lithography," *Proc. SPIE* **11323**, p. 113230J, 2020.
34 P. De Bisschop and E. Hendrickx, "Stochastic printing failures in EUV lithography," *Proc. SPIE* **10957**, p. 109570E, 2019.
35 R. L. Bristol and M. E. Krysak. "Lithographic stochastics: beyond 3σ." *Journal of Micro/Nanolithography, MEMS, and MOEMS* **16**, no. 2 (2017): 023505.
36 T. A. Brunner, X. Chen, A. Gabor, C. Higgins, L. Sun, and C. A. Mack. "Line-edge roughness performance targets for EUV lithography," *Proc. SPIE* **10143**, p. 101430E, 2017.
37 H. J. Levinson, Y. Ma, M. Koenig, B. La Fontaine, and R. Seltmann. "Proposal for determining exposure latitude requirements," *Proc. SPIE* **6924**, p. 69241J, 2008.
38 C. P. Ausschnitt and T. A. Brunner, "Distinguishing dose, focus, and blur for lithography characterization and control," *Proc. SPIE* **6520**, p. 65200M, 2007.
39 Yuansheng Ma, private communication.

Chapter 8
Metrology for EUV Lithography

Much of the metrology for EUV lithography is similar to that for optical lithography, with the caveat that EUV lithography is practiced at very small dimensions. Measurements of overlay and critical dimensions are needed, but since they have the same issues as they did for optical lithography, they will not be discussed in detail in this book. On the other hand, there are aspects of EUV technology without counterparts in optical lithography, mostly related to masks and pellicles, and these have special metrology requirements. Importantly, many metrology tools involve measurement at EUV wavelengths, which necessitates the use of specialized light sources and operation in vacuum.

Measurement tools are needed for the development and manufacturing of certain components, such as EUV mask blanks. These are of interest to practicing lithographers, even though such tools are not necessarily used in wafer fabs or masks shops, since it is often important for lithographers to understand the quality control capabilities of their suppliers. One of the earliest tools to be built in support of EUV technology development was a reflectometer at EUV wavelengths.[1] Such tools are used to measure multilayer reflectivity and uniformity on EUV mask blanks. Typically arranged to provide measurements of reflectivity at a 6° angle of incidence, the same as the chief ray angle of 0.33-NA exposure tools, these reflectometers can measure absolute reflectance over a range of wavelengths about 13.5 nm. These data can be used to determine the wavelength of peak reflectivity and the reflectance uniformity across mask blanks. Prior to the introduction of such standalone tools in 2002, measurements of reflectivity at EUV wavelengths were typically performed at electron storage rings. Standalone tools are much more convenient for manufacturers of EUV mask blanks. They can also be used to measure the impact of processing on multilayer reflectivity and changes in reflectivity over time. Standalone tools are currently available from EUV Technology, Inc.[2] and Research Instruments GmbH.[3] Laboratories using synchrotron light sources continue to provide important calibration (as well as other) services.[4,5,6]

8.1 Mask Blank Defect Inspection

The topic of phase defects in EUV mask blanks was discussed in Chapter 4, where it was noted that it is possible for very small defects to be printable. Because of their small size and their phase nature at EUV wavelengths, inspecting for these defects has represented a metrology challenge using DUV inspection tools, both for reasons of resolution and limited sensitivity to phase defects. DUV light does not penetrate far into Mo/Si multilayers (Fig. 8.1), further reducing the effectiveness of non-actinic defect inspection. Nevertheless, good progress was made to reduce EUV mask blank defects using optical inspection tools, notably the Lasertec M1350 (λ = 488 nm) and M7360 (λ = 266 nm) systems. Although the penetration into Mo/Si multilayers is less at $\lambda = 266$ nm than at 488 nm, the shorter wavelength provided better resolution and overall better inspection capability.

The sensitivity of optical inspection for detecting small bumps and pits, which can result in printable phase defects, can be increased by using phase contrast imaging for inspection (Fig. 8.2). Intensities for the interference between rays reflected from the top of a bump (or bottom of a pit) and rays reflected from the flat portion of the substrate are proportional to the square of the phase difference δ, which can be small for small values of δ (see Problem 8.1). On the other hand, phase contrast methods generate signals that are directly proportional to the phase difference, thereby improving detection.[10] This has enabled the use of DUV inspection tools, such as the Teron Phasur tool from KLA,[11] to find many (but not all) phase defects that otherwise were not detected by direct mask blank inspection at DUV wavelengths.

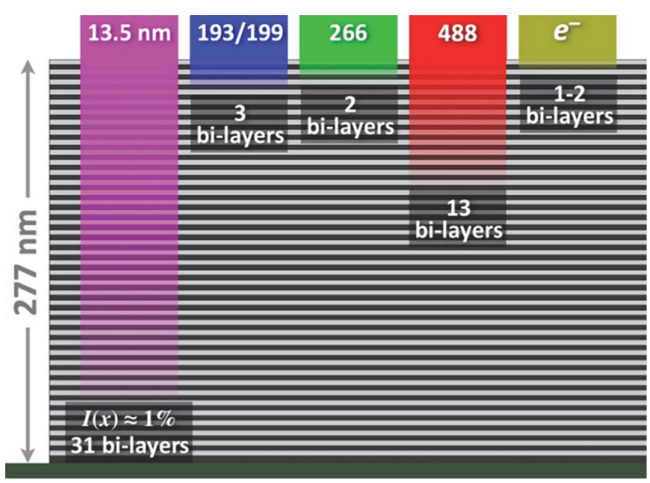

Figure 8.1 The penetration of light at various wavelengths through Mo/Si multilayers.[7,8,9] The number of bilayers is indicated through which the light propagates before falling to 1% of the initially transmitted value.

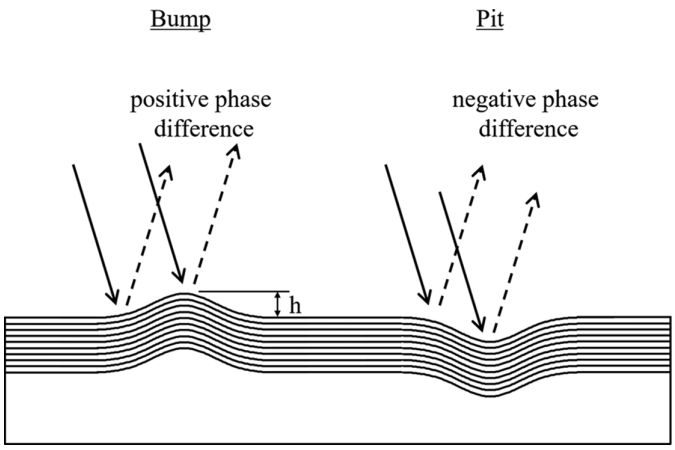

Figure 8.2 Illustration of phase differences in reflected light rays due to bumps and pits in the surface being measured.[12] Measurement systems that can distinguish positive and negative phase differences enable classification of defects as bumps or pits.

Advances in metrology were essential for the production of HVM-quality EUV mask blanks. In going from the M1350 measurement tool to the more sensitive Teron Phasur inspection system, nearly three orders of magnitude more defects were found.[13] The ability to measure is foundational for improvement, so the improved metrology at DUV wavelengths was invaluable, and it led to considerable improvement in the number of defects in EUV masks blanks.

In spite of the advances in optical defect measurement, studies found that not all printable defects were found by optical inspection[11,14] (Fig. 8.3). Consequently, there were activities to develop actinic mask blank inspection tools. Initially, development took place through research consortia, such as Sematech and MIRAI-SELETE in Japan. Eventually, the core technology was transferred to Lasertec,[15] resulting in the ABICS E120 actinic blank inspection tool (Fig. 8.4) that is now commercially available.

In addition to finding defects, mask blank inspection tools also need to be able to determine the locations of detected defects, relative to mask fiducials, with nanometer accuracy, in order to support the pattern-shift defect mitigation scheme described in Chapter 4.[17] Accordingly, mask blank inspection tools need to have systems that can align to mask fiducials, and such tools also need to have precise stages. The requirements for alignment capability, precise stages, and inspection at EUV wavelengths combine to increase the cost of blank inspection tools, ultimately increasing the costs of EUV masks, relative to optical masks.

Many small defects, although detectable on an actinic inspection tool, may not print. For distinguishing between printable and unprintable defects, the ABICS E120 tool can be switched from a scanning mode to a

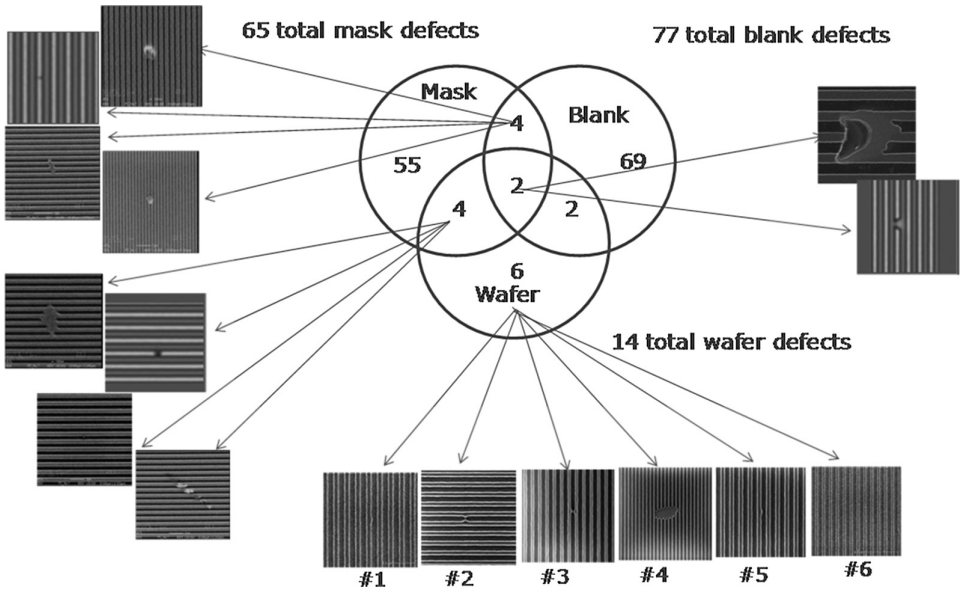

Figure 8.3 Venn diagram of blank, mask and wafer defects, along with representative SEM images.[11]

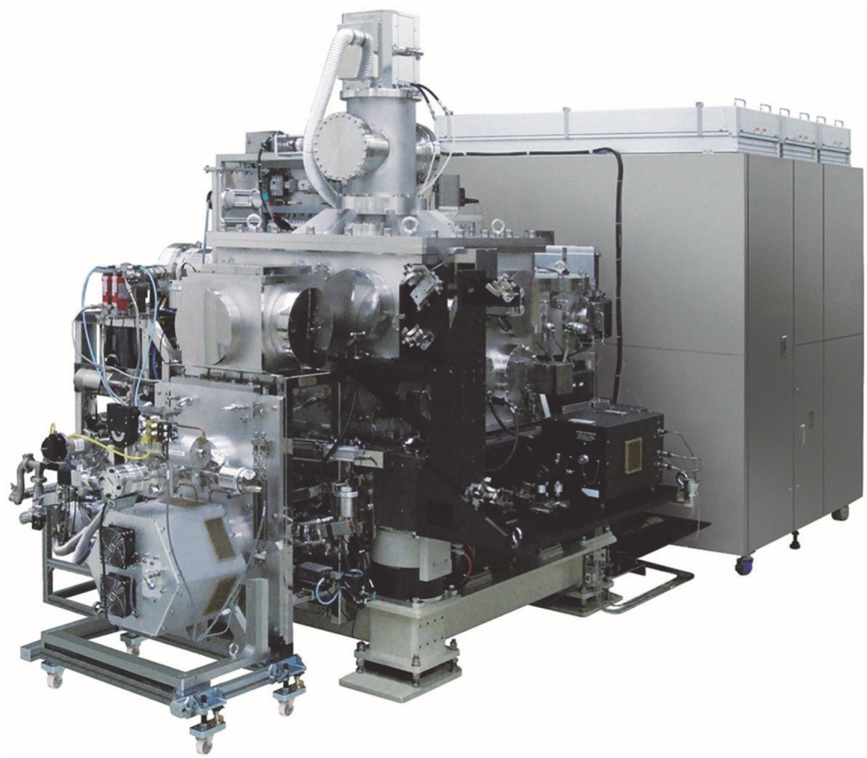

Figure 8.4 Picture of the Lasertec ABICS E120 actinic blank inspection tool.[16]

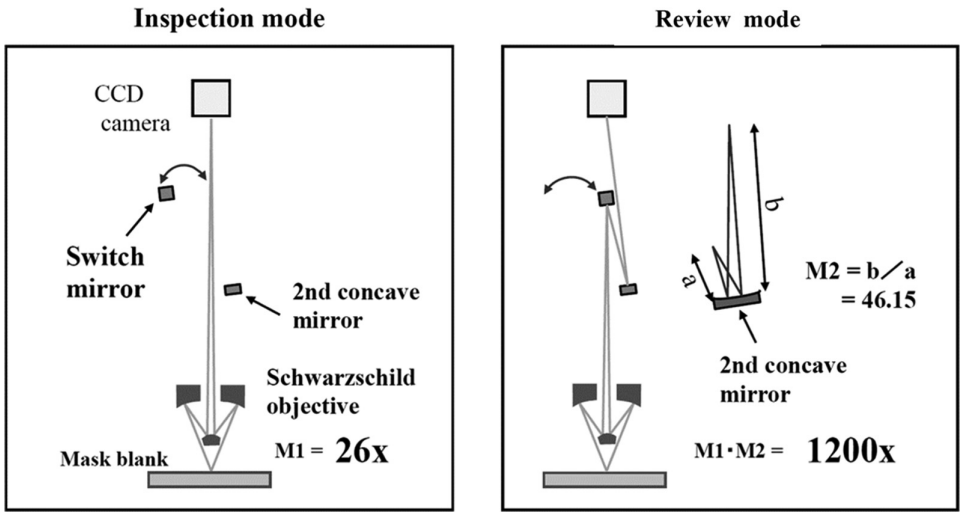

Figure 8.5 Two modes of operation of the ABICS E120 actinic blank inspection tool. The mode depicted on the left is used for detecting defects, while the configuration on the right is used for reviewing defects at high magnification.[18]

high magnification review mode (Fig. 8.5). Scanning a mask blank is targeted to take less than 45 minutes, in order to meet the needs of HVM.

8.2 EUV Mask Qualification Tools

Another type of tool used to review defects is the Aerial Image Measurement System—AIMS™. This class of tools emulates the projection optics and illumination of exposure tools, enabling direct measurements of aerial images. Such metrology tools have long been used in optical lithography to determine whether or not mask defects need to be repaired, and if so, the tools can subsequently be used to assess the efficacy of the repair. Such capabilities are also of value for EUV lithography. Intrinsically, AIMS tools need to operate at actinic wavelengths. Images from an AIMS tool built by Carl Zeiss were shown in Fig. 4.17. These images provided direct measurements of the image LER induced by mask blank surface roughness.

The situation for EUV lithography is somewhat more complex than that which occurs in optical lithography, since the angle of incidence on the mask varies across the illumination slit, as described in Chapter 3. For the EUV AIMS tool built by Zeiss, the angle of incidence for the illumination is fixed, regardless of position on the mask. Calculations are used to account for the effects of the varying azimuthal angles.[19]

Predecessors of the EUV AIMS tool were mask inspection microscopes using synchrotron light sources (Fig. 8.6). These tools provided researchers with aerial image measurement capability that was important for the

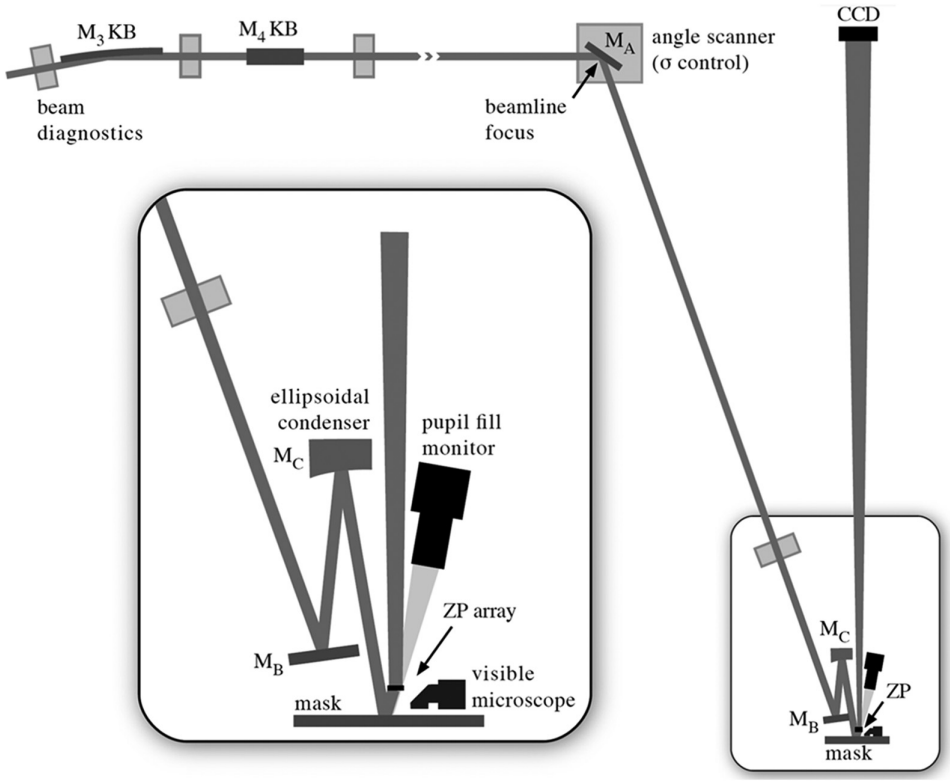

Figure 8.6 Schematic of a synchrotron-light-source-based EUV Fresnel zone plate mask-imaging microscope.[22]

development of EUV mask technology. Two such tools, the Actinic Inspection Tool (AIT) and the Sematech High-NA Actinic review Project (SHARP), were supported by Sematech and used the Advanced Light Source (ALS) at Lawrence Berkeley National Laboratory. The SHARP tool continues to be used under the auspices of the EUREKA consortium.[20] There were also tools developed and deployed in Japan.[21] For these inspection microscopes, Fresnel zone plates were typically used for the optics (Fig. 8.7).[22] Although the imaging of such optics differed somewhat from that of mirror-based projection optics, the zoneplates had the virtue of being relatively easy to fabricate, across a range of numerical apertures, thus enabling early studies of mask defects. Various types of illumination could be created by the use of a movable mirror that scanned the illumination at various angles. Such tools were used by chip makers to explore mask defect printability.[23] More recently, a mask imaging microscope employing zone plate optics has been used for qualifying EUV masks, essential in place of an AIMS tool.[24] Although the imaging with zone plates does not match exposure tools optics as well as an AIMS tool with reflective optics, it provides useful capability at a relatively low cost.

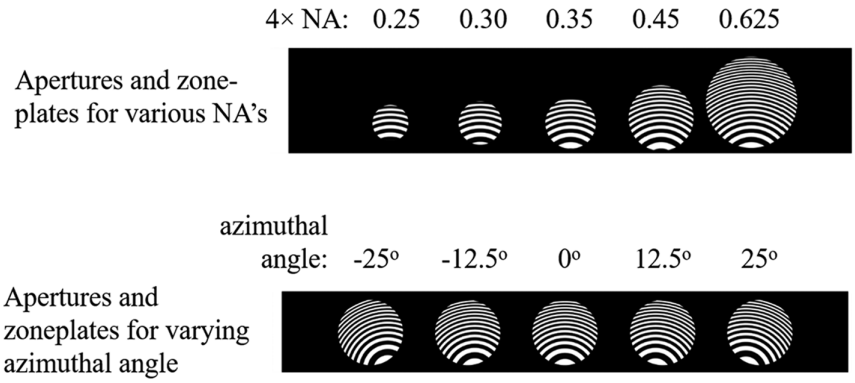

Figure 8.7 Schematic representations of arrays of off-axis zone plates. The top array is for different NAs and angles of incidence. Black areas are opaque to EUV light. The bottom array shows zone plates for emulating the variations across the curved slits of EUV exposure tools.[22]

8.3 Tools for Qualifying Fabricated Masks

Another requirement unique for EUV lithography is reticle backside defect inspection. As noted in Chapter 4, defects on the backsides of masks can cause overlay errors, and it is important to detect backside defects before the masks are loaded into exposure tools; otherwise, the particle could transfer to the mask chuck, in which case it would be necessary to do exposure tool maintenance, bringing at least part of the tool up to air.

Many of the tools available for detecting particles on unpatterned reticles can be used to inspect reticle backsides. However, what is important for the inspection of EUV mask backsides is the height of the particles, more so than their lateral extent, and not all tools that detect particles on unpatterned surfaces are capable of height measurements. One set of tools that can measure particle heights is the Lasertec BASIC series, which also incorporates mask backside cleaning capabilities.[25]

The size of particle that can be tolerated is a critical factor. If the full height of a backside particle would be manifest as frontside non-flatness, extremely stringent backside cleanliness would be required. Fortunately, clamping of the reticle to the electrostatic chuck results in compression of the particle and deformation of the mask substrate, so that the full particle height does not transfer to the frontside.[26] Examples of calculated deformations are shown in Fig. 8.8. Particles softer than the substrate are crushed during clamping, while harder particles become embedded into the mask substrate. Even in the latter case, a degree of particle compression can be seen, as well as that of the mask substrate material (ULE). Because the backside conducting coating is very thin, it does not have a significant impact on the mechanical deformations. Currently, it is assumed that backside particles <10 μm can be tolerated.[27]

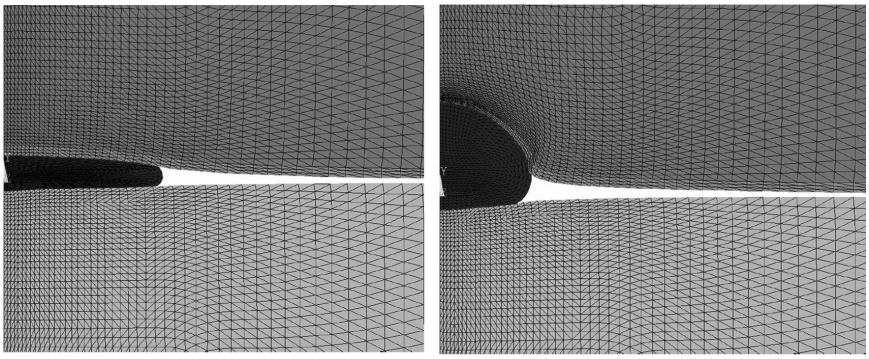

(a) (b)

Figure 8.8 The results of finite-element calculations of the clamping of an EUV mask with an initially spherical 1.0-mm backside particle.[26] (a) The particle has lower yield strength than the mask substrate; and (b) the particle has higher yield strength.

Note that ASML offers a Reticle Backside Inspection (RBI) option that can be used to detect backside defects without removing reticles from the exposure tool.[27] This is efficient for determining whether or not reticle backsides have become contaminated or damaged during usage, while standalone backside inspection tools can be used to avoid putting contaminated reticles into the exposure tools. Such standalone backside defect inspection tools are useful in both mask shops and wafer fabs.

Inspecting patterned masks for defects at the exposure wavelength or a wavelength close to the exposure wavelength has long been a practice in optical lithography. This has been done for two important reasons. First, shorter exposure wavelengths have been used to print smaller features, which resulted in a need for inspecting masks at higher resolution, something that was facilitated by inspecting at shorter wavelengths. Inspection at or near the exposure wavelength also ensured that the inspection images were more representative of the actual lithographic imaging process.

These issues are particularly relevant for EUV lithography. As noted earlier in this chapter, phase defects are not reliably detected at non-actinic wavelengths, so there are advantages for inspecting patterned mask at EUV wavelengths, just as there was for qualifying mask blanks. In spite of the clear advantages and prior practice of inspecting mask at or near the exposure wavelength, the expected cost and poor reliability of EUV patterned mask defect inspection tools, coupled with the size of the expected market, delayed the development of such tools until very recently. The first such commercially available tool, the ACTIS A150 from Lasertec, was announced in 2019.[28,29,30]

In addition to phase defects, the size of features on EUV masks represents an additional challenge for defect inspection. With EUV lithography being introduced at ~40-nm pitch at the wafer level, this results in ~80-nm

minimum primary features on the mask, with SRAFs of ~50 nm or somewhat smaller in size. Such feature sizes are at the edge of (or beyond) the resolution of DUV inspection tools. For example, measuring defects on 24 nm (at wafer level) trenches was found to be marginal using 193-nm inspection tools.[30] Hence, for first-generation EUV lithography, optical inspection tools provided only marginally adequate resolution capability, while better resolution will be needed for subsequent nodes to avoid situations where mask defects are first detected on printed wafers. The ability to inspect EUV mask blanks with actinic tools has reduced the concern over detecting phase defects, since those in the multilayers will already have been found when the blanks were inspected, but high efficacy of pattern shift for mitigated blank defects is needed.

Ever since it was first recognized that the printability of mask defects was dependent on their proximity to features as well as their size,[31] mask defect printability has been studied upon introduction of every new lithographic technology. Printability is relevant for the appropriate resolution of defect inspection and also the dispositioning of defects once detected. An example of results from a study of mask substrate defect printability is shown in Fig. 8.9 for equal line/space gratings of 16-nm to 22-nm half-pitch. In the case of defects that produce strong signals, the situation is unambiguous, and the defects print across multiple lines and spaces. Many small defects that could be detected by the actinic blank inspection tool were not found to print. Characterization for a specific process is needed to avoid rejection of masks with defects that are unlikely to print.

To address the fundamental resolution requirements for EUV patterned-mask defect inspection tools, electron beam systems are being given serious consideration.[33] This is particularly important for wafer defect inspection, which involves features typically smaller than those on 4× masks, even taking sub-resolution assist features into consideration. In general, this would not be considered an EUV-specific issue, but wafer prints are often used to determine whether or not there are printable defects on EUV masks. As with beam writers, multibeam defect inspection systems are being developed to address the speed problem inherent in single-beam tools.[34]

A very innovative method for defect inspection that is in the early stages of development is ptychography, where only the intensity of the light that is scattered is measured. Overlapping regions are illuminated by a coherent beam of EUV light, and the phase information of the image is constructed using the information redundancy of the overlapping illuminated regions.[35,36] Image construction is facilitated for mask inspection because there is knowledge from the design about what is being imaged. Ptychography is a lensless technology; the only optics are the mirrors used to focus the beam onto the mask. Such mirrors are small and have far less stringent requirements

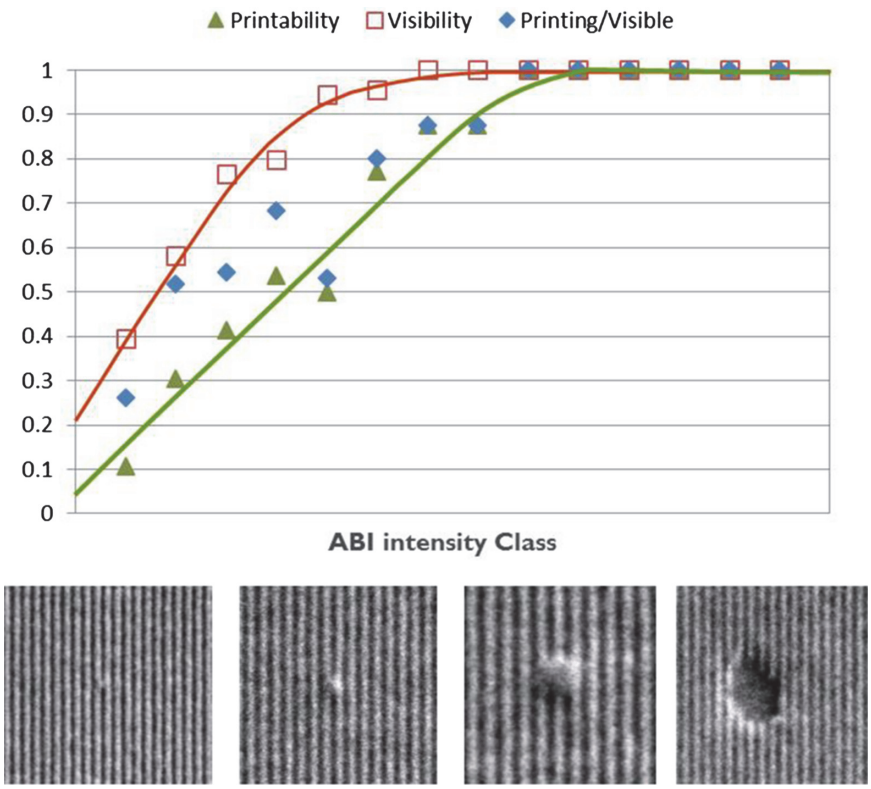

Figure 8.9 Printability on an 0.33-NA EUV exposure tool and visibility as a function of the ABI signal intensity.[32]

than the optics of high-resolution imaging systems. This means that actinic defect inspection systems could be built with inexpensive optics.

8.4 Tools for Material Testing

The consideration of pellicles for EUV masks comprising thin membranes has been accompanied by a need for measurement of critical parameters, such as transmission. Tools for measuring transmission and uniformity of EUV pellicles are available from EUV Technology, Inc.[37,38] and Research Instruments GmbH.[39] Because of the reflection geometry for EUV lithography, the EUV and DUV reflectance from the pellicle, unless very small, can cause unintended exposure of resist (Fig. 8.10), so measurement tools are also needed to provide capability for measuring light reflectivity from pellicles at EUV and non-actinic wavelengths.

People developing materials for EUV lithography need many other types of specialized measurement equipment that may not be needed by lithographers who work in wafer fabs. For example, for the development of

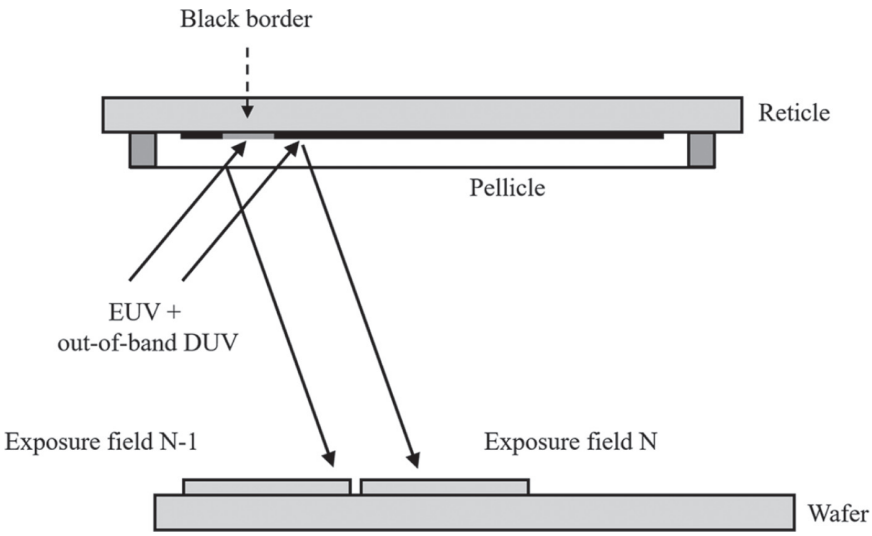

Figure 8.10 In-band and out-of-band light can expose field $N - 1$ during the exposure of field N, even for a mask with a black border, due to reflections from the pellicle.[40]

pellicles, tools are needed to measure their mechanical strength or resilience to a pressure differential between the two sides of the pellicle. Such tools have been built for these specialized test purposes in support of the development of EUV pellicles,[41] even though such tools may not be needed in wafer fabs or even mask shops.

For many years there was considerable concern about materials outgassing from EUV resists and contaminating the exposure tool optics. Consequently, tools were built to measure material deposition on a witness plate, resulting from the exposure of resist to radiation (see Fig. 8.11).[42,43,44] Because deposition on optics can be affected by EUV light, the witness plate was typically exposed to EUV light during the testing and comprised

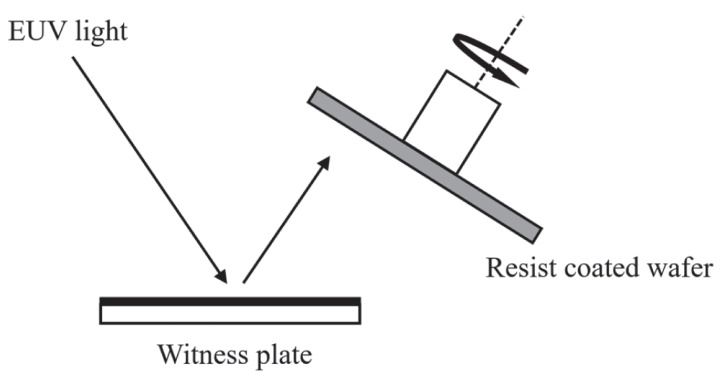

Figure 8.11 System for measuring resist outgassing.[44] The resist and witness plate could also be exposed using electron beams.

ruthenium-coated multilayers, similar to surfaces of the mirrors used in EUV projection optics. The resist could be exposed with EUV light or electrons. Composition of the materials deposited on the witness plate was typically measured, in addition to total quantity, because of a different degree of concern between the deposition of materials such as carbon, which could be cleaned from the optics, and other materials, such as a metal that cannot. Such systems are available at research centers to support the development of new resist platforms.[45]

Problems

8.1 Consider two plane waves Ae^{ikx} and $Ae^{i(kx+\delta)}$, shifted in phase by δ, that combine coherently:

$$Ae^{ikx} + Ae^{i(kx+\delta)}. \tag{8.1}$$

Show that the change in intensity due to the phase shift is proportional to δ^2.

References

1 D. C. Houser, F. Dong, C. N. Perera, and R. C. C. Perera. "Challenges in constructing EUV metrology tools to qualify the EUV masks for HVM implementation," *Proc. SPIE* **9661**, p. 96610K, 2015.
2 https://www.euvtech.com/
3 https://research-instruments.de
4 C. Laubis, A. Babalik, A. Babuschkin, A. Barboutis, C. Buchholz, A. Fischer, S. Jaroslawzew, et al. "Photon detector calibration in the EUV spectral range at PTB," *Proc. SPIE* **10957**, p. 109571, 2019.
5 K. Tsuda, T. Harada, and T. Watanabe, "Development of an EUV and OoB Reflectometer at NewSUBARU synchrotron light facility," *Proc. SPIE* **11148**, p. 111481N, 2019.
6 R. Miyakawa and P. Naulleau, "Preparing for the Next Generation of EUV Lithography at the Center for X-ray Optics," *Synchrotron Radiation News* **32**, no. 4 (2019): 15–21.
7 A. Barty, K. A. Goldberg, P. Kearney, S. B. Rekawa, B. LaFontaine, O. Wood II, J. S. Taylor, and H-S. Han, "Multilayer defects nucleated by substrate pits: a comparison of actinic inspection and non-actinic inspection techniques," *Proc. SPIE* **6349**, p. 63492M, 2006.
8 K. A. Goldberg, A. Barty, P. Seidel, K. Edinger, R. Fettig, P. Kearney, H. Han, and O. R. Wood II, "EUV and non-EUV inspection of reticle defect repair sites," *Proc. SPIE* **6517**, p. 65170C, 2007.
9 H. J. Kwon, J. Harris-Jones, R. Teki, A. Cordes, T. Nakajima, I. Mochi, K. A. Goldberg, Y. Yamaguchi, and H. Kinoshita, "Printability of native

blank defects and programmed defects and their stack structures," *Proc. SPIE* **8166**, p. 81660H. 2011.

10 J. W. Goodman, "Introduction to Fourier Optics," McGraw-Hill, San Francisco (1968).

11 U. Okoroanyanwu, J. Heumann, X. Zhu, C. H. Clifford, F. Jiang, P. Mangat, R. Ghaskadavi, et al, "Towards the optical inspection sensitivity optimization of EUV masks and EUVL-exposed wafers," *Proc. SPIE* **8352**, p. 83520V, 2012.

12 S. Stokowski, J. Glasser, G. Inderhees, and P. Sankuratri, "Inspecting EUV mask blanks with a 193nm system," *Proc. SPIE* **7636**, p. 76360Z, 2010.

13 S-S. Kim, "EUV Lithography– Progress and Perspective," *presented at SPIE Advanced Lithography Symposium* (2016).

14 R. Jonckheere, D. Van den Heuvel, T. Bret, T. Hofmann, J. Magana, I. Aharonson, D. Meshulach, E. Hendrickx, and K. Ronse, "Evidence of printing blank-related defects on EUV masks missed by blank inspection," *Proc. SPIE* **7985**, p. 79850W, 2011.

15 A. Tchikoulaeva, H. Miyai, T. Suzuki, K. Takehisa, H. Kusunose, T. Yamane, T. Terasawa, H. Watanabe, S. Inoue, and I. Mori, "EUV actinic blank inspection: from prototype to production," *Proc. SPIE* **8679**, p. 86790I, 2013.

16 https://www.lasertec.co.jp/en/

17 Z. J. Qi, J. Rankin, E. Narita, and M. Kagawa. "Viability of pattern shift for defect-free EUV photomasks at the 7nm node," *Proc. SPIE* **9635**, p. 96350N, 2015.

18 H. Miyai, T. Suzuki, K. Takehisa, H. Kusunose, T. Yamane, T. Terasawa, H. Watanabe, and I. Mori, "The capability of high magnification review function for EUV actinic blank inspection tool," *Proc. SPIE* **8701**, p. 870118, 2013.

19 R. Capelli, A. Garetto, k. Magnusson, and T. Scherübl, "Scanner arc illumination and impact on EUV photomasks and scanner imaging," *Proc. SPIE* **9231**, p. 923109 (2014).

20 R. H. Miyakawa, W. Zhu, G. Gaines, C. Anderson, and P. Naulleau, "Berkeley MET5 update: commissioning, interferometry, and first prints (Conference Presentation)," *Proc. SPIE* **10809**, p. 1080911, 2018.

21 T. Harada, M. Nakasuji, T. Kimura, Y. Nagata, T. Watanabe, and H. Kinoshita, "The coherent EUV scatterometry microscope for actinic mask inspection and metrology." *Proc. SPIE* **8081**, p. 80810K, 2011.

22 K. A. Goldberg, I. Mochi, S. B. Rekawa, N. S. Smith, J. B. Macdougall, and P. P. Naulleau, "An EUV Fresnel zoneplate mask-imaging microscope for lithography generations reaching 8 nm," *Proc. SPIE* **7969**, p. 796910, 2011.

23 P. Mangat, E. Verduijn, O. R. Wood II, M. P. Benk, A. Wojdyla, and K. A. Goldberg, "Mask blank defect printability comparison using optical and SEM mask and wafer inspection and bright field actinic mask imaging," *Proc. SPIE* **9658**, p. 96580E, 2015.
24 J. Na, D. Lee, C. Do, H. Sim, J. Lee, J. Kim, H. Seo, H. Kim, and C. U. Jeon, "Application of actinic mask review system for the preparation of HVM EUV lithography with defect free mask," *Proc. SPIE* **10145**, p. 101450M, 2017.
25 https://www.lasertec.co.jp/en/products/semiconductor/mask_semicon/basic.html
26 V. Ramaswamy, K. T. Turner, R. L. Engelstad, and E. G. Lovell. "Predicting the influence of trapped particles on EUVL reticle distortion during exposure chucking," *Proc. SPIE* **6349**, p. 634938, 2006.
27 T. Liang, J. Magana, K. Chakravorty, E. Panning, and G. Zhang, "EUV mask infrastructure readiness and gaps for TD and HVM," *Proc. SPIE* **9635**, p. 963509, 2015.
28 H. Miyai, T. Kohyama, T. Suzuki, K. Takehisa, and H. Kusunose, "Actinic patterned mask defect inspection for EUV lithography," *Proc. SPIE* **11148**, p. 111480W, 2019.
29 A. Tchikoulaeva, H. Miyai, T. Kohyama, K. Takehisa, and H. Kusunose, "Enabling EUVL high-volume manufacturing with actinic patterned mask inspection," *Proc. SPIE* **11323**, p. 113231K, 2020.
30 T. Liang, Y. Tezuka, M. Jager, K. Chakravorty, S. Sayan, E. Frendberg, S. Satyanarayana, F. Ghadiali, G. Zhang, and F. Abboud. "EUV mask infrastructure and actinic pattern mask inspection," *Proc. SPIE* **11323**, p. 1132310, 2020.
31 H.J. Levinson, "Impact of reticle imperfections on integrated circuit processing," *Proc. Third Annual Sym. Bay Area Chrome Users Soc.* (BACUS), September 14 and 15, 1983, Sunnyvale, California, as described in Semicond. Int., pp. 22–23 (December, 1983).
32 R. Jonckheere, "Overcoming EUV mask blank defects: what we can, and what we should," *Proc. SPIE* **10454**, p. 104540M, 2017.
33 T. Shimomura, S. Narukawa, T. Abe, T. Takikawa, N. Hayashi, F. Wang, L. Ma, et al., "Electron beam inspection of 16nm HP node EUV masks," *Proc.s SPIE* **8522**, p. 85220, 2012.
34 E. Ma, K. Chou, M. Ebert, X. Liu, W. Ren, X. Hu, M. Maassen, et al., "Multiple beam inspection (MBI) for 7nm node and beyond: technologies and applications," *Proc. SPIE* **10959**, p. 109591R, 2019.
35 I. Mochi, P. Helfenstein, I. Mohacsi, R. Rajendran, D. Kazazis, S. Yoshitake, and Y. Ekinci, "RESCAN: an actinic lensless microscope for defect inspection of EUV reticles," *Journal of Micro/Nanolithography, MEMS, and MOEMS* **16**, no. 4 (2017): 041003.

36 I. Mochi, S. Fernandez, R. Nebling, U. Locans, R. Rajeev, A. Dejkameh, D. Kazazis, et al., "Quantitative characterization of absorber and phase defects on EUV reticles using coherent diffraction imaging," *Journal of Micro/Nanolithography, MEMS, and MOEMS* **19**, no. 1 (2020): 014002.
37 C. Perera and R. Perera. "EUV mask and pellicle metrology for high-volume manufacturing (Conference Presentation)," *Proc. SPIE* **10810**, p. 1081019, 2018.
38 https://www.euvtech.com/euv-pellicle-transmission-tool
39 Research Instruments, EUVL Symposium (2019).
40 D. Brouns, P. Broman, J. van der Horst, R. Lafarre, R. Maas, T. Modderman, R. Notermans, and G. Salmaso, "ASML NXE pellicle update," *Proc. SPIE* **11178**, p. 1117806, 2019.
41 M. Y. Timmermans, M. Mariano, I. Pollentier, O. Richard, C. Huyghebaert, and E. E. Gallagher, "Free-standing carbon nanotube films for extreme ultraviolet pellicle application." *Journal of Micro/Nanolithography, MEMS, and MOEMS* **17**, no. 4 (2018): 043504.
42 R. Brainard, C. Higgins, E. Hassanein, R. Matyi, and A. Wüest, "Film quantum yields of ultrahigh PAG EUV photoresists." *Journal of Photopolymer Science and Technology* **21**, no. 3 (2008): 457–464.
43 G. Denbeaux, Y. Kandel, G. Kane, D. Alvardo, M. Upadhyaya, Y. Khopkar, A. Friz, et al., "Resist outgassing contamination growth results using both photon and electron exposures," *Proc. SPIE* **8679**, p. 86790L, 2013.
44 Y. Kikuchi, K. Katayama, I. Takagi, N. Sugie, T. Takahashi, E. Shiobara, H. Tanaka, et al., "Correlation study on resist outgassing between EUV and e-beam irradiation," *Proc. SPIE* **9048**, p. 90482W, 2014.
45 T. Watanabe and T. Harada, "Research activities of extreme ultraviolet lithography at the university of Hyogo," *Synchrotron Radiation News* **32**, no. 4 (2019): 28–35.

Chapter 9
EUV Lithography Costs

Because the equipment and materials for semiconductor lithography are expensive, the overall cost of lithography has received considerable attention. There are a number of components that contribute to lithography costs (Table 9.1), and each of these will be discussed in more detail in this chapter as they pertain to EUV lithography. Because the impact of mask costs is highly dependent on the number of wafers produced per mask, wafer and mask costs are considered separately, although the situation for EUV lithography is somewhat more complex than for optical lithography, at least for situations in which pellicles are not in use.

Table 9.1 Categories for EUV lithography costs.

Wafer costs	Capital costs: tool prices, throughput, availability
	Maintenance costs
	Metrology, including mask qualification
	Operating costs: consumables, utilities
Mask costs	Blank costs
	Capital costs

9.1 Wafer Costs

9.1.1 Capital costs

EUV exposure tools cost in excess of \$120M.[1,2] In order to realize a positive return on investments in such equipment, a high level of productivity per tool is necessary. The basic capital cost per wafer exposed is

$$\text{cost/wafer} = \frac{C_{ED}}{T_p U}, \tag{9.1}$$

where C_{ED} is the capital depreciation per hour, T_p is the raw throughput of the system (in wafers per hour), and U is the fractional equipment utilization.

Because the numerator in Eq. (9.1) is large, considerable attention has been paid to the denominator, involving throughput and utilization.

Throughput is considered first. The difficulties in producing EUV photons, combined with the need to avoid low exposure doses that would result in excessive line-edge roughness and stochastics-induced defects, has made it challenging to produce scanners that can expose a large number of wafers per day. This pecuniary problem can be understood in more detail by looking at cost models. There are various possible levels of complexity for cost models, with accuracy increasing with greater model complexity. In this section, simple models are used, because they have reasonable accuracy and allow for insight into the factors that drive EUV lithography costs, and they are sufficient for understanding the fundamental issues. As noted, EUV exposure tools are very expensive, even relative to immersion exposure tools, which have long been recognized as among the most expensive pieces of equipment used for semiconductor manufacturing. As with optical photo-clusters, EUV exposure tools are interfaced directly with resist processing equipment, so the capital cost that needs to be considered is the total for the exposure tool plus the resist processing equipment.

For the current discussion, EUV exposure prices are estimated as \$120M. The capital cost of resist processing equipment that is integrated with the exposure tools must also be included in cost calculations. Here, it is assumed that the cost of such resist processing equipment is \$15M. Finally, facilities hardware, estimated here as \$15M per exposure system, should also be included as capital. The brings the total capital cost for a single EUV cluster to ~\$150M. If we further assume five-year depreciation, then the capital depreciation per hour is ~\$3420. With such capital costs, it is clearly important to maximize throughput and utilization.

In Eq. (9.1), T_p is the EUV cluster throughput. Given the very high cost for the exposure tool, the resist processing equipment is usually configured to ensure that the throughput is always limited by the exposure tool. Since tools for resist processing exist that can match the throughput of optical exposure tools, which have much higher throughput than EUV exposure systems, the basic technology is available to ensure that productivity of the EUV lithography cluster is scanner-limited. The basic model for the raw scanner throughput, in wafers per hour, is

$$\text{throughput} = \frac{3600}{t_{OH} + N(t_{exp} + t_{step})}, \tag{9.2}$$

where N is the number of exposure fields per wafer, t_{exp} is the exposure time per field, and t_{step} is the amount of time required to move between fields, including the time for the wafer and reticle stages to accelerate to well-controlled and synchronized exposure scan speeds. The overhead time per

wafer t_{OH} is the time required to swap stages on dual-stage exposure tools. All times on the right side of Eq. (9.2) are measured in seconds, and for this equation it is assumed that only a single reticle is used per wafer.

The exposure time t_{exp} is given as

$$t_{exp} = \frac{H_F + \Delta}{v}, \tag{9.3}$$

where H_F is the height of the scanned field, Δ is the total height of the curved slit, and v is the scanning speed (Fig. 9.1). All dimensions and speeds must consistently refer to either the wafer or reticle. There needs to be a certain amount of scanning startup time, so the stages are moving at a constant and controlled speed when exposure actually occurs, and this time can be included in t_{step}. To incorporate resist sensitivity into the model, the relationship among light intensity, scan speed, and the exposure dose S needs to be established. If $I(y)$ is the light intensity at position y in the slit, then the scan speed v is given by

$$v = \frac{\int_0^H I(y)dy}{S}, \tag{9.4}$$

where H is the slit height. In terms of the average intensity $\bar{I}$,

$$v = \frac{\bar{I}H}{S}. \tag{9.5}$$

From Eq. (9.5), it is clearly seen that high doses and low light intensity result in slow scan speeds, which result in low throughput.

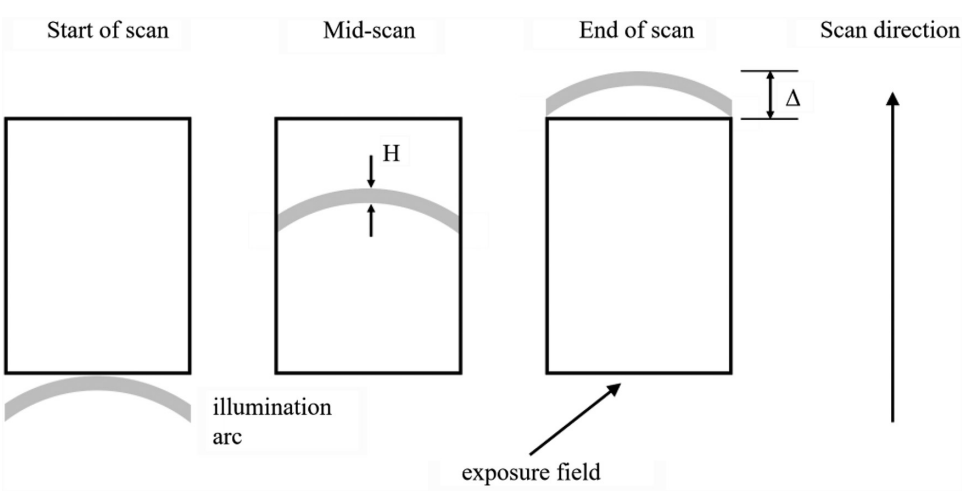

Figure 9.1 Scanning with a curved illumination slit.

Because light intensity tends to scale with the slit height, the product $\bar{I}H$ tends to depend primarily on the total number of photons produced by the light source. The exposure time, in terms of the resist sensitivity, is given by

$$t_{exp} = \left(\frac{S}{\bar{I}H}\right)(H_F + \Delta). \tag{9.6}$$

This equation shows that exposure times are directly proportional to the resist sensitivity and inversely proportional to the source intensity. As discussed in Chapter 4, S cannot be too low without line-edge roughness and defects resulting from high photon shot noise, so there is a need for high-power light sources to maintain process control and cost-effective throughput.

The number of exposure fields N is product dependent. Equipment suppliers often assume full-field (26 mm × 33 mm) exposures and no exposure of partial fields, which results in $N = 96$ shots on 300-mm-diameter wafers. The actual number is typically quite higher. Shown in Fig. 9.2 are the number of shots for a sampling of 160 products in a leading-edge foundry.[3] As can be seen, the number of shots is considerably greater than 96, with sometimes more than double! Note that larger values of N result from smaller exposure field sizes, for which the scan length will typically be shorter. Hence, the throughput reduction accompanying a larger N is somewhat offset by shorter exposure times. This is particularly important for proposed high-NA EUV systems, with half-size exposure fields, which will be discussed further in Chapter 10.

Note that the curvature of the slit on EUV systems does have some impact on throughput, as Δ in Eq. (9.3) would equal H for a rectangular slit. The extra

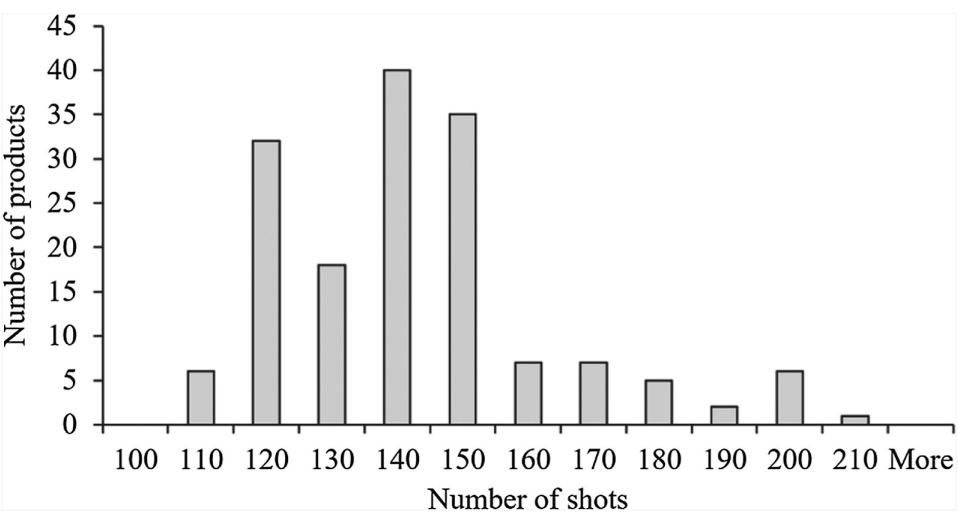

Figure 9.2 A sampling from a foundry of the number of products exposed with numbers of shots. Full-field (26 mm × 33 mm) exposure systems were used.[3]

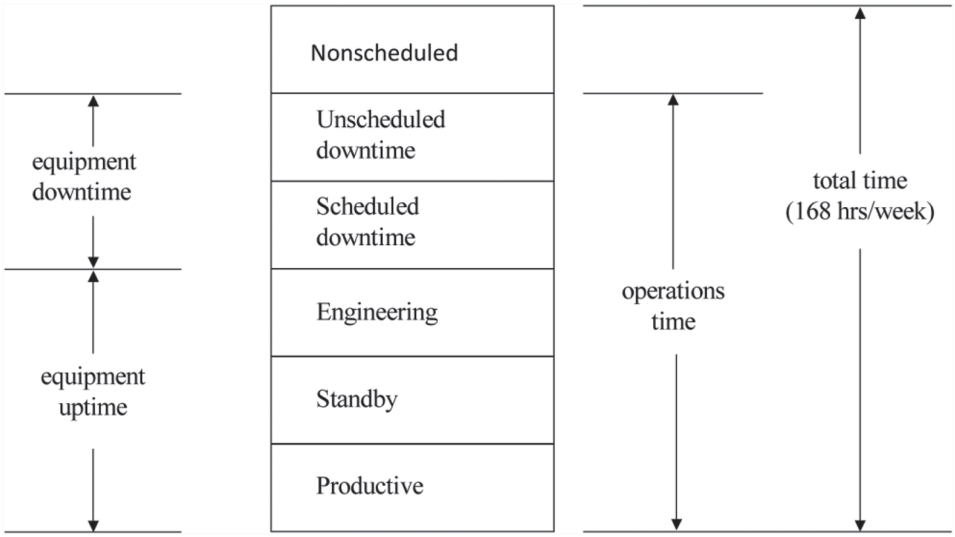

Figure 9.3 Equipment states per SEMI E-10 standard.

scanning distance due to the curvature on 0.33-NA EUV exposure tools is ~2.1 mm at wafer level. If $H_F + H$ would equal 30 mm for a rectangular field situation, then the curvature results in a ~7% increase in t_{exp}.

In addition to throughput, the other key factor in the denominator of Eq. (9.1) is the utilization U, a dimensionless number between 0.0 and 1.0. Total time is divided into states, illustrated in Fig. 9.3. The total amounts of time that tools are in particular states is usually very unequal, and for tools used in high-volume manufacturing, tools are in the productive state for most of the time. For the purposes of calculating the capital cost per wafer,

$$U = \frac{\text{productive time}}{\text{total time}}. \tag{9.7}$$

For EUV lithography, the most significant detractor from productive time is downtime, both scheduled and unscheduled. Downtime is more significant for EUV than for optical lithography, due to a combination of system complexity and the immaturity of EUV technology, although improvements in utilization are occurring with engineering advances over time.

A certain amount of scheduled downtime is required for all exposure tools. Consider, for example, light sources. Excimer lasers require periodic maintenance for replacement of components that degrade over time, such as windows, prisms, and entire discharge chambers. EUV light sources also require periodic scheduled maintenance, although the uptime for EUV light sources has not yet reached the levels achieved with excimer lasers. In fact, the downtime on EUV exposure systems has been dominated by the light source, even though considerable progress has been made.

It was noted in Chapter 3 that the need for good vacuum inside the exposure tool increases the time needed to return a tool to production after the completion of maintenance. Time is needed to recover good vacuum, and more time is needed for EUV exposure tools to reach thermal stability than is needed for optical tools. This results in longer mean-time-to-repair for EUV exposure tools, detracting from productive time.

A benchmark of $U = 0.8$ is usually considered an appropriate minimum level for HVM. With this degree of utilization, and if we assume a throughput of 100 wph, the capital cost per wafer exposure is ~$42.80. While this is considerably higher than the cost of exposing a wafer using immersion lithography, it should be viewed from the perspective that single-exposure EUV lithography will replace process layers previously patterned with triple and quadruple optical exposures, at least for the initial technologies for which EUV lithography is used. Additionally, this has value in cycle time reduction, which is not considered directly in wafer costs.

9.1.2 Maintenance costs

As noted above, equipment downtime has a large impact on the contribution of capital to wafer costs, by reducing the amount of material that can be processed during a given period of time. There are also direct maintenance costs. Exposure tool complexity contributes to reliability challenges, but it also means that the people who repair the tools need to be highly trained. Often, sub-system specialists are needed, which leads to a need for more maintenance technicians. All in all, this contributes to higher maintenance costs for EUV exposure tools than their optical counterparts, apart from higher downtime.

Broken components need to be replaced, and such parts have direct costs that contribute to the cost of maintenance, as do inventory costs for spare parts. Initially for EUV lithography, inventory costs can be considerable. Inventory costs per tool will decline as more EUV exposure systems are operated. Such costs will also become less as the technology matures, and there are fewer sub-system designs, as redesigned sub-systems require additional inventories of replacement parts.

Certain components with high failure rates or rapid degradation need periodic replacement, and these are sometimes categorized as consumables. These are very different in character from other consumables, such as gases and photochemicals, in that maintenance technicians are required for performing replacements, so they are classified as maintenance costs in this book. For EUV exposure systems, components in the light source, particularly collector mirrors and droplet generators, are among those with the shortest lifetimes. These are components that require precision fabrication and are hence costly. Fortunately, most collector mirrors and

droplet generators can be refurbished, significantly reducing replacement costs.

Maintenance is often accomplished with service contracts with the equipment supplier, particularly for very complex pieces of equipment with many components unique to the tool. If such service contracts are paid on an annual basis, then the cost per wafer is dependent on system output. For example, assume an annual maintenance contract that costs $3M per tool, including the cost of replacement components charged to the chip maker. With 100 wph net throughput per tool, and with 80% utilization, the maintenance cost per wafer is $4.28, or about 10% of the capital costs.

9.1.3 Operating costs

As with all advanced exposure tools, EUV scanners have considerable consumable and facility requirements, and several of the most significant of these are discussed in this section. Electricity is one consumable for EUV lithography that has received considerable attention. As noted in Chapter 1, EUV lithography is practiced at a wavelength where there are multilayer coatings with good reflectivity, not where there are sources that can produce EUV light efficiently. Consequently, more electricity is required to power EUV light sources than the excimer lasers or mercury arc lamps of optical lithographic exposure tools.

The amount of electricity required to produce EUV light can be estimated. Over 250 W of collected in-band EUV power is required to achieve cost-effective throughput for early generations of EUV lithography, and much higher powers will be required for subsequent nodes. To achieve this, CO_2 laser power of 20 kW and higher are being used. With laser conversion efficiencies of 2% (electricity to light), ~1 MW of electrical power will be required to sustain light sources producing 250 W of collected in-band power. Such electrical consumption is high but not inconsistent with the electricity requirements of advanced wafer fabs.

However, the electricity to drive the CO_2 lasers is not the only electricity required for EUV light sources. Considerable hydrogen is flowed through EUV source chambers, and the pumps involved consume quite a bit of electricity. The exposure tool exclusive of the source needs electricity for driving stages, maintaining temperature control, mechanical handling of wafers and reticles, along with the associated electronics. It is estimated that ~1.5 MW of electricity is required to power a single EUV exposure tool.[2] The average price of electricity in the United States is currently $0.13/kWh, so the electricity costs for EUV exposure tools run at a rate of ~$195/hr. Again, assuming 100-wph net throughput per tool, with 80% utilization, this results in $2.44/wafer. This cost is non-negligible but substantially less than capital and maintenance costs.

As just noted, hydrogen is a consumable that is needed for EUV exposure tools but not optical ones, and high flows (100s SLM) are required. Very pure hydrogen is needed, since impurities could contaminate the optics, and purity affects cost. Supplying large volumes of hydrogen involves special considerations and not just because of its flammability. Gases in large quantities are often transported in condensed form as liquids, but hydrogen has a very low boiling point (~21 K). As a consequence, on-site generation is often considered.[4] Hydrogen costs are estimated to be ~$1/wafer.

As with optical exposure tools, EUV scanners require cooling water and clean, dry air; and deionized water is required for resist processing. The costs for these need to be included, but they are typically comparable to the costs for optical exposure tools.

Photochemicals include an important class of consumables, typically used on a per-wafer basis. The most expensive chemical is photoresist, with EUV resists costing $5000 per liter or more. Resist coaters use 1–2 cc per wafer (300 mm), with additional amounts for dummy dispenses to maintain low levels of defects. So, resist costs per wafer, in manufacturing, can run $6.00 or more per wafer, assuming the lower volume/wafer resist use. Developer costs can add another $0.20 to $0.50 per wafer. If underlayer films are used, their costs must also be included.

9.1.4 Metrology costs

Much of the metrology for EUV lithography, such as for measuring critical dimensions and overlay, is similar to what is required in optical lithography but with very good capability that is consistent with the fine features being patterned. While mask defect inspection within wafer fabs is usually conducted on a regular basis, there are additional needs for EUV masks. For example, backside defect inspection is needed for EUV masks, something not required for optical masks. Significantly, backside defection inspection capability is needed not only in the mask shop but also in the wafer fab, where it is important to check masks periodically for backside contamination in order to avoid the overlay problems described in prior chapters.

Because high-transmission (≥90%) pellicles are not yet available at the time of the writing of this book, there are use-cases for practicing EUV lithography without pellicles in high-volume manufacturing.[5] In this situation, mask contamination must be checked on a much more frequent basis that for optical tools. Because there is a risk of acquiring defects while transferring masks in and out of the scanner and inspection tools, repeating defects are often detected by wafer defect measurement. The wafers are often specially designed in order to provide the greatest sensitivity for defect detection. An inspection flow is outlined in Fig. 9.4. In addition to the direct metrology costs, there is also an impact to cycle time.

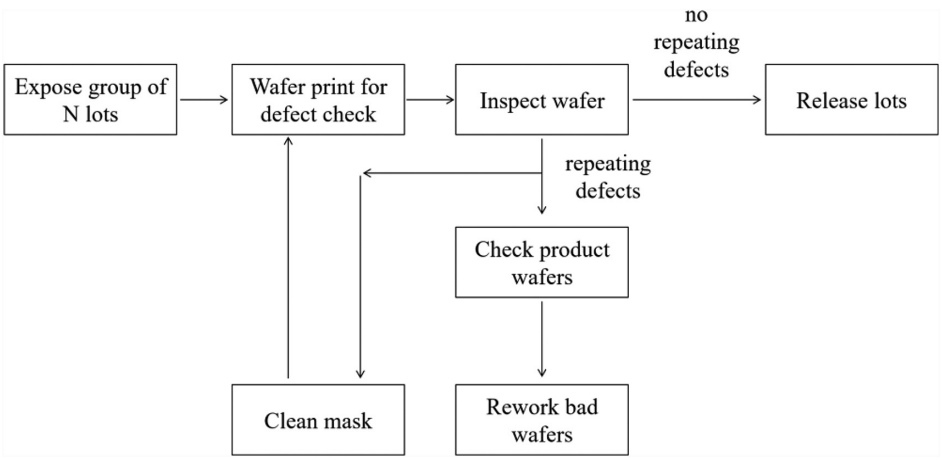

Figure 9.4 Process flow for qualifying masks as defect-free.

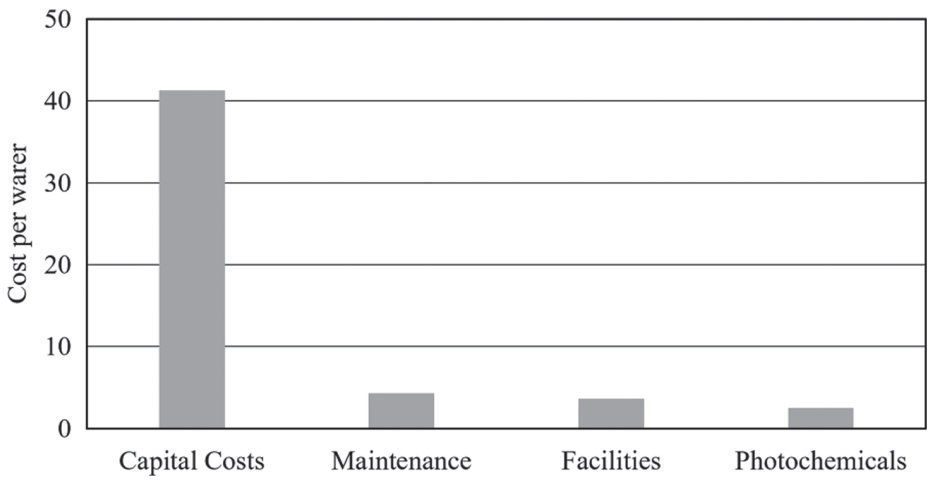

Figure 9.5 Estimated wafer costs for EUV single exposures. Metrology costs are not included, since they depend significantly on the availability of HVM-quality pellicles.

9.1.5 Wafer cost summary

The contributors to wafer costs from EUV lithography ($NA = 0.33$) are summarized in Fig. 9.5. Clearly, capital costs dominate wafer costs. The development and manufacturing of EUV optics, exposure tools, and sources has required considerable investment, and the exposure tools themselves are very complex, so it is not unexpected that EUV systems are more expensive than optical ones. This makes it essential to maximize the reliability and throughput of EUV exposure tools in order to offset their high prices. The costs for future generations of EUV lithography, such as high-NA and multiple patterning, will be discussed in the next chapter.

9.2 Mask Costs

The cost of masks has long been an important consideration for lithography, with costs increasing for each new node. EUV masks are also expensive, costing $250k and more. This cost is driven by a number of factors. To begin, EUV mask blanks are considerably more expensive than optical ones, with low defect blanks that have been qualified with actinic inspection costing $100k or more.[6] As yields improve, this cost can be expected to decrease, but EUV mask blanks will likely continue to cost more than optical blanks due to the need for expensive ULE glass substrates and very tight flatness requirements. Complex film stacks are also deposited on the front-side of EUV masks, which adds to costs even without considering the need for extremely low levels of defects in the multi-layer reflector. Finally, a backside film is needed, unlike the situation that occurs in optical lithography.

The metrology described in Chapter 8 contributes to mask blank costs. Maintaining reflectivity of the multilayer reflector requires measurement at EUV wavelengths, necessitating the use of specialized tools.[7,8] It has also proven necessary to perform defect inspection of the multilayer film stack at EUV wavelengths. Moreover, in order to enable the pattern-shift methodology to cover remaining multilayer defects with absorbers, as described in Chapter 4, defect inspection tools for EUV blanks need to have capability for alignment to mask fiducials and need to have precise stages. This results in greater metrology costs for the defect inspection of EUV mask blanks than for optical ones, for which defect inspection already contributed significantly to cost.

Because LER can transfer more readily from mask to wafer for EUV lithography, due to the higher resolution of the exposure tools, it is important to minimize mask absorber LER. As discussed in Chapter 4, multibeam mask writers have enabled the use of higher e-beam doses to produce small features with acceptable mask absorber LER. The need to use leading-edge mask writers, which cost on the order of $50M, contributes to EUV mask costs.

Defect inspection of patterned masks is a large cost for mask making, even optical ones. When DUV tools are used to inspect EUV masks, the inspection costs are comparable to the costs for optical masks. As noted in Chapter 4, there are benefits to inspecting at EUV wavelengths. Actinic defect inspection tools are more expensive than DUV ones, leading to an increase in inspection costs, although there are benefits in the ability to ensure that masks are defect free. While DUV inspection tools provide reasonable capability for inspecting patterned EUV masks, AIMS tools (used to confirm the printability of defects and assessing the efficacy of defect repair) must necessarily be actinic, making them more expensive than their DUV counterparts.

The contribution of mask costs is highly dependent on the number of wafers exposed per mask. In a study of mask usage at Advanced Micro Devices (AMD), it was found that an average reticle was used to expose only 1800–2400 wafers.[9,10] From a follow-up survey of SEMATECH member companies, it was found that this level of mask usage was not atypical, although there was a wide range of reticle usage that varied according the type of product being produced. With only a few thousand wafers produced per mask, the contribution of masks to die costs would be considerable. Accordingly, EUV lithography is most appropriate for products produced in high volumes. Note that EUV lithography can have advantages when single EUV exposures are replacing three or more optical exposures.

Problems

9.1 At a cost of $250k per mask, show that over 6000 wafers need to be exposed per mask in order to have a mask contribution to wafer costs that is less than the contribution of exposure tool capital costs.

References

1 https://www.eetimes.com/euv-tool-costs-hit-120-million/#
2 https://www.laserfocusworld.com/blogs/article/14039015/how-does-the-laser-technology-in-euv-lithography-work
3 E. R. Hosler, "Next-generation EUV lithography productivity (Conference Presentation)," *SPIE Vol.* **10450**, p. 104500X, 2017.
4 P. Stockman, "EUV lithography adds to increasing hydrogen demand at leading-edge fabs," *Solid State Technology*, pp. 12–16 (March, 2018)
5 M. Lercel, C. Smeets, M. van der Kerkhof, A. Chen, T. van Empel, and V. Banine. "EUV reticle defectivity protection options," *Proc. SPIE* **11148**, p. 111480Y, 2019.
6 https://semiengineering.com/euv-mask-blank-biz-heats-up/
7 D. C. Houser, F. Dong, C. N. Perera, and R. C. C. Perera. "Challenges in constructing EUV metrology tools to qualify the EUV masks for HVM implementation," *Proc. SPIE* **9661**, p. 96610K, 2015.
8 A. Biermanns-Föth, C. Phiesel, T. Missalla, J. Arps, C. Piel, and R. Lebert, "Actinic inband EUV reflectometry AIMER compared to ALS blank qualification and applied to structured masks," *Proc. SPIE* **10957**, p. 109571G, 2019.
9 K. Early and W.H. Arnold, "*Cost of ownership for soft x-ray lithography*," OSA Topical Meeting on EUV Lithography, Monterey, CA (May, 1993).
10 K. Early and W.H. Arnold, "Cost of ownership for 1× proximity x-ray lithography," *Proc. SPIE* **2087**, pp. 340–349 (1993).

Chapter 10
Extending EUV Lithography

Lithographic technology has been extended for several decades through a combination of reduced k_1, increased numerical aperture, shorter wavelengths, and the use of multiple patterning. All of these are possible for EUV lithography and are the topics of this chapter. Because this chapter addresses future technologies that are still undergoing development, much of the text consists of descriptions of known problems that engineers need to solve, rather than explanations of solutions.

10.1 How Low k_1 Can Go

In the 1980s, it was conventional wisdom that k_1 needed to be 0.8 or larger in order to have a manufacturable process. Over time, improvements were made in resists, optics, and process control, and wavefront engineering was introduced, leading to useable values of k_1 for optical lithography below 0.3 and close to the physical limit of 0.25. For the full potential of EUV lithography to be realized, such low values of k_1 also need to be reached. EUV lithography has first been applied in high volume manufacturing to technologies with pitches ~40 nm, which represents a k_1 of 0.49, indicating that opportunities exist for the further reduction of k_1, although there are challenges.

The fabrication of lenses with extraordinarily low aberrations was a significant reason that k_1 could be lowered for optical lithography. Aberrations on EUV exposure tools are below 0.2 nm rms.[1] Although impressive on an absolute scale, this level of aberrations is ~15 mλ, which is much higher than the levels achieved in optical exposure tools (<4 mλ).[2] As a consequence, it will be difficult with EUV lithography to achieve the same low levels of k_1 reached with optical lithography. Nevertheless, with the level of aberrations existing in EUV lenses, substantial reductions below k_1 = 0.49 can still be expected. Further decreases in aberrations in EUV optics can also be expected, even if the same level of aberrations found in state-of-the-art immersion lenses is not achieved. Exactly how small a value of k_1 can be achieved will depend on how successfully the problems discussed in this chapter are solved.

A factor perhaps limiting optical contrast even more than aberrations is the image blur induced by mask 3D effects, as described in Chapter 6. This is particularly true for logic technologies, since multiple pitches need to be patterned, and there are few situations where an imaging solution can be found that eliminates image blur for all patterns. It remains to be seen how limiting this is for EUV lithography, since many solutions, such as new mask absorbers, are in the early stages of development.

Resist capability has long been limiting EUV lithographic performance. As noted in Chapter 5, photoacid diffusion limited resolution on 0.3-NA micro-exposure tools during the development of EUV lithography in the 2000s.[3] As this specific problem was addressed, and resolution improved, line-edge roughness and stochastics-induced defects emerged as the primary issues with EUV resists. Development of resists that could support low values of k_1 proceeded slowly due to a continuing restriction to low exposure doses. As this constraint was relaxed, progress in EUV resists resumed, and capability is approaching 28-nm pitch on 0.33-NA tools, representing $k_1 = 0.34$.

As features continue to shrink, fundamental materials issues become limiting. Consider the molecule, adamantane, that is often used in the formulation of photoresists in order to improve etch resistance, which is illustrated in Fig. 10.1. Also shown are dimensions for process control from the 2020 International Roadmap for Devices and Systems (IRDS) for the year 2025, in which the minimum logic half-pitch is projected to be 10.5 nm. As can be seen, a single molecule of adamantane is a sizable fraction of process control requirements. Moreover, other molecules, such as photoacids, are typically larger than adamantane, while resist polymers are 2–3 nm in diameter. This suggests that the sizes of the molecular units from which EUV resists are made need to be smaller than those currently in chemically amplified resists in order to meet the process control requirements of future

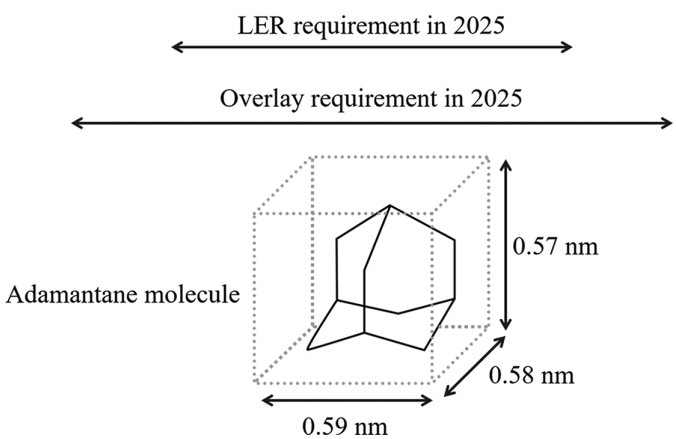

Figure 10.1 Illustration of the molecule, adamantane, along with process control requirements from the 2020 International Roadmap for Devices and Systems (IRDS).

nodes. Alternative resist platforms, such as metal-oxide and scissioning resists, have advantages in this regard, and extension of EUV lithography may require the use of non-chemically-amplified resists.

Tools are available for testing resists in advance of the availability of full-field high-NA EUV exposure systems.[4] A microexposure tool with 0.5 NA is in operation at the Advanced Light Source at Lawrence Berkeley Laboratory under the auspices of the EUREKA consortium.[5] There is also interferometric lithography capability at the Paul Scherrer Institute in Switzerland that can be used for testing resists at very tight pitches.[6]

10.2 Higher NA

Since ASML has already announced their intention to produce EUV exposure tools at 0.55 NA, the discussion in this section will focus on the issues associated with lithography at that specific NA.[7] Many of the issues associated with an increase in NA were encountered during similar transitions with optical lithography. For example, the depth of focus decreases with larger numerical aperture, according to the following well-known relationship:

$$\text{depth of focus} = k_2(\lambda/NA^2). \tag{10.1}$$

If we assume that $k_2 = 1.0$, then the depth of focus is only 45 nm for $NA = 0.55$. As noted in Chapter 7, the effect of resist thickness on the depth of focus is essentially the full thickness of the resist film, unlike the situation that occurs in optical lithography. This increases the difficulties associated with focus for high-NA EUV lithography, and there will need to be considerable effort regarding focus control. Not all activities will be specific to lithography; wafer flatness and chemical-mechanical polishing (CMP) capabilities will also need to be consistent with the overall focus budget.

Before proceeding with examination of the other engineering challenges of high-NA EUV lithography, some specific characteristics of the 0.55-NA tool already shared by ASML and Zeiss are discussed. The mask 3D issues that were a topic of Chapter 6 have had a significant influence on the architecture of high-NA EUV tools. As noted in Chapter 3, the chief ray angle needs to be sufficiently large so that the mask can be illuminated through the full angular spread of the illumination, and this range increases with NA at the mask. (It should be noted that the NA at the mask is the NA at the wafer divided by the lens reduction.) As can be seen in Table 10.1, the largest angle of incidence on the mask would be much larger at 0.55 NA than at 0.33 NA, assuming 4× lens reduction in both cases. This would make the mask 3D issues described in Chapter 6 significantly worse.

One way to mitigate mask 3D effects is to increase the lens reduction, and increasing lens reduction to 8× is the approach being taken by ASML and Zeiss.

Table 10.1 Chief-ray angles and maximum angles of incidence on the mask for various combinations of NA (wafer level) and lens reduction.[8]

NA	Reduction	Chief-ray angle	Maximum angle
0.33	4×	6°	10.8°
0.55	4×	9°	17.3°
0.55	8×	5.3°	9.5°

However, with 8× lens reduction, field size on the wafer must necessarily be reduced without an increase of reticle size, and such an increase is currently not planned. To avoid decreasing the wafer field area by 4×, an anamorphic lens design has been proposed, with lens reduction different in the x and y directions: 8× in the y direction and 4× in the x direction. The 26 mm × 33 mm field size of 4× isomorphic systems becomes 26 mm × 16.5 mm on the wafer. This enables the benefit of higher lens reduction to reduce the mask 3D effects substantially, while reducing field size by only 2× .

This change of field size has many ramifications. Stitching of exposure fields will be required for chips larger than 26 mm × 16.5 mm. With stitching, every layer requires two (or more) masks and exposures. For contact and via layers, it is straightforward to assign features entirely to one mask or another, but for interconnects, it may be necessary for features to cross the boundary between the two exposures. Maintaining good dimensional control across the boundary is a lithographic challenge when stitching is necessary. The problem of printing dies that are larger than a single exposure field have also been considered for the fabrication of displays and other devices, so stitching is being addressed by many lithographers.[9]

There is also a mix-and-match issue with reduced field sizes for EUV exposure tools, regardless of die size, since it would undesirable to reduce the field size on optical tools used for patterning noncritical layers, as this would reduce optical tool productivity. This results in a situation where the EUV and optical exposure fields are no longer concentric (Fig. 10.2). This can lead to interesting overlay control problems.[10] For example, suppose that there is a small magnification error in the EUV exposure field. This will lead to a discontinuity in the overlay in the middle of the field in the y direction, which is difficult to fit using a third-order intrafield overlay model (Fig. 10.3). Such considerations are particularly important for large die which require stitching, as several types of overlay errors will lead to mis-aligned features at the stitch boundary.

Pattern placement needs to be controlled at stitching boundaries, illustrated in Fig. 10.4, particularly when there are circuit features that cross boundaries. For Fig. 10.4(a), measurement of the pattern placement of Subfield 1 relative to Subfield 2 is possible only in the outer scribe area, while

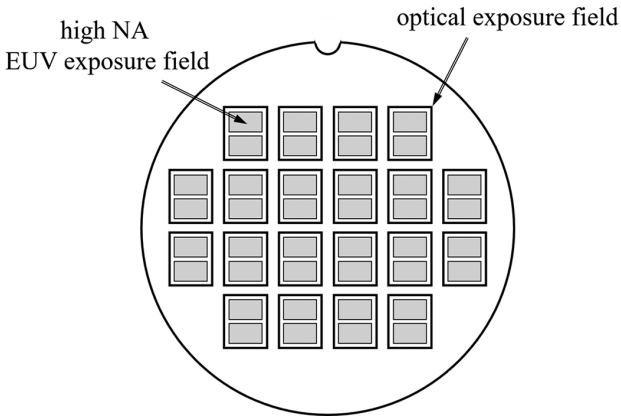

Figure 10.2 Illustration of mix-and-match between small-field, high-NA EUV exposure tools and full-field optical tools.

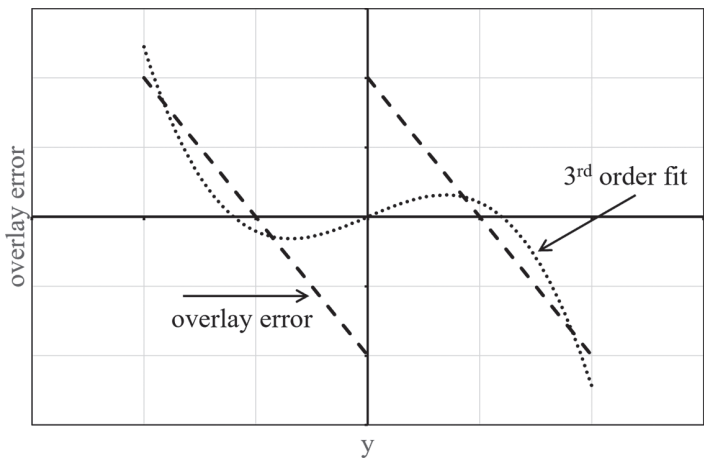

Figure 10.3 Overlay error in the *y* direction when the small-field EUV exposures have a magnification error.

such measurements can be made across the stitching boundary when the two subfields overlap, as in Fig. 10.4(b), and in-die overlay measurement structures will be required. The analysis of overlay data from overlapping fields requires the use of models different from those described in Chapter 7. An example of this is shown in Fig. 10.5.

Overlapping exposures are done routinely in optical lithography,[11,12] but it is somewhat more complex for EUV lithography. As discussed in Chapter 4, a "black border" is frequently added to EUV masks to address the residual reflectance from absorbers on the masks. The etching of the multilayer to create a black border will cause mechanical distortion of the mask near the border due to stress in the multilayers,[13] and this needs to be taken into account when

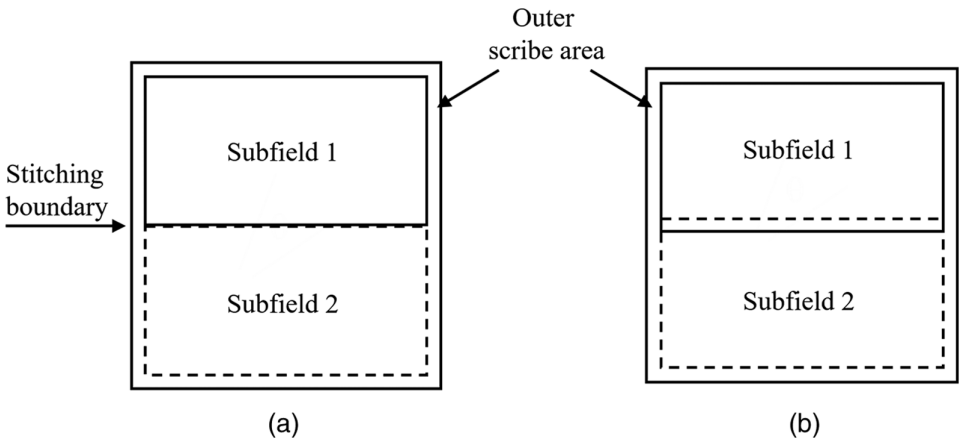

Figure 10.4 Examples of stitched fields: (a) Abutted fields and (b) overlapping fields.

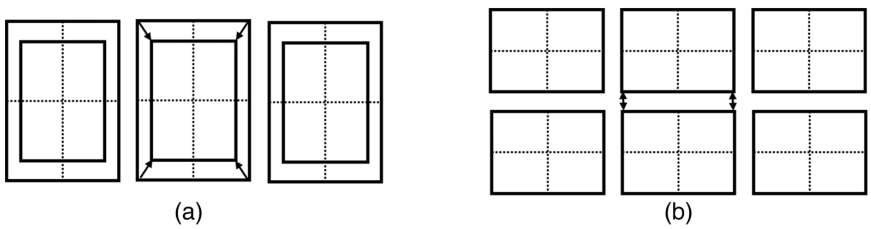

Figure 10.5 (a) Overlay errors for a magnification error for layer-to-layer overlay. (b) Overlay errors for stitching when each exposure has a magnification error.

stitching. The impact of such distortion can be different between the stitching and non-stitching cases. Consider, for example, second-order distortion induced by the etching of the multilayer. Such distortions could substantially replicate mask-to-mask, so it will not contribute significantly to overlay errors in the non-stitching case, between two exposures on EUV tools. On the other hand, if the second-order distortion has opposite curvature at the tops and bottoms of reticles, this distortion will contribute to overlay errors in the case of stitching.

There will be an effect resulting from the residual light that reflects from the absorber on the mask. It is usually intended for areas in the overlapping regions to be exposed with just one mask, but residual reflected light from both subfields will expose the overlapping regions. Compensation for this effect needs to be included in the OPC.

As is typical, larger-NA optical systems require sizeable optical elements, and this is certainly the case for high-NA EUV lithography. A comparison is given in Table 10.2 of the largest mirrors in the EUV projection optics produced by Zeiss for 0.33 NA and 0.55 NA. With the considerable weight of the large mirrors, manual handling is not an option. A robot used to handle large mirrors for high NA is shown in Fig. 10.6. For EUV, metrology must be

Table 10.2 Parameters of large mirrors in EUV projection optics.[14]

NA	Diameter of largest mirror	Mass of heaviest mirror
0.33	0.65 m	40 kg
0.55	1.2 m	360 kg

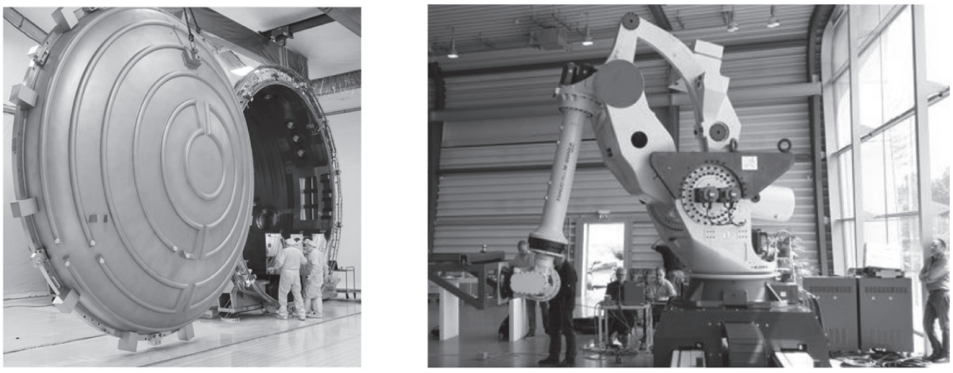

Vacuum vessel for mirror metrology

Robot for handling large mirrors

Figure 10.6 Pictures of equipment for mirror metrology at Zeiss for 0.55-NA projection optics.[14]

done in a vacuum, and very large vacuum vessels are needed to test the mirrors intended for use in 0.55-NA optics (Fig. 10.6).

With 8× lens reduction in the scan direction, for a given wafer stage scan speed, the reticle stage in an 8× reduction system must scan faster by a factor of two than for a 4× reduction system. Although scan speeds in EUV tools are typically slower than with optical scanners, primarily due to the weakness of EUV light sources, improvements in scan capability are still required to ensure good throughput for high-NA EUV exposure tools because of the increased speed for the reticle stage required by the increase in lens reduction. In particular, it is important to improve stage acceleration, which contributes to t_{step} in Eq. (9.2). With the smaller field size leading effectively to a doubling of the number of exposure fields, minimizing t_{step} is important for maintaining good throughput.

In going to 0.55 NA, the transmission of the overall optical train has been improved, which helps to reduce the impact on throughput of the higher-exposure doses needed to pattern small features (see Eq. (9.5)). More light is also delivered to the wafer due to the larger collection angle of the lens, which enables extra light to be collected into the projection optics. Additionally,

there are significant innovations in the designs of the illumination and projection optics.

A change in optical design of significance to practicing lithographers was the move to high-NA optics with a central obscuration. As described in Chapter 1 and illustrated in Fig. 6.16, the reflectivity of multilayer mirrors is dependent on the angle of incidence, and reflectance falls off steeply at large angles. Extending the type of lens used in 0.33 NA to a high NA would result in such large angles, leading to lenses with lower transmission and greater apodization (Fig. 10.7).

The central obscuration will have an effect on imaging. As can be seen in Fig. 10.8, the central obscuration will not have an impact on tight pitches with off-axis illumination, but looser pitches will be affected. This is relevant for mask layouts with a range of pitches, which is typical for logic devices. This obscuration does not necessarily result in a degradation of imaging, but it is something that will be a factor in the computation of OPC for high-NA EUV lithography.

The throughput predicted by ASML for 0.55-NA tools is shown in Fig. 10.9, as a function of source power divided by the resist sensitivity. This graph can be understood in terms of Eq. (9.5), as the factor $\bar{I}H$ is proportional to the source power. At the highest source powers and lowest exposure doses, the 0.55-NA tool throughput becomes limited by the fastest speed at which the

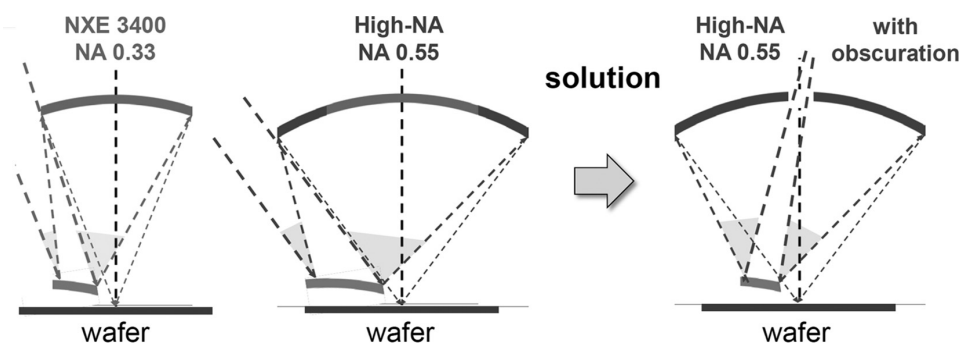

Figure 10.7 The final two mirrors in EUV projection optics, illustrating the reduction in the range of deflection angles through the use of a central obscuration.[14]

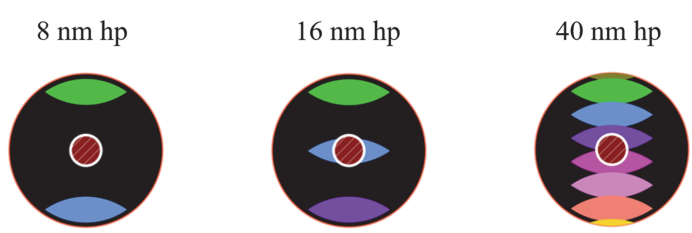

Figure 10.8 Illustration of the diffraction orders inside the projection pupil for a single pole of illumination and for multiple pitches.[15]

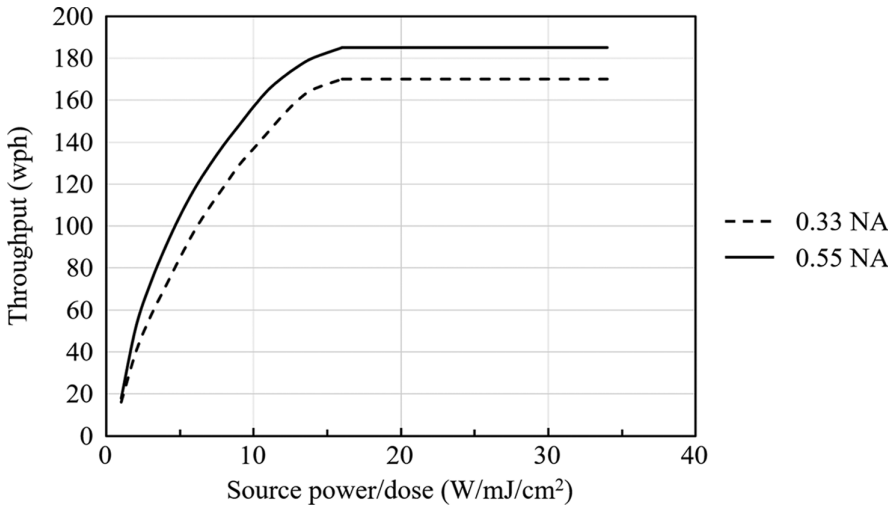

Figure 10.9 Predicted throughput (in wafers per hour) of EUV exposure tools.[17]

stages can be scanned. According to the International Roadmap for Devices and Systems (IRDS), exposure doses will be ~100 mJ/cm^2 for the nodes at which high-NA systems will be used,[16] implying that light sources will be need to be >1 kW before high-NA exposure tool throughput will be limited by the stages.

The throughputs graphed in Fig. 10.9 are based on the assumption that the number of fields for 0.55-NA exposure tools is 188 (roughly double that of 0.33-NA tools, for which the tool supplier's assumption is 96 shots per wafer). However, for real products in production using 26-mm $\times$ 33-mm-size fields, the number of shots is typically ~150, since it is usually not possible to utilize 100% of the available exposure field while always including integral numbers of dies (see Fig. 9.2). Lithographers are long accustomed to actual throughputs in wafer fabs being less than the reference throughput providing by equipment suppliers, in large measure due to less than 100% efficient field utilization. A similar situation will also occur for the half-fields of 0.55-NA tools.

A study was made of the actual number of shots per wafer that can be expected when using exposure tools with half-fields, using actual die sizes for products fabricated in a silicon foundry.[18] Assuming that the reticle contains only integral numbers of dies (so stitching is not involved), the distribution of shot counts is shown in Fig. 10.10. As can be seen, there are many die sizes that would lead to more exposures than the 188 shots assumed for Fig. 10.9.

As numerical apertures increased over time in optical lithography, the impact of polarization on image quality was recognized,[19] and eventually polarization control became a capability of the illumination systems on immersion exposure tools.[20] The importance of polarization can be understood

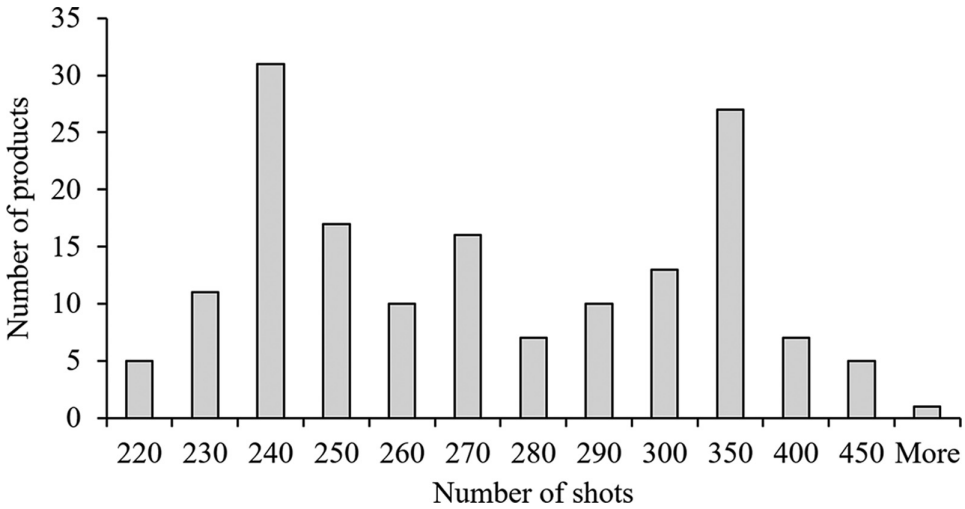

Figure 10.10 Number of shots for a half-field exposure system, based on actual die sizes for products made in a leading-edge foundry.[18]

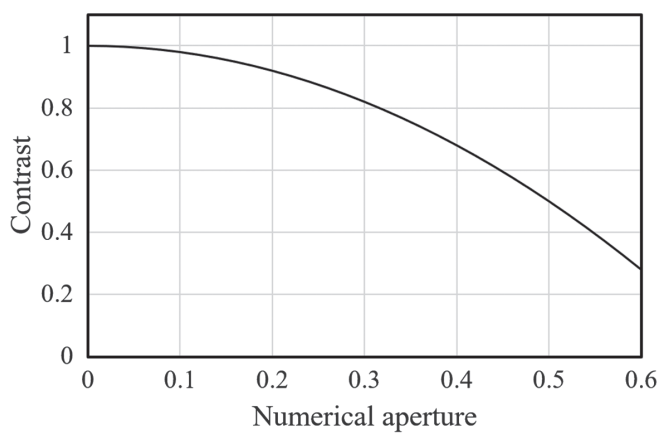

Figure 10.11 Image contrast for interfering plane waves with P-polarization, at the maximum angles within the numerical aperture.[19]

by considering an image formed by two light rays that are incident on a wafer. For S-polarized (also referred to as transverse electric or TE polarized) light, the polarization vectors for the two waves are parallel and complete interference between the two waves occurs. However, for P-polarization (transverse magnetic or TM polarization), the polarization vectors have orthogonal components that do not interfere, which reduces image contrast (Fig. 10.11; see Problem 10.1). This contrast reduction becomes appreciable as the numerical aperture increases from 0.33 to 0.55.

The resist issues discussed in Chapter 5 are very germane for high-NA EUV lithography. Stochastic issues are mitigated to some degree by the high resolution of the lens that maintains the image log-slope, but photon shot noise, secondary electron range, and molecular-level effects remain relevant. In some ways they are even more pertinent, because high-NA EUV lithography will be applied to very small features. However, if a higher NA enables further scaling beyond the resolution limit of 0.33-NA exposure tools, transistor costs may continue to decrease. Using high-NA simply to mitigate resist stochastics is a very expensive solution. The price of a high-NA exposure tool is not publicly available information, but estimates can be made. Historically, exposure tool prices have increased ~20% per year.[21] If we assume that high-NA EUV tools will be available in volume in the year 2024 and that 0.33-NA EUV exposure tools cost $120M in the year 2020, then the estimated price of a high-NA exposure tool is ~$250M. Note that substantial investments are needed to produce high-NA tools (see Fig. 10.6). Continuing improvements in throughput will be needed to offset the costs of high-NA tools.

10.3 Shorter EUV Wavelengths

Shorter wavelengths are another path taken previously to extend lithography to better resolutions, so it is natural to consider such a route for EUV lithography. As noted in Chapter 1, EUV lithography at a wavelength ~11 nm was considered, using Mo/Be multilayer reflectors. However, beryllium was rejected as a material for multilayers due to concerns regarding that metal's toxicity, but other multilayers have been studied as potential reflectors for $\lambda < 13.5$ nm. In particular, it has been found that multilayers consisting of lanthanum, boron, and various compounds of each, have reflectances of 70–80% at wavelengths ~6.7nm.[22,23]

Although good reflectivity at $\lambda = 6.7$ nm has been achieved at near-normal incidence with La/B multilayers, high-NA lenses require good reflectivity over a wide range of angles (Fig. 10.7). Calculated reflectivity is shown in Fig. 10.12 for a Mo/Si multilayer film at $\lambda = 13.5$ nm and a La/B multilayer film at $\lambda = 6.7$ nm. As can be seen, high reflectivity can be maintained over a much smaller range of angles with the La/B multilayer reflector. This will limit the numerical aperture of lenses for lithography at $\lambda = 6.7$ nm, unless a highly innovative lens design is invented.

Light sources will also have to be developed for providing good power at $\lambda = 6.7$ nm. Gadolinium has been shown to have good efficiency as a fuel for producing photons at the desired wavelength from laser-produced plasmas,[24] but its high melting temperature (1312°C) suggests that targets will need to be different from the liquid droplets of tin-based sources used to produce photons at $\lambda = 13.5$ nm. Free-electron lasers can be designed to operate at $\lambda = 6.7$ nm.

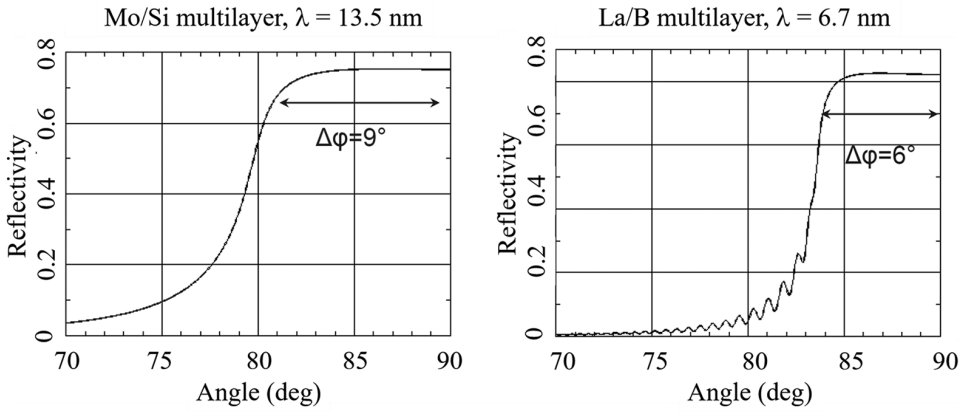

Figure 10.12 Calculated reflectivity vs. angle for a Mo/Si multilayer film at λ = 13.5 nm and a La/B multilayer film at λ = 6.7 nm. Normal incidence is 90°.[22]

10.4 EUV Multiple Patterning

As with optical lithography, EUV lithography can be extended by means of multiple patterning, based on the same principles. Many techniques, such as methodologies for layout, have already been developed and can be reapplied at smaller dimensions (although improved process control will be needed). On the other hand, EUV multiple patterning is an expensive solution. With EUV single patterning costs approximately equal to optical triple patterning, the addition of a single EUV exposure is a considerable expense, which can make solutions used for optical multiple patterning impractical for EUV lithography. For example, consider the use of multiple patterning for the formation of metal interconnects.[25] Spacer processes are often used for the formation of line/space patterns with very tight pitches without requiring very tight line-to-line overlay, but very good overlay is required for the block masks used to form metal line tip-to-tip features and for the masking steps used to eliminate unwanted lines. This can be appreciated by considering the process flow depicted in Fig. 10.13. Lines and spaces are formed using a spacer process. Block masks are then used to retain volumes that are not to be filled with metal. However, process tolerances for the blocks are tight. If we consider a line/space pitch of 20 nm, with equal lines and spaces, then control requirements for the gap between the block and the adjacent feature is ±5 nm, which includes dimensional control for the block feature and the lines, plus overlay. Tight process control requirements have been avoided in optical lithography by the use of self-aligned processes. For example, if the etch process for the "red" material in Fig. 10.13 has a slow etch rate for the "blue" material, and vice versa, the process window can be widened substantially. However, this process would require a minimum of two block masks to work. Thus, using this self-aligned approach requires a minimum of

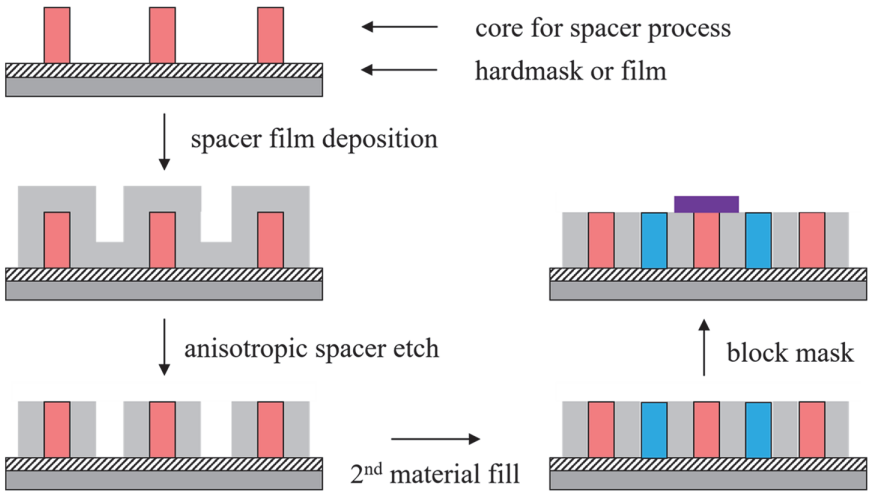

Figure 10.13 Process flow for patterning an interconnect layer using a spacer process.

three masking steps. Multiple patterning for EUV lithography can imply triple or quadruple patterning, rather than double patterning,[25] which will be expensive. However, given the high prices for high-NA exposure tools, it may make sense to use multiple patterning with less expensive, and perhaps depreciated, 0.33-NA exposure tools.

10.5 The Future of EUV Lithography

As discussed in this chapter, there are multiple approaches that can enable the extension of EUV lithography. These include higher numerical apertures, shorter wavelengths, and multiple patterning. The development of higher-NA optics and exposure tools has been progressing for several years, and EUV multiple patterning is an extension of well-known methods. For these reasons, it is reasonable to expect that EUV lithography can be extended to meet the requirements contained in the International Roadmap for Devices and Systems (IRDS). With multiple technical options, technology choices will be driven to a significant degree by economics.

Optimism notwithstanding, there are many problems that need to be solved to extend EUV lithography. Resist stochastics need to be contained at the low levels required to yield highly integrated circuits, and the limits to resolution due to the range of photoelectrons and secondary electrons still need to be understood. It will be necessary to address resolution issues at the molecular level. Process control, particularly focus and edge placement, will be very challenging. Nevertheless, it is quite reasonable to expect that engineers will continue to find solutions to technical progress, and EUV lithography capability will continue to improve for at least the next decade.

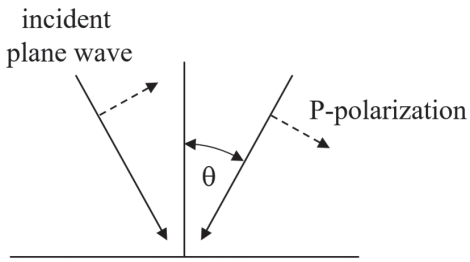

Figure 10.14 Interfering plane waves.

Problems

10.1 Show that the Rayleigh resolution of an EUV (λ = 13.5 nm) lithography system with an NA = 0.33 is 25 nm and that the Rayleigh depth of focus is 124 nm. Show that the resolution and depth-of-focus are 15 nm and 45 nm, respectively, for an EUV lens with 0.55 NA.

10.2 Consider the situation in Fig. 10.14. For two interfering plane waves, show that the resulting contrast for P-polarized plane waves is reduced by a factor of $\cos(2\theta)$ relative to the contrast for S-polarization (for which the polarization vectors are perpendicular to the page).

References

1 M. van de Kerkhof, H. Jasper, L. Levasier, R. Peeters, R. van Es, J. Bosker, A. Zdravkov, et al., "Enabling sub-10nm node lithography: presenting the NXE: 3400B EUV scanner," *Proc. SPIE* **10143**, p. 101430D, 2017.

2 B. Geh, "EUVL: the natural evolution of optical microlithography," *Proc. SPIE* **10957**, p. 1095705, 2019.

3 T. I. Wallow, R. Kim, B. La Fontaine, P. P. Naulleau, C. N. Anderson, and R. L. Sandberg, "Progress in EUV photoresist technology." In *23rd European Mask and Lithography Conference*, pp. 1–9. VDE, 2007.

4 P. Naulleau, P., C. Anderson, M. Benk, W. Chao, K. Goldberg, E. Gullikson, M. Miyakawa, and A. Wojdyla. "EUV extendibility research at Berkeley Lab." In *2017 International Symposium on VLSI Technology, Systems and Application (VLSI-TSA)*, pp. 1–2. IEEE, 2017.

5 R. Miyakawa, C. Anderson, W. Zhu, G. Gaines, J. Gamsby, C. Cork, G. Jones, et al., "Achieving diffraction-limited performance on the Berkeley MET5," *Proc. SPIE* **10957**, p. 109571X, 2019.

6 X. Wang, L-T. Tseng, T. Allenet, I. Mochi, M. Vockenhuber, C.-K. Yeh, L. van Lent-Protasova, J. G. Santaclara, R. Custers, and Y. Ekinci, "Progress in EUV resists status towards high-NA EUV lithography," *Proc. SPIE* **11323**, p. 113230C, 2020.

7 S. Kim, R. Chalykh, H. Kim, S. Lee, C. Park, M. Hwang, J. Park, et al., "Progress in EUV lithography toward manufacturing," *Proc. SPIE* **10143**, p. 1014306, 2017.
8 C. Zahlten, P. Gräupner, J. van Schoot, P. Kürz, J. Stoeldraijer, Bernhard Kneer, and W. Kaiser, "High-NA EUV lithography: pushing the limits." *Proc. SPIE* **11177**, p. 111770B, 2019.
9 M. May, B. Minghetti, J. Dépré, Y. Blancquaert, P. Lam, C. Lapeyre, and J. Lee, "Stitched overlay evaluation and improvement for large field applications," *Proc. SPIE* **11325**, p. 113251L, 2020.
10 M. E. Preil, T. M. Manchester, A. M. Minvielle, and R. J. Chung, "Minimization of total overlay errors when matching nonconcentric exposure fields," *Proc. SPIE* **2197**, pp. 753–769, 1994.
11 S. Owa, H. Nagasaka, Y. Ishii, K. Shiraishi, and S. Hirukawa, "Full-field exposure tools for immersion lithography," *Proc. SPIE* **5754**, pp. 655–668, 2005.
12 C. P. Auschnitt, J. D. Morillo, and R. J. Yerdon, "Combined level-to-level and within-level overlay control," *Proc. SPIE* **4689**, pp. 248–260, 2002
13 N. Davydova, R. de Kruif, N. Fukugami, S. Kondo, V. Philipsen, E. van Setten, B. Connolly, et al., "Impact of an etched EUV mask black border on imaging and overlay," *Proc. SPIE* **8522**, p. 852206, 2012.
14 C. Zahlten, P. Gräupner, J. van Schoot, P. Kürz, J. Stoeldraijer, Bernhard Kneer, and W. Kaiser, "High-NA EUV lithography: pushing the limits." *Proc. SPIE* **11177**, p. 111770B, 2019.
15 A. Erdmann, P. Evanschitzky, G. Bottiglieri, E. van Setten, and T. Fliervoet, "3D mask effects in high NA EUV imaging," *Proc. SPIE* **10957**, p. 109570Z, 2019.
16 https://irds.ieee.org/
17 J. van Schoot, E. van Setten, K. Troost, F. Bornebroek, R. van Ballegoij, S. Lok, J. Stoeldraijer, et al., "High-NA EUV lithography exposure tool progress," *Proc. SPIE* **10957**, p. 1095707, 2019.
18 E. R. Hosler, "Next-generation EUV lithography productivity (Conference Presentation)," *Proc. SPIE* **10450**, p. 104500X, 2017.
19 D.G. Flagello and A.E. Rosenbluth, "Vector diffraction analysis of phase-mask imaging in photoresist films," *Proc. SPIE* **1927**, pp. 395–412 (1993).
20 H. Jasper, T. Modderman, M. van de Kerkhof, C. Wagner, J. Mulkens, W. de Boeij, E. van Setten, and B. Kneer. "Immersion lithography with an ultrahigh-NA in-line catadioptric lens and a high-transmission flexible polarization illumination system," *Proc. SPIE* **6154**, p. 61541W (2006).
21 H. J. Levinson, *Principles of Lithography*, SPIE Press, 2019.
22 V. Banine, A. Yakunin, D. Tuerke, and U. Dinger. "Opportunity to extend EUV lithography to a shorter wavelength," *2013 International Symposium on Extreme Ultraviolet Lithography (Brussel)*, 2012, with permission of the authors; http://euvlsymposium.lbl.gov/pdf/2012/pres/V.%20Banine.pdf

23 I. A Makhotkin, E. Zoethout, E. Louis, A. M. Yakunin, S. Müllender, and F. Bijkerk, "Spectral properties of La/B-based multilayer mirrors near the boron K absorption edge." *Optics Express* **20**, no. 11 (2012): 11778–11786.
24 A. von Wezyk, K. Andrianov, T. Wilhein, and K. Bergmann. "Target materials for efficient plasma-based extreme ultraviolet sources in the range of 6 to 8 nm," *Journal of Physics D: Applied Physics* **52**, no. 50 (2019): 505202.
25 S. Decoster, F. Lazzarino, D. Vangoidsenhoven, V. M. B. Carballo, A-H. Tamaddon, E. Kesters, and C. Lorant. "Exploration of EUV-based self-aligned multipatterning options targeting pitches below 20nm," *Proc. SPIE* **10960**, p. 109600L, 2019.

Index

2-bar structure, 150
3D effects, 147

A
aberrations, 54, 143, 174
ABICS E120, 190
actinic blank inspection, 189
ACTIS A150, 194
Aerial Image Measurement System (AIMS), 191
AGILE, 176
anamorphic lens, 218
attenuated phase-shifting masks, 99
attenuation length, 73
azimuthal angle, 59

B
backside nonflatness, 171
black border, 75
Bragg condition, 6

C
capital cost, 203
carbon contamination, 47
carbon nanotube, 92
central obscuration, 222
chemical gradient, 157
CO_2 laser, 19
collector mirror, 22
contrast, 154
convection, 46
conversion efficiencies, 25
Corning, 57
curved slit, 59
Cymer, 29

D
debris, 18, 20
defect printability, 82
discharge-produced plasma (DPP) sources, 32, 34
droplet generator, 27
dynamic gas lock (DGL), 48

E
electron backscatter, 86
electrostatic chuck, 50
emissivity, 90
Energetiq, 33
etched multilayer, 101
EUV Limited Liability Corporation (LLC), 2

F
field facet mirror, 51
flare, 144, 145
free-electron laser (FEL), 36
  seeded EUV, 38
fuel, 18

G
Gigaphoton, 24
GPU-based computing, 161

grid-matching correction for thickness variation (GMC-TV), 83

H
high-NA EUV lithography, 217
horizontal–vertical correction, 142
hot spots, 181

I
in-plane distortion, 170
intermediate focus, 21
intermixing, 10
inverse lithography technology (ILT), 160

L
laser-produced plasma (LPP), 17
Lasertec BASIC, 193
Lasertec M1350, 188
LER transfer function (LTF), 85
line-edge roughness (LER), 177

M
mag-lev stage, 61
magnetic bearings, 61
mask error enhancement factor (MEEF), 146
mask flatness, 83
mask nonflatness, 170
mask roughness, 84
master-oscillator power-amplifier (MOPA), 20
mix and match, 218
multilayer reflector, 225
multilayer reflectors, 4
multiple patterning, 226

N
nonrandom variation, 178

O
OPC, 143
  process window, 153
out-of-band light, 30
overlay measurement sampling, 171
overlay model, 171

P
pattern-shift, 80
pedestal, 26
pellicles, 87
phase contrast imaging, 188
phase defect, 78
polarization, 223
pre-pulse, 25
process variability (PV) band, 158
ptychography, 195
pulse duration, 20
pupil facet mirror, 52

R
regenerative amplifier free-electron laser (RAFEL), 39
reticle backside defect inspection, 193
reticle backside inspection (RBI), 194
reticle pod, 97

S
scattered light, 54
self-compression, 32
self-amplified spontaneous emission (SASE), 38
Sematech, 2
SEMI Standards, 76
standoff distance, 97
stannane, 22
stitching, 218
sub-resolution assist feature (SRAF), 151, 160

T
telecentricity, 150
temperature control, 46, 173
Teron Phasur, 188
tin hydride, 22
tip-to-tip feature, 146

U
ultra-low expansion glass, 57
ultra-low thermal expansion material (ULTEM), 75

V
vacuum, 45

W
wall plug efficiency, 20

Y
yield, 178

Z
zonal ring approximation method (ZRAM), 146
zoneplate, 193
Z-pinch light sources, 33

Harry J. Levinson is currently an independent lithography consultant and Principal Lithographer at HJL Lithography. He has spent most of his career working in the field of lithography, starting at AMD. He also held positions at Sierra Semiconductor and IBM before returning to AMD in 1994. When wafer operations were spun off from AMD, he moved to GLOBALFOUNDRIES and worked there until mid-2018. During the course of his career, Levinson has applied lithography to many different technologies, including bipolar memories, 64-Mb and 256-Mb DRAM development, the manufacturing of application-specific integrated circuits, thin-film heads for magnetic recording, flash memories and advanced logic. He was one of the first users of 5× steppers in Silicon Valley and was an early participant in 248-nm, 193-nm, and EUV lithography.

Levinson served for several years as the chairman of the USA Lithography Technology Working Group that participated in the generation of the lithography chapter of the International Technology Roadmap for Semiconductors. He has published numerous articles on lithographic science, on topics ranging from thin-film optical effects and metrics for imaging, to overlay and process control, and he is the author of two other books: *Lithography Process Control* and *Principles of Lithography*. He holds over 70 US patents. Levinson is an SPIE Fellow, previously chaired the SPIE Publications Committee, and served on SPIE's Board of Directors. In recognition of his contributions to SPIE, he received the Society's 2014 Directors' Award.

He has a B.S. in engineering from Cornell University and a Ph.D. in physics from the University of Pennsylvania. His Ph.D. thesis, titled "Resonances and Collective Effects in Photoemission," addressed certain phenomena involving the interactions of light and matter. For this work, he received the Wayne B. Nottingham Prize in surface science.